AUTHOR: OKON, E.P.

TITLE: Preparation, characterization and carrier gas transport characteristics of inorganic and organic membranes for application in lactic acid esterification with ethanol.

YEAR: 2018

OpenAIR citation: OKON, E.P. 2018. Preparation, characterization and carrier gas transport characteristics of inorganic and organic membranes for application in lactic acid esterification with ethanol. Robert Gordon University, PhD thesis.

This work was submitted to- and approved by Robert Gordon University in partial fulfilment of the following degree:
Doctor of Philosophy, School of Engineering

PREPARATION, CHARACTERIZATION AND CARRIER GAS TRANSPORT CHARACTERISTICS OF INORGANIC AND ORGANIC MEMBRANES FOR APPLICATION IN LACTIC ACID ESTERIFICATION WITH ETHANOL

BY

EDIDIONG PRIMUS OKON

A THESIS SUBMITTED IN PARTIAL FULFILMENT OF THE

REQUIREMENTS OF THE

ROBERT GORDON UNIVERSITY

FOR THE DEGREE OF DOCTOR OF PHILOSOPHY

SCHOOL OF ENGINEERING

ROBERT GORDON UNIVERSITY

ABERDEEN, SCOTLAND, UNITED KINGDOM

APRIL 2018

ABSTRACT

Ethyl lactate (EL) plays a major role as green solvent and also a replacement for most petrochemical solvents. The esterification process of lactic acid and ethanol to produce EL is an equilibrium-limiting reaction and the selective removal of one of the reaction products can be improved using a membrane reactor and when coupled with a heterogeneous catalyst offers an opportunity for process intensification. This thesis investigates the batch process esterification reaction involving lactic acid (LA) and ethanol (EL) in the presence of a water selective membrane using different cation-exchange resin catalysts. The product was analysed using gas chromatograph coupled with mass spectrometry detector (GC-MS). The analytical methods used for the characterisation of the cation-exchange resins and membrane include Fourier transform infrared coupled with attenuated total reflectance (FTIR-ATR), scanning electron microscopy attached to energy dispersive analyser (SEM/EDAX), Liquid nitrogen physisorption and nuclear magnetic resonance (NMR) respectively. A novel method was developed for carrying out esterification reaction in a gaseous phase system using a flat sheet polymeric membrane. Prior to the esterification reaction, different carrier gases were tested with ceramic membrane to determine the suitable carrier gases for the analysis of esterification product. The four carrier gases used for the permeation test were argon (Ar), helium (He), carbon dioxide (CO_2) and nitrogen (N_2). A 15nm pore size commercially available tubular ceramic support, consisting of 77%Al_2O_3 and 23%TiO_2 with the porosity of 45% was used for the carrier gas investigation. The support was modified with silica based on the sol-gel dip-coating techniques.

The dip-coated membrane exhibited a higher molar flux with He (0.046mol $m^{-2}s^{-1}$) and Ar (0.037mol $m^{-2}s^{-1}$) with a much lower flux for N_2 (0.037mol $m^{-2}s^{-1}$) and CO_2 (0.035 mol $m^{-2}s^{-1}$) at 0.30 bar. Helium gas with the highest permeation rate were identified as the suitable carrier gas for the analysis of esterification product with GC-MS. The esterification reaction in the presence of four cation-exchange resins to produce ethyl lactate was carried out between 60-160 ºC in a batch and membrane processes to determine the effectiveness resin catalysts for LA esterification. The effect of external mass transfer diffusion limitation between the liquid components and the resin catalysts was avoided by increasing the agitation time of the esterification reaction. The percentage conversion rate of the lactic acid feed from the batch process esterification was found to be in the range of 98.6 to 99.8%. The reaction kinetics of the esterification reaction was described based on two simplified mechanisms of Langmuir Hinshelwood model to describe the adsorption components on the surface of the catalysts. The lactic acid feed gave a conversion rate of up to 100 % confirming the effectiveness of the acetate membrane impregnated resin catalysts in the selective removal of water for the separation of ethyl lactate. The significance of producing ethyl lactate through batch process intensified by a water-selective membrane processes can be recommended for industrial LA production.

Index Keywords: Carrier gas, Cation-exchange resin, Esterification, Ethyl lactate, Characterisation, Adsorption isotherm, Inorganic membrane, membrane reactor, Lactic acid, Permeability, Ethanol, cellulose acetate membrane, process intensification and Langmuir Hinshelwood model and Conversion.

DEDICATION

I will like to dedicate my thesis to the Glory of the almighty God the supreme provider of all my needs and to my entire family members especially to my husband, my parents and siblings for the family support throughout this period.

ACKNOWLEDGEMENT

I would like to return all glory to the almighty God for his faithfulness, enablement, strength, grace, favour and mercy throughout this period. ‘’Abasi Amanam obogo Sosongo’’ (Lord you have done so much, I thank you).

My profound appreciation goes to my supervisor Professor Edward Gobina for his professional support and guidance throughout this period.

My heartfelt appreciation goes to my beloved parents Sir and Lady Primus Eyo Okon, for their encouragement, support and prayers which gives me the strength throughout this journey.

My deepest appreciation goes to my husband Mr Emmanuel Dan for his invaluable support, patience, prayers and encouragement throughout this period. Words alone cannot explain how much I am indebted to you.

My warm appreciation goes to my siblings (the boys) Mr Kufre, Mr Nsikan, Mr Imo, Fr. Anthony and Joseph for all their support, encouragement and prayers.

My sincere appreciation goes to my sponsor, the Petroleum Technology Development Fund (P.T.D.F), a parastatal of the Nigerian government for funding this research and for all their support towards the success of this work.

I would also like to appreciate my colleagues at the CPIMT lab, RGU for their useful contributions during this period. Also, the technical staff of the School of Engineering, RGU are also acknowledged.

Table of Contents

Appendix A: Relevant Publications Resulting from this work
Appendix B: Published Conference Proceedings
Appendix C: Conferences Attended

List of Figures

List of Tables

NOMENCLATURE

Abbreviations

Symbols	***Description***
Ar	Argon
ATR	Attenuated Total Reflectance
BET	Brunauer-Emmett-Teller
BJH	Barrette-Joyner-Halenda
BOC	British Oxygen Company
CA	Cellulose Acetate
CO_2	Carbon dioxide
COSHH	Control of Substances Hazardous to Health
CFCs	Chlorofluorocarbons
CI	Chemical Ionisation
CMC	Carboxyl Methyl Cellulose
CPIMT	Centre for Process Integration and Membrane Technology
CTI	Ceramiques Techniques et Industrielles
DMR	Distributor Membrane Reactor
E	Ethanol
EDAX	Energy Dispersive x-ray analyser
EI	Electron Ionisation
EL	Ethyl Lactate
EMR	Extractor Membrane Reactor
EPA	Environmental Protection Agency
ER	Eley-Rideal model
FDA	Food and Drug Administration
FID	Flame Ionisation detector
FTIR	Fourier Transform Infrared
GC	Gas Chromatography
GHG	Greenhouse gas
He	Helium
ICP-MS	Inductive Coupled Plasma-Mass spectrometry
IUPAC	International Union of Pure and Applied Chemistry
LA	Lactic acid
LH	Langmuir Hinshelwood model
MSD	Mass Spectrometry Detector
N_2	Nitrogen

NIST	National Institute of Standards and Technology
NMR	Nuclear Magnetic Resonance
PCs	Principal Components
PH	Pseudo-homogeneous model
RGU	Robert Gordon University
S	Vacant site on catalyst surface
SEM	Scanning Electron Microscopy
STP	Standard Temperature and Pressure
TCD	Thermal conductivity detector
TGA	Thermogravimetric analyser
iTR	Infrared total reflection
TIC	Total Ion Currents
U.S.A	United State of America
VOCs	Volatile Organic Compounds
W	Water

Description	***Units***
Part per million	(ppm)
Thickness	(m)
Permeability	(mol m $m^{-2}s^{-1}Pa^{-1}$)
Membrane surface area	(m^2)
Initial weight of the membrane	(g)
Final weight of the membrane	(g)
Pore diameter	(m)
Temperature	(K)
Universal Gas molar constant	(8.314 J mol^{-1} K^{-1})
Initial concentration of lactic acid	(mol dm^{-3})
Final concentration of lactic acid	(mol dm^{-3})
Activation energy	(J mol^{-1} K^{-1})
Reaction rate	(mol/g)
Pore radius	(m)
Equilibrium constant	-
Gas flux	(mol m^{-2} s^{-1})
Flow rate	($mols^{-1}$)
Absolute pressure	(Pa)

Atmospheric pressure	(Pa)
Mean pressure	(bar)
Gas molecular weight	(g/mol)
Gas Permeance	$(molm^{-2}s^{-1}Pa^{-1})$
Arrhenius-type pre-exponential factor	(m^2s^{-1})
Molecular volume at the normal boiling point	(cm^3mol^{-1})
Effective Knudsen diffusion	(m^2s^{-1})
Pressure drop across the membrane	(bar)
Molecular diffusion coefficient	$(m^2\,s^{-1})$
Knudsen diffusion	(m^2/s)
Viscous Flow	-
Knudsen number	-
Relative vapour pressure	(Pa)
Saturation vapour pressure	(Pa)
Partial vapour pressure	(Pa)
Concentration	(mol/dm^3)
Initial molar amount of lactic acid	(mol)
Adsorption coefficient	-
Rate constant	$(molg^{-1}min^{-1})$
Reaction equilibrium constant	-
Concentration of i at the surface of the catalyst	(mol/L)
Time	(min)
Reaction rate	$(molg^{-1}min^{-1})$
The concentration of vacant site on catalyst surface	(mol/dm^3)
Constant representing viscous flow	-
Constant representing Knudsen flow	-
Mean pressure	(bar)
Outer diameter	(mm)
Inner diameter	(mm)

Greek Symbols

Words	***Units***
Angstrom	(m)
Mean free path	(m)
Tortuosity	(m)
Porosity	(%)
Association coefficient	-
Selectivity of species A with respect to B	-
Gas viscosity	(Pa s^{-1})
Pi	(2.134)
Theoretical density of alumina	($3.95x10^{-3}kgm^{-2}$)

CONVERSIONS

Pressure	1 bar = 100,000 Pa 1MPa = 1bar = 1.967 atm. Gauge pressure (bar) = 0.1x100,000 Pa
Temperature	(T) K = T °C + 273K

CHAPTER 1

1.0 INTRODUCTION

In the past decades, there has been an increasing interest in lactate esters due to emphasis on eco-friendly solvents from bio-derived sources [1]. Ethyl lactate (EL) plays a major role as one of the drop-in solvents in the petroleum and chemical industries. It is normally used in various industries including food, pharmaceutical, paint, adhesive, agriculture and can dissolve a wide range of organic compounds including acetic acid and cellulose [1]. In chemical reactions which are equilibrium limited such as esterification, etherification, transesterification and hydrolysis, in order to improve the productivity, it is possible to shift the position of equilibrium towards the products by using an excess of reactants or by removal of one of the product. However, using an excess of reactant may result in increased cost of the subsequent separation as the product stream is in diluted form. In several industrial chemical reactions, for example water is a by-product which has a severe inhibitor effect on catalytic activity causing low productivity and conversion [2]. Esterification reaction is an equilibrium limited reaction and therefore has a slow reaction rate. It produces ester and water as product from the two reactants of alcohol with acid. Although esterification is said to have a long history with numerous reports concerning the performance of different catalysts and kinetics of several esters synthesis, there are still numerous essential problems that remain unsolved including the fact that the water generated during esterification reaction may have an adverse effect on the conversion of the feed [3].

The use of homogeneous catalysts such as hydrochloric acid and sulfuric acid in esterification reactions suffers some drawbacks including the fact that the yield of ethyl lactate is limited by thermodynamic equilibrium and homogeneous catalysts cause a lot of problems including equipment corrosion and acid contamination of the esterification product [4-5]. Nevertheless, different approaches have been employed in order to improve the yield of the ethyl lactate product in the reaction mixture and this include; application of catalysts and increasing the reaction temperature using a higher ratio of alcohol to lactic acid [4]. Aside from thermodynamic equilibrium limitation, reaction yields are also limited by other factors such as mass transfer and heat that is generated during the esterification. Such limitations can be removed by altering the reaction design to enhance the product yield [6]. Heterogeneous catalysts and membrane technology have recently attracted a lot of attention in the equilibrium process of esterification reaction due to their numerous advantages including higher yield of the product, minimum corrosion problems and cost effectiveness [7-9].

Membrane reactor is a device that can incorporate both separation and reaction in one single unit. It can also be described as an intensive reactive system [10]. This study is therefore a novel technology for the process intensification of lactic acid (LA) and ethanol (ET) using membrane and different heterogeneous catalysts to combine reaction and separation in one unit. Current literatures have shown that ethyl lactate yield can be enhanced using cation-exchange resins and membrane [11-12]. Therefore, the aim of this research is to test and perform esterification reaction of lactic acid and ethanol to produce ethyl lactate (EL) by incorporating different cation-exchange resins impregnated flat sheet cellulose acetate membrane, for solving the thermodynamic problems to obtain a higher percentage conversion of lactic acid and ethanol [13]. The reason for carrying out the study is to confirm the effect of membrane in thermodynamic equilibrium shift. Although work has been carried out on the batch process esterification of lactic acid with different alcohols [14] including isobutanol, propanol and methanol catalysed by homogeneous catalysts, very few work have mentioned the synthesis of ethyl lactate with different heterogeneous catalysts such as cation-exchange resin [13].

Although much work has been carried out for the separation of the produced ethyl lactate and water using membrane, only few work have mentioned the impregnation of cellulose acetate membrane with resin catalysts with the use of a carrier sweep gas on the permeate side of the reactor to assist in the shift of the thermodynamic equilibrium process. Also, several studies have used membrane processes for the esterification process by employing a vacuum on the permeate side of the reactor for selective removal of water to obtain a higher conversion of the ester product, but much work has not been carried out for the esterification reaction in gas phase system with the use of a sweep gas [15-16]. In the present work, the process intensification by the use of carrier gas to determine the shift in chemical equilibrium to the forward reaction and avoid the reverse reaction.

1.1 Research Aim and Objectives of the Present Study

1.1.1 Research Aim

The aim of this work is to carry out the batch process esterification of lactic acid (LA) and ethanol (ET) in the presence of different solid cation-exchange resins attached to cellulose acetate membrane in a gas phase system to improve the conversion of LA and ET feed, thus avoiding the use of corrosive homogeneous acid catalysts such as sulphuric acid.

1.1.2 Research Objectives

The major objectives of the present study in line with the aim of the research are listed below:

1) Compare the carrier gas transport with tubular inorganic porous ceramic support and dip-coated membranes at high and at room temperature for comparison before employing the most appropriate carrier gases for the analysis of lactic acid feed conversion.

2) To investigate the esterification reaction using different methods: cellulose acetate membrane attached to cation-exchange resins by employing carrier gases on the permeate side of the reactor and a batch process esterification method with different cation-exchange resin at the same temperatures for comparison.

3) To investigate the effect of esterification parameters such as catalyst performance, temperature, catalyst type, catalyst loading and the mass transfer resistance.

4) To investigate the reaction kinetics for EL production at different temperatures with different catalysts and identifying the components with the strongest adsorption strength on the surface of the resin catalysts using FTIR-ATR method, and correlate with the experimental data.

5) Develop a mathematical description based on two simplified mechanisms of Langmuir-Hinshelwood model that could best describe the esterification reaction mechanism.

6) To investigate the mechanical strength and thermal stability of the resin catalysts and characterise both the resin catalysts and membrane pore size and specific surface area and compare with literature.

1.2 Motivation and Relevance of the Present Study to the Industry

The utilisation of a catalytic membrane reactor for effecting equilibrium shift in esterification process is recently a new research field which has attracted a lot of attention in the chemical process industries as an energy saving and eco-friendly technology [10]. The present research will serve as an avenue for the choice of catalysts and membranes in eliminating the thermodynamic equilibrium problems of esterification reaction in the chemical process industries for enhancing the conversion of LA and ET.

1.2.1 Motivation

The motivation for this research involves the need to enhance LA and ET esterification process by avoiding the use of homogeneous acid catalysts and enhance ethyl lactate product yields through process intensification by combined reaction and water separation.

1.3 Structure of this Research

This section details the structure of the thesis and is divided into 7 chapters:

Chapter 1 presents an overview of the thermodynamic equilibrium limitation problems in the use of homogeneous acid catalysts in the chemical industry.

Chapter 2 provides the literature review, discusses the existing problems, and the different analytical techniques used to solve these problems. It also gives the general background on the use of EL solvent in the different industries and the need for the production of this solvent. It provides the advantages of heterogeneous catalyst over homogeneous catalyst and catalytic membrane including the thermal stability and mechanical strength. It looks at the use of equilibrium shifting in esterification reaction for the enhancement of the yield of the EL product.

Chapter 3 presents the carrier gas permeation tests for the commercial available alumina support and silica membranes at various temperatures using a membrane reactor. The experimental design, material selection, preparation, methodology are presented.

Chapter 4 gives the details of the batch esterification process catalysed by different cation-exchange resins and cellulose acetate membrane impregnated resin catalysts at various temperatures. The material selection, reactor fabrication description, experimental procedure, Gas chromatography-mass spectrometry analysis of esterification product with suitable carrier gas. The chapter also presents the results and discussion for the batch and process intensification. The chapter also describe the effect of the esterification parameters including; effect of temperature, catalysts type, catalysts loading, swelling nature of catalysts and effect of mass transfer.

Chapter 5 presents the reaction kinetics of the EL by identification of the components with the strongest adsorption strength on the surface of the cation-exchange resins catalysts using Fourier transform infrared spectroscopy coupled attenuated total reflection (FTIR-ATR) and proton nuclear magnetic resonance (^{1}H NMR). The development of mathematical model based on two simplified mechanisms of Langmuir-Hinshelwood model for the description of the esterification reaction mechanism are also presented for the chapter. The material selection, experimental procedure, results and discussion are also presented for the chapter.

Chapter 6 presents the thermal stability, mechanical strength and characterisation of both the cation-exchange resin and membrane by analysing the pore size distribution and surface area using different methods including Liquid nitrogen adsorption/desorption and scanning electron microscopy-energy dispersive analysis of x-ray (SEM/EDAX). Material selection, methodology, results and discussion are presented.

Chapter 7 presents the conclusion, recommendation for future work.

CHAPTER 2

2.0 Literature Review

2.1 Background

The recent dependence on fossil fuels for energy and production of chemicals has attracted significant attention on the possible solution for alternative renewable resources for production of biofuels and chemicals due to the adverse effects of greenhouse emissions of the climate [17-19]. Biomass-based feedstock provides a sustainable alternative. However, conversion possibilities and technologies must be further realized to offer practical and economically possible sources of production [19]. The generation of product through biotechnological processes makes it possible to discover and explore several chemical routes to obtain products with very low environmental impact and high yields [17,20]. Most solvents being used today are manufactured from fossil fuel feedstock obtained from natural gas and crude oil [21]. Studies have shown that the use of some fossil fuel derived solvents may result in serious health and environmental problems. One of the major challenges faced by the petrochemical industry has been the replacement of traditional petroleum-derived solvents [22-23]. It is therefore essential to develop new solvents with less toxic and hazardous characteristics [23]. These types of chemicals are referred to as green solvents. Green in the sense that it is aimed at reducing the environmental effect resulting from their use in chemical production. Solvent are generally regarded as green if they are recyclable, non-toxic, possess a low vapour pressure, inexpensive and can readily dissolve other organic compounds [23]. Although the use of solvents with potential detrimental effects on the environment is decreasing due to strongest international environmental regulations, the industrial need for solvents will lead to an increasing demand for new solvents [24]. The world demand for solvents is approaching 20 million tons per year, and forecasts suggest that this demand will increase in the coming years [24]. Because of this, there is a need for alternative solvents including solvents from lactate ester family (e.g ethyl lactate) that could replace the current ones because of their low volatility and low environmental and toxic nature. Despite the numerous good qualities, the use of EL solvent in the large scale industrial processes is very limited [124].

The U.S Food and Drug Administration (U.S FDA) has approved the use of EL in food products due to its low toxicity [1,24-25]. The industrial preparation of lactate esters by esterification of an acid with alcohol in the presence of a catalyst, involves two processes [26]. The first step is the reaction itself which stops when the equilibrium is reached, whilst the second step is separation of the products from the equilibrium mixture containing the unconverted reactant and product [26-28]. Ethyl lactate can be produced and efficiently separated with high conversions by esterification process of lactic acid and excess amount of reactant [5] and through the use of a single operational step from the reactive distillation process [29]. Although the reactive distillation concept is based on the combination of distillation and reaction processes in order to increase the performance of both processes, this is an old method [30]. On the other hand, the use of membranes and membrane technologies for the selective removal of product to shift the equilibrium towards higher yield of the product in equilibrium limiting reaction system have attracted a lot of attention [11,31-32]. Some researchers have focused on the water-permeable membrane reactors which can be applied to liquid-phase reversible reactions such as esterification of carboxylic acids with alcohols due to lack of suitable membranes with good permselectivity and solvent resistance [12,32-34]. Although several studies have employed heterogeneous catalyst such as cation-exchange resin for lactic acid esterification with different alcohols, much work has not been done with lactic acid and ethanol catalysed by cation-exchange resin [4,13,15] and membrane reactor in a gas-phase system. Several studies have been performed on the kinetics of ethyl lactate production since 1954, but there has been a recent resurgence of interest due to its numerous functions as a green solvent and an alternative to the traditional solvents derived from petroleum products [26]. Figure 2.1 presents the schematic diagram of the overview of the research, the two main approaches have been used for the investigation of ethyl lactate separation, methodologies and the different cation-exchange resins.

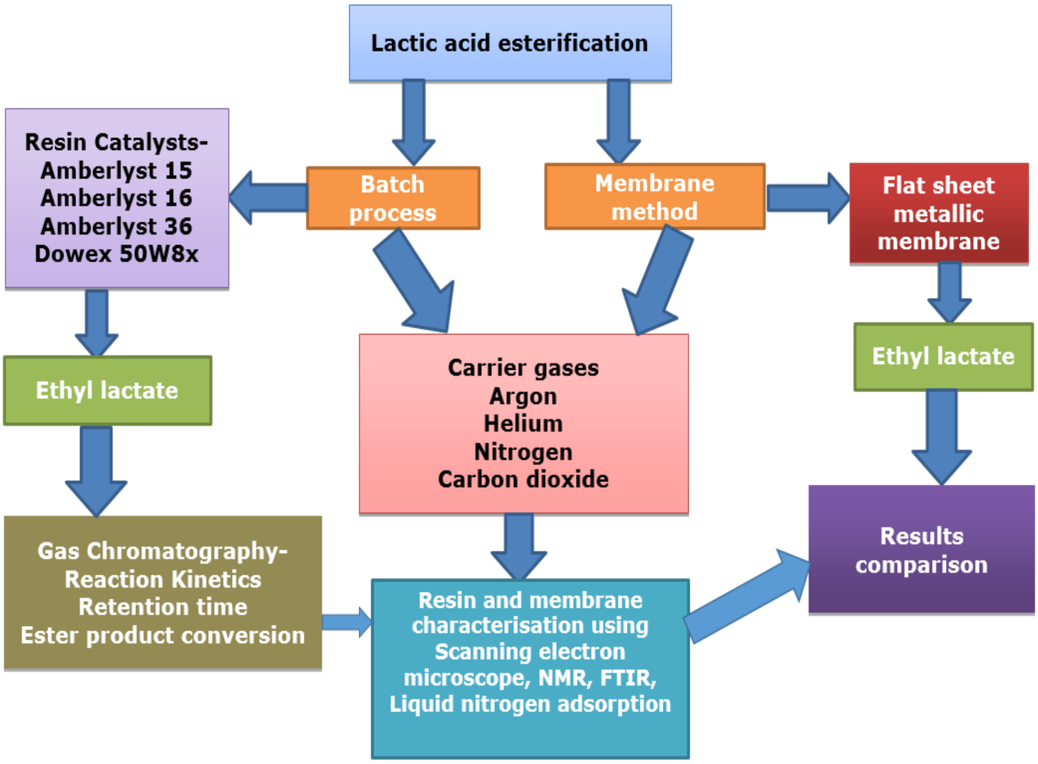

Figure 2.1: Schematic diagram of the research overview.

2.2 Applications of Ethyl Lactate

Organic esters are an important class of chemicals and have shown a wide range of applications in different areas including plasticizers, perfumes, pharmaceuticals, flavours, paint, agricultural, solvent and chemicals intermediates [7, 35-37]. Figure 2.2 shows the demand for EL by application.

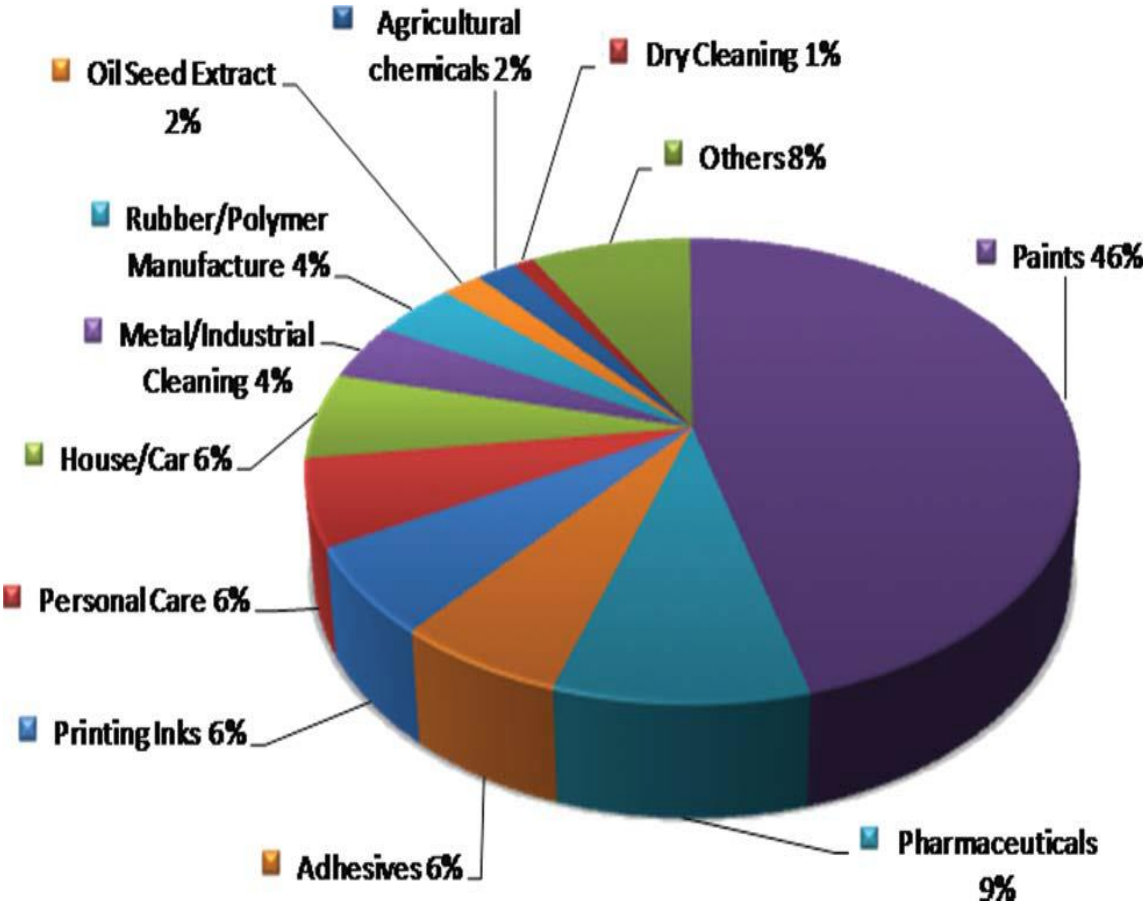

Figure 2.2: Solvent demand by industries [37].

Besides the numerous applications, esters obtained from nonedible crops are potential candidates in carbon emission reduction. In other to ascertain the future energy supplies and environmental impact, low-carbon technologies will play a major role in this regard. In addition to the energy efficiency, different types of renewable energy systems, as well as new technologies in the production of new solvent including solvent from biomass sources that could replace the petroleum solvent must be widely developed to reach the emission targets [7]. From figure 2.3 it can be seen that solvents obtained from the biomass sources contribute a higher percentage in the greenhouse gas (GHG) emission reduction process.

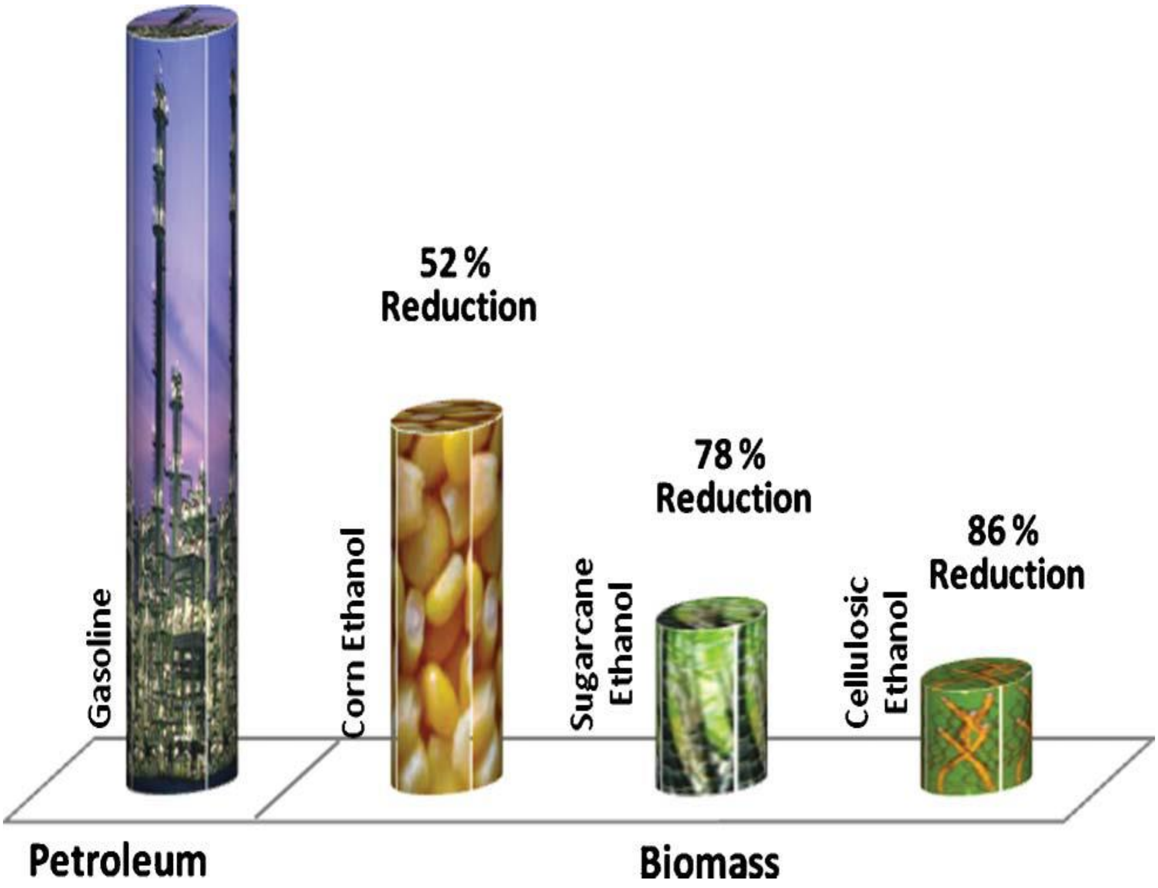

Figure 2.3: Percentage change in the greenhouse emission reduction process [37].

2.3 Renewable Resources for Ethyl Lactate Production

The use of biomass as a source of energy has a lot of advantages including: (i) biomass as a low sulphur content, (ii) biomass usage could be a way to prevent more carbon dioxide emissions in the atmosphere as it does not increase the atmospheric carbon dioxide level [38]. The major application of biomass is for food and has been estimated to feed the world's population of about 9 billion people in 2050. Carbohydrates are said to be an abundant renewable resource and are considered as an important feedstock for the future green chemistry as shown in figure 2.4 [36,39]. From figure 2.4, it can be seen that lactic acid and ethanol are obtained from carbohydrate which is biomass and can be converted into a pure ethyl lactate. Nevertheless, research has shown that biorefineries could be the basis for the new bio-industry. Although biorefinery and petroleum refinery are similar, the major difference is that biorefinery utilises biomass for the conversion to product energy chemical and materials instead of crude oil in the case of a petroleum [37].

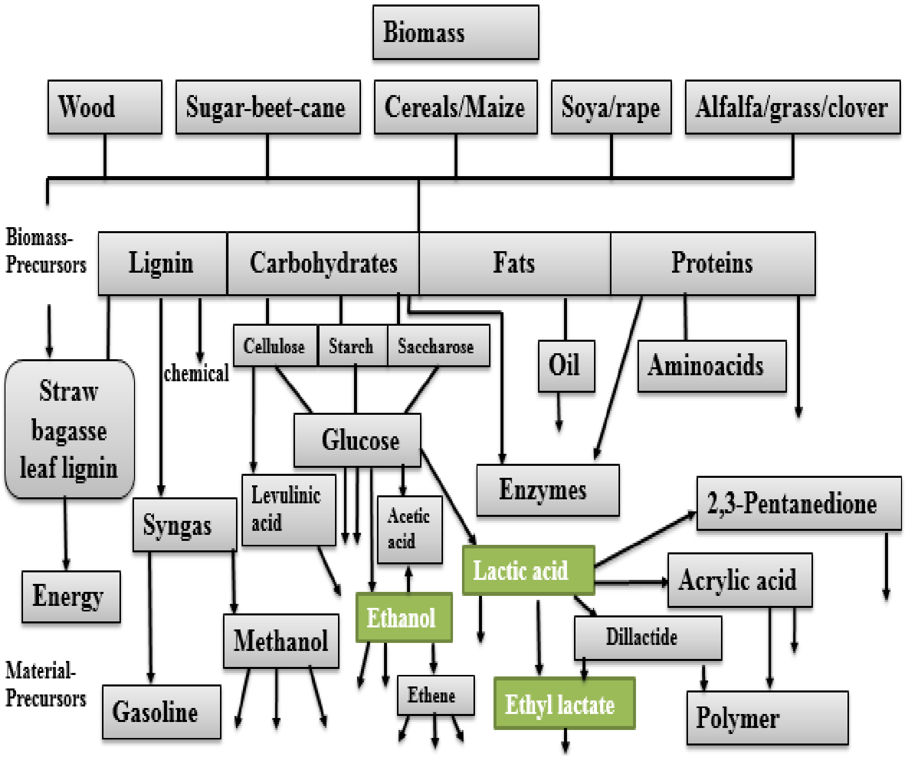

Figure 2.4: Schematic diagram of a biorefinery for the production of chemicals, energy and materials [37].

2.3.1 Lactic Acid Solvent

Lactic acid (chemically, 2-hydroxypropanoic acid) also known as milk acid, is the most commonly used acid with higher occurrence in nature [40]. It was first manufactured from sour milk by the Swedish chemist named Carl Wilhelm Scheele in 1780, and was first produced commercially by Charles E. Avery at Littleton, Massachusetts, USA in 1881 [40-42]. Lactic acid can be used traditionally in different industries including pharmaceutical, food and chemistry industries, however, its market is expanding continuously as a result of the improvement and commercialization of new applications such as the synthesis of green solvent (ethyl lactate) [40]. Lactic acid is the simplest hydroxyl carboxylic acid with an asymmetric carbon atom. It can be obtained from biomass feedstock, petroleum or natural gas and coal. Lactic acid can be produced through the fermentation process or through chemical synthesis of several carbohydrates including glucose (from starch) [37,43]. However, copolymers and polymers of lactic acid are known to be eco-friendly. Due to their degradability, they can be used as alternatives to petrochemical polymers [44]. The production of another grade of lactic acid which is used traditionally as a solvent with acid quality and food preservative has attracted the attention of world researchers over the last few years [15,45]. Due to the possession of two organic functional groups (carboxylic and hydroxyl groups), lactic acid can be used in various chemical reactions including condensation, substitution and esterification reactions [13] and this has contributed to its exceptional potential as a platform chemical for the manufacture of several products which can be employed in both industrial and consumer products [45]. The synthesis of polylactic acid (lactic acid with more than one polymer) from lactic acid requires a high purity lactic acid. However, different techniques including solvent extraction, electrodialysis and adsorption have been employed in order to achieve a high purity lactic acid for fermentation process. However, due to low volatility of lactic acid, and its affinity to water during fermentation process, none of these purification techniques have successfully produce high-purity lactic acid. In the esterification process, lactic acid can play a part in two different ways; by its –OH functional group leading to alkanoyl lactic acid or by its –COOH functional group resulting in alkyl lactate. Both type of esters can be prepared commercially [46-47].

Esters obtained from lactic acid and alcohols are commonly referred to as high boiling liquids. They can be used as biodegradable specialty solvents or as plasticizers in cellulose and vinyl resins. Esters of lactic acid including ethyl lactate can be obtained from commercial lactic acid or from a salt of lactic acid. Generally, commercially available lactic acid consists of a mixture of free lactic acid (65-80%), dimers and polymers of lactic acid (10-25%) and water (5-20%). Salt of lactic acid are generally the crude product obtained from the fermentation reaction and can thus be considered as cheap lactic acid sources in esterification reaction [47]. Polymers derived from lactic acid such as polylactic acid have shown a lot of promise as biodegradable and biocompatible polymer materials and have been employed in different processes including drug delivery systems, internal bone fixation and surgical suture [46]. The physical and chemical properties of lactic acid are summarized in table 2.1. Figure 2.5 shows the chemical structure of lactic acid.

Table 2.1: Physical and Chemical properties of Lactic acid

Properties	**Values**
Melting point (°C)	53
Boiling point (°C)	122
Specific gravity (g/mL)	1.2
Molecular weight (g/mol)	90.08
Molecular formula	$CH_3CH(OH)COOH$

Adapted from Jin Ren 2010 [40].

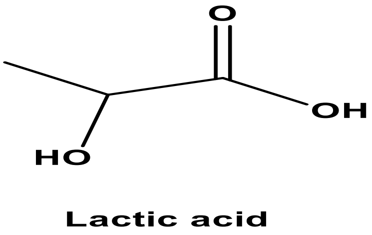

Figure 2.5: Structural representation for lactic acid [40].

2.3.2 Ethanol Solvent

Ethanol has proven to be an important raw material in the chemical industry and has a lot advantages as the most widely used biofuel for transportation [47]. This solvent can be obtained through fermentation process of various biomass crops including starch crops (e.g cassava and corn), cellulosic feedstock (e.g grasses, agricultural residues and wood) and sugar crops (e.g sugar cane) [32,36]. USA is the leading country in ethanol production globally with 59% share of the global production, followed by Brazil with 24% share [47]. Ethanol obtained from cellulose crop material has shown a lot of advantages since it broadens the scope of other feedstock beyond starch and sugar-based feed crops. Additionally, cellulosic ethanol can be more effective and promising as an alternative renewable biofuel in contrast to ethanol obtained from corn because it can reduce the total greenhouse gas (GHG) emissions even more [32]. The physical and chemical properties of ethanol are described in table 2.2. Figure 2.6 shows the structure of ethanol.

Table 2.2: Physical and chemical properties of ethanol

Properties	**Values**
Melting point	-114.1 °C
Boiling point	78.37 °C
Specific gravity	789 (kg/m^3)
Molecular weight (g/mol)	46.069 g/mol
Molecular formula	CH_3CH_2OH

Adapted from Pereira et al. [44].

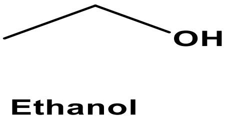

Figure 2.6: Structural representation for ethanol [40].

2.4 Recent development for Ethyl Lactate Process Intensification.

Process intensification requires novel equipment with less processing steps and low energy consumption as well as new process methodology. Besides the methodology and equipment, other steps include reusable and recyclable catalysts, less by-product, process safety, reduced plant volume, safe operating conditions, non-hazardous and renewable raw material [10]. Membrane reactor is a device that can incorporate both separation and reaction in one single unit. It can also be described as an intensive reactive system. Based on the property of the membrane, membrane plays a major role including active and inactive role in the reactor. Generally, membrane reactor can be classified into 3 different types including an active contactor (ACR), extractor membrane reactor (EMR) and Distributor membrane reactor (DMR). In the EMR, the membrane is catalytically inert and ultimately contributes to enhancing the reaction conversion by shifting the reaction equilibrium as shown in figure 2.7a [10],[48].

The DMR acts as an inert membrane support which controls the addition of reactant molecules in such a manner to limit side reaction as shown in figure 2.7b. In an active contactor, the controlled diffusion of reactants to the catalysts and reaction zone can result in an engineered catalytic reaction zone as shown in figure 2.7c [48]. From the industrial point of view, catalytic membrane possesses a lot of advantages including the ease of operation, energy saving and cost effectiveness. It is regarded as promising system with respect to the process intensification [8]. Generally, in the reaction that is affected by thermodynamic equilibrium such as esterification reaction, the reaction yield may be increase by the removal of one of the product from the reaction medium. Based on the reaction type, inorganic, polymeric, organic materials can be employed as membrane. Catalytic membrane reactors have been applied in several applications including oxidation, waste water treatment, esterification reaction and hydrogen production process [10].

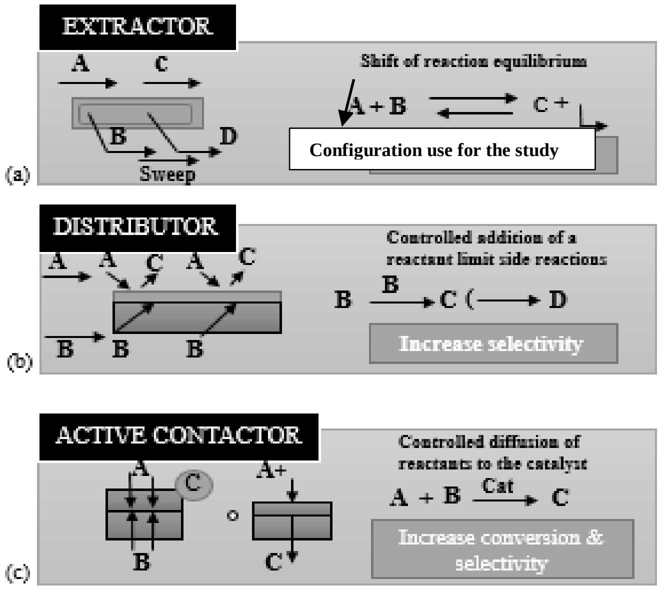

Figure 2.7: Schematic diagram of the membrane reactor function [48].

2.5 Kinetic models for Esterification reactions

Based on the heterogeneous and homogeneous approaches, the esterification reactions in the presence of ion-exchange resins can be explained using several kinetic models including Langmuir Hinshelwood (LH) model, Eley-Rideal (ER) and pseudo-homogeneous (PH) model [15,49-50]. Although the PH model does not consider the sorption effect on the resin by various components in the reactant mixture, the ER and LH models consider the sorption effects in their reactions kinetics [15]. The ER model takes place when a reaction occurs between an adsorbed and the non-adsorbed reactant species [50].

2.5.1 Langmuir Hinshelwood (LH) model

The fundamental principle of the LH model is that during esterification reactions, adsorption of all the reactants on the surface of the catalyst takes place first, before any chemical reaction [15,51]. LH and ER model can be derived based on the fact that the rate-determining step is the surface reaction between two molecules or between a molecule in the reaction mixture and the adsorbed molecules [52]. LH model also represents the rate determining step which explains the reaction of both reactants (acid and alcohol). Although the reaction rate in gas-phase can be well explained by LH model indicating the heterogeneous nature of the catalysts, there is no best kinetic model that could describe the liquid-phase reaction. Several researches have reported a good correlation of results for liquid-phase system using LH [53].

2.5.2 Eley-Rideal (ER) Model

In Eley-Rideal (ER) mechanism, an atom in form of a gas phase collide directly with an adsorbed atom on the surface. However, this reaction may take place in a single collision. The different between ER and LH mechanism is the transfer of energy to the products. The ER model is more exothermic than the LH mechanism [54]. The ER model is applied when the reaction occurs between an adsorbed and a non-adsorbed reactant from the bulk of the liquid phase [15,51].

2.5.3 Pseudo-homogeneous (PH) Model

According to Delgado et al. 2007 [15] the principle of the PH model is that it does not consider the sorption effect into the resin of the different species in the reactant mixture.

2.6 Reaction Mechanism for Esterification Process

In esterification reactions, esters and water molecules can be formed as the products of reaction between an alcohol and a carboxylic acid. The reaction is reversible in nature and is referred to as intermolecular dehydrogenation (removal of hydrogen) which is very essential and frequently employed in the chemical industries [50]. In the reaction mechanism involving the formation of ester, the first step involves the transfer of proton from the catalyst to the carboxylic acid as shown in figure 2.8. The proton is attached to one of the lone pair of oxygen which is double bonded to the carbon (step 1). The reaction is reversible, and the proton attacks the double bond to give a positive charge on the carbon atom. The positive charge on the carbon atom is then attacked by the hydroxyl group of the alcohol losing a molecule of water from the ion in the second step. Finally, the catalyst is restored by the transfer of a proton from the ion to the surface of the catalyst as shown in figure 2.8. The transfer of proton step (step 1) is usually assumed to be the fastest step, the nucleophilic substitution step (step 2) is the slowest step followed by the formation of water and ester with the recovery of the catalyst which is also assumed to be the fastest step [50].

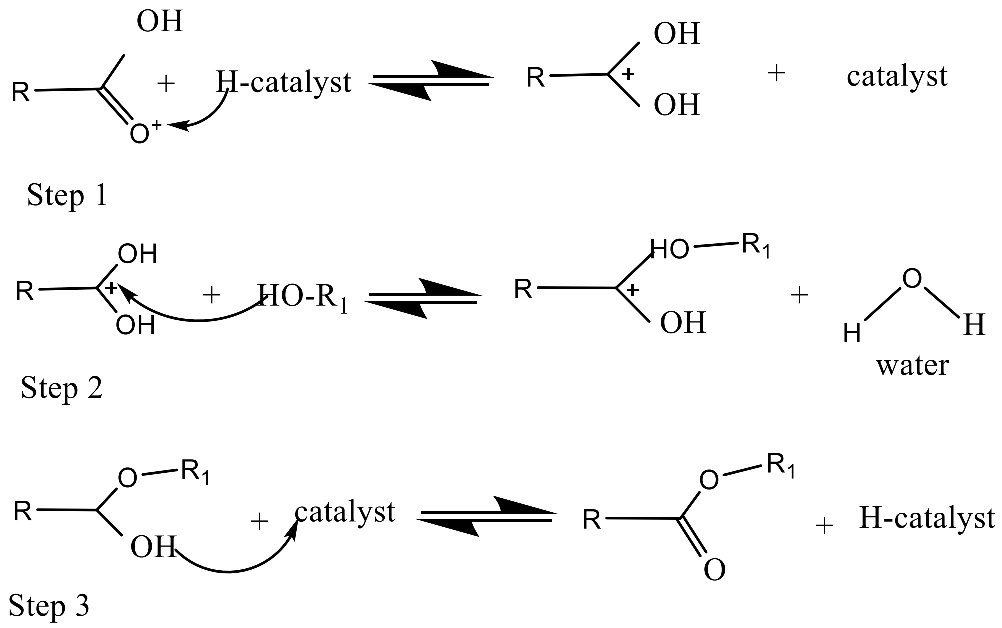

Figure 2.8: Schematic representation of esterification reaction mechanism. Adopted from Ali et al. [50].

2.7 Catalysts for Esterification Reactions

The problem of low conversion in esterification reaction can be resolved by the use of a suitable catalyst [55]. Generally, heterogeneous and homogeneous catalysts are the two major catalysts that can be employed to speed up the rate of reactions [55-56]. The major role of a catalyst during esterification reaction lactic acid is to give a proton (hydrogen) for a chemical reaction between the molecules of the carboxylic acid [57-58]. Basically, in the esterification reaction of lactic acid with alcohol, there are two type of catalysts that can be used including homogeneous and heterogeneous catalysts [57].

2.7.1 Heterogeneous Catalysts

The simplest route to obtain an ester with high yield is through the direct esterification of acids with alcohol using homogeneous (mineral acid) and heterogeneous (ion exchange resin) catalysts [59]. The use of heterogeneous catalysts has the following inherent advantages over homogenous catalyst; (a) purity of products is larger since side reactions can be completely eliminated or are less significant, (b) they can avoid corrosive environment (c) the catalysts can be removed easily from the reaction mixture by decantation or filtration process, (d) they offer higher yield of the product and are relatively inexpensive, (e) they can be reused and regenerated without the need for neutralisation steps and are relatively inexpensive [60]. Several variety of solid catalysts can be used for esterification reaction, among them, cation-exchange resins are the most commonly used solid acid catalysts in organic reactions.

2.7.2 Cation-Exchange Resin

Cation-exchange resins have shown a lot of advantage for in several liquid phase catalysed reaction. These acid catalysts can possess higher mechanical stability, highly acidic, environmentally friendly, inexpensive as well as chemically compatible with several liquids [61]. Several ion-exchange resins especially the cation-exchange resins such as dowex and amberlyst series are manufactured usually by sulfonation of ethylbenzene, followed by a cross-linking with divinyl-benzene [62]. Recently, solid cation-exchange resin catalysts have been found to be very effective in enhancing the rate of reaction and also the separation of the product [63].

2.8 Membrane Technology

Membrane technology has attracted a lot of attention from several industrial sectors and academics due to the fact that the technology gives the most relevant means of reducing costs and environmental problems [64]. The production of esters is one typical application of membrane-based process [65]. Membrane technology is based on the interaction of specific gases with the membrane material by chemical or physical means. However, membrane processes are considered to be effective and visible technologies for the separation of gaseous mixtures at the industrial scale because of their high efficiency, low cost and simple operations. Generally, membrane is defined as a selective barrier between two phases. It is characterised by selectivity and flux properties (permselectivity) that gives functional transport across the barrier. Moreover, the driving force for transport through the membrane is the chemical potential gradient, while the flux is determined by the physical structure of the membrane. The field of membrane gas separation is very competitive both between companies developing membrane technologies and with other gas separation technology developers. Membranes are commonly classified based on the pore size and the driving force including reverse osmosis (RO), microfiltration (MF), ultra-filtration (UF) and ion-exchange (IE) processes [64].

2.8.1 Membrane Separation Process

Membrane-based separation technologies has been successfully employed over the years in several industrial applications [66] including food, biotechnology, pharmaceutical and in the treatment of industrial effluents [66] and has also replaced a lot of conventional technologies because of the following advantages including: reliability, simple to operate, absence of moving parts and ability to tolerate fluctuations in flow rate and feed composition [67]. Based on the number of applications in the industry as well as in laboratory research, ceramic and polymeric membranes are the two main categories of separation membranes. They cover all various types of membrane applications including fuel cells, filtration, batteries and gas separation. Polymeric membranes are currently used in most commercial and industrial applications [68]. During membrane preparation process, the presence of layer defects including cracks and pinholes should be avoided because they strongly affect the separation efficiency of the membrane [64,68].

2.8.2 Reactions in a Catalytic Membrane Reactor

The development of processes based on the integration of new technologies is of growing interest to industrial catalysis. Currently, significant efforts have been focused on the design of catalytic membrane reactors to improve process performance. Specifically, the use of membranes, that allow a selective permeation of water from the reaction medium, has a positive effect on the reaction evolution by improving conversion for all reactions thermodynamically or kinetically limited by the presence of water [2]. Over the years, membrane reactors have received a lot of attention because of their excellent advantages in liquid-phase reaction. These advantages include close contact with the reactant, improvement of selectivity usually with respect to one of the reactant species, combination of both the reaction and separation system, and enhancement of reaction conversion [69]. A catalytic membrane reactor, a process that combines heterogeneous catalytic reaction with membrane separation, has shown a lot of advantages in oxidation catalytic processes [70].

In a catalytic membrane reactor, coupling of the membrane with catalysts can be achieved mainly in three different ways as shown in figure 2.9. As shown in figure 2.9a, the membrane is coupled with conventional pellet catalysts, with the membrane forming the inner wall in the case of a tubular reactor. The membrane top layer which enables the separation forms only a small part of the overall membrane thickness with the support layer forming the major part. In the second arrangement, the membrane itself is catalytically active as shown in figure 2.9b. The active catalyst is a thin dense membrane layer deposited on the surface of a porous support. In the third arrangement, the catalyst is impregnated into the pores of a microporous material either as individual particles or as a layer as shown in figure 2.9c. This arrangement in figure 2.9c is the suitable method of introducing catalysts into the membrane and has been employ in different reactions such as dehydrogenation reactions [48,71].

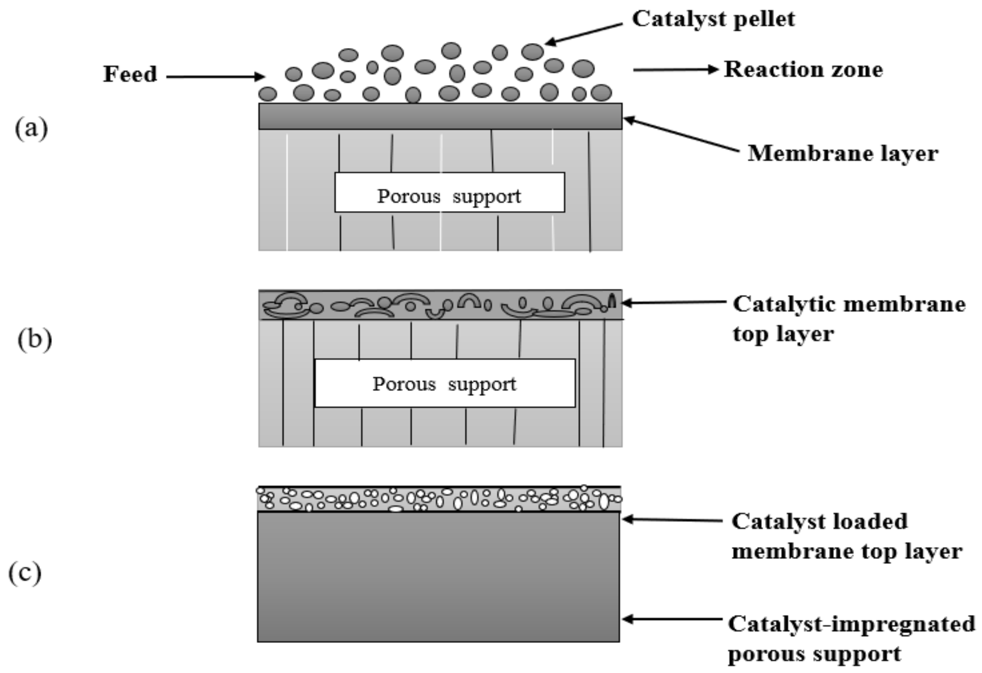

Figure 2.9: Schematic diagram of coupling of membrane reactor coupled with conventional pellet catalysts (a), membrane reactor itself has catalytically active (b), catalyst impregnated into the pores of micro-porous membrane (c). Adapted from Li, 2007 [71].

Furthermore, organic and ceramic membranes can lose their performance in the presence of strong acid including sulphuric acid during esterification process. As a result, heterogeneous catalysts such as cation-exchange resin have been suggested for esterification processes in order to solve the acid degradation problems with sulphuric acid [72]. Figure 2.10 shows the schematic diagram of an esterification reaction using a catalytic membrane reactor. These consists of the bulk liquid feed (lactic acid and ethanol) and (product water and ester), catalytic layer (cation-exchange resin), selective layer (flat sheet membrane) and support layer. The major role of the membrane as shown in figure 2.10 is that it works both as a catalyst and as a selective layer for the removal of the produced water to shift the equilibrium to the product side [73,74]. In order to generate a driving force for the mass transport of water through the membrane, the partial pressure of the water on the permeate side has to be lower than that on the reactor side. This can be, by diluting the permeate side with an inert component or by introducing a carrier gas [69] to enhance the driving force for the removal of water from the permeate side [74,75].

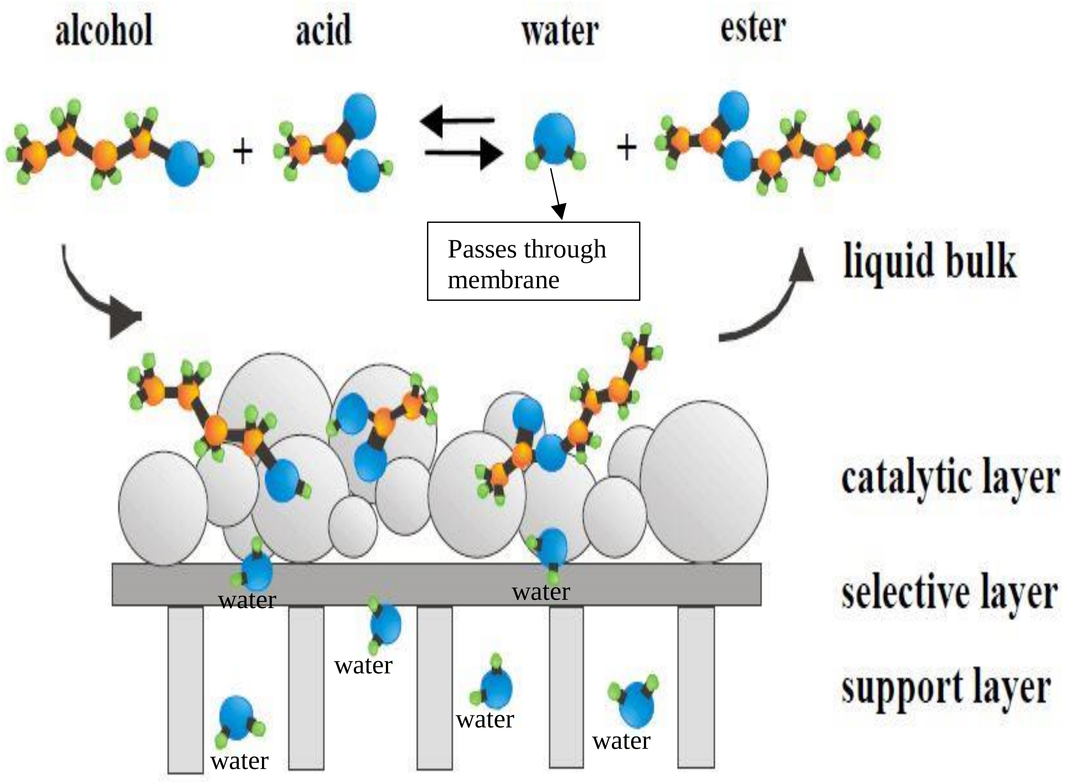

Figure 2.10: Schematic diagram of esterification reaction mechanism in a catalytic membrane reactor process. Adapted from Peter et al. [73].

2.9 Classification and Types of Membrane

Membrane may be classified as heterogeneous or homogeneous, asymmetric or symmetric, solid or liquid, charge or uncharged, organic or inorganic. The different types of membranes include: dense, porous and composite membranes [76-78]. Organic membranes may further be classified as polymeric (including polyethersulfone, polyamides, or cellulose acetate) and biological, whereas inorganic membranes may be further divided into dense phase (metallic), composite and ceramic (porous and non-porous) [79]. Table 2.3 shows the classification of inorganic membranes based on their nature and their most essential characteristics, permeability and selectivity.

Table 2.3: Summary of the Classification of Inorganic membrane

Types of Membrane	Materials	Permeability	Selectivity
Composite	Metal-metal	Moderate	Very selective
	Ceramic-metal	high	high
Dense	Metallic	low/moderate	high
	Solid-electrolyte	low/moderate	moderate
Porous	Microporous	moderate	very selective
	Mesoporous	moderate/high	low/moderate
	Macroporous	high	non-selective

2.9.1 Inorganic Membranes for Gas Separations

Ceramic porous inorganic membranes have been widely employed in different fields such as chemical and petrochemical, bioengineering, and environment engineering [80]. According to IUPAC (International Union of Pure and Applied chemistry) definition, membranes pores structure are classified as mesoporous (2-50 nm), microporous (< 2nm) and macroporous (> 50nm) layers [71,79, 81,82]. Porous membranes with the pore size greater than 0.3 nm are normally used as sieves for larger molecules [83]. Materials such as zirconia, zeolite, metals, glass, alumina and carbon are used as commercially available porous inorganic membranes [71]. Other materials used for the manufacture of inorganic membranes include silica, titania, tinoxide, cordierite and silicon nitride [83].

Membranes are commercially available in different module formats, including tubular, hollow fibre, flat sheet, spiral wound, etc. Membranes can be fabricated with pore diameters ranging from < 1nm (mostly non-porous) to 10µm. Macroporous membranes, including α-alumina, gives no separation function but can be used as support layers for smaller pore size to form composite membranes, or in applications where a well-controlled reactive interface is required [79]. The preparation of ceramic membranes can be achieved through several steps as shown in figure 2.11. From figure 2.11, the preparation of a support layer is first of all carried out to provide mechanical strength for the membrane, followed by coating one or more intermediate layers on the support layer before a fabrication of the finial separation layer.

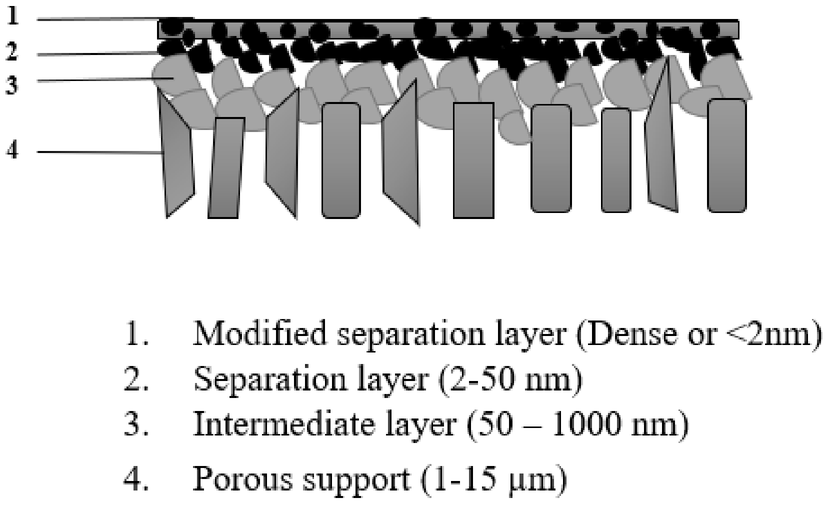

Figure 2.11: Schematic representation of an asymmetric composite membrane. Adapted from Li, 2007 [71].

In general, mesoporous materials for membranes have pore sizes between 2-50nm, hence selectivity and permeation are governed by Knudsen or bulk diffusion. Microporous membranes including carbon molecular sieves, porous silica and zeolites serve as molecular sieves, separating molecular based on kinetic diameters with very high separation factors [79]. Although inorganic membranes are generally expensive in contrast to their organic polymeric counterparts, they have a lot of advantages in gas separation including well defined stable pore structure, chemical inertness and wear resistance [83]. These numerous advantages make them adaptable in some essential heterogeneous catalytic reactions, specifically under harsh operating conditions such as high temperature and pressure [80]. In spite of these advantages, the major drawback of porous membrane is the low selectivity offered by some mesoporous materials for gas separations [82]. Inorganic membranes can be prepared using different methods including sol-gel, chemical vapour deposition, sintering and spin-coating [84]. However, sol-gel has been found to be the most suitable method for depositing thin films on the porous support in contrast to other methods [68,82,85-86,]. In the sol-gel method, a sol is synthesized, deposited on a substrate, and thermally treated to calcine and optionally sinter the layer. The sol evolves into a gel layer during coating which gives the process its name ‘’sol-gel coating’’ [68].

McCool et al. [86], used the dip-coating method for the membrane fabrication and deposition on a polished surface of an alumina support disk and reported the gas permeation for N_2, Ar, O_2 and He gas to be strongly governed by Knudsen mechanism [86]. Jin et al. [87] prepared an α-Al_2O_3 microfiltration pinhole-free membrane using a modified dip-coated process to prevent pinhole defects in ceramic membranes. Figure 2.12 shows a schematic diagram of a laboratory membrane gas permeation system [88].

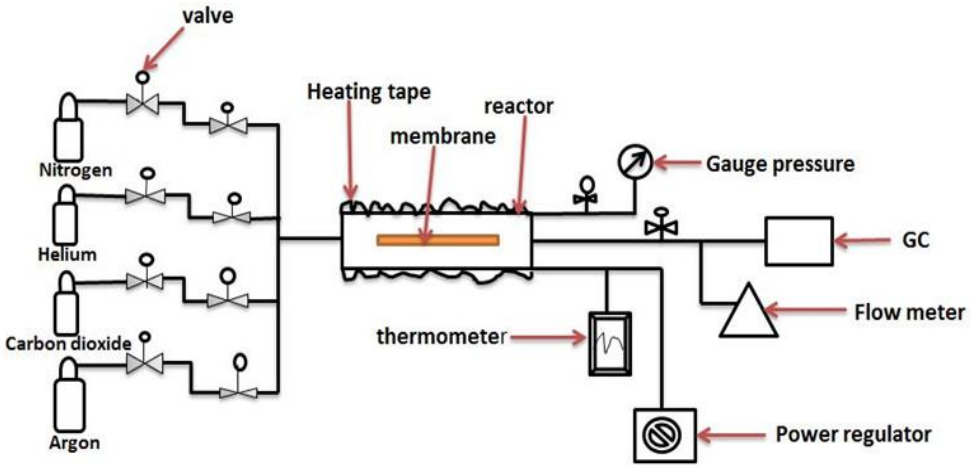

Figure 2.12: Schematic diagram of a membrane gas separation testing unit [88].

2.10 Phenomenon of Carrier Gas Permeation

In order to determine the suitable carrier gas for the analysis of the esterification product, permeation tests for various carrier gases was carried out to determine the separation and permeability of the carrier gases with the ceramic support membrane. The permeation designed of the gases through the membrane can be carried out in various ways depending on the feeding gas (single or mixtures). According to Criscuoli et al. [89], when gases are fed singularly, the selectivity is higher than that of the mixed gas. This is because of the fact that by using mixed gas feeds, the fluxes values are influence by the multicomponent interactions which strongly affect the overall behaviour of the gas [89].

2.10.1 Helium Carrier Gas

Helium gas has gained a prominent role in our daily life as shown by the steadily growing markets [90] in medical, industrial and scientific applications due to inertness, small molecules size and non-flammability [91]. These characteristics in turn make helium highly attractive as a cryogenic and protective fluid media especially as a gas coolant in nuclear reactor, a carrier gas in gas chromatograph, a protective gas for welding and metallurgical processing [91]. Helium is a finite, non-renewable resources that can be extracted from only a few natural gas fields around the globe. Because of a delicate balance between helium availability and increasing demand, it is important that human-producing industry work with helium end users to conserve, recover and recycle this resource [92].

2.10.2 Transport of Carrier gases through porous membrane

The transport through porous membranes can be explained using various transport mechanisms based on several factors such as the size of the permeating gas molecules, the membrane material, the driving force (pressure and temperature) and the average pore size [78,84,93]. The different mechanisms of gas transport through porous membranes include surface diffusion, Knudsen diffusion, capillary condensation, poiseuille or viscous flow, and molecular sieving mechanisms [94-96].

2.10.2.1 Knudsen Diffusion

In Knudsen diffusion mechanism, gas molecules diffuse through the pores of the membrane and then get transported by colliding more frequently with the pore walls [95, 97-98], indicating a higher permeance but a low selectivity. Knudsen mechanism also occurs if the mean free path (λ) of the permeating gas molecule is greater than pore diameter (d). This indicates that the Knudsen number (K) is greater than 1, i.e $K = \lambda/d > 1$ [96]. The controlling rate mechanisms of transport in mesoporous membranes are Knudsen, viscous and surface diffusion mechanism. In the mesoporous and macroporous regime, Knudsen diffusion is the dominate flow mechanism and the gas selectivities is proportional to the inverse square root of the gas molecular weights whereas in the microporous range, the selectivities are additionally influence by difference in potential between the gas molecules and the membrane surface [99]. Figure 2.13 shows the carrier gas flow mechanism based on Knudsen diffusion mechanism.

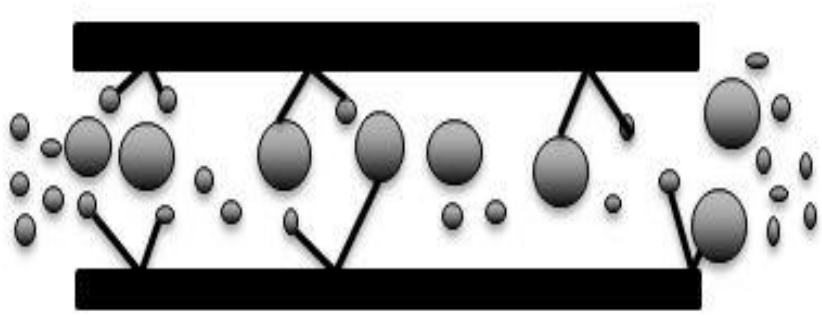

Figure 2.13: Schematic diagram of gas transport mechanism based on Knudsen flow. Adapted from Ohwoka et al. [100]**.**

The expression for Knudsen flow in porous membrane can be written using the following equation [95]:

$$D = \frac{\varepsilon \delta \rho}{3\tau} \left(\frac{8RT}{\pi M} \right)^{1/2} \qquad \text{...(2.1)}$$

Where F is the Knudsen diffusion (m^2/s), ε = porosity of the membrane (%), R = gas molar constant ($Jmol^{-1}K^{-1}$), M = the molar weight of the diffusing gas (g/mol), $\delta\rho$ = pore diameter (m), τ = tortuosity (m) and T = temperature (K), π = 2.134 [95].

2.10.2.2 Viscous Flow

Viscous flow mechanism takes place if the pore radius of the membrane is greater than the mean free path of the permeating gas molecule [99,101]. In this case more collision will take place between the permeating gas molecules (molecule-molecule collision) than between the molecule and the pore wall of the membrane as shown in figure 2.14 [102,98]. Figure 2.14 shows the transport of the carrier gas through the membrane based on viscous flow mechanism.

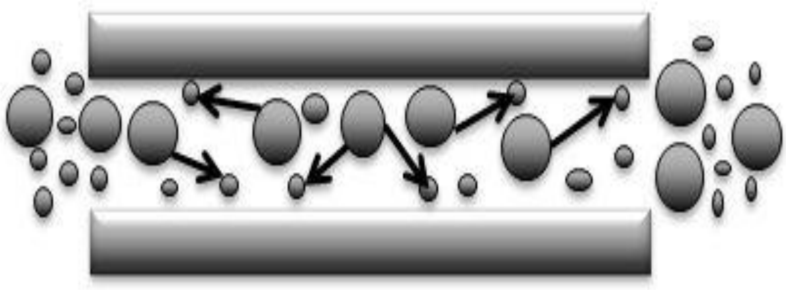

Figure 2.14: Schematic diagram of gas transport based on viscous flow. Adapted from Ohwoka et al. [100].

The viscous flow mechanism of gas transport can be express as:

$$\boldsymbol{F_{viscous}} = \frac{\boldsymbol{r_p{}^2(P_{1-}P_2)}}{\boldsymbol{16L\mu RT}}\left(\frac{\boldsymbol{mol}}{\boldsymbol{m^2s}}\right) \quad \ldots\ldots\ldots\ldots\ldots\ldots\ldots\ldots\ldots\ldots\ldots\ldots\ldots\ldots\ldots\ldots\ldots\ldots\ldots\ldots\ldots\ldots\ldots\ldots\ldots\ldots.(2.2)$$

Where P_1=absolute pressure (Pa), P_2= atmospheric pressure (Pa), μ = gas viscosity ($Pa.s^{-1}$), L = membrane wall thickness (m), = membrane pore size (m), R = gas molar constant ($Jmol^{-1}K^{-1}$), T = atmospheric temperature (K).

2.10.2.3 Molecular Sieving

Gas separation by molecular sieving mechanism takes place when the pore diameter of the inorganic ceramic membrane are roughly the same as those of the permeating gas molecules [97,71,83]. However, as the pores become smaller than approximately 0.5nm, separation factors greater than 10 are usually achievable. If the pore size of the membrane is between the diameters of the larger and smaller gas molecules, then only the smaller gas molecule can permeate through the membrane leading to a more efficient separation [98],[78]. Figure 2.15 shows the schematic diagram of the transport mechanism based on the molecular sieving.

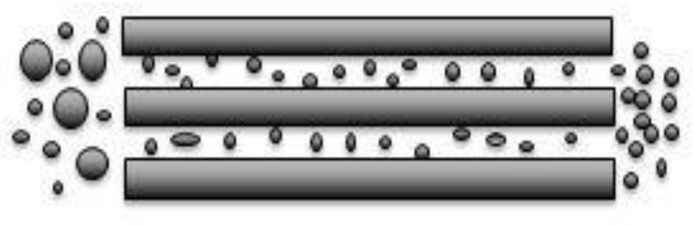

Figure 2.15: Schematic diagram of gas transport based on molecular sieving. Adapted from Ohwoka et al. [100].

2.10.2.4 Capillary Condensation

In the capillary condensation mechanism, separation can take place in the pores of the membrane with mesoporous layer in the presence of condensable gas specie such as water vapour [102]. Typically, in the mesoporous region, at a certain relative pressure, the pores become completely filled up the condensed gas [103]. However, this mechanism of gas transport can be considered as the final limit of the process of adsorption as the pressure increases. Theoretically, capillary condensation can be used to achieve very high selectivities as the formation of the liquid layer of the condensable gas will block and stop the diffusion of the non-condensable gas components resulting in separation [103-104]. Figure 2.16 shows the schematic diagram of the transport mechanism based on the capillary condensation.

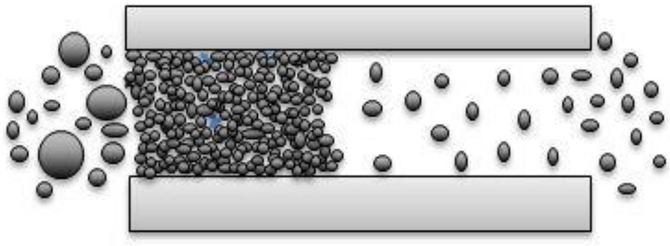

Figure 2.16: Schematic diagram of gas transport based on capillary condensation. Adapted from Ohwoka et al. [100].

2.10.2.5 Surface Diffusion

In surface diffusion mechanism, the adsorption of the permeating gas molecules are considered to be adsorbed on the surface of the pore walls of the membrane material there by increasing the gas transport performance [103]. Surface diffusion normally occurs in line with other diffusion mechanisms including Knudsen flow mechanism [64,103]. This mechanism can only be useful at the relatively low temperature region that relies upon the sorption energy of the gas molecules [95]. Figure 2.17 shows the carrier gas mechanism of gas transport based on surface diffusion mechanism. Figure 2.17 shows the carrier gas mechanism of gas transport based on surface diffusion mechanism.

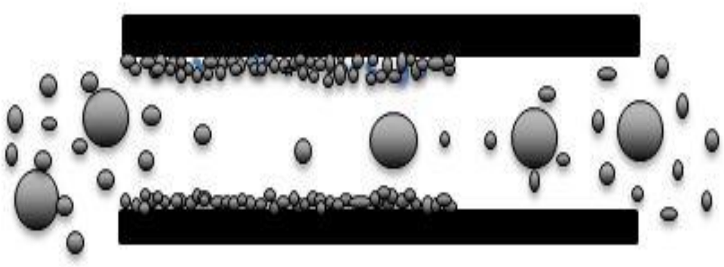

Figure 2.17: Schematic diagram of gas transport mechanism based on surface diffusion. Adapted from Ahmad et al. 2015 [64].

2.10.2.6 Solution Diffusion

This mechanism takes place when the permeating gas molecule exhibits a strong affinity for the membrane surface and adsorb along the pore walls [103]. In this mechanism, separation takes place because of the differences in the amount of adsorption of the permeating gas molecules [64,103]. Figure 2.18 shows the carrier gas mechanism of gas transport based on surface diffusion mechanism.

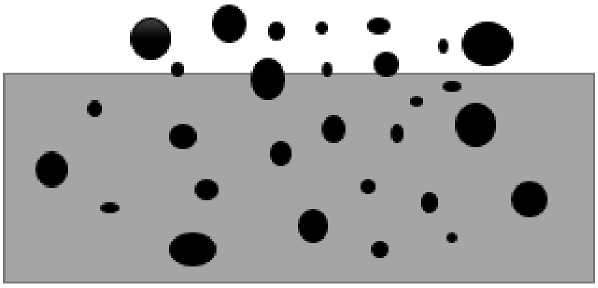

Figure 2.18: Schematic diagram of gas transport mechanism based on solution diffusion mechanism. Adapted from Ahmad et al. 2015 [64].

2.11 Contribution to Knowledge

Figure 2.19(a-e) describes several conceptual configurations from the literature investigations for effecting membrane esterification reactions are shown [105,106]. Most commonly used configurations for pervaporation (PV) and vapor permeation (VP) studies are the stirred batch reactor. When the stirred batch reactor integrated with an external separation unit (Figure 2.19a, recycle tank reactor, TR+PV or TR+VP), the stream that leaves the catalytic reactor (vapour or liquid in the case of VP of PV respectively), constituted by the unconverted reactants and the products, transports through the membrane for the selective removal of product or by-product and the retentate is returned to the reactor with some advantages in the case where the permeability of the membrane is low or in the case of fast reactions. In this case, two membrane modules could be used, to enable clean-up or regeneration steps to be easier and, if one membrane should fail, the chemical reactor can continue operation in combination with the second one. Moreover, by using such a configuration [107], it is possible to optimize the selective and the catalytic properties independently. Instead, in the case where the reactor and separation are integrated in a single unit (Figure 2.19b, TRPV or TRVP), the membrane is placed directly into the stirred reactor, in a tubular or flat sheet configuration. This integration could offer major benefits including high process efficiency and compactness along with more flexibility due to its design modularity, with consequent energy input reduction, investment in capital, and process costs [2].

Moreover, these reactive separation techniques could be further improved by heat-integration, and the use of solid catalysts such as resins could avoid the conventional operations which employ homogeneous catalysis, with consequent advantages in raw materials conservation and reaction reduction in reactor volume. Simultaneously, this results in enhanced conversion of the feed and high selectivity values for the desired product. Most often, batch processes are more advantageous when multiple products are produced in a relatively small volume within the same equipment, as opposed to the continuous processes which are usually employed for the manufacture of large volume products since these processes do not involve high labour intensity. In the continuous stirred tank reactor (CSTR) with recycle both feed and retentate streams are incorporated to the configuration so as to obtain products continuously with the membrane either external (Figure 2.19c) or internal (Figure 2.19d) to the reactor. Similarly, the same situation could be proposed for the case of the plug flow reactor (PFR), even if the membrane and reactor are more frequently combined in a single unit (Figure 19e,f).

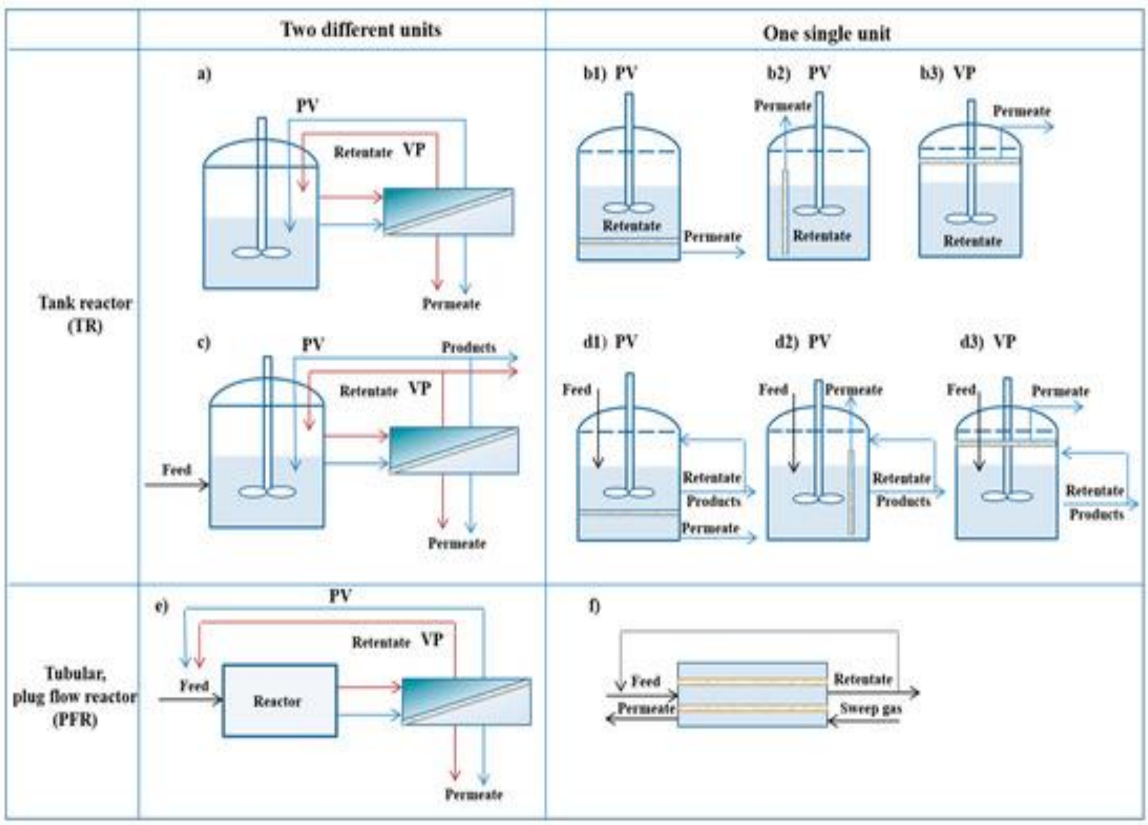

Figure 2.19: Examples of reactor-membrane separator configurations. TR with external separation unit, TR+PV or TR+VP (a); TR with internal flat membrane in PV mode, TRPV (b1), or VP mode TRVP (b3) and tubular membrane, TRPV (b2); (c) recycle continuous stirred tank reactor (CSTR) with external separation unit, CST+PV or CST+VP (c), or internal unit, CSTPV or CSTVP (d1–d3); PFR with external separation unit, PFR+VP or PFR+PV (e) or internal unit, PRFVP (f) [2].

Commonly, in membrane-based esterification reactions the permeate partial pressure is guaranteed by vacuum or using an inert sweep gas and the partial vapor pressure difference across the membrane is achieved by employing a sweep gas or vacuum at the permeate side as shown in Figure 2.20. In industrial pervaporation (PV), vacuum is generally used to avoid the necessity of an additional separation step from the sweep gas and then vapors are condensed in a pre-condenser and a pump consisting of a liquid-ring pump. In modeling of the transport process, the boundary layer resistance at the vapor phase is assumed to be negligible and the concentration of the solute is considered to be zero at the permeate side, where a low vacuum level is maintained. When permeate pressure increases, the resistance to transport on the vapor side will increase too, becoming significant. When the selective and catalytic functions are integrated into one single layer, specific material properties are required: in fact, to attain high water selectivity, the diffusion of all components except water through the catalytic membrane should be low, while for an efficient use of the catalyst, high diffusion of the reactants is required. In the esterification reaction of an acid with an alcohol, for example, the reactants diffuse into the catalytic layer to be converted to ester and water; then the ester returns to the liquid mixture whereas the water is removed in situ. Consequently, the hydrolysis of the ester is limited while the conversion is enhanced compared to the values obtained using a non-catalytic membrane reactor. Figure 2.20 shows the application of a carrier gas transport through a polymeric membrane [2].

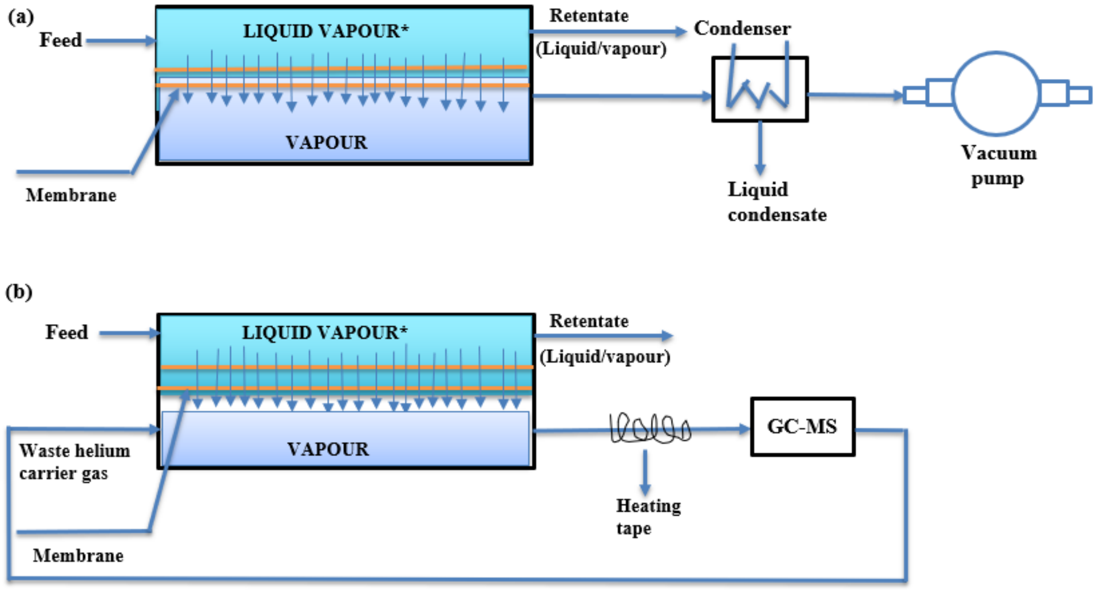

Figure 2.20: Schematic PV or VP process: (a) by vacuum; (b) by carrier gas. * For PV, the feed is liquid; for VP, the feed is vapor [2].

As the process scale becomes large, vacuum costs increase significantly and condenser power demands become significant. Additionally, in the case of lactic acid esterification with alcohol, the ‘’sucking’’ action of the vacuum pump can also result in extraction of alcohol from the feed through the membrane, thus reducing process efficiency. In the case where a carrier gas is employed, in addition to condenser load, the cost of the carrier gas is a major factor. Helium for example is very expensive. The contribution to knowledge is to utilize a waste stream containing the carrier gas and purify it using hybrid inorganic membranes for use in the esterification permeate side as shown in Figure 2.21. Therefore, a study has been undertaken to study carrier gas transport and purification characteristics using inorganic membranes and esterification of lactic acid and ethanol to produce ethyl lactate with simultaneous water removal in a membrane reactor. The novelty in this approach lies in the use of environmentally friendly processes to produce a replacement of a petroleum-derived solvent.

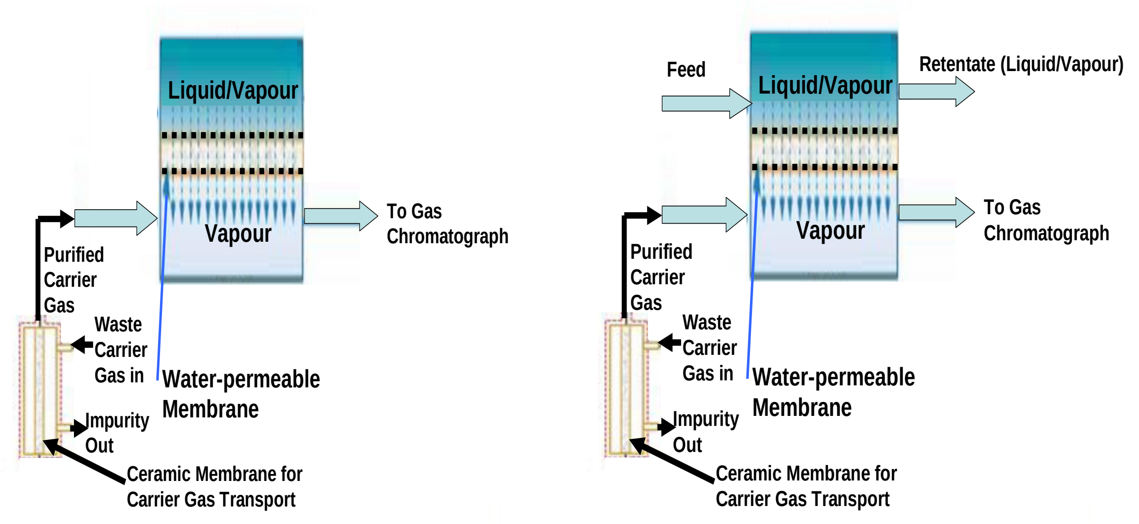

Figure 2.21: Combination of Carrier Gas Transport Ceramic Membrane Purifier and Equilibrium-Shift in Esterification using Water Permeable Membrane (batch process-left and continuous process-right).

CHAPTER 3

3.1 Permeation Tests for Support and Modified membrane with Carrier Gases.

This chapter describe the different experimental setup, design and operation for the different research objectives. The tubular alumina membrane test with the carrier gases was to determine the different carrier gas that was most suitable for the analysis of ethanol and lactic acid feed and ethyl lactate with the gas chromatography-mass spectrometry after the esterification process. This tubular membrane is thermally stable with uniform pore structure and can withstand the effect of heat at higher temperatures. The investigation was carried out using carrier gases including argon (Ar), helium (He), carbon dioxide (CO_2) and nitrogen (N_2) with a 15nm pore size commercially available tubular ceramic support, consisting of 77% Al_2O_3 and 23% TiO_2 and a porosity of 45%, at varying temperatures before esterification reactions. Table 3.1 shows the different physical parameters for the support. Figure 3.1 shows the schematic diagram of the dimension for the α-Al_2O_3 support membrane that was used for the investigation with carrier gases.

Table 3.1: Physical Parameters for Support Membrane

Membrane Support Parameters	
Total Length (L_{total})	0.366m
Effective permeable Length (L_{eff})	0.342m
Impermeable Length (L_{im})	0.02m
Inner Diameter (D_{inner})	0.007m
Outer Diameter (O_{outer})	0.10m
Total Weight (W_{total})	48.3g

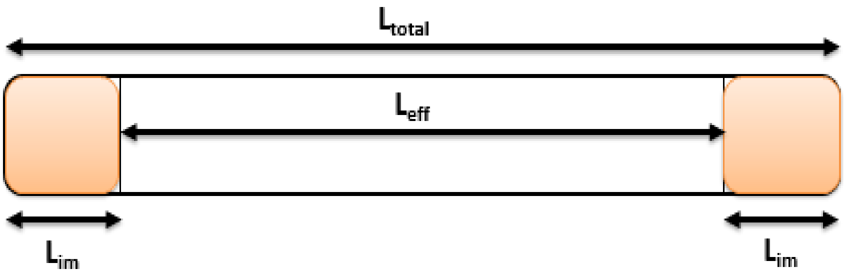

Figure 3.1: Schematic diagram for tubular support membrane.

3.2 Materials and Methods

3.2.1 Silica membrane dip-coating Preparation

The dip-coating technique is schematically shown in figure 3.2. A 545 mL silica solution was used for the support membrane dip-coating. To achieve this, a sol-gel dip-coating membrane preparation method was used. The γ-alumina support membrane was prepared by subjecting both the external and internal surface of the tubular α-alumina support membrane to a silica solution comprising of the 500mL of iso-pentane (2-methyl butane), 1/10 (50mL) for the silicon elastomer solution and 5mL for 30 minutes at immersion and withdrawal speed of 1min/sec using 1000 mL measuring cylinder (Sigma Aldrich, UK). Prior to the permeation test, the support was weighed before the test to determine the actual weight before and after modification using a weighing balance. Figure 3.2 shows the schematic diagram of the dip-coating system.

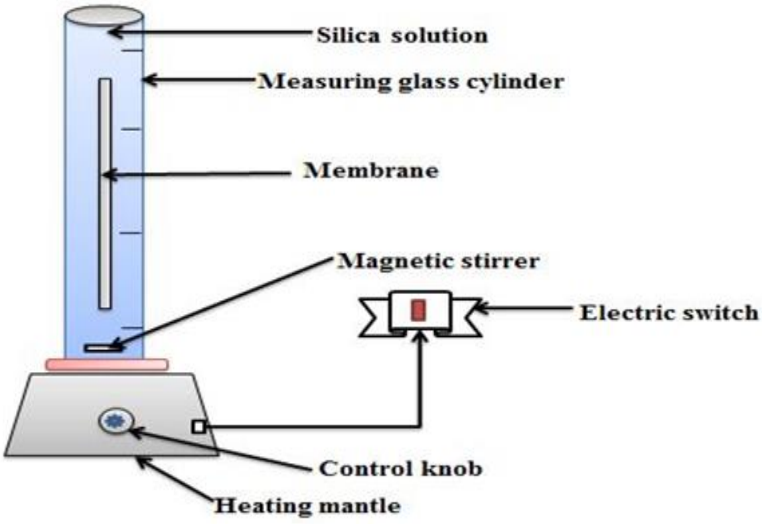

Figure 3.2: Schematic diagram of dip-coated system for silica membrane preparation.

The actual weight of the membrane before the dip-coating process was 48.3g. The membrane preparation was carried out based on the patented innovation by Gobina [108] and Gobina [109] as thus: A 500 mL of iso-pentane (Sigma Aldrich ≥ 99%), was measured into 1000 mL glass measuring cylinder and 50 mL of silicon elastomer was added and mix together to obtain a colourless and clear solution. 5 mL of the curing agent (hardener) which correspond to one-tenth of the elastomer was added and the three solutions were mixed at room temperature. The cylinder was covered with a clean film to prevent the solution from evaporating. The components of the silica that was used for the dip-coating process is detailed in table 3.2 below:

Table 3.2: Composition of Silica Compound

Components	Quantity (mL/g)
Iso-pentane (2-methylbutane)	545mL
Sylgard®184 Silicone Elastomer	50mL
Sylgard®184 Curing agent	5mL
Measuring cylinder	1000mL
Weight of membrane before modification	48.3g
Weight of membrane after modification	49.1g

A magnetic stirrer (supplied by Fisher scientific, UK) was used to thoroughly mix the three solutions and the mixture was allowed to age for 30 minutes in other to obtain a homogeneous solution as shown in figure 3.3a. After 30 minutes, fresh ceramic support was immersed into the prepared solution as shown in figure 3.3b and allowed in the solution for 30 minutes. After 30 minutes, the support was withdrawn from the solution and was air dried on a customize rotatory evaporator (Weir 413 D model dryer) for approximately 1 hr as shown in figure 3.4. After air drying, the support was then transferred to the oven and was calcine for 2 hrs at a constant oven temperature of 65 °C [108,109].

The essence of dipping the alumina support is to obtain an ultra-thin silica layer on the support. The pictorial view of the membrane preparation process before and after the dip-coating process is shown in figure 3.3a and b. This same dip-coating procedure was repeated for subsequent membrane dip-coatings. A total of three dip-coated membranes were prepared for permeation test evaluation with carrier gases. This was carried out as a preliminary experiment to determine the suitable carrier gas on interaction with the membrane before employing the carrier gases for the esterification reaction product analysis.

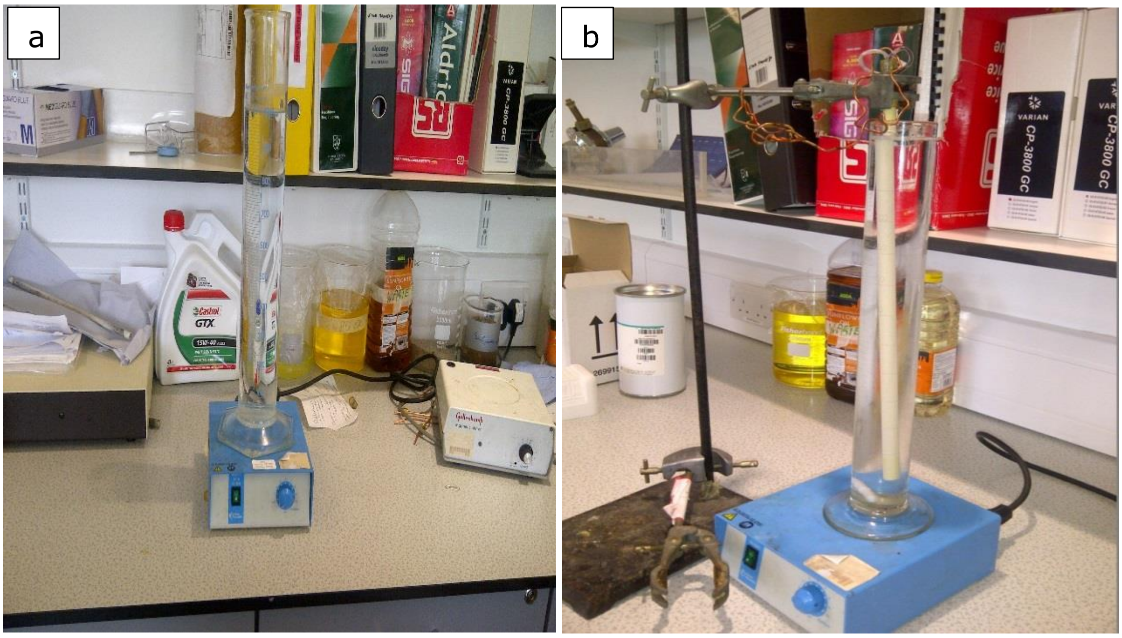

Figure 3.3a and b: Pictorial diagram of dip-coating process without (a) and with (b) membrane.

After the dip-coating process, the membrane layer was measured as 49.0g. The preparation of membrane dip-coating process was carried out in a clean area. The essence of carrying out the membrane preparation in a clean area was to avoid contamination which may cause a defect or pin-hole on the surface of the membrane support [110,111]. The essence of dipping the membrane before the carrier gas permeation test was to reduce the pore size of the membrane for easy interaction of the gas with pore walls of the membrane [99]. However, the thickness of the support membrane before and after dip-coating process of the membrane was calculated using the following formula [87].

$$L = \frac{W_2 - W_1}{A\rho(1-\varepsilon)} \quad \ldots\ldots\ldots\ldots\ldots\ldots\ldots\ldots (3.1)$$

Where L = membrane thickness (m), A = membrane area (m^2), ρ = the theoretical density of alumina (3.95×10^{-3} kgm^{-2}) [160], W_1= initial weight of the alumina support (g), ε = membrane porosity (45%), W_2 = total weight of the support and membrane (g) [87].

Figure 3.4 shows the pictorial view of the membrane dryer. The sol-gel dip-coating process was carried out in a clean room in order to reduced particle contamination on the membrane coated layer. The dipping process was repeated for a reproducible result to determine a thin-film layer on the γ-alumina support membrane. All the dipping process, drying and calcining was repeated in order to repair any defect that occurred on the γ-layer [110].

Figure 3.4: Pictorial view of the membrane dryer.

3.2.1.1 Membrane rig set-up

The reactor used for the experiment was a stainless-steel reactor with the internal diameter of 28mm, outer diameter of 36mm, 5mm thick and 395mm long that can be stable at high temperatures. This reactor was a tubular stainless membrane reactor in a shell configuration. Figure 3.5a and b shows the pictorial view of the stainless-steel reactor before welding (3.5a) and membrane reactor rig without the heating jacket wrap around the reactor (3.5b).

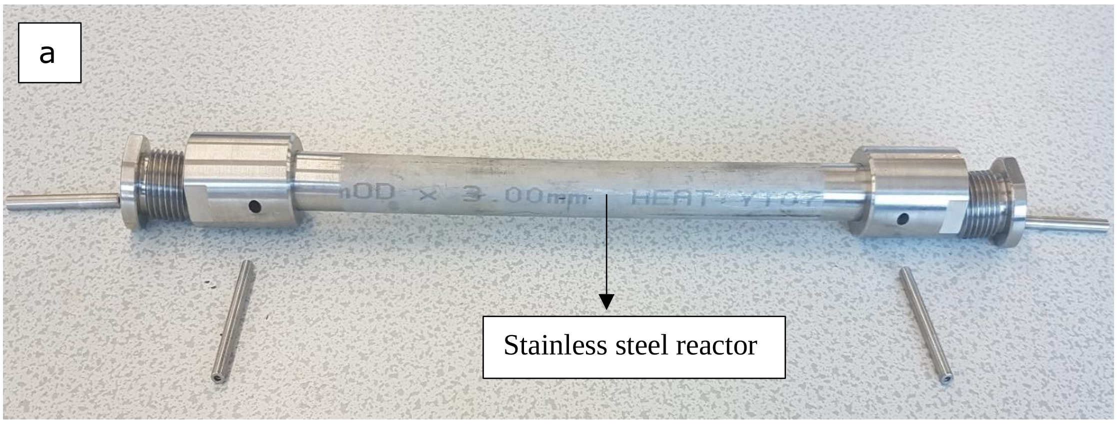

Figure 3.5a: Pictorial view of stainless steel reactor parts before welding.

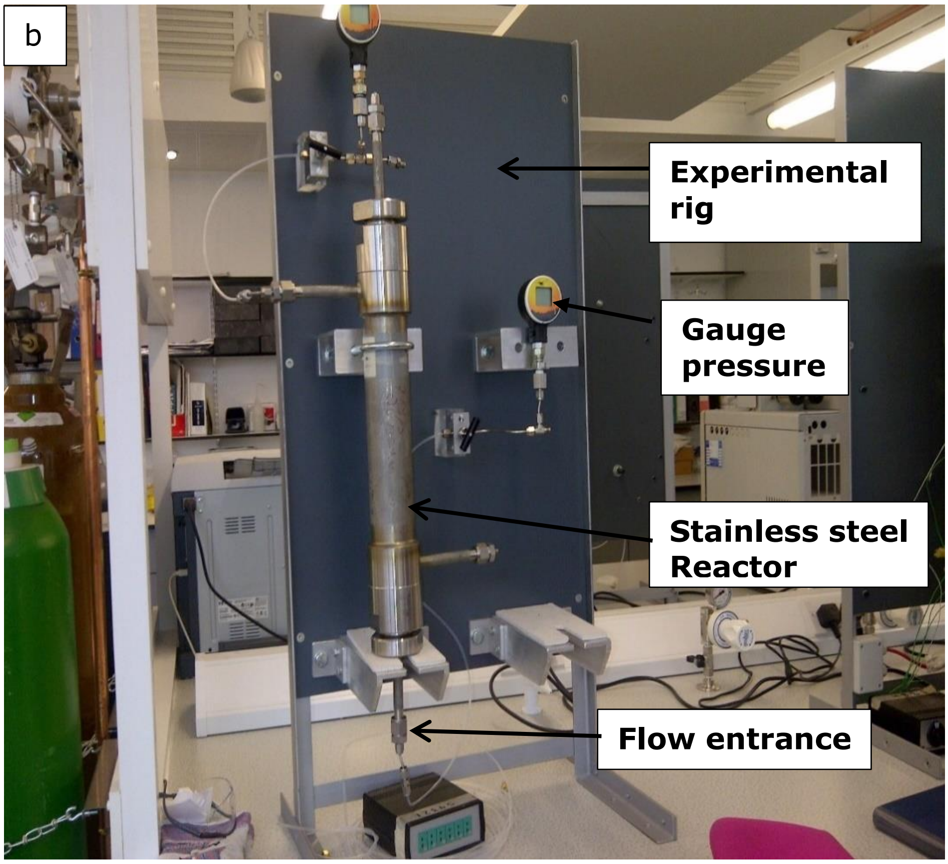

Figure 3.5b: Pictorial view of the stainless steel membrane reactor rig setup without the heating jacket wrap around the reactor.

3.2.1.2 Stainless Steel Reactor

Figure 3.6 shows the pictorial view of the stainless-steel reactor that was used for the experiment. This reactor is 32.1 cm long with the thickness of 0.3cm. The lower pictorial view of the stainless-steel reactor shows the plain stainless-steel reactor before the permeation test experiment while the upper diagram shows the pictorial view of the reactor after the temperature experiment. From figure 3.6, it can be seen that there was a clear colour change of the stainless-steel reactor from silver (down) before the permeation test experiment to black (up) after the permeation test experiment at different temperatures. Figure 3.7a shows the pictorial view of one end of the reactor showing the membrane pore fitted with the graphite seal while figure 3.7b shows the pictorial view of the reactor screw cap with the Swagelok fitting on it. Figure 3.7c shows the pictorial view of the support with seals at both ends while 3.7d shows the stainless-steel reactor without seal and membrane.

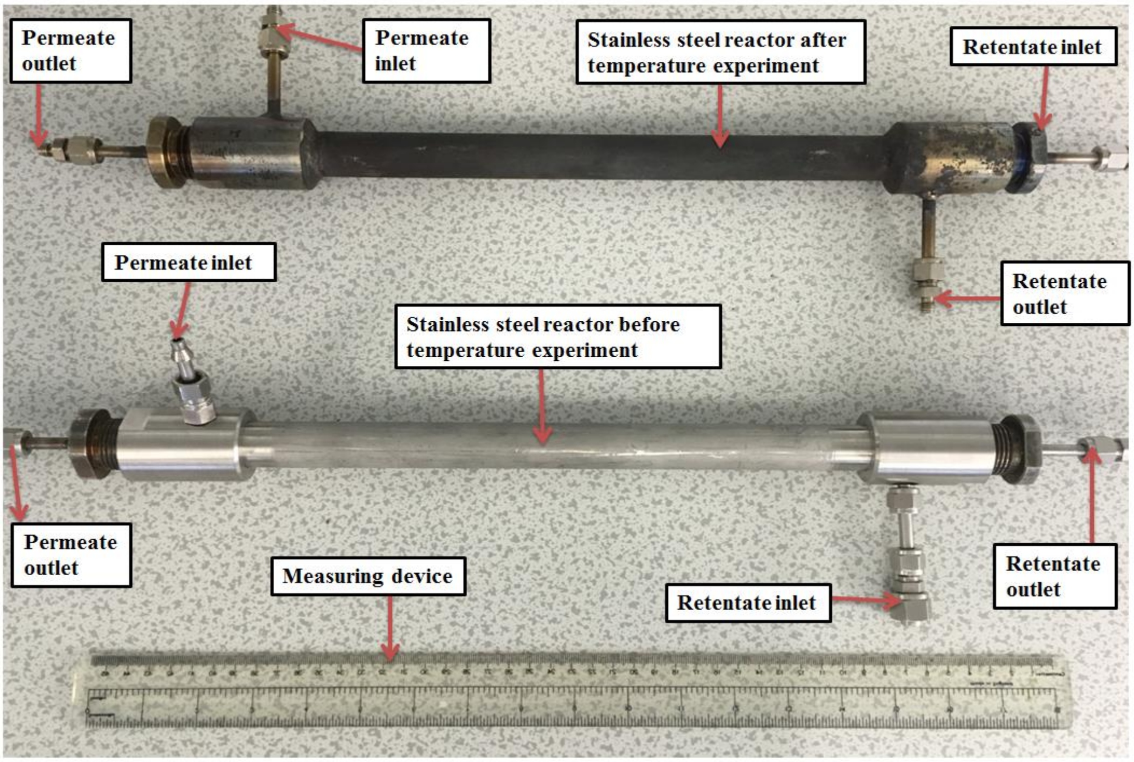

Figure 3.6: A pictorial view of the stainless steel reactor before (down) and after (up) permeation test experiment.

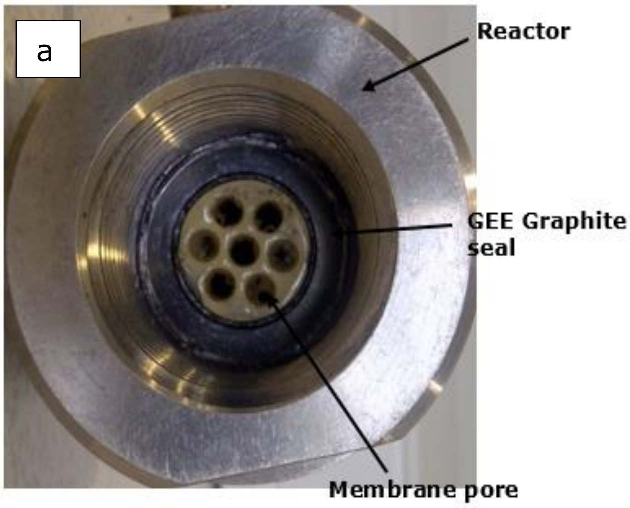

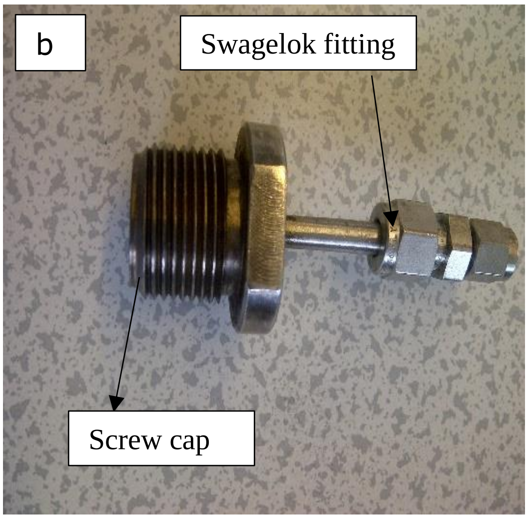

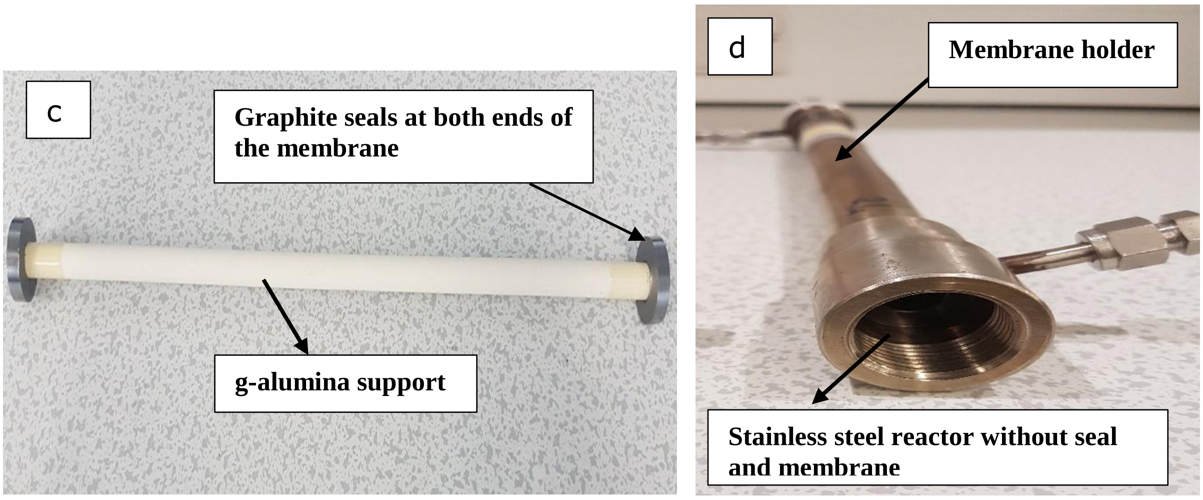

Figure 3.7: Pictorial view of one end of the reactor showing the membrane pore/fitted Gee graphite seal (3.7a), the pictorial view of the reactor screw cap (3.7b), pictorial view of plan ceramic support with both end covered with seal (3.7c) and stainless-steel reactor with membrane and seal (3.7d).

3.2.1.3 Tubular Alumina Ceramic Membrane

The commercial available tubular alumina ceramic membrane used for the experiment was supplied by ceramiques techniques et industrielles (CTI SA), France. This membrane was 15 nm in pore size and composed of 77% Al_2O_3 and 23% TiO_2 with the porosity of 45%. The inner and outer diameter of the support was 7 and 10 mm respectively with the total length of 36.6 cm and effective length of 34.2 cm. Additionally, various factors such as membrane area were put into consideration in selecting the alumina membrane.

The membrane area was calculated using the equation:

$$A = \frac{\pi L(r_1 - r_2)}{\mathrm{In}(r_1 / r_2)} \quad \ldots\ldots\ldots\ldots\ldots\ldots\ldots\ldots\ldots\ldots\ldots\ldots\ldots\ldots(3.2)$$

Where A = membrane surface area (m^2), L = length of the membrane (m), r_1 = membrane outer pore diameter (m), r_2 = membrane inner pore diameter (m), π = constant (3.142) [112].

The alumina membrane was selected for the test with the carrier gas because it can also be affordable they are inexpensive and exist in different sizes and shapes. However, they are thermally stable at higher temperatures, and have good resistance to corrosion properties as well as high mechanical stability. Figure 3.8 shows the pictorial view of the tubular alumina ceramic membrane that was used for the experiment. The pictorial view of stack of the fresh commercial available tubular ceramic membrane showing the pores is presented in figure 3.9.

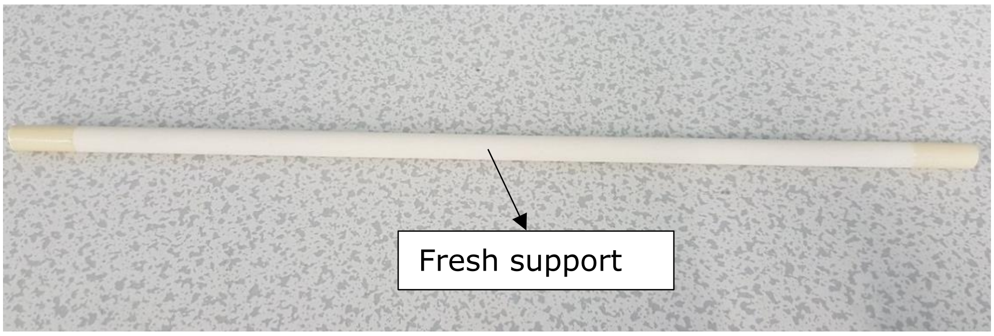

Figure 3.8: Pictorial view of a fersh commercial avaliable 15nm alumina ceramic membrane.

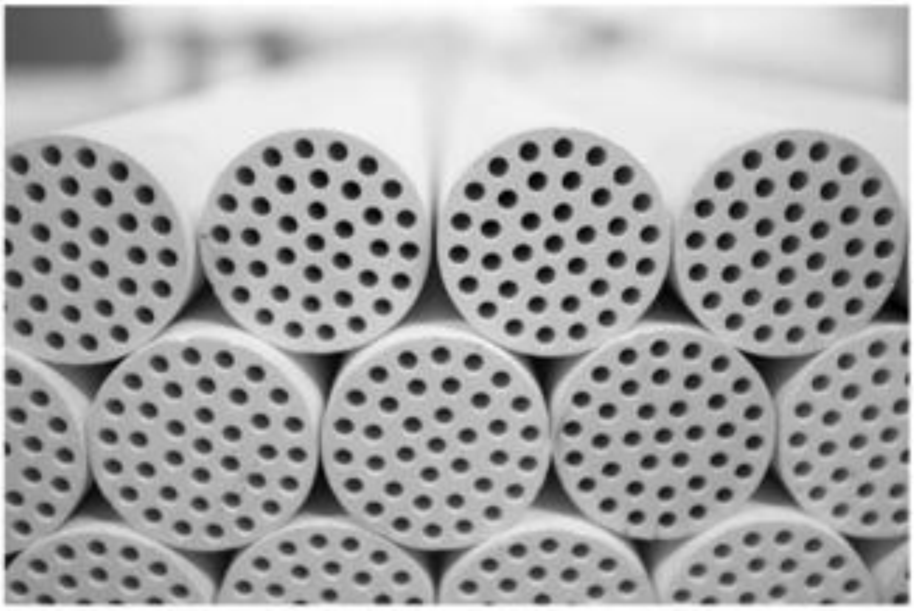

Figure 3.9: Pictorial view of the stack of fresh commercial available 15nm alumina ceramic membrane showing the pores [113]**.**

3.2.1.4 Vernier Calliper

The veneer calliper was used for the measurement of the outer and the inner pore diameter of the commercial available alumina support membrane before the experiments. The pictorial view of the veneer calliper is shown in figure 3.10a. The measurement of how the inner and outer pore diameter of the fresh membrane was carried out is shown in figure 3.10b and c.

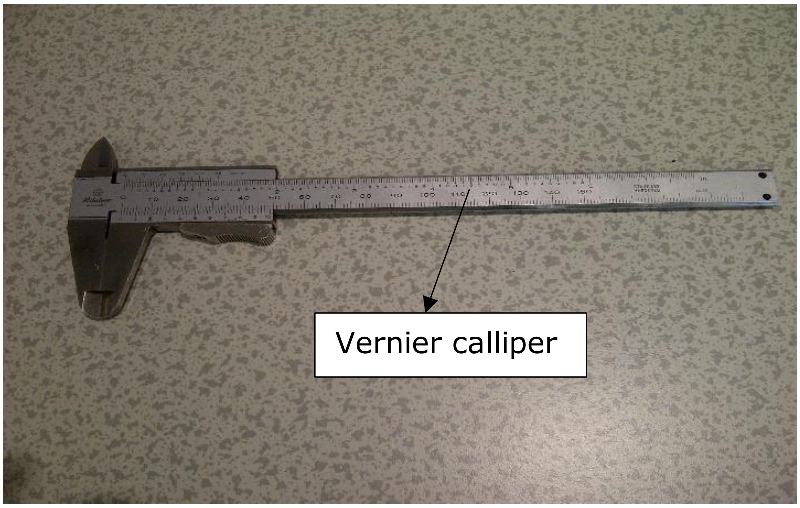

(a): Pictorial view of the Vernier calliper.

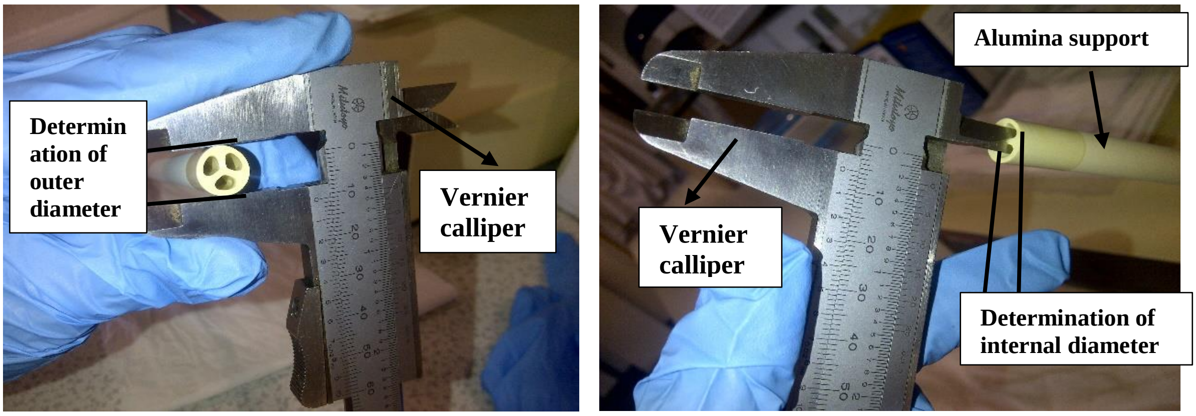

(b) (c)

Figure 3.10: Pictorial view of the Vernier calliper (a), outer (b) and inner (c) diameter of the alumina membrane using the veneer calliper.

3.2.1.5 Graphite Seals

The graphite seal with the dimension 23mm outer diameter x 11mm internal diameter x 6mm thick, 1.6g/cc density, 98% purity were used to block both ends of the reactor for air tight in other to prevent any leakage into the reactor. Supplied by Gee Graphite Ltd, Dewsbury, England, UK.

3.2.1.6 Gauge Pressure and Connectors, Thermometer and Flow meter

The inlet gauge pressure through the reactor was measured using highly certified digital gauge pressure (Keller druckmesstechnik Winterthur, Switzerland) with the room temperature factory setting accuracy of 0.1% and the working pressure range between –1 to 30 bar. Figure 3.11a-b shows the gauge pressure and the valve. Certified analytical digital EExia IICT4 Digitron thermometer supplied by Sifam

Instrument Ltd, woodland, Torquay, UK) was used for measuring the temperature. This instrument operates within the temperature range of -50 + 950 ºC. The flow rate of the different carrier gases were measured using a highly accurate digital 32908-71 flow meter supplied by Cole-Palmer Instrument Co Ltd, London, UK. Figure 3.11c-d shows the pictorial view of the thermometer and the digital flow meter respectively.

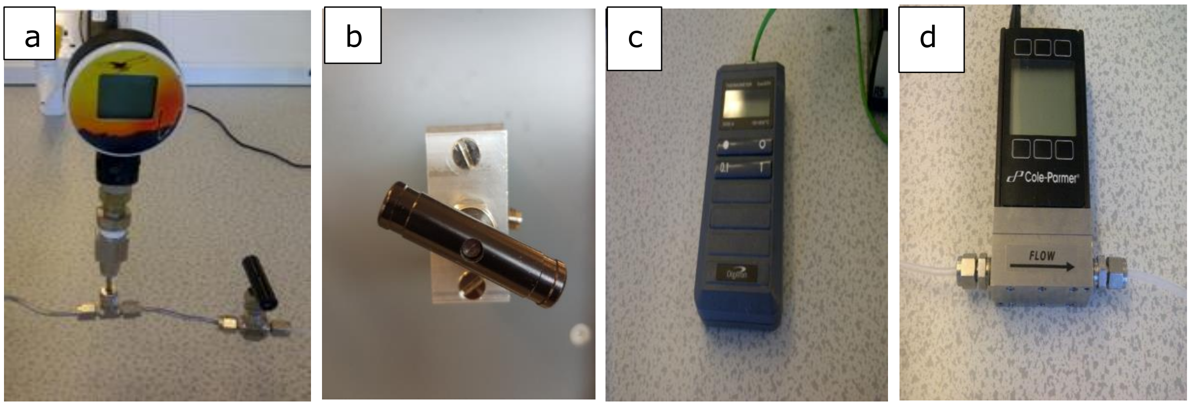

Figure 3.11a-d: Gauge pressure (a), connectors (b), Digitron Thermometer (c) and Digital flow meter (d).

3.2.1.7 Heating Tape

Electrothermal heating tape (HT9) with a temperature capacity of up to 450 ºC and 230V was used for the experiment which serves as a protective cover for the membrane at high temperatures.

3.2.1.8 Fume Cupboard

The experiments involved using of gases and different toxic chemicals including iso-pentane which is highly flammable and as such, all the solution preparations were carried out in the fume cupboard for health and safety purposes. The waste gases from the retentate side of the reactor during the carrier gas permeation test was release through the outlet flow tube that was connected to one end of the flow meter into the fume cupboard through which the gases exit into the atmosphere as shown in figure 3.12.

Figure 3.12: Pictorial diagram of the fume cupboard.

3.2.1.9 Thermocouple box and thermocouple wire

A 6-way type K (selector model) digital thermocouple box (figure 3.13a) was used to determine the temperature of the membrane at each point. Thermocouple housing box consist of metallic wires which was connected the reactor. This serves as the sensor in detecting the temperature of the membrane. The thermocouple wire (Cole-Palmers, London, UK) that were used to detect the temperature of the reactor at each stage as the membrane was being heated in the reactor. The thermocouple wires were (Fig 3.13b) connected through the back end of the thermocouple housing box and the different stations were labelled as shown in figure 3.13a. The Barnstead electrothermal model power regulator was used to regulate the temperature of the reactor in the rage of 0 to 1000 with 230Volts ~50/60Hz and 2300Watts. Supplied by Bio Surplus Inc. California, USA. Figure 3.13c shows the Barnstead Electrothermal power regulator.

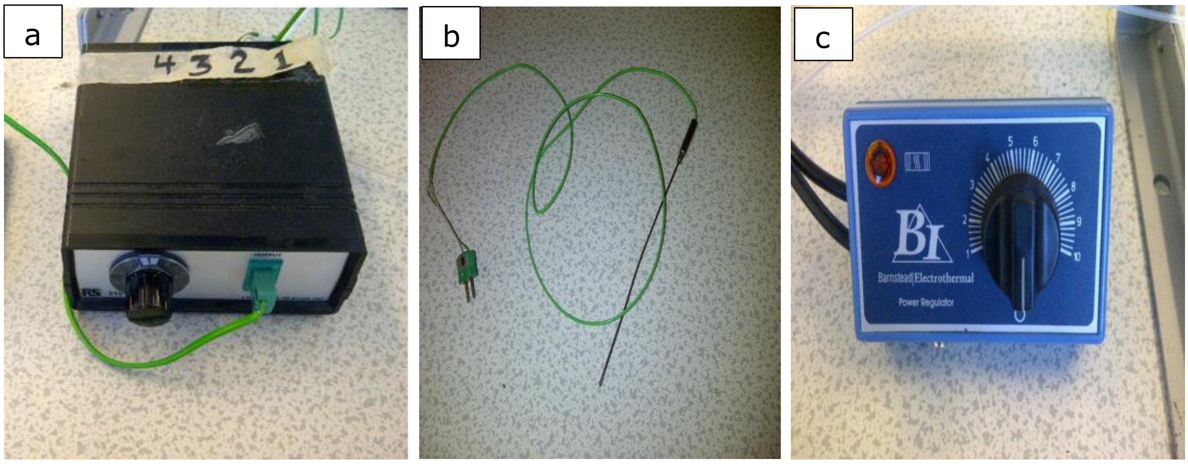

Figure 3.13: Pictorial diagram of the thermocouple box (a), thermocouple wire (b) and Barnstead Electrothermal power regulator (c).

3.2.1.10 Sylgard®184 Silicone Elastomer

The 184 silicone elastomer sylgard (R) kit was purchased from Dow Corning Corporation (U.S.A). This kit consists of silicone elastomer bottle with 50 mL bottle of curing agent (hardener). The silicone elastomer is sticky and colourless.

3.2.1.11 Iso-Pentane (2-methylbutane)

The 1000 mL bottle of iso-pentane (2-methylbutane) was in used for the experiment and was supplied by Sigma Aldrich, UK.

3.2.1.12 Sylgard®184 Curing agent

The curing agent used for the membrane dip-coating process was obtained from the Dow corning corporation (U.S.A). The curing agent also referred as the hardener is a colourless solvent was allowed the silicone elastomer to bind to the surface of the membrane during the modification process. Fig. 3.14 shows the materials that were used for the membrane modification process including the silicone elastomer, iso-pentane (2-methyl butane) and the curing agent. Figure 3.14 shows the Pictorial view of silicone elastomer kit consisting of the Sylgard®184 silicone elastomer, sylgard®184 curing agent and the iso-pentane (2-methylbutane).

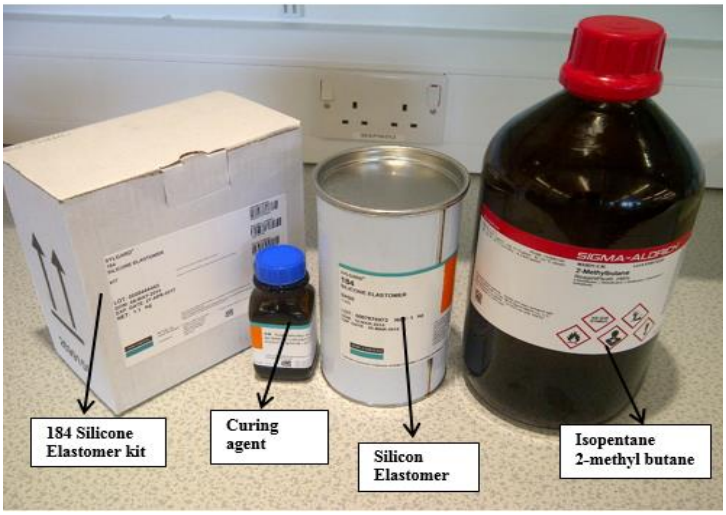

Figure 3.14: Pictorial view of silicone elastomer kit consisting of the silicone elastomer and curing agent.

3.2.1.13 Carbolite Oven

A certified industrial oven (Carbolite oven PF 120, UK) with maximum temperature of 300 °C was employed for the drying of samples and glass wares and sample bottles. Figure 3.15a and b shows the pictorial view of carbolite oven (3.15a) and the inside of the oven with a dried alumina support membrane (3.15b).

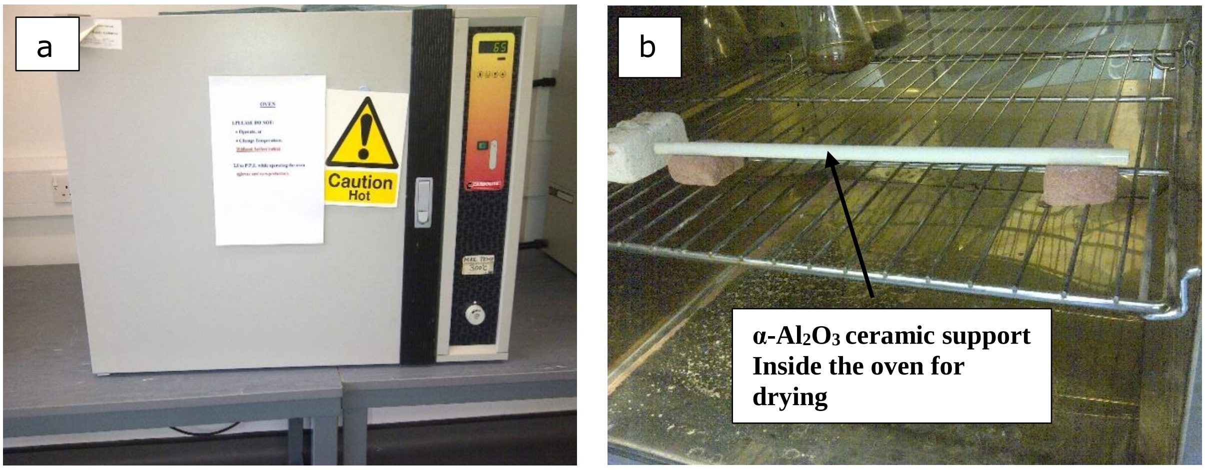

Figure 3.15: Pictorial view of carbolite oven (a) and the inside of the oven with a dried alumina support membrane (b).

3.2.1.14 Magnetic Stirrer

This is a small round whitish equipment that was inserted into the measuring cylinder containing the silica solution during each dip-coating process to carefully mix the solution for uniform modification of the support.

3.3 Choice of Carrier Gases

The four carrier gases used for the permeation test were the single gases that are generally use as carrier gases with the GC to analyse esterification reaction product solvents depending on the detector that is connected to the GC-MS. These gases can also work both as a carrier gas and as also as a detector gas. As a carrier gas it helps to transport the liquid sample to the column for analysis to take place in the GC. While as a detector, it helps to detect the different ions in the esterification product solvent. From reviewing the literature, the choice of the carrier gas was made based on the detector that is being coupled to the GC. Also, if a wrong carrier or detector gas is being used for the analysis, it might react with the solvent and may also damage the column. For flame ionisation detector (FID), hydrogen is normally used as the carrier gas to analyse the reaction product while mass spectrometry detector (MSD) uses helium, nitrogen, carbon dioxide or argon as the carrier gases. According to Sunarso et al. [91], helium gas can be used as a carrier gas with gas chromatograph. The essence of carrying out the membrane permeation test with single gases was to first of all determine the behaviour of the gases to see the behaviour and different transport mechanism before employing these gases for the analysis of the esterification reaction product with GC-MS at different temperatures.

3.3.1 Helium gas (He)

Helium gas (99.999% pure, BOC Gases, UK) was use for the analysis. This gas was supplied by BOC, UK with maximum working pressure of 288.15 K at 2bar. It was used as supplied without any additional purification. An HP1500 Series single stage regulator (HP 1500 series 851750) used for the helium gas was supplied by BOC Gases, UK.

3.3.2 Argon gas (Ar)

Argon gas with 99.999% purity (BOC Gases, UK) was use for the analysis and was purchased from BOC, UK. The maximum working pressure was 2 bar at 288.15K. It was used as supplied without any further purification. An HP1500 Series single stage regulator (HP 1500 series 851750) used for the argon gas was supplied by BOC Gases, UK.

3.3.3 Nitrogen gas (N_2)

Nitrogen gas (99.999% pure, BOC, Gases, UK) was supplied in a cylinder by BOC, UK. The maximum working pressure of the gas was 288.15K at 2 bar. The gas was used as purchased without any further purification. An HP1500 Series single stage regulator (HP 1500 series 851750) used for the nitrogen gas was supplied by BOC Gases, UK.

3.3.4 Carbon dioxide gas (CO_2)

The carbon dioxide gas with 99.9% purity (BOC, Gases, UK) was supplied in a cylinder by BOC, UK with the maximum working pressure of the gas was 288.15K at 2 bar. An HP1500 Series single stage regulator (HP 1500 series 851750) used for the carbon dioxide gas was supplied by BOC Gases, UK.

3.4 Experimental Procedure for α-Al_2O_3 Support Membrane

The commercial available ceramic α-Al_2O_3 membrane with a diameter of 30nm that was used as the support for the study possess a permeable length of 34.2cm, as well as 7mm and 10mm for the internal and outer diameter respectively. This membrane was used direct as purchase from the manufacturer. The feed gauge pressure used for the permeation test with the carrier gases was varied in the range of 0.10 to 1.00 bar at both room and at different temperatures. Prior to the 1st dipping, the support structure was access to be defect-free.

3.5 Membrane Reactor Operation Procedure

The gas permeation test between the commercial available support membrane with 15nm pore size and 7mm and 10mm inner and outer radius and total permeable length of 34.2 mm as well as the silica membrane was used for the study. The permeation test was conducted at room temperature and at different temperature of 60 ºC and up to 160 ºC (333-433 K) at the feed gauge pressure range of 0.10 to 1.00 bar. Prior to the experiments, the support membrane was found to be defect free before it was inserted into the reactor. The single carrier gas used for the experiments were He, CO_2, N_2 and Ar with at least 99.99% purity and was supplied by BOC, UK. Figure 3.16 shows the schematic diagram of the carrier gas permeation test setup which consists of; carrier gas cylinder (1), gas feed inlet (2), permeate pressure gauge (3), control valve (4), O-ring graphite seal (5), reactor (6), heating tape (7), temperature regulator (8), thermocouple (9), thermocouple box (10), retentate pressure gauge (11), flow meter (12) and fume cupboard (13).

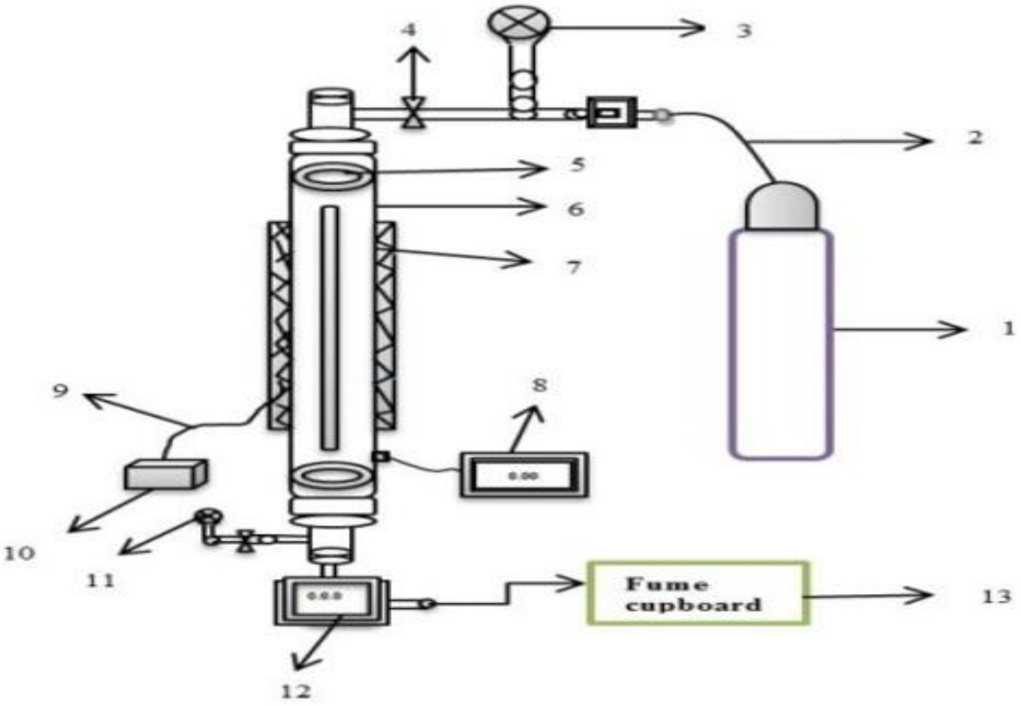

Figure 3.16: Schematic diagram of the Gas permeation setup for investigation of the effect of temperature on Ar, He, N_2 and CO_2 gases through silica membrane [114].

3.5.1 Permeation Cell

The permeation cell consisted of a stainless-steel shell with high-temperature resistant. The membrane was centralized in the tube using a graphite seals at either end. Through the use of various connections and valves the cell permits the measurement of the gas flux through the membrane at various feed pressures. A heating tape was wrapped over the stainless steel to enable high-temperature studies to be carried out. Prior to permeation experiments, a leak test was carried out by monitoring the downstream pressure increment while the system remained totally closed. The reactor had a dimension of 32.1 cm long with the thickness of 0.3 cm. The membrane reactor used for the experiment was made up of stainless steel tubular reactor with the thermocouples at four different positions as well as the power controller connected to the reactor to monitor the temperature of the tubular membrane centralized inside the stainless-steel tube. The two ends of the membrane were blocked with an O-ring graphite seals (GEE Graphite, Dewsbury, UK) to make it air tight before the two ends of the reactor were covered with screw caps, the stainless steel that is fitted to the reactor which prevent the passage of air into the reactor. Four thermocouples wires (Cole-Palmers, London, UK) are inserted into the heating tape at four positions with the ends connected to the thermocouples box (K-type). The temperature at the four-different position were controlled using the power regulator which was connected to the reactor.

The dip-coated membrane was inserted into a stainless-steel reactor and both end were sealed with a G-graphited seals to make it air tight and to avoid gas leakage from the reactor into the atmosphere during the experiments. The stainless-steel reactor was wrapped with heating tape which serves as a protection for the membrane at higher temperatures. The carrier gas test was carried out for single gases including helium, argon, nitrogen and carbon dioxide at room temperature and at different temperature respectively. The carrier gas was introduced through the permeate side of the reactor which penetrate through the pores of the dip-coated membrane at different feed pressures. A mass flow controller was also connected to the reactor to determine the flow rates of the gases. The carrier gas interaction with the membrane takes place within the stainless-steel reactor, with the retentate side of the reactor fully closed.

3.6 Carrier Gas Permeation Analysis

Prior to the gas permeation test experiment, a leak test was first of all carried out at each end of the connection to ensure that there was no gas leakage in the reactor before the experiment. The permeation using a carrier gas was carried out at the gauge pressure range of 0.10 to 1.00 bar and temperature between 298K - 433 K. Some of the carrier gas cylinders (CO_2, Ar and He) were connected to the membrane reactor from the gas manifold connection point as shown in Figure 3.17 exception of N_2 cylinder which was connected directly to the reactor. Figure 3.17 shows the pictorial view of the gas manifold connection.

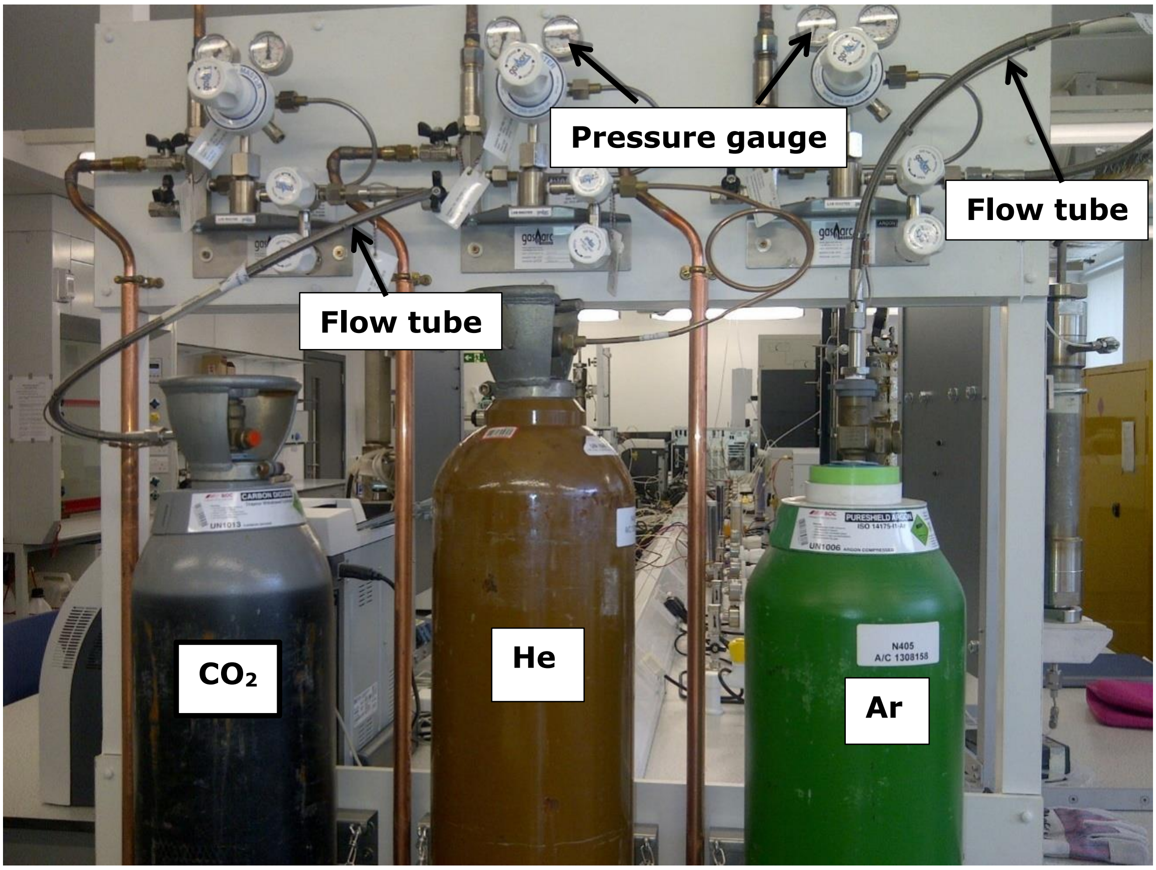

Figure 3.17: Pictorial diagram of carrier gas manifold connection unit.

A similar method to that of Poshusta et al. [115], was adopted and modified by changing the pressures and temperature. The effect of permeance on the gas molecular weight, kinetic diameter, gas viscosity and temperature were investigated. Also, the effect of feed gauge pressure on the gas flow rate, permeance and flux was investigated as the inlet gauge pressure was adjusted in 0.10 bar increments from 0.10 to 1.00 bar to determine the various transport mechanisms controlling the gas flow through each membrane. The values of the experimental gas permeation were recorded for both the support and silica throughout the temperature ranges of 298K – 413K and comparisons were made between the membranes. The carrier gas transport was measured using the permeation setup as shown in figure 3.18.

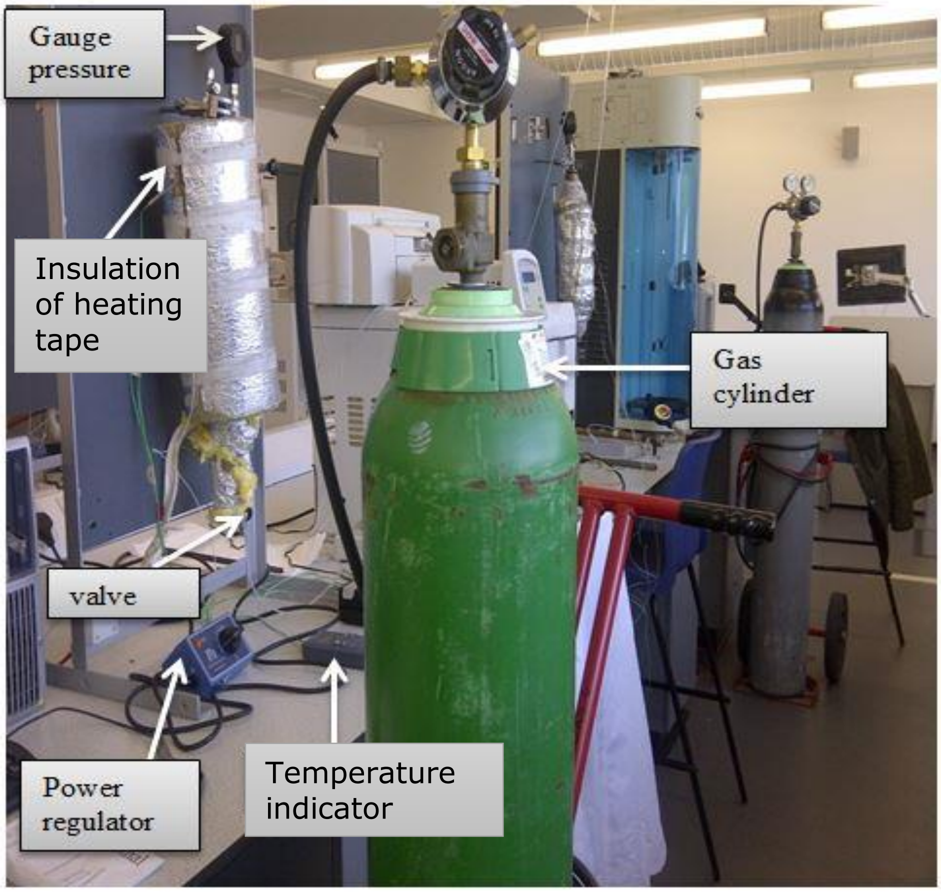

Figure 3.18: Pictorial view gas permeation setup and membrane reactor setup enclosed in the heating system.

CHAPTER 4

4.0 Batch Process using different Cation-exchange resin Catalysts and Cellulose Acetate Coupled Resin Esterification Reaction.

This chapter presents the batch process esterification reaction process and the different cation-exchange resin catalysts that were used for the batch process analysis. These catalysts possess a higher catalytic effect for the reactant solvent to act upon and can also withstand the effect of higher concentration of lactic acid and ethanol. This chapter also explain the experimental setup for the esterification process of lactic acid to produce ethyl lactate using a flat sheet cellulose acetate membrane impregnated with resin catalysts. The polymeric membrane possesses a higher permeability of up to 4000 molmm^{-2}s^{-1}Pa^{-1} which seem to be more efficient for the shifting of chemical equilibrium and removal of water from the esterification reaction. This chapter is divided into two different methods. The first part involving the batch process esterification reaction of lactic acid and ethanol using different cation-exchange resin catalysts at different temperatures of 60, 80 and 100 ^{o}C for the reaction kinetics analysis with Gas chromatography coupled with mass spectrometry (4.1a).

The second part detailed the process intensification of ethyl lactate using a flat sheet cellulose acetate membrane reactor impregnated catalyst at the same identical temperatures in other to make comparison (4.1b). The significant of employing the two methods is to compare the efficiency of the methods. In the first method, the batch method does not require membrane. However, the process intensification membrane method does incorporate both catalysts and membrane. The membrane act both as a separator and also as catalyst. As a separator, the flat sheet membrane will react with the reactant components to remove water from the reaction medium to give the lactic acid feed conversion, but as a catalyst the membrane will react with the reactant components thus shifting the equilibrium to the forward reaction to prevent a reversible backward reaction. The different analytical methods used for the cation-exchange resin and membrane (cellulose acetate) preparation and the esterification product analysis technique are also presented in the chapter.

4.1 Materials and Methods for Batch Process Esterification

4.1.1 Experimental set-up

The batch process experimental setup consists of a two-necked conical flask, fitted with a reflux condenser and a vacuum pump. This was design for the purpose of the background study. The schematic diagram of the batch reactor experimental setup is shown in figure 4.1.

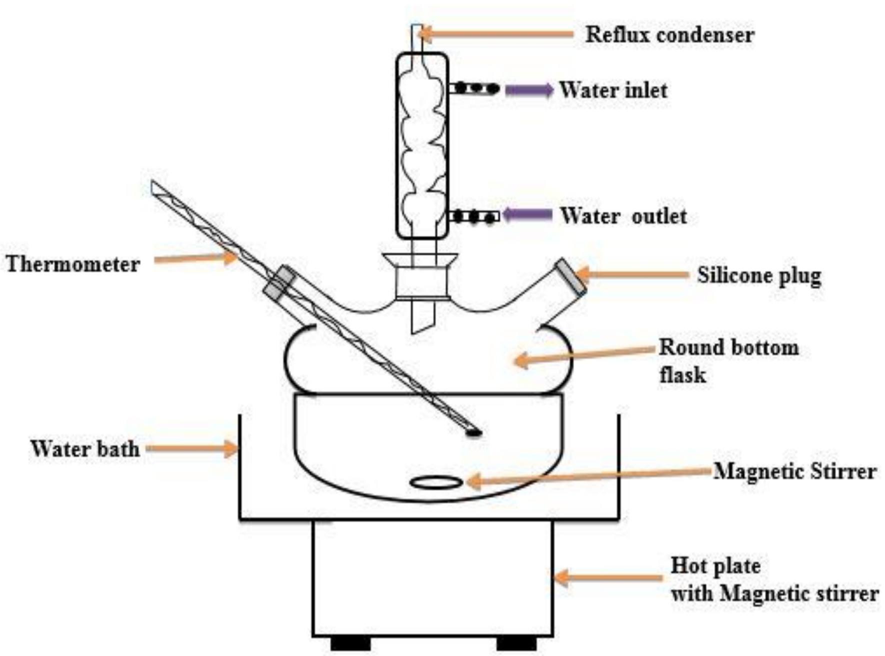

Figure 4.1: Experimental set-up for batch process esterification.

4.1.2 Batch Process Reactor and Round bottom flask

The batch process esterification setup consists of the thermometer, hot plate magnetic stirrer and round bottom flask batch reactor. The reactor was a three-necked round bottom conical flask of 500 mL capacity fitted with a condenser. One neck of the reactor was fitted with a glass reflux condenser with a spiral design which allows the flow of water through and out of the system. A three-necked round bottom flask of 500 mL capacity was used for the analysis. This reactor was purchased from Sigma-Aldrich, UK. Figure 4.2 shows the pictorial view of the round bottom flask that was used for the esterification process. Due to the even heat distribution that can be produced through the use of a heating mantle, the round bottom flask is the preferred option when the solvent is required to be heated at different temperatures.

Figure 4.2: Pictorial view of a two neck-round bottom flask.

4.1.3 Volumetric Flask and Beaker

The different sizes of volumetric flask including 25mL, 50mL and 100mL volumetric flask used for the esterification reaction experiments were all purchased from Sigma-Aldrich, UK. The different size of beaker including 10mL, 25mL, 50mL, 75mL and 100mL beaker used for the experiments were all supplied by Fisher Scientific, UK.

4.1.4 Deionised water

The deionised water used for the experiments was collected from the water dispenser instrument (ELGA, England, UK) at the CPIMT (centre for process integration and membrane technology) Lab, School of Engineering, Robert Gordon University (RGU), Aberdeen, UK. The resistivity of the instrument was program at 18.9 mΩ cm.

4.1.5 Vacuum Pump and Reflux Condenser

The vacuum pump used for the batch process esterification was purchase from Fisher Scientific UK. The pump was used for the removal of water during the esterification process. Figure 4.3a shows the pictorial view of the vacuum pump that was used for the experiment. The reflux condenser used for the analysis was purchase from Fisher Scientific UK. The glass reflux condenser prevents the solvent mixture from evaporating out of the reaction system. The reflux condenser was a glass tube with two opening by the side of which the two vacuum pumps were connected for the water inlet and outlet through the system. Figure 4.3b shows the pictorial view of the reflux condenser that was used for the experiment.

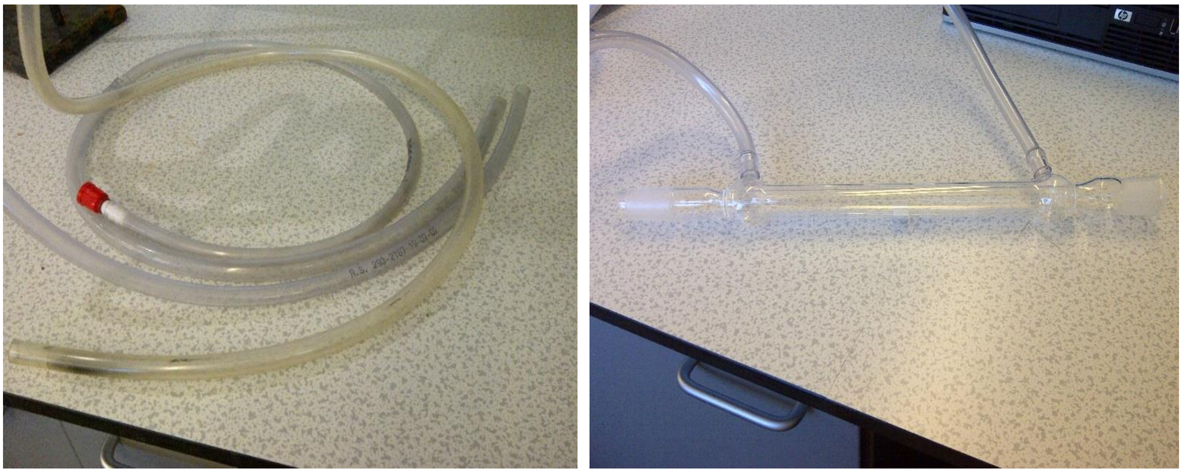

Figure 4.3: Pictorial view of vacuum pump (a) and reflux condenser (b).

4.1.6 Heating Mantle and Temperature Probe

The Barnstead Electrothermal model heating mantle was used to regulate the temperature of the esterification reactant in the rage of 0 to 1000 °C. The heating mantle was supplied by BioSurplus Inc, California, USA. Figure 4.4a shows the pictorial view of the heating mantle. Certified analytical digital EExia IICT4 Digitron thermometer supplied by Sifam Instrument Ltd, woodland, Torquay, UK connected to a metallic probe was used for test the temperature of the esterification reaction during the batch process esterification analysis. This instrument operates within the temperature range of -50 + 950 °C. Figure 4.4b shows the pictorial view of the temperature probe.

Figure 4.4: Pictorial diagram of the heating system (a) and Pictorial diagram of the temperature probe (b).

4.1.7 Magnetic stirrer

The magnetic stirrer was inserted into the beaker during each batch esterification reaction to ensure that the reactant solvent are well mix and was placed unto the electric stirrer to properly mixed the solvent with the different cation-exchange resin catalysts to achieve uniform esterification product before it was transferred into the batch reactor for the selective removal of water from the system at each temperature.

4.1.8 Cation-exchange resin selection

The catalysts were selected based on reviewing the literature to see what is obtainable in the literature. On reviewing the literature, it was found that different catalysts have been used for esterification of lactic acid with other alcohols in the presence of different amberlysts and the dowex catalysts but much work has not been carried out on esterification of lactic acid with ethanol to produce ethyl lactate [4,13,15]. Cation-exchange resin were also chosen because these catalysts possess higher mechanical stability, low cost, environmentally friendly are and chemically compatible with several liquids [50]. This catalyst offer several advantages over homogenous catalysts. They can be removed easily from the reaction medium and can be recycled. Additionally, the effect of the resin in the reaction system allow high selectivity and eliminate or reduce undesirable side reaction [116]. Also, they are commercially available in different shape and sizes and exist in solid form. The different cation-exchange resins used in the experiment were: amberlyst 36, amberlyst 15, amberlyst 16 and dowex 50W8x. These catalysts are commercial available solid cation-exchange resins supplied by Sigma-Aldrich, UK. Figure 4.5 shows the pictorial diagram of the different cation-exchange resins. Figure 4.5 shows the sample bottles of the different cation-exchange resins that were used for the esterification analysis.

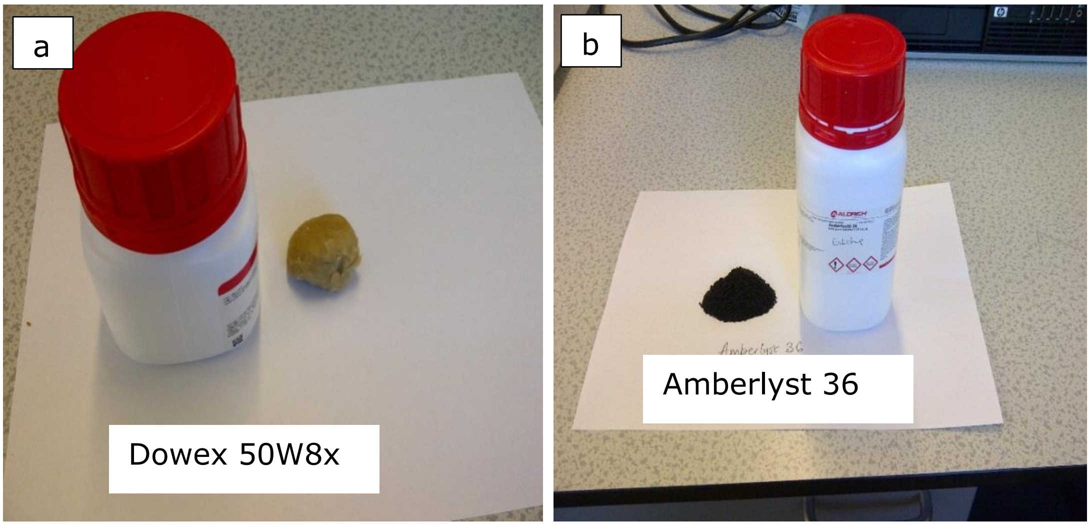

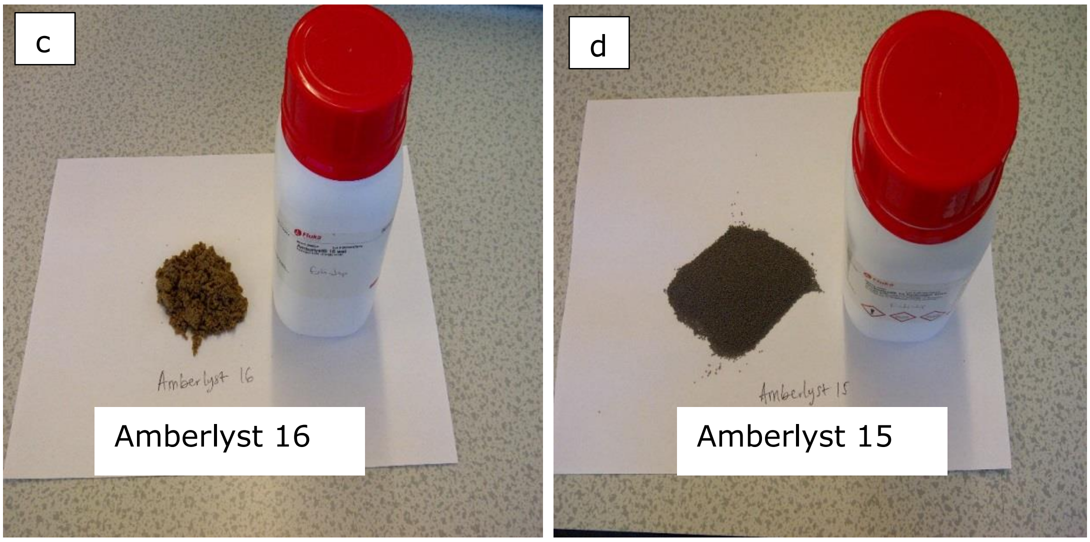

Figure 4.5: Pictorial diagram of dowex 50W8x (a), amberlyst 36 (b), amberlyst 16 (c) and amberlyst 15 (d) sample bottles containing the fresh commercial available cation-exchange resins.

4.1.9 Lactic acid, Ethanol and Commercial Ethyl lactate solvent

Aqueous lactic acid (99.99wt%) solutions was used for the analysis and was purchased from Sigma-Aldrich, UK. This solution was used as received without and further purification or dilution. Analytical grade ethanol (99.98 wt%) solution was used for the analysis and was purchased from Sigma-Aldrich, UK. This solution was used as received without and further purification or dilution. Analytical grade ethyl lactate (99.99 wt%) solvent used for the analysis was purchased from Sigma-Aldrich, UK. This solution was used as received without any further purification or dilution. The commercial available ethyl lactate solvent was tested in other to compare the GC-MS results with that of the produced esterification reaction product. Figure 4.6 pictorial view lactic acid solvent bottle (a), ethanol (b) and ethyl lactate (c) solvent bottles.

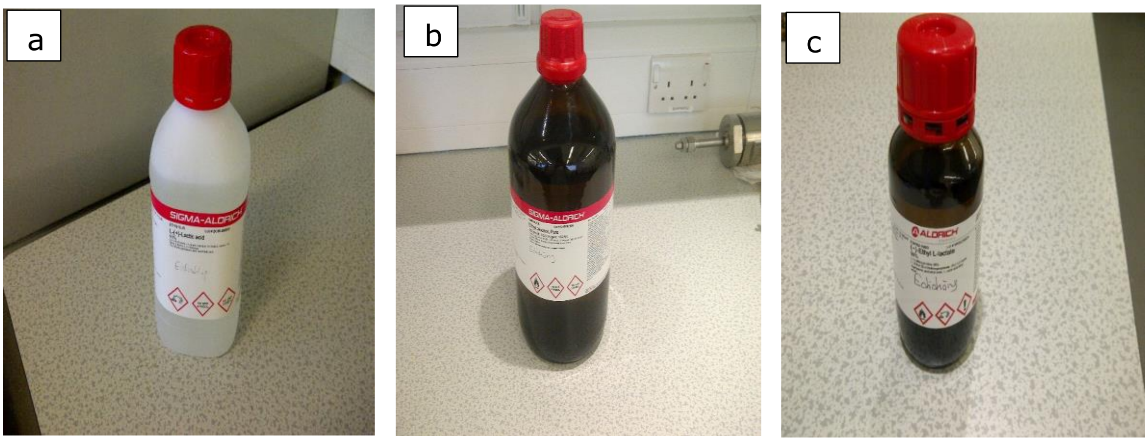

Figure 4.6a-c: Pictorial view of lactic acid (a), ethanol (b) and ethyl lactate (c) solvent bottles.

4.1.10 Pipette

The Hamilton HM80300 microliter TM pipette was used to measure the esterification product into the sample vial before the sample analysis with GC-MS. The dilution solvent was collected using the Hamilton pipette (1000mL of the dilution solvent) while the microliter pipette (10µL) was used to collect the esterification product for the analysis. Figure 4.7 shows the Hamilton HM80300 microliter TM pipette (a) and microliter pipette (10µL) (b). The Hamilton pipette was used to measure the required amount of diluting solvent.

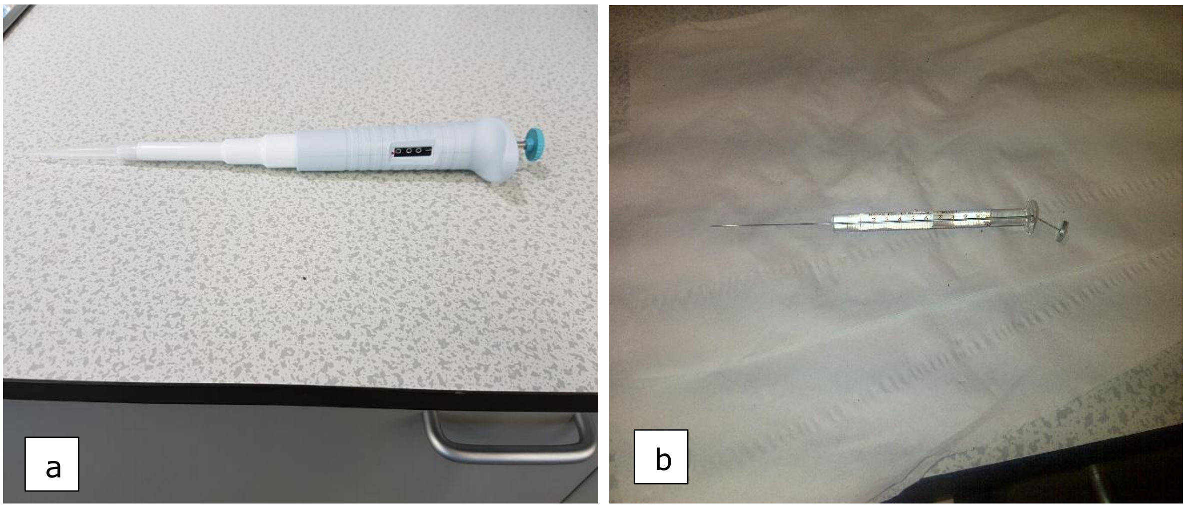

Figure 4.7: Manual pipette with pipette tip (a) and Hamilton HM80300 microliter TM pipette (b).

4.1.11 Fume cupboard and Oven (Carbolite)

As the experiments involved using high concentrations of lactic acid, ethanol and cation-exchange resins. All the chemical preparations and cation-exchange resins cleaning process before each esterification process were carried out in the fume cupboard. The carbolite oven was used for drying of the cation-exchange resin catalysts after each catalyst cleaning process before it was used for the esterification reactions.

4.2 Batch process Esterification method and Procedure

4.2.1 Catalyst Cleaning

Prior to the analysis, about 100 g of each of the fresh commercial available cation-exchange resin amberlyst 36, amberlyst 16, amberlyst 15 and dowex 50W8x was weighed into a 50mL beaker using the weighing balanced as shown in figure 4.8. The catalysts were further rinsed with 2 mL of deionised water and 5mL of ethanol. The cation exchange resin cleaning process was based on a similar method to that of Jogunola et al. [117] was adopted and modified for the catalysts cleaning process. The importance of cleaning the cation-exchange resins before the experiment was to remove any poisonous substances, impurities, moisture and also to reduce the concentration of the solid exchange resins before the esterification analysis. Figure 4.9 shows the analytical weighing balance. The composition of the solvent for the cation-exchange resin cleaning is explained in table 4.1.

Figure 4.8: Analytical weighing balance.

Table 4.1: Composition of the solvents used for the esterification process

Substance	Amount (mL) and g
Ethanol	5mL
deionised water	2mL
Resin catalysts	100g
Beaker	50mL

After rinsing, the cation-exchange resins were oven dried at the programmed temperature of 65 °C for 24 hrs to remove the moisture completely. After drying, the resins was retrieved from the oven and used for the esterification reaction analysis at the temperatures of 60, 80 and 100 °C. Figure 4.9a and b shows the pictorial view of the instruments that supplied the deionised water (a) and the inside of the carbolite oven (b). The pictorial view of each resin catalysts after drying in the oven is shown in figure 4.10.

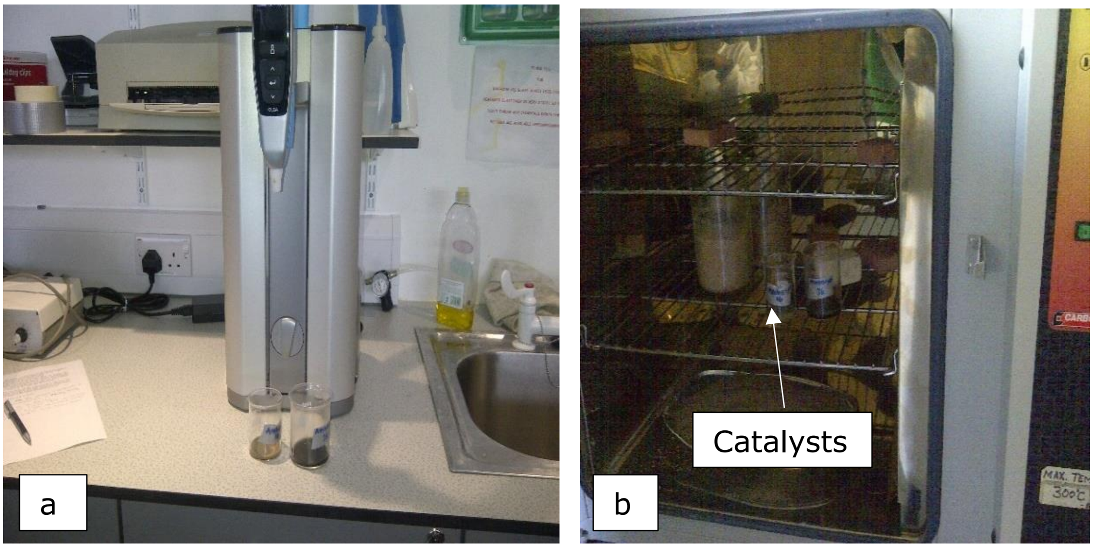

Figure 4.9a and b: Resin catalysts before rinsing with deionised water (a) and catalyst drying in the oven (b).

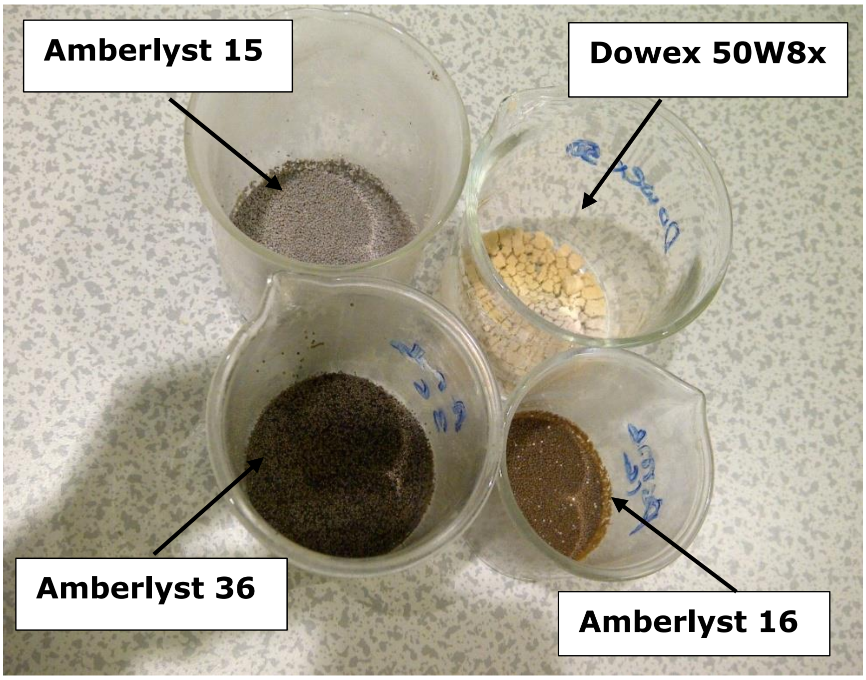

Figure 4.10: Cation-exchange resin catalysts after drying in the oven.

4.2.2 Batch process esterification reaction

Prior to the esterification process, about 5g of each of amberlyst 36, 16, 15 and dowex 50W8x which has pass through the cleaning process was accurately weighed into a 100mL beaker and 60 mL of aqueous lactic acid solution (98.9 wt%) was measured into the same beaker and heated for 30 minutes as shown in figure 4.11. After 30 minutes, 80 mL of ethanol (99.9 wt%) which was heated separately using the heating system was added into the beaker containing the lactic acid and the resin catalysts and was allowed to stir for another 30 minutes. After 30 minutes, the solution was allowed to cold for 10 minutes before it was transferred into a two-neck conical flask reactor of 500 mL fitted with a reflux condenser and was placed in a heating rota-mantle which was equipped with a stirrer speed control knob and a heat control knob. The reflux condenser was connected horizontally to the reaction conical flask. The essence of connecting the reflux condenser to the reactor was to condense the vapour and mix them back with the bulk mixture and the condenser was used to avoid the vapour from escaping out of the reacting mixture and this was achieved by blocking the ends of the condenser with a glass stopper. The solution was stir for 24 hrs using a magnetic stirrer in other for the bulk solution to mix together and also to attain equilibrium. The composition of the different solvent is explained in table 4.2.

Table 4.2: Composition of the Solvents used for the Esterification Process.

Substance	**Amount (mL) and g**
Lactic acid	60mL
Ethanol	80mL
Resin catalysts	5g

The rotational speed of the magnetic stirrer was controlled from the heating rota-mantle system at the speed of about 400-800 rpm by using the speed control knob. The lactic acid and each resin catalyst were first of all heated separately before the ethanol was added. The reason for carrying out the analysis using the heating mantle before transferring to the batch reactor was to avoid the breaking of the glass reactor at higher temperatures. The heating was control manually in other to achieve the desired temperatures. After the addition of ethanol, the reaction mixture was transferred to the batch reactor through the opening of the reactor. The temperature of the reaction system was controlled using a temperature probe connected to a thermometer as shown in figure 4.11, and the experiment was carried out at different temperatures of 60, 80 and 100 ^{o}C. The temperature probe was inserted into the solvent mixture after each 5 minutes to test the solution at each reaction temperature.

Figure 4.11: Heating system with reactant mixture.

The heating was done separately using a 100 mL beaker before the bulk solution was transfer to the batch reactor for the solution to mix together. Figure 4.12 shows the batch process apparatus for the esterification reaction process. Two peristaltic pumps were connected to the necks of the reactor for the water inlet and out. The water from the reaction product was removed by connecting two vacuum pumps to the openings of the reactor i.e the inlet and the outlet water flow. The inlet water that flows through the pump was used to flush the evaporated water through the system while the outlet displaced the evaporated water from the reaction system as shown in figure 4.12. The mixture was left in the reactor with a magnetic stirrer to mix the solution together and for it to attain equilibrium before the analysis with GC-MS. A retort stand was used to support the reactor and this experiment was carried out in the fume cupboard. A similar method as that of Jogunola et al. [117] adopted for the batch esterification process. The same experimental procedure was repeated for the temperatures of 80 and 100 ^{o}C for each cation exchange resin. After each batch esterification process at each temperature with respective catalysts, about 1mL of the esterification product was injected to gas chromatography coupled with mass spectrometry (GC-MS) for qualitative and quantitative analysis [8,118]. Figure 4.12 shows the pictorial view of the batch process esterification reaction setup. Figure 4.13 shows the pictorial diagram of the cation-exchange resin after the esterification process.

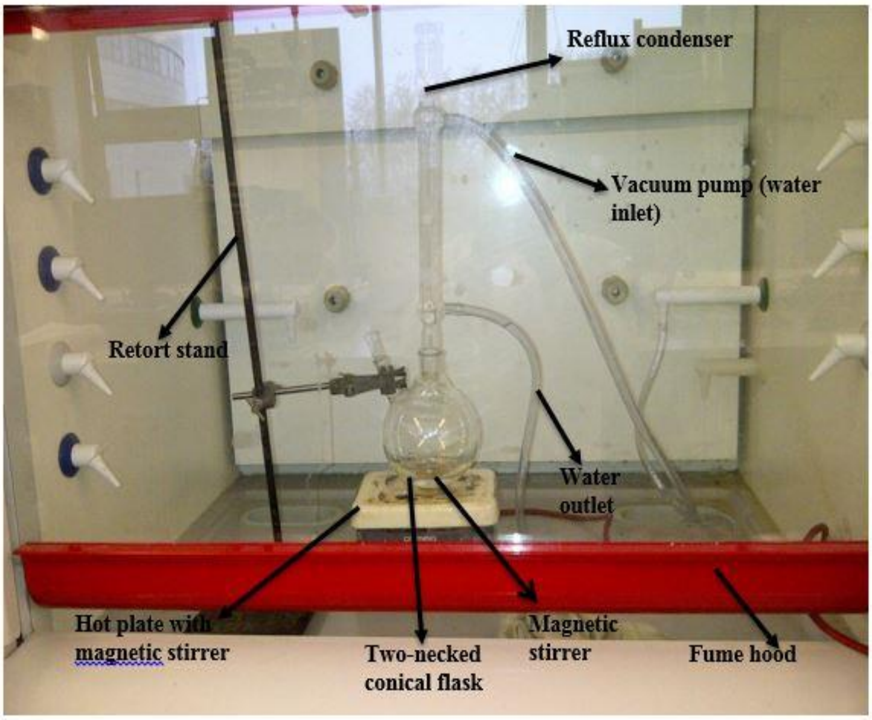

Figure 4.12: Schematic diagram of a batch process reactor for ethyl lactate separation without a membrane.

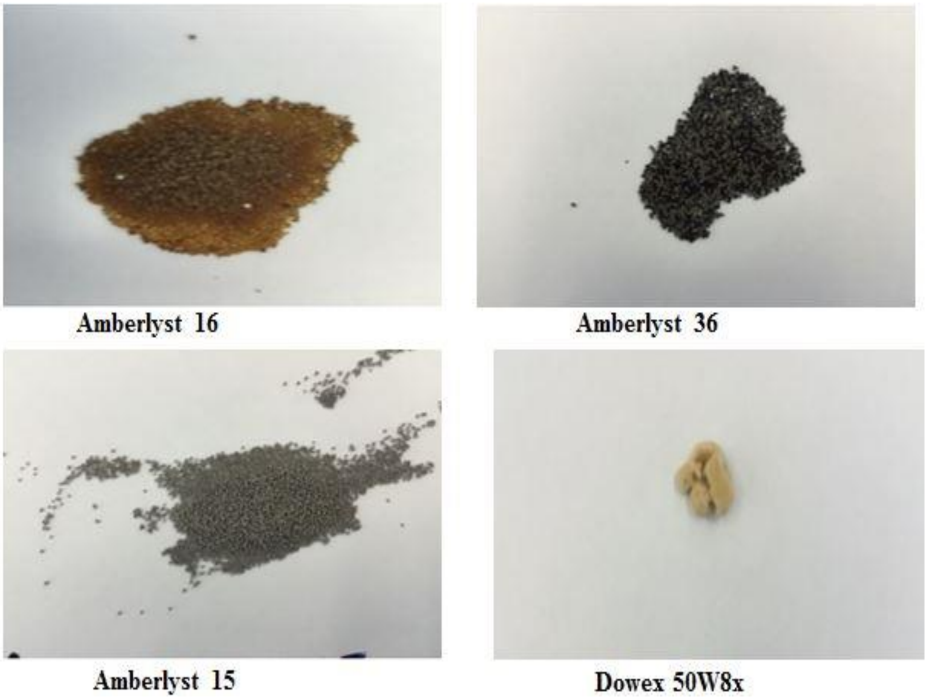
Amberlyst 16

Amberlyst 36

Amberlyst 15

Dowex 50W8x

Figure 4.13: Pictorial diagram of commercial available cation-exchange resin after esterification process

4.2.2.1 Optimum Operating Conditions for the GC-MS

The analysis of the reaction product catalysed by different cation-exchange resin catalysts was carried out using a 7693 autosampler which inject 1µL of sample and a 7890B gas chromatograph (Agilent Technologies, Santa Clara, California, USA) equipped with a split/splitless injector coupled to a 5977A mass spectrometry detector (Agilent Technologies, Santa Clara, California, USA). Barbosa et al. [119] also used a similar for the analysis of product. The GC-MS was also equipped a HP-5MS 5% Phenyl Methyl Silox capillary column (Agilent Technologies, Santa Clara, California, USA) with the column dimensions of 30 m x 250 µm x 0.25 µm was used for the analysis and was heated at the rate of 10 ^{o}C/min, at the pressure of 63.063 kPa, with the average velocity of 39.723 cm/sec. Figure 4.14 shows the pictorial view of GC-MS that was used to detect and identify the esterification reaction product. Analytical grade Helium gas with 99.9% purity (BOC, United Kingdom) was used as both carrier and detector gas. The front injector was set at 10µL. The injection port was operated at 300 ^{o}C. The oven temperature was programmed at 40 ^{o}C with the holding time of 2 ^{o}C/min at the maximum operating temperature of 325 ^{o}C and held constant for an additional 6 min. The Helium gas temperature was set at 40 ^{o}C at with the flow rate of 1.2 L/min with the equilibration time of 0.25 min while the inlet pressure was 100 PSI. The solvent analysis was set on split mode with the split mode with the split ratio of 50:1. The commercial ethyl lactate was used as reference for the sample analysis. A similar method to that of Komon et al. [120] was adopted in the analysis. The NIST GC software program was used for the data collection.

Figure 4.14: Agilent 7890B autosampler Gas chromatograph (GC) system coupled with Agilent 5977A mass spectrometry detector (MSD) at Centre for process integration and membrane technology (CPIMT), RGU.

4.2.2.2 GC Column

The central heart of any GC system is the column where the separation of component takes place. Selecting a proper column (stationary phase) for a particular separation to be carried out is the most important factor in GC. The stationary phase is generally an inert solid particle or a non-volatile supported on a capillary wall [121]. The GC column can be classified into two types; packed and capillary (or open tubular) column. Although packed columns are still used for several chromatographic analysis, currently, the direct coupling of capillary columns to the ion source of the mass spectrometer is so far, the most common attractive method capillary columns have become much more popular because of their excellent advantages including increased efficiency and resolution. Capillary generated peaks are narrower which improves sensitivity to detection of low level components compared to that of packed column. [122]. Figure 4.15 shows a typical diagram of capillary GC column.

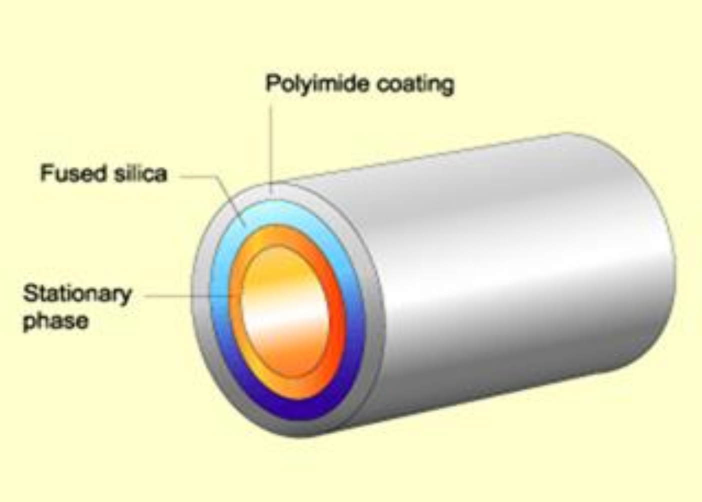

Figure 4.15: A typical diagram of capillary GC column

4.2.2.3 Chemical Ionization Gas Purifier and Ultra-Clean Moisture Cartridges

The chemical ionization gas purifier which is made up of the gas inlet and outlet was used to pass the carrier gas through the purifier whilst the carrier gas filters also filter the dry inert gas from any impurities before the gas entering into the GC-MS. The carrier gas filters and chemical ionization gas purifier and the carrier gas filters used for the analysis were all purchased from the Agilent, Technologies, UK. Figure 4.16a and b shows the chemical ionisation gas purifier and carrier gas filters. The ultra-clean moisture cartridge allows the effluent gases leaving the membrane reactor to go through a moisture trap to extract only trace quantity of water vapour during the process intensification reaction. This instrument was purchased from Perkin Elmer moisture filter, Llantrisant, UK.

Figure 4.16: Chemical ionisation gas purifier (a) and Perkin Elmer moisture filter (b).

4.2.3 Procedure for GC-MS analysis of the Batch Process Esterification Product

The sample preparation for injection to the GC-MS instrument was carried using H08200511 Fisherbrand® EX pipette (Fisher Scientific). The GC-MS vials were carefully clean and dried in the oven prior to each esterification product analysis. The sample vial was carefully inserted into the sample rage embedded in the injector port of the GC-MS were the carrier gas transfer solvent to the GC column. The sample vial containing 0.1, 0.5, 1.0, 1.5 and 2.0 mL of the reaction product (ethyl lactate) and the commercial available ethyl lactate which was used as the reference sample was inserted into a 300 ^{o}C interface connected to the injection port of the GC system.

4.3: Esterification reaction using Cellulose Acetate Membrane at different Temperatures.

The second part of the chapter was to carry out the process intensification of ethyl lactate using a flat sheet cellulose acetate membrane reactor impregnated with resins catalysts in a gaseous phase. This method is a novel method, as very few work have mention the process intensification of ethyl lactate by using a carrier gas on the permeate side of the reactor, which will help to shift the chemical equilibrium to improve the conversion of ethyl lactate for the selective removal of water from the esterification product. The significant of carrying out this process was to evaluate the conversion of ethyl lactate and for comparison with the batch process esterification in order to determine the efficiency of the two methods. The resulting esterification reaction product was analysed using GC-MS.

4.3.1 Materials and Methods

4.3.1.1 Flat Sheet Cellulose Acetate Membrane

The cellulose acetate flat sheet membrane used for the process was obtained from Good fellow, Cambridge Limited, England, UK. The properties of the cellulose acetate membrane used for the analysis is shown in table 4.3 (Good fellow, Cambridge Limited, England, UK). Other materials used for the membrane preparation process before esterification was boric acid and carboxyl methyl cellulose.

Table 4.3: Properties of the Cellulose Acetate Membrane

Property	**Dimension**
Thickness	0.035mm
Dimension	150mm x 150mm
Effective membrane area	0.0155m^2
Heat sealing temperature	176 – 232 °C
Permeability to Water at 25 °C	x10^{-13} cm^3.cm.cm^{-2}s^{-1}Pa^{-1} 4000-5000
Permeability to Nitrogen at 25 °C	x10^{-13} cm^3.cm.cm^{-2}s^{-1}Pa^{-1} 0.2
Permeability to Carbon dioxide at 25 °C	x10^{-13} cm^3.cm.cm^{-2}s^{-1}Pa^{-1} 17
Permeability to Oxygen at 25 °C	x10^{-13} cm^3.cm.cm^{-2}s^{-1}Pa^{-1} 0.6
Permeability to Hydrogen at 25 °C	x10^{-13} cm^3.cm.cm^{-2}s^{-1}Pa^{-1} 2.5
Colour	Clear
Condition	Biopolymer
Condition	Biodegradable

Figure 4.17a-d shows the pictorial view of the cellulose acetate membrane that was used for the process intensification process of ethyl lactate.

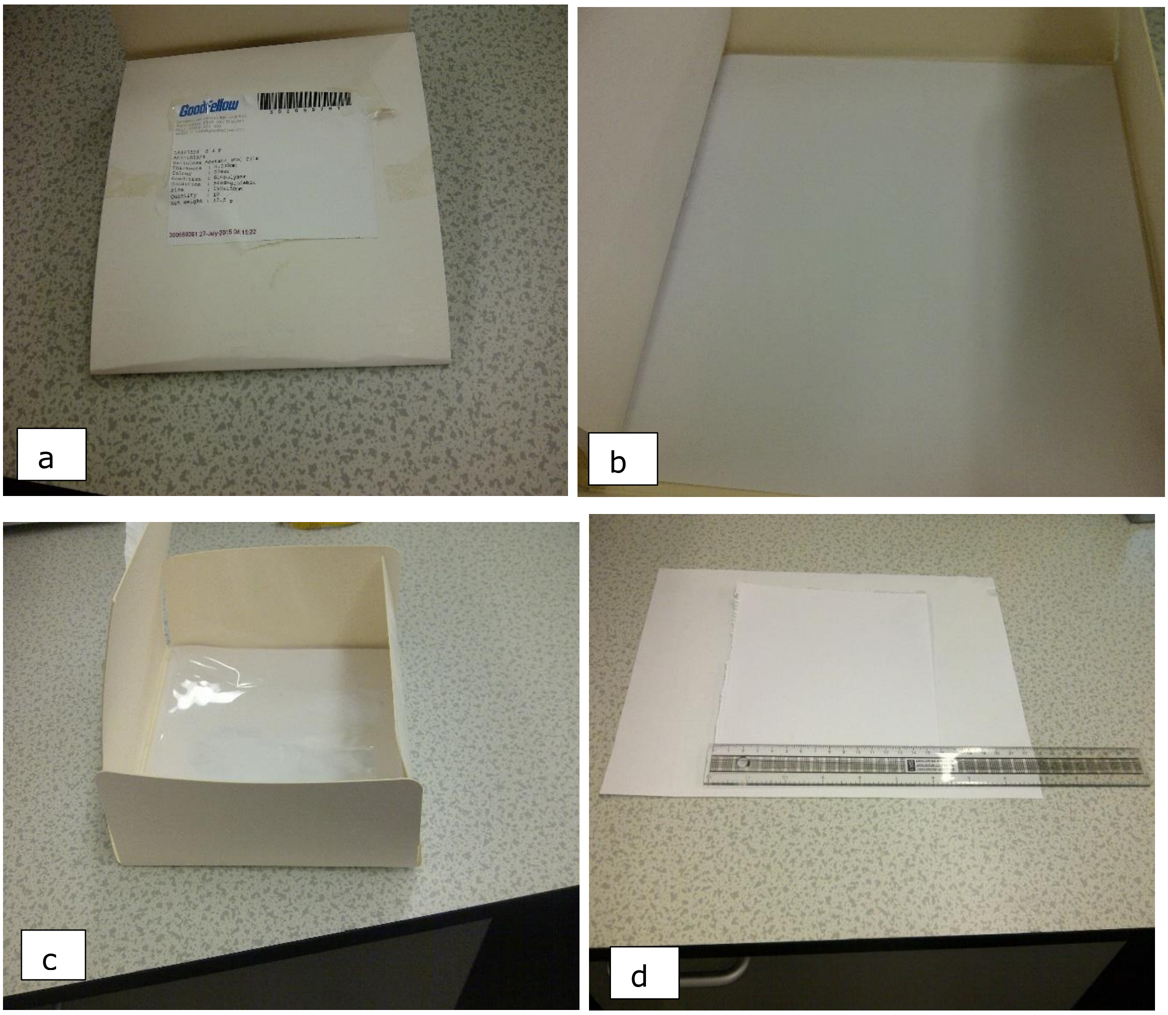

Figure 4.17a-d: Cellulose acetate membrane in a pack (a), outer surface of the cellulose acetate membrane (b), cellulose acetate covered with a protective clean film (c) and cellulose acetate membrane length/weight measurement (d).

4.3.1.2 Boric acid and Carboxyl methyl cellulose (CMC)

The boric acid used for the analysis was in solid form (tablet) and was purchased from Sigma-Aldrich, UK. The boric acid was used as purchased directly from the manufacturers without any further purification. The carboxyl methyl cellulose used for the analysis was supplied by Sigma-Aldrich, UK. This solution was used as received without and further dilution.

4.3.1.3 Membrane Process Equipment set-up

The fabricated reactor membrane experimental setup consists of a stainless steel cell (upper and lower part), core holder, fittings and inlet pressure gauge. The details of the parts that makes up the fabricated reactor is explained in the section below. Figure 4.18 shows the schematic diagram of the flat sheet cellulose membrane esterification reaction set-up.

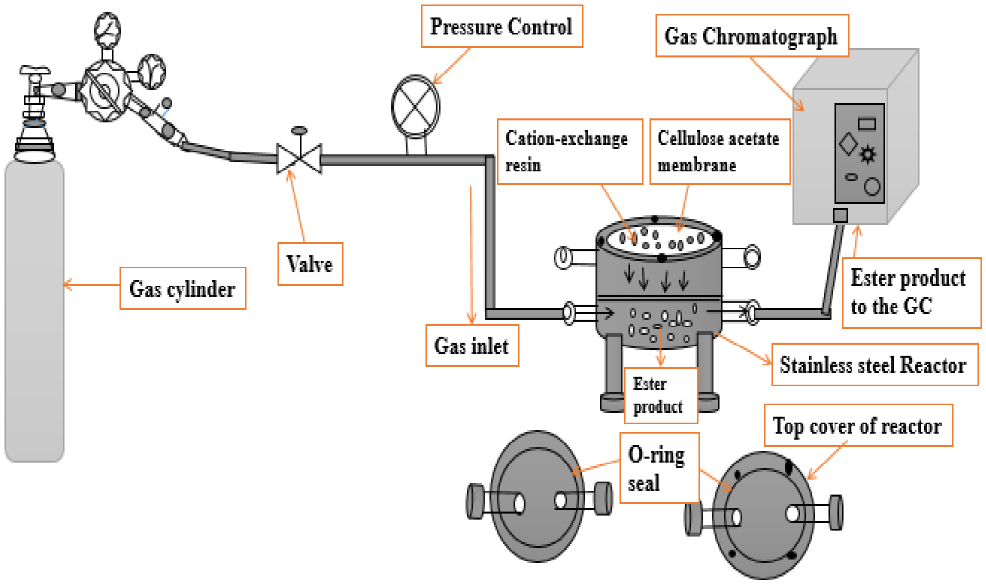

Figure 4.18: Cellulose acetate membrane process intensification set-up.

4.3.1.4 Spherical stainless steel Flat Sheet Separator

The spherical separator was made up of a stainless steel material having a surface area of about 127mm x 150 mm long and with an inner and outer diameter of 25 mm and 125 mm respectively. Figure 4.19a-d shows the pictorial view of the stainless steel reactor compartment. The core holder saves as the inner compartment of the cell. It is usually located at the midway in between the upper and the down part of the cell. The rubber gasket allows the upper compartment and the core holder to align together to avoid a leakage during the analysis. Figure 19a-d shows the pictorial view of the stainless steel separator compartments. A similar method to that of Stanford et al. [19] was adopted.

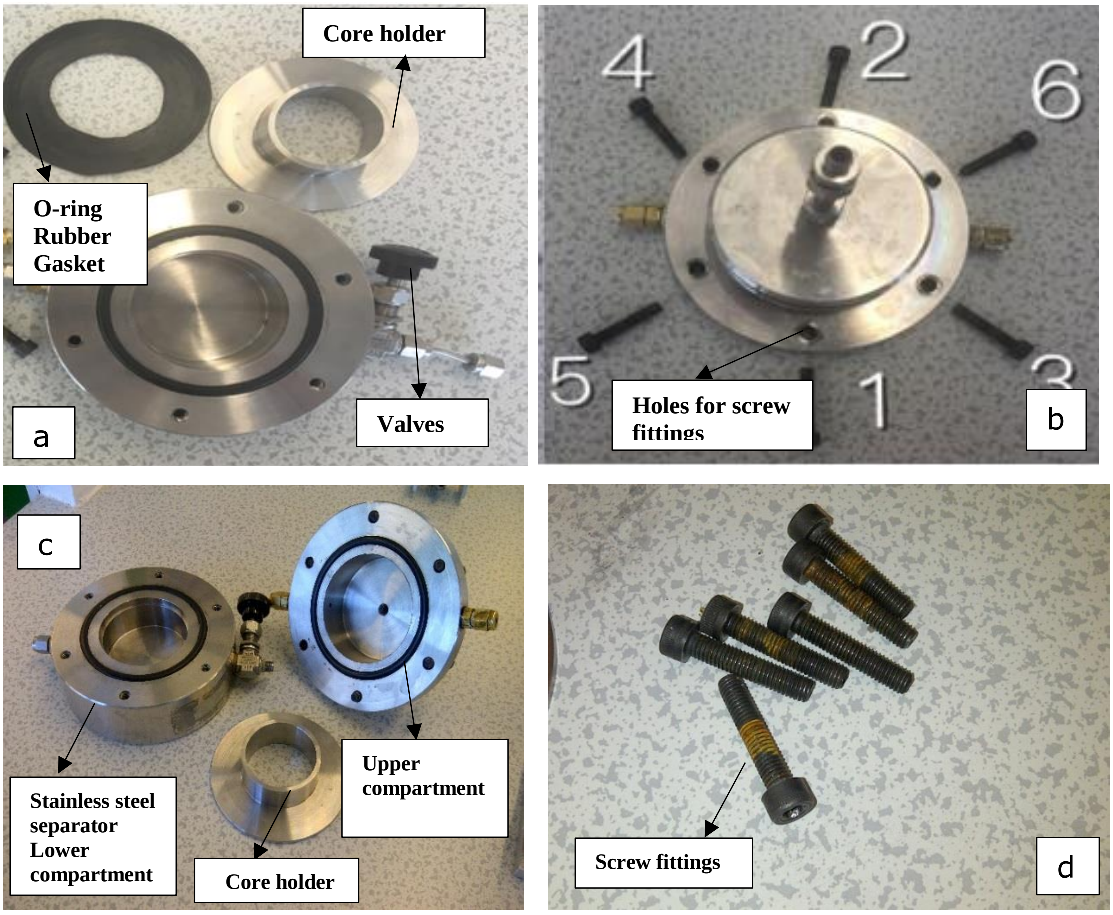

Figure 4.19a-c: Pictorial view of the stainless steel flat sheet separator parts showing the O-ring rubber gasket (a) holes for screw fittings (b), core holder (c) and screw fittings (d).

4.3.2 Cellulose acetate membrane esterification Procedure

4.3.2.1 Preparation of Cellulose Acetate Membrane

Prior to the analysis, two layers were prepared i.e the catalytic and the separation layer. The two layers were prepared separately before being mixed together to obtain a homogeneous solution before the cellulose acetate membrane immersion into the liquid. The separation layer was prepared as thus: The carboxyl methyl cellulose (CMC in powdered form as shown in figure 4.20a) with weight of 0.5wt% was measured into a 100mL beaker and 50 mL of deionised water was used to dissolve the solid CMC. The solution was allowed to stir for 10 hours in order to attain a homogeneous mixture. The catalytic layer was prepared separately by weighing 2wt% boric acid into a 100 mL beaker and adding a 50 mL of the deionised water to the beaker containing boric acid and allowed to stir for 10 hours to dissolve the boric acid (in a tablet form as shown in figure 4.20b). After 10 hrs, the solution containing the CMC was poured into the beaker containing the boric acid solution.

The two solutions (catalytic and separation solutions) were allowed to mixed together while stirring for 3hrs in order to obtain a homogenous mixture. The cellulose acetate membrane was prepared based on a similar work by Nigiz et al. [123]. Figure 4.20 shows the pictorial view of the separation and the catalytic layer solutions that were prepared prior to the cellulose acetate membrane immersion process. The compositions of the CMC and boric acid that were used for the preparation of the catalytic and separation layers are presented in table 4.4. The weight of the cellulose acetate membrane and the cation-exchange resins was determined in grams while the concentration of the feedstocks was determined in mL. Figure 4.20 a-d shows the pictorial view of the powered CMC (a), boric acid in tablet form (b), CMC dissolved in deionised water (c) and boric acid dissolved in deionised water (d) before analysis.

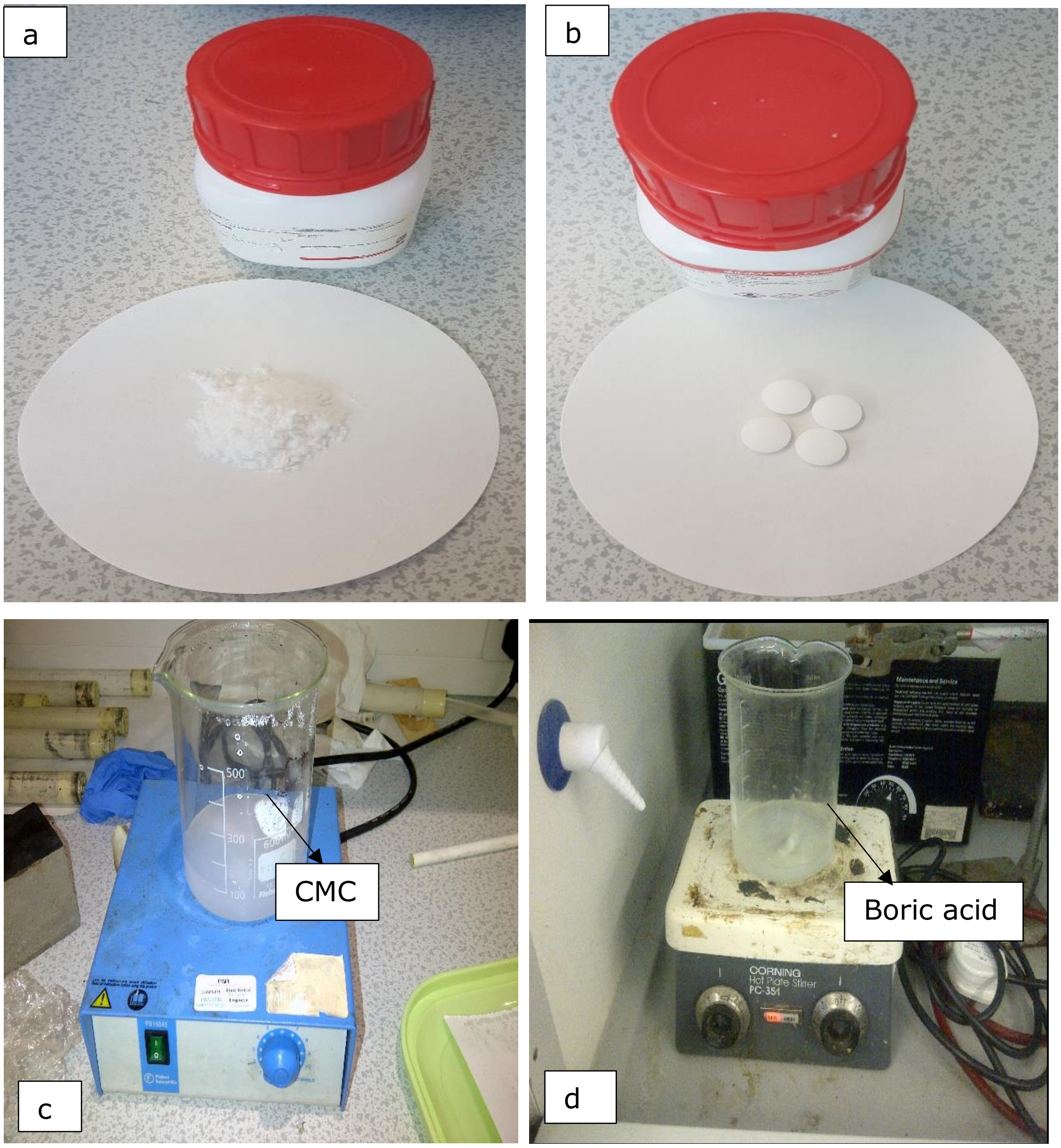

Figure 4.20: Pictorial view of the powered CMC (a), boric acid in tablet form (b), catalytic layer containing CMC (c) and separation layer containing boric acid (d) solutions.

Table 4.4: Composition of the solvents used for the cellulose acetate membrane preparation

Substance	Amount (mL) and g
Carboxyl methyl cellulose (CMC)	5g
Boric acid	2g
Deionised water	50mL
Beaker	100mL

After 3hrs, the cellulose acetate membrane was immersed into the solution consisting of the CMC, boric acid and deionised water and was allowed in the solution for 3 minutes to allow a uniform coating. After 3minutes, the membrane was taken out of the solution and allowed to air dry for 3-days at room temperature before the esterification reaction. The importance of drying the cellulose acetate membrane in air was for the homogenous solution of the catalyst to penetrate into the porous surface of the membrane sample to obtain a uniform coating on the surface and also to avoid the acetate membrane burning in the oven. Figure 4.21a and b shows the pictorial view of the membrane immersion and drying process.

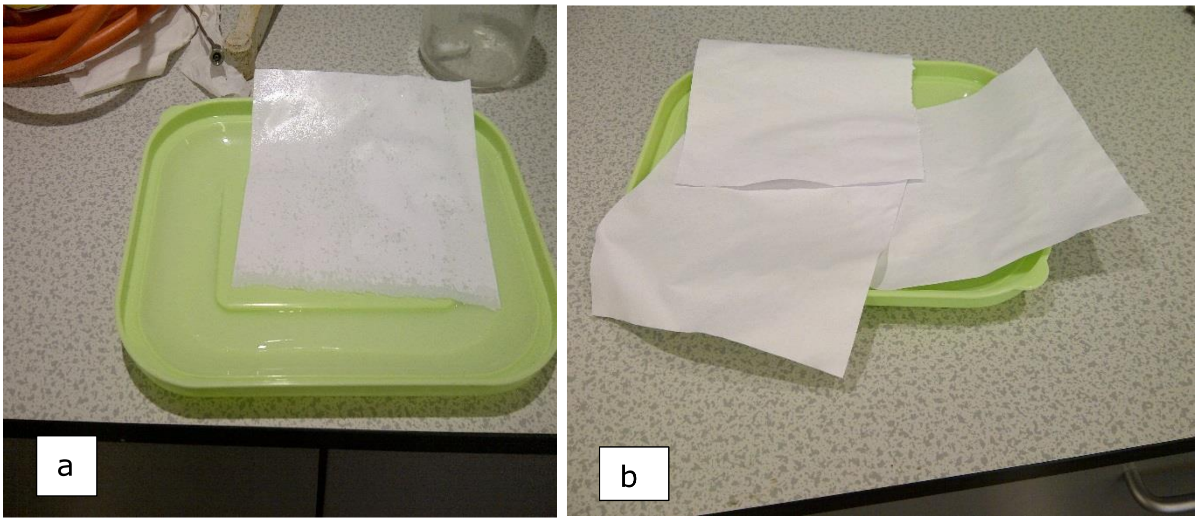

Figure 4.21: Pictorial view of the cellulose acetate membrane immersion (a) and drying (b) at room temperature.

4.3.2.2 Flat Sheet Cellulose Acetate Membrane Esterification Procedure

After the drying process, the membrane was then used with the resins for the esterification experiment. The reactants solvent consisting of lactic acid and ethanol was heated separately to the desired reaction temperature before it was added to the reactor-separator. The heating was done at different temperatures of 60, 80 and 100 ºC. The esterification reaction was carried out separately before it was transferred to the reactor thus: 20mL of the lactic acid solution was added to a 100mL beaker and heated for 30minutes. After 30 min, 40 mL of ethanol solution was added to the beaker and allowed to stir thoroughly for 30 min for the two solution to mix very well before it was transferred to the separator for the process intensification. The molar ratio of lactic acid to ethanol for the experiment at each temperature was 1:2 wt% and 2:3 wt%. The major reason for heating the system separately to avoid the condensation of the solution when it evaporates in the separator. Figure 4.22 shows the reactant solvent (lactic acid and ethanol) heating before it was transferred to the flat sheet separator.

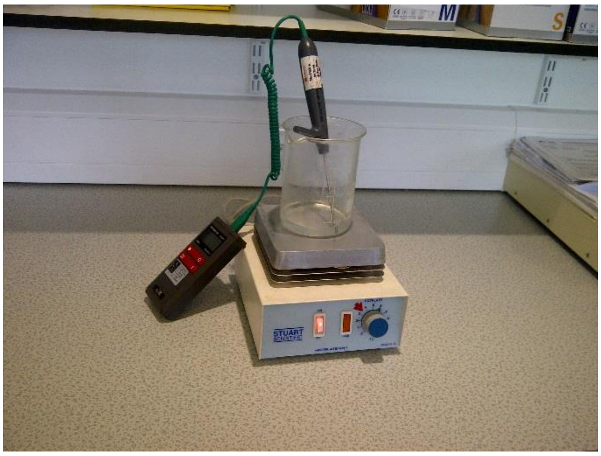

Figure 4.22: Reactant solvent heating before transferring to the reactor.

The stoichiometric equation for the reaction from the experimental procedure was given as:

$$2C_3H_6O_3 + 3C_2H_5OH \rightleftharpoons 5CH_3CH_2OCOOC_2H_5 + H_2O$$ ....(equation 4.1)

Lactic acid   Ethanol   Ethyl lactate   water

Before the cellulose acetate membrane was placed on the permeation separator, the membrane was cut into a spherical form to size of the flat sheet separator as shown in figure 4.23.

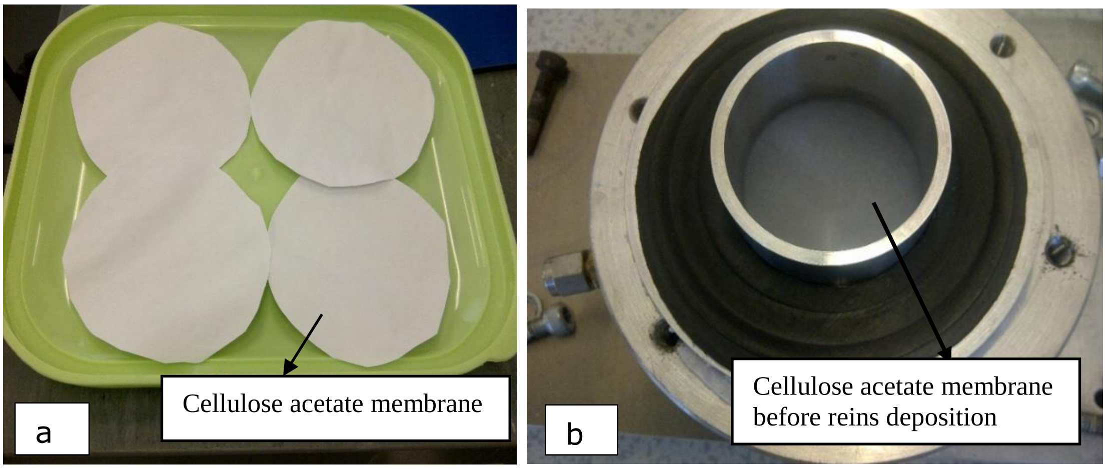

Figure 4.23: Pictorial view of the cellulose acetate after trimming with scissors (a) and pictorial view of the stainless steel reactor showing the cellulose acetate membrane before catalyst impregnation (b).

4.3.2.3 Cation-exchange Resin Impregnation on Membrane

The pictorial of the catalyst impregnation on the cellulose acetate membrane is shown in figure 4.24a-d. Prior to analysis, the cellulose acetate membrane weighing 1.5g was placed on the lower compartment of the cell. 0.5g of each cation-exchange catalyst was attached directly onto the surface of cellulose acetate membrane as shown in Figure 4.24a-d. The prepared reactant solvents which has been prepared separately was also added to the separator through the opening of the separator, which interacts with the impregnated resins and membrane to selectively shift the chemical equilibrium to the forward. The core holder, rubber gasket, the upper compartment of the cell and 6 screw fittings were placed at each point on the upper compartment and were carefully tightened. Figure 4.24a-d shows the pictorial view of the different cation-exchange resin catalysts attached on the surface of the cellulose acetate membrane.

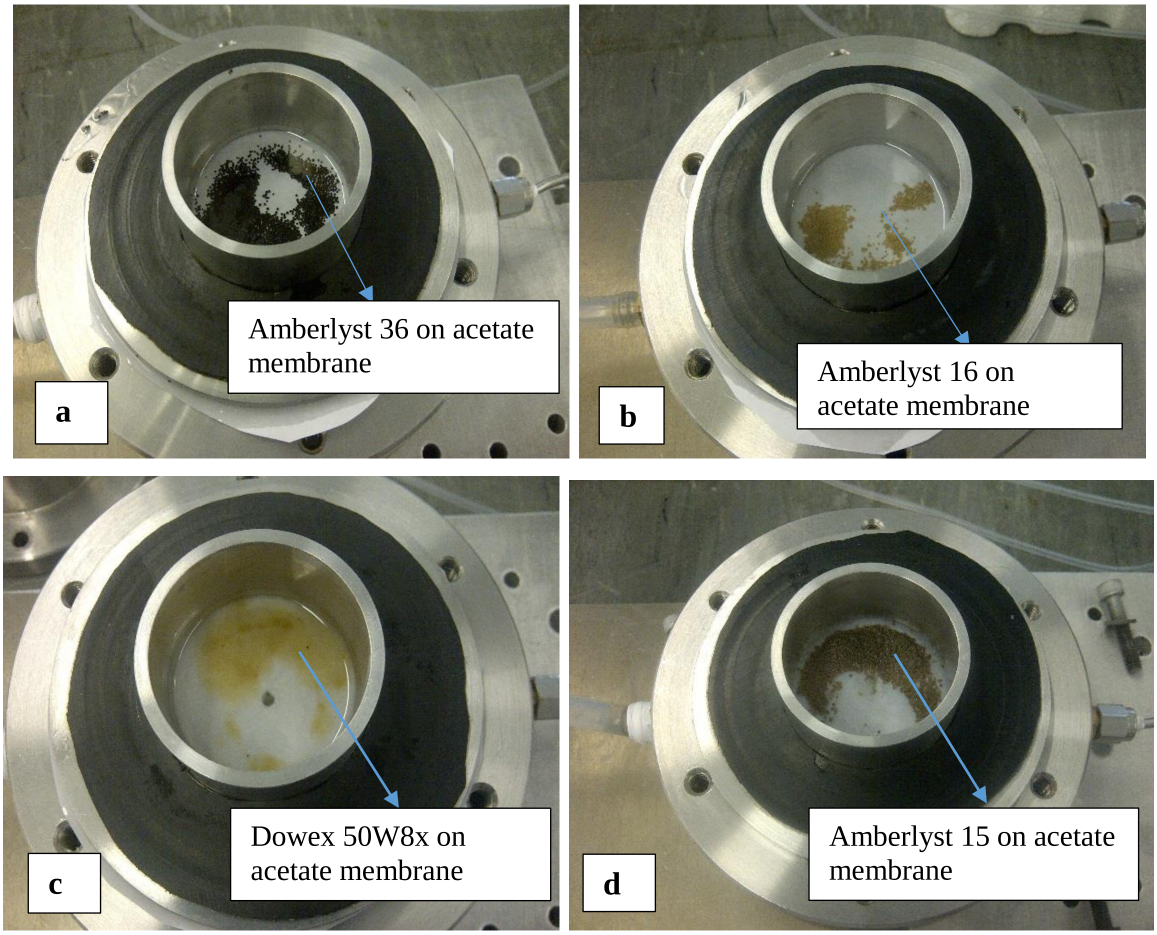

Figure 4.24: Pictorial view of the cellulose acetate/amberlyst 36 (a), cellulose acetate/amberlyst 16 (b), cellulose acetate/dowex 50W8x (c) and cellulose acetate/amberlyst 15 (d).

A carrier gas was connected on the permeate side of the separator and pressure was maintained at the gauge pressure range of 0.10-0.30 bar with a 0.10 increment. A valve was used to control the sweep flow rate which was monitoring between the range of 0.30 - 0.50L/min using a digital flow meter. The significance of connecting a sweep gas was for it to serve as a driving force for the shift in thermodynamic equilibrium to the forward reaction for the removal of water from the reaction medium. A similar method to that of Kwon et al [124], was used for the analysis. The separated esterification reaction product was further analysis with the GC-MS to determine the percentage conversion. Figure 4.25 shows the pictorial view of the stainless steel separator connection.

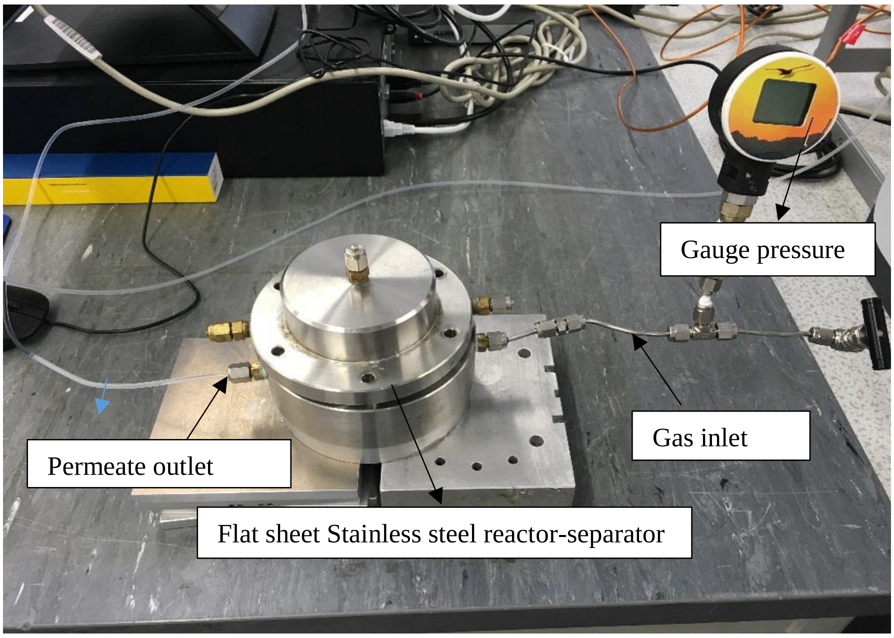

Figure 4.25: Pictorial view of a stainless steel separator.

4.3.2.4 Stainless Steel flat sheet Permeation Separator Setup

The experimental setup consists of a gauge pressure, valve, gas cylinder, flow meter, O-ring seal, reactor upper and lower compartment, core holder, stainless steel reactor, gas cylinder [125]. This work is a novel method of using a carrier gas on the permeate side of the stainless steel separator instead of vacuum to improve the yield of the ethyl lactate. The experimental set up was based on a similar work by Siti Khadijah et al. [126]. Figure 4.26 shows the pictorial view of the cation exchange of the experimental.

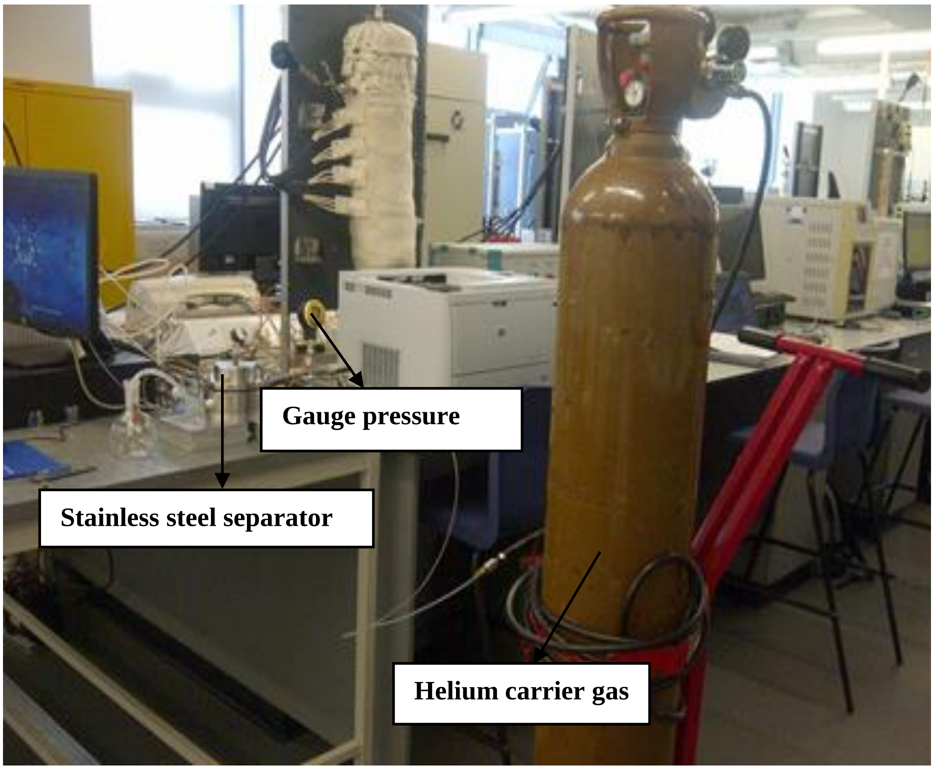

Figure 4.26: Pictorial view of cation-exchange resin/cellulose acetate membrane process intensification set-up.

CHAPTER 5

5.0: Identification of Adsorption Components

This chapter also explain the investigation of the components of adsorption on the surface of the different cation-exchange resins catalyst during the esterification reaction. The aim of the analysis was to determine the phenomenon of components that adsorbed most on the surface of the resin catalysts after the batch process esterification. This was achieved using the Fourier transform infrared spectroscopy coupled with attenuated transform infrared (FTIR-ATR). It was determined based on the structural analysis of the spectra of each cation-exchange resin catalyst using the characteristic library spectra. The adsorption of the components was further confirmed using ^{1}HNMR method. The interpretation of the results was carried out based on the IR library spectra provided by the school of Pharmacy and Life Sciences, RGU [127]. After the identification of the adsorption components on the surface of the resin catalysts, the identified functional groups were used to develop a mathematical model based on Langmuir Hinshelwood model to describe the adsorption reaction mechanism of the esterification process.

5.1 Materials and Methods

5.1.1 FTIR-ATR Instrument

The FTIR-ATR instrument used for the analysis was Thermo Scientific Nicolet iS10 Fourier transform infrared (FTIR, Fisher Scientific Ltd, Bishop Meadow Road, Loughborough, UK) equipped with a PIKE 15337 Attenuated Total Internal Reflectance detector (ATR, PIKE Technologies, Shelton, USA) device, with a zinc selenide (Zn-Se) crystal.

5.1.2 FTIR-ATR Procedure for Membrane

The FTIR-ATR method was used to determine the presences of functional groups in the membrane samples. A similar method to that of Karimi et al. [128] was adopted for the FTIR-ATR analysis of the membrane sample. Prior to the experiment, the membrane samples were first of crushed using mortar and pestle to obtain the fragment as shown in figure 5.1a and b respectively before the experiment. All the spectra were recorded from 400-4000 cm^{-1} with the resolution of 4 cm^{-1} at room temperature using the double side forward-backward acquisition mode. A total number of 32 scans were co-added and the signal was average at an optical resolution of 4cm^{-1} using the transmission measurement of the potassium bromide discs containing about 1mg of the sample. Figures 5.1a and b shows the membrane fragment and the crushed membrane sample for the FTIR-ATR analysis.

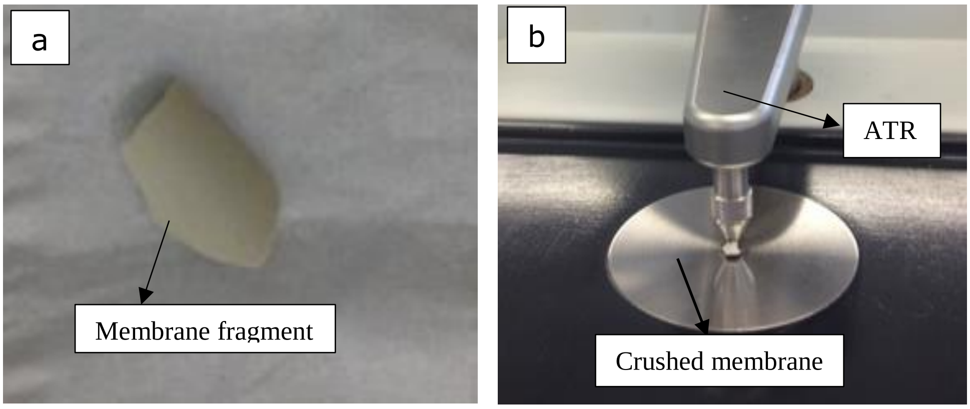

Figure 5.1: Membrane fragment (a) and crushed membrane sample (b) for FTIR-ATR analysis.

5.2. Method and Procedure for the FTIR-ATR Esterification Product Catalysed with the different Cation-exchange resins

The lactic acid feed was also analyse using the FTIR-ATR instrument. Prior to the sample analysis, the ATR crystal plate was first of all clean gently with ethanol and tissue paper. The tissue paper was carefully soaked with a small amount of ethanol before the cleaning process. The reason of cleaning the ATR crystal plate before the analysis is to ensure that the crystal is free from impurities. A small quantity of the lactic acid feed (less than 1mL) was place on the smart iTR (infrared total reflection) crystal (figure 5.2a) using a glass dropper as shown in Figure 5.2a. After placing the sample on the ATR crystal plate, the ATR was manoeuvred upwards to allow the sample to be exposed to the IR light as shown in figure 5.2b, the ATR was screwed in the direction of the sample to overlap with the sample before each scan across the sample. A similar method to that of Kaur et al. [9] was employ for the analysis. The reason for overlapping the ATR on the sample is for the instrument to scan across the sample to generate spectra and also prevent the evaporation of the sample before the scanning process.

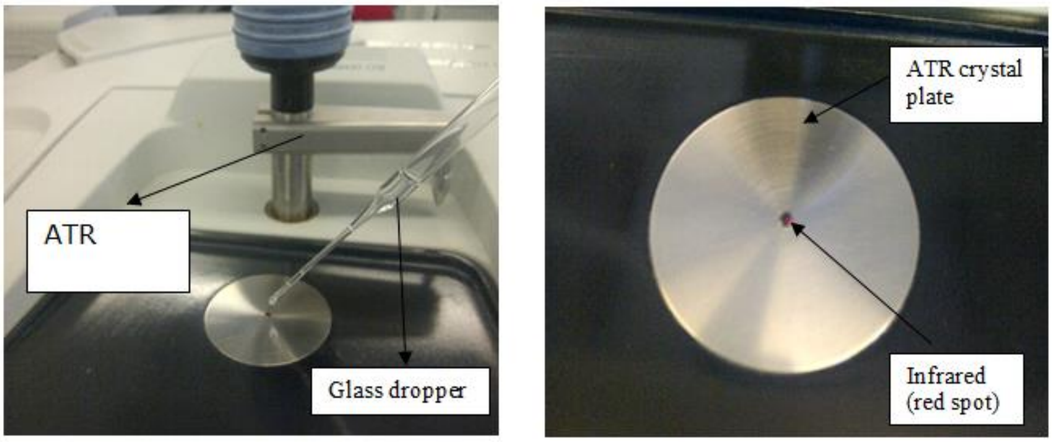

(a) **(b)**

Figure 5.2: ATR crystal plate (a) and ATR instrument coupled with FTIR for the analysis of the liquid esterification product (b).

Prior to the analysis of the sample, a background spectrum of air (without any solvent) was first scan before the analysis of sample. By selecting a background spectrum and using the EZ OMNIC software, the FTIR-ATR analysis was performed. Each sample scan was carried out at the instrument programmed number of 32 scans for 5 minutes before the spectra were generated. The same procedure was repeated for the analysis of the sample at the temperatures of 80 and 100 ^{o}C. Figure 5.3a and b shows the FTIR instrument that used for the sample analysis.

FTIR Instrument Thermo Nicolet 6700

Figure 5.3a and b: Pictorial view of the Nicolet iS10 Thermo Scientific Fourier Transform infrared coupled with attenuated total reflection (a) and the pictorial view connected to the PC (b), School of pharmacy Life Science, RGU.

5.5 Characterisation of Esterification Product Using Proton NMR (Nuclear Magnetic Resonance)

The esterification reaction product was also characterised using the proton NMR to determine the structure of organic compounds that were involved in the esterification product to further validate the results FTIR-ATR spectroscopy.

5.5.1 Materials and Methods

5.5.1.1 Sample Drying using Rotavapor Instrument

Prior to the analysis of the esterification product with the NMR instrument, the preparation of the sample was carried out to remove excess water and ethanol from the esterification feed catalysed by different resins to obtain the pure ethyl lactate before it was used for the ^{1}H NMR analysis. Figure 5.4 shows the sample bottles containing the different samples.

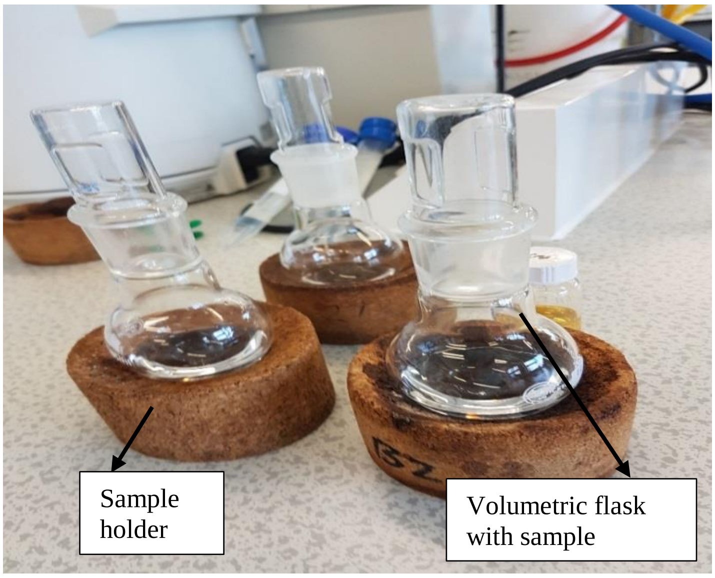

Figure 5.4: Pictorial view of sample bottle containing the different samples.

The sample was heated up in a rotavapor instrument (Buchi Rotavapor Evaporator R-210, Atlanta, US) to remove the ethanol and water from the esterification reaction feed to obtain the pure lactic acid feed that has been converted. The temperature of the instrument was set to correspond with the boiling point of ethanol between 78-80 °C. Two pipe were connected to the vacuum instrument for the water inlet to cold the condenser out of the system. The vacuum was set at a low pressure of 7bar before the water bath was allow to run constantly. The sample spinning rate was set at 5rpm (rotation per minutes). The sample was allowed to spin in the bath for 30- 45min during which the ethanol was found to drip into the waste round bottom flask as shown in figure 5.5. Prior to each experiment, the vacuum was open gradually to release the build-up pressure. After the sample drying, the sample was further prepared for the ^{1}HNMR analysis.

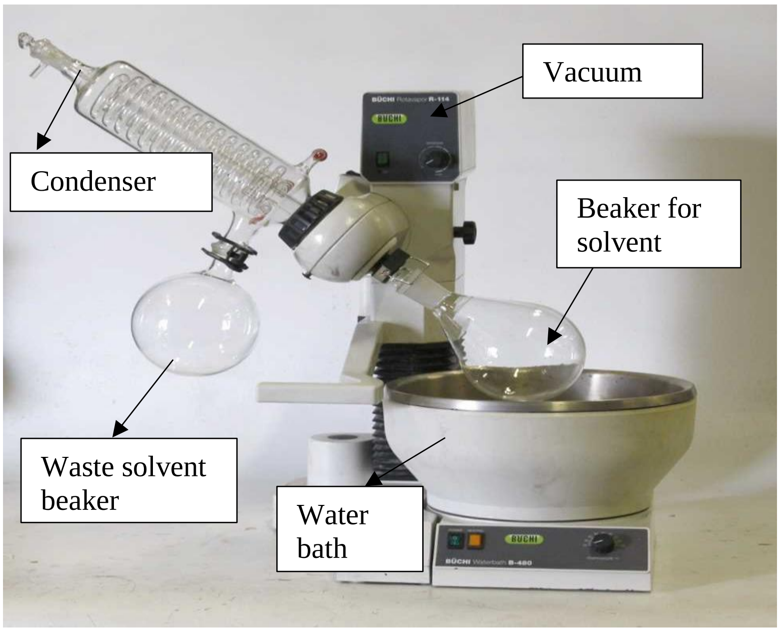

Figure 5.5: Pictorial view of Buchi R 114 Rotavapor Evaporator.

5.5.1.2 Procedure for NMR analysis of Esterification Products

Prior to the ^{1}HNMR analysis, 10 mg (0.1000g) of the lactic acid feed which was prepared, was weighed into a glass sample bottle using analytical weighing balance. 0.7mL of a deuterated solvent (methanol) was added to the sample bottle containing the lactic acid feed to dissolve the solvent. The important of diluting the sample in a deuterated solvent was to avoid the large solvent adsorption that could damage the ^{1}HNMR spectrum. ^{1}HNMR spectra of substances acquire in a non-deuterated solvent normally show a large solvents signal on the spectra leading to difficulties in interpretation [127]. The sample bottle containing the two solvents (deuterated solvent and sample) was carefully shake to obtain the homogeneity of the two solutions. The mix sample was further transferred using a pipette into a clean and dry ^{1}HNMR sample tube. The tube containing the sample was carefully covered with a plastic lid before inserting into the Bruker 400 MHz Ultra Shield Spectrometer instrument for analysis. The sample tube was placed on a magnetic field where it is subjected with a burst of radio frequency (rf) with the wavelength (MHz) corresponding to the frequency of the nucleus at the magnet field. The ^{1}H NMR analysis of the lactic acid feed was carried out using three replicates for each sample. Figure 5.6 shows the pictorial view of the Bruker 400 Ultrashield^{TM} NMR instrument that was used for the analysis. The same procedure was repeated for amberlyst 16, amberlyst 15 and dowex 50W8x resins.

Figure 5.6: Pictorial view of Bruker 400 UltrashieldTM NMR instrument at School of Pharmacy and Life Science, RGU.

CHAPTER 6

6.1: Membrane and Cation-exchange Resin Characterisation

The major reason for this objective was to investigate the surface morphology of the cation-exchange resin catalysts, tubular and flat sheet membranes before and after the esterification process to determine the thermal stability and mechanical strength of the cation-exchange resin catalysts. The tubular membrane that used for the permeation test analysis with the carrier gas was also analysis with the SEM/EDAX to compare the surface morphology of the membrane before and after the gas permeation analysis. The cellulose acetate flat sheet membrane was also analysed using this method to determine the surface morphology of the membrane before and after the esterification process.

6.2 Method and Procedure for Cation-exchange Resin

6.2.1 Catalyst and Membrane Preparation before SEM/EDAX Analysis

Prior to sample analysis, the samples were first of all placed on the gold stopper with each of the sides (cross section, inner, outer surface) to be analysed facing upward. After the sample preparation, the gold stopper in which the samples were placed on for analysis were further placed on the sample carousel of the SEM. The electron beam was set to scan across the sample at the magnification to generate the different images. The electron beam was set to scan across the sample at different magnifications of 100X, 200X, 10X, and 20X at different scale of 10 µm, 20 µm, 100 µm and 200 µm. The chamber pressure of the analysis was done at 100 Pa, at the working distance of 7.5 mm with voltage of 25.0KV. Figure 6.1a and b shows the Zeiss EVO LS10 SEM (6.1a) and Oxford instruments INCA EDAX (6.1b) instruments that was used for the analysis.

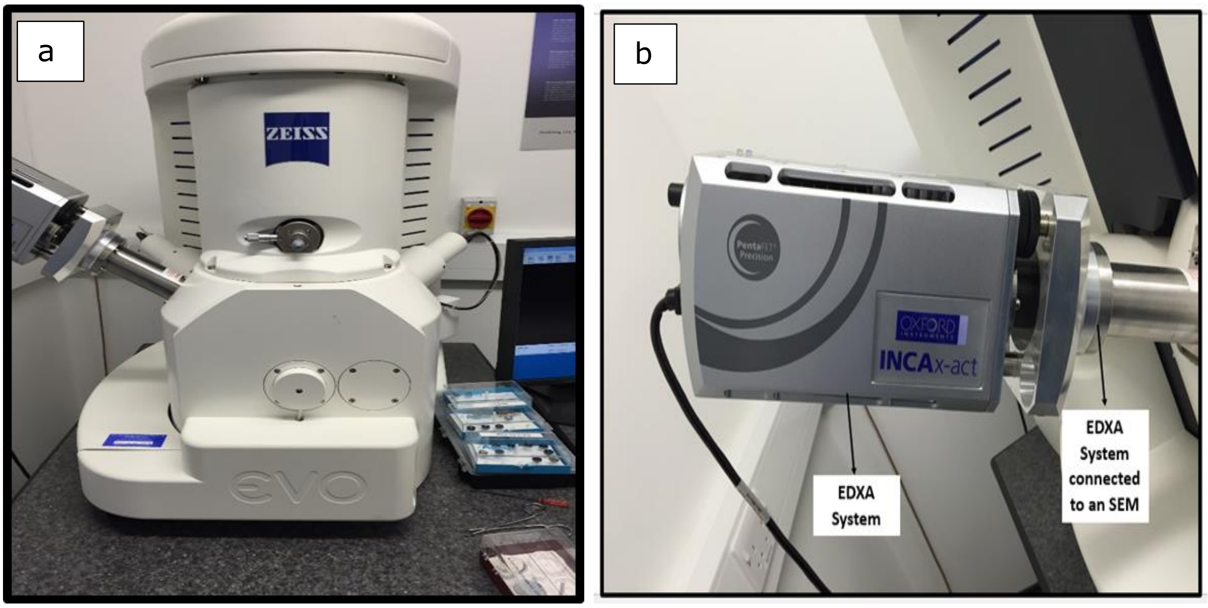

Figure 6.1: Pictorial diagram of the Zeiss EVO LS10 scanning electron microscopy (a) and Oxford instruments INCA Energy Dispersive X-ray Analyser (b) from school of pharmacy life science RGU.

6.3 Characterisation of the Membrane and Cation-exchange Resin using Liquid Nitrogen Physisorption method

This method was employed in the characterisation of both membrane and the cation-exchange resin sample in other to determine the surface area and pore size of the samples. According to Lee et al. [97], when the gas molecules interact with the solid surface, the amount of the gas molecule adsorbs on the surface equals the total partial pressure of the gas molecule. However, the measurement of the adsorbed amount of gas over a range of partial pressure at a single temperature produces an adsorption isotherm. Hence, the resulting adsorption isotherm shows the various types based on the pore structure of a porous media and intermolecular interaction between the gas molecule and the surface [97]. According to IUPAC (International Union of Pure and Applied Chemistry), the physisorption isotherm can be classified into six different types [82,129]. Figure 6.2 shows the schematic diagram of the liquid nitrogen adsorption isothermal setup.

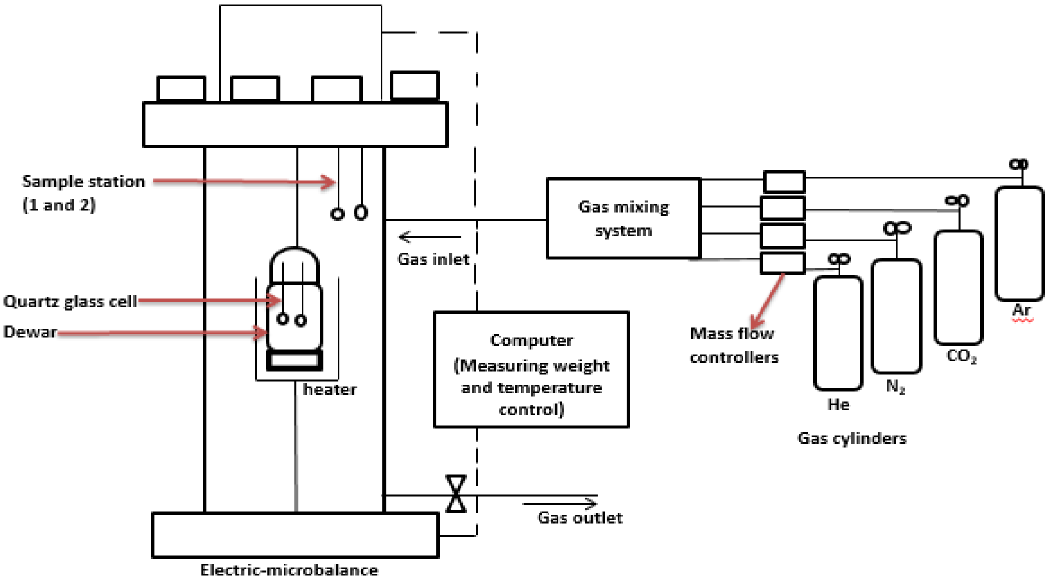

Figure 6.2: Schematic diagram of the liquid nitrogen adsorption isothermal setup [130]**.**

6.3.1 Method and Procedure for membrane

Prior to each analysis, the fragment of the support and the silica membrane were crushed and used for the liquid nitrogen adsorption analysis. Figure 6.3a and b shows the membrane fragment before and after the modification process respectively.

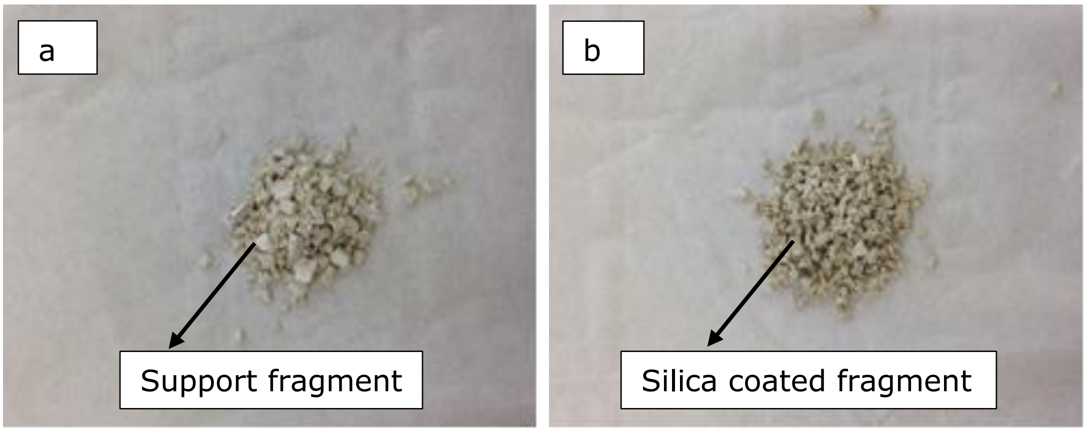

Figure 6.3: Diagram membrane fragment before modification (a) and after modification (b).

Both the support and the silica membrane (the modified silica fragment) were carefully crushed to a fine powdered form prior to the analysis with liquid nitrogen adsorption instrument at 77 K. The crushing of the membrane sample was carried out using a mortar and a pestle as shown in figure 6.4a and b. The significant of crushing the sample into a powdery form before the analysis was for the liquid nitrogen to adsorb through the pores of the membrane sample to generate the isotherm. The membrane was weighed before and after the modification process. The same preparation method for the tubular membrane was adopted with 10 mL of silicon elastomer, 100 mL of isopentane, 1 mL of curing agent (hardener) was measured into 100 mL beaker as shown in figure 6.5.

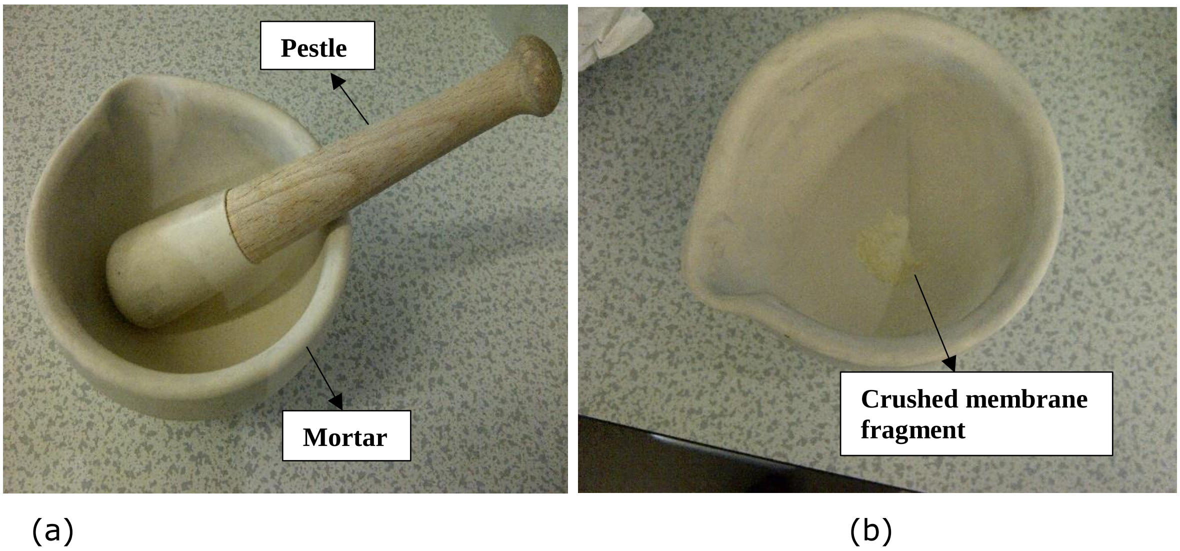

Figure 6.4: Pictorial view of the mortar and pestle (a) and the crushed membrane fragment (b).

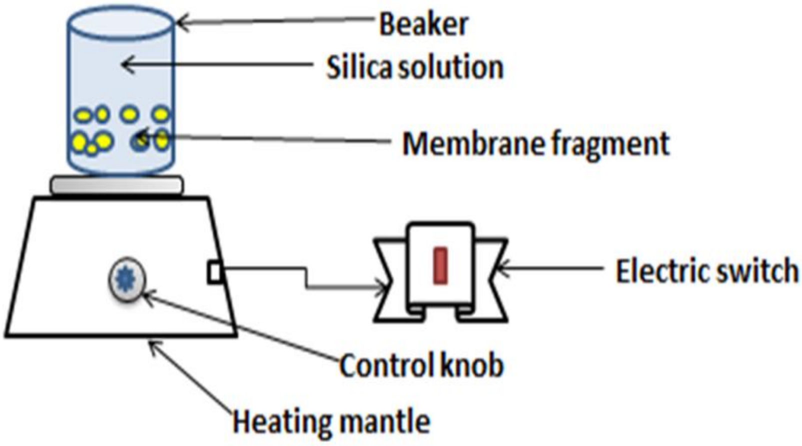

Figure 6.5: Schematic diagram of the membrane fragment dip-coating process for liquid nitrogen adsorption experiment.

After the membrane preparation process, the sample was first of all degassed before the main analysis. A similar method to that of Markovic et al. [99], was adopted and modified by changing the temperature. Prior to the analysis, the membrane support was weighed and charged into the sample cell and was degassed at 350 °C for 180 minutes to clean the adsorbed contaminant from the sample by introducing a vacuum or flow of dry inert gas and preferably some heat [131].

6.3.2 Method and Procedure for Cation-exchange Resins

Prior to the analysis, the fresh amberlyst 36, 15, 16 and dowex 50W8x commercial resins was weighed into a 50 mL beaker and rinsed with 50 mL of deionised water and 2 mL of ethanol. After rinsing, the resin was oven dried at a constant temperature of 65 °C for 24 hrs to remove any poisonous substances and moisture completely before the degassing process. Prior to the degassing process, about 0.1g of the sample was accurately weighed into the sample cell using an electronic weighing balance as shown in figure 6.6a-c. The degassing temperature for the degassing process was different from that of the dip-coated membrane because the catalysts are polymeric material and is not the same as the silica sample. Figure 6.6a-c shows the pictorial diagram of the weighing balance (a), empty sample cell (b) the sample + cell (c).

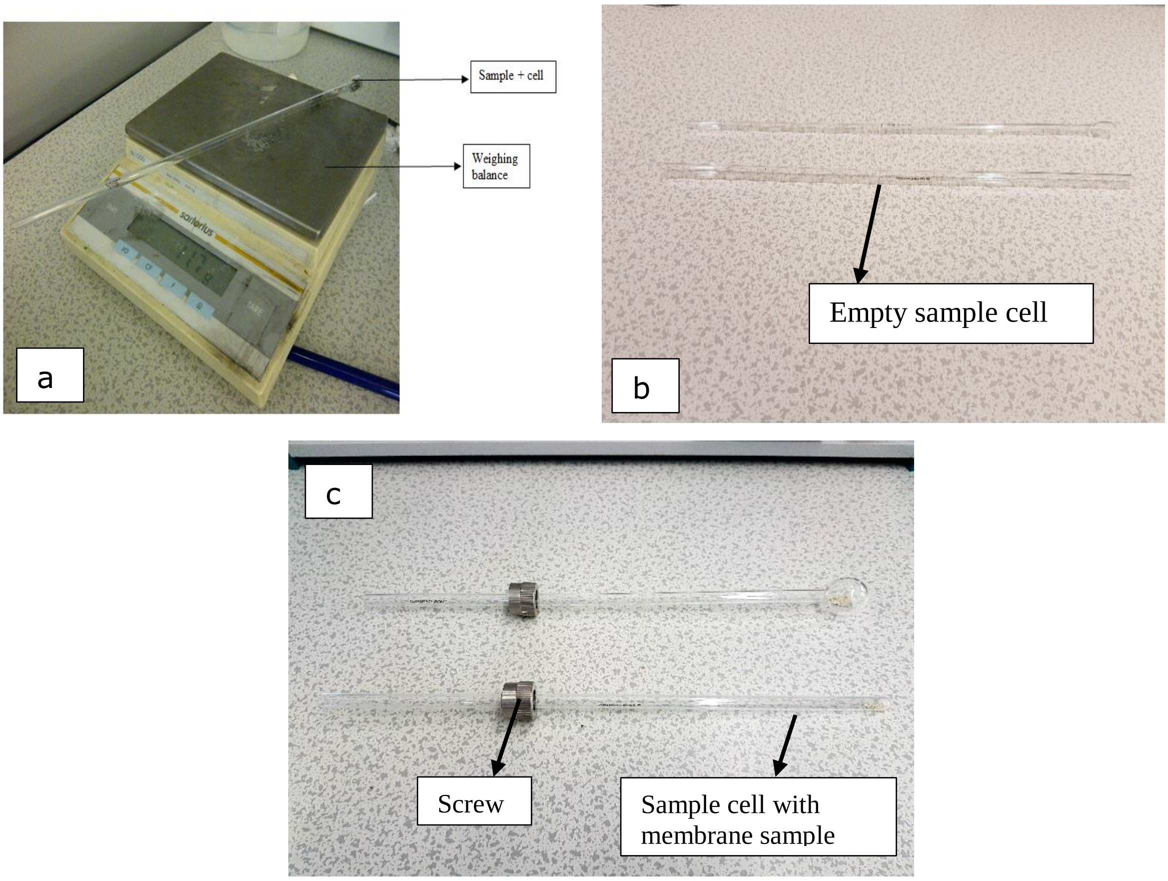

Figure 6.6: Pictorial view of the weighing balance (a), empty sample cell (b) sample cell with sample and screw fitting before degassing (c).

The weight of sample cell, the different cation-exchange resin was measured before and after the degassing process with sample cell of different dimensions including 6, 9 and 12 mm of size were used for the analysis. Prior to the analysis, the sample was degassed at 1.00 ^{o}C/min rate per mins for 3 hours at 300 ^{o}C on the degassing port of the outgasser. The adsorption isotherms were obtained by dosing the nitrogen (99.99% purity) onto the catalyst contained within a liquid nitrogen bath at 77 K. The helium and nitrogen gas pressure were set at 0.7 and 0.5 bar respectively. After degassing process of the different cation-exchange resin and the silica membrane fragment, the sample was loaded unto the liquid nitrogen instrument as shown in figure 6.7. The rate of the sample analysis was 10 ^{o}C/minutes whereas the analysis time was set for 6 hrs. The liquid nitrogen adsorption temperature was programmed at 77 K (-196 ^{o}C). The weight of the sample was inputted prior to the analysis. Table 6.1 shows the operating condition of the degassing process before the analysis.

Table 6.1: Optimum operating condition of liquid Nitrogen for degassing process.

Target temp (^{o}C)	**Rate ^{O}C/min**	**Soak Time (min)**
50.00	1.00	30
100.00	1.00	60
300.00	1.00	180

After 15 minutes of loading the sample the dower was observed to go up to the level of the instrument, where the liquid nitrogen adsorbed into the membrane/resins samples to generate the adsorption isotherm. However, the temperature of the system increases to the target temperature (350 ^{o}C) with respect to pressure. The amount of gas adsorbed depends on the relative vapour pressure (P/P_o), where P_o indicates the saturation vapour pressure and P is the partial vapour pressure of a component in the system [129]. A similar procedure to that of Vospernik et al. [132] was employed in the analysis. The relationship between the amount of gas adsorbed at a certain temperature and the relative vapour pressure (P/P_o) is regarded as an adsorption isotherm [129],[97]. Figure 6.7 shows the pictorial view of Quantachrome adsorption gas analyser (Hartley, Wintney, UK) used to carry out the surface area and pore size analysis of the resin catalysts and the membrane respectively. The instrument consists of the sample stations (1 and 2), dewar, sample cell, thermometer, heating mantle, helium and nitrogen gas inlet. The interpretation of the results was carried out using the Quantachrome VersaWIn software.

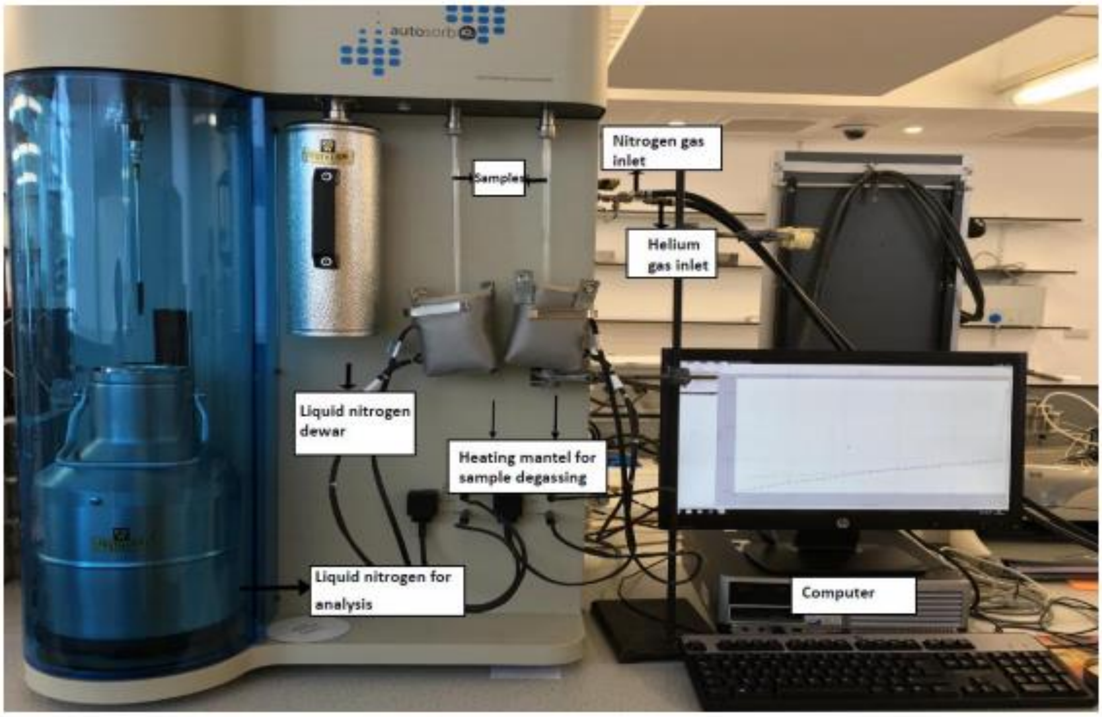

Figure 6.7: Pictorial view of the Quantachrome 2013 liquid nitrogen adsorption instrument.

6.3.3 Specific Surface area and Pore Size Distribution

The specific surface area of the cation-exchange resins, support and membrane was determined using Brunauer-Emmett-Teller (BET) isotherm whereas the pore diameter of both membranes and cation-exchange resins were determined using Barrette-Joyner-Halenda (BJH) [133]. Figure 6.8a and b shows a schematic diagram of the different types of physisorption isotherms (a) and different types of hysteresis (b) [75].

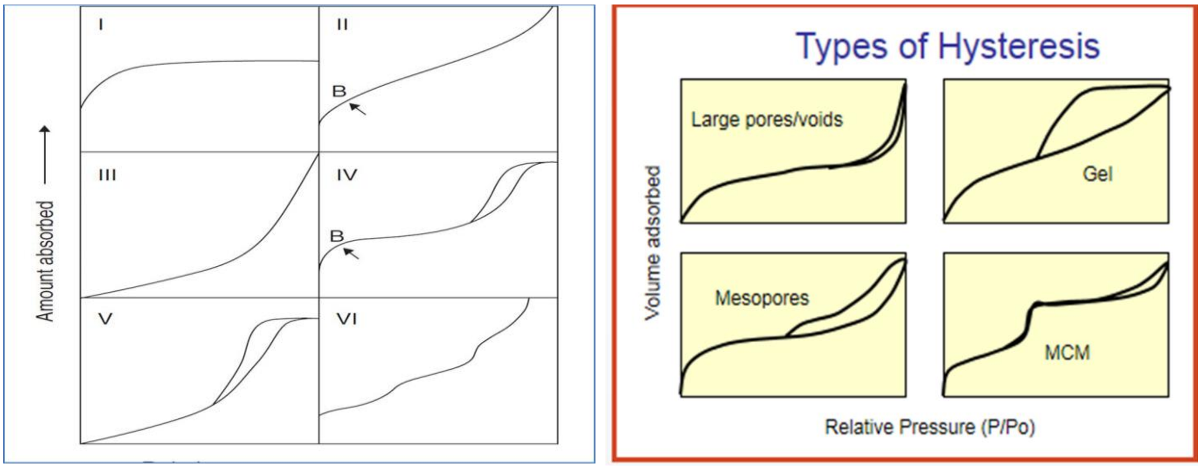

Figure 6.8: Schematic representation of the different types of isotherm (a) and different types of hysteresis (b) for adsorption/desorption of porous materials [75].

CHAPTER 7

7.0 Results and Discussion

7.1 Carrier Gas Transport and Recovery

7.1.1 Effect of Gauge pressure on Permeate flow rate of the support membrane at room temperature and at different temperatures.

Figure 7.1 presents the flow rate of the pure carrier gases including He, N_2, Ar and CO_2 with α-alumina support at the gauge pressure range of 0.10 to 1.00 bar and at room temperature of 298 K. It was found that at 298K, He gas with the least molecular weight permeate faster with the commercial α-alumina support membrane than other gases. Although the molecular weight of CO_2 gas is higher than that of N_2 gas, it was found that N_2 gas permeate faster in contrast to CO_2 gas. It was also found that at 298K, Ar and N_2 gases exhibited almost the same permeation though their molecular weight is different. It was suggested that Knudsen and viscous flow mechanisms were in operation since this mechanism takes into account that gases with the light molecular weight (weakly adsorbed gas) permeate faster than gases with the heavier molecular weight [134], also as the pressure gradient across the membrane increases the flow regime changes from Knudsen to viscous flow mechanism [135]. This further confirms the fact that the flow of the gases depend on their respective molecular weight. The results of the present study are published in Okon et al. [88],[114].

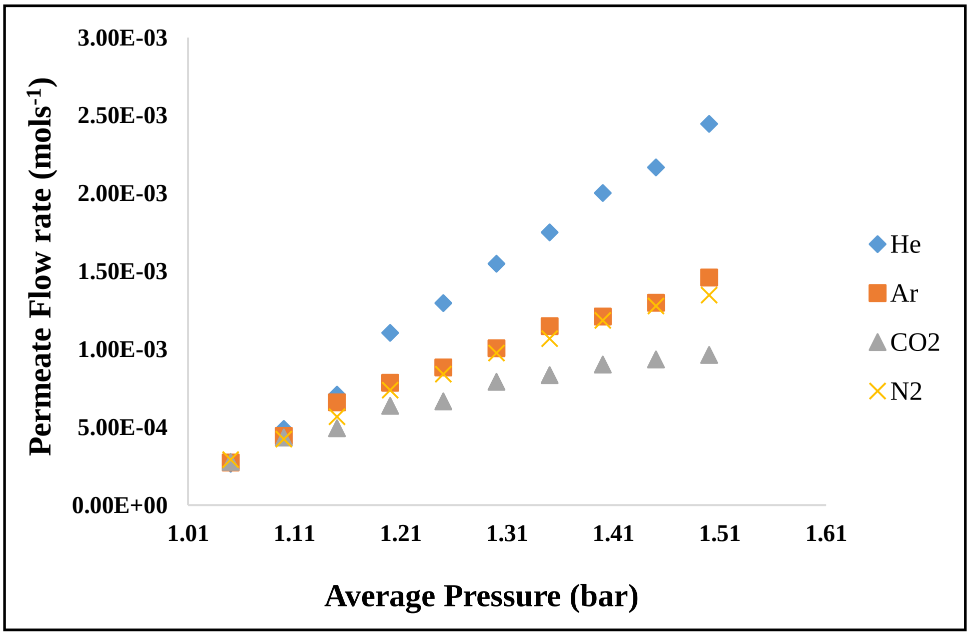

Figure 7.1: Permeate Flow rate against average pressure (bar) for support membrane at room temperature of 298 K.

Figure 7.2-7.4 presents the flow rate of He, N_2, Ar and CO_2 gases with α-Al_2O_3 support membrane at the average pressure range of 0.10 to 1.00 bar and at different temperatures of 60 °C (333 K) and up 160 °C (433 K). In contrast to the gas flow rate with the support membrane at room temperature, He gas was observed to still exhibit the highest flow rate at different temperatures although there was a bit of alteration in the trend. At 333 K, Ar and N_2 gases were observed to permeate almost at the same rate which was similar to the flow at room temperature of (298 K). However, at 353 K, the faster permeation rate of Ar and He are very obvious whereas N_2 and CO_2 exhibited nearly the same permeation at this temperature (353 K). Additionally, at 373 K, the reverse was the case. At 373 K, it was found that though the Ar, CO_2 and N_2 seems to have permeate at the same level. The sequential order of the gas flow with the α-alumina support membrane at 373 K was found to be He (4 mol/g) > N_2 (28 mol/g) > Ar (40 mol/g) and CO_2 (44 mol/g). From the results obtained He and Ar gases were identified and suggested as the carrier gases for the esterification feed analysis. The permeation behaviour of the carrier gases with the α-alumina support were further compared with the results of the γ-Al_2O_3 silica membrane.

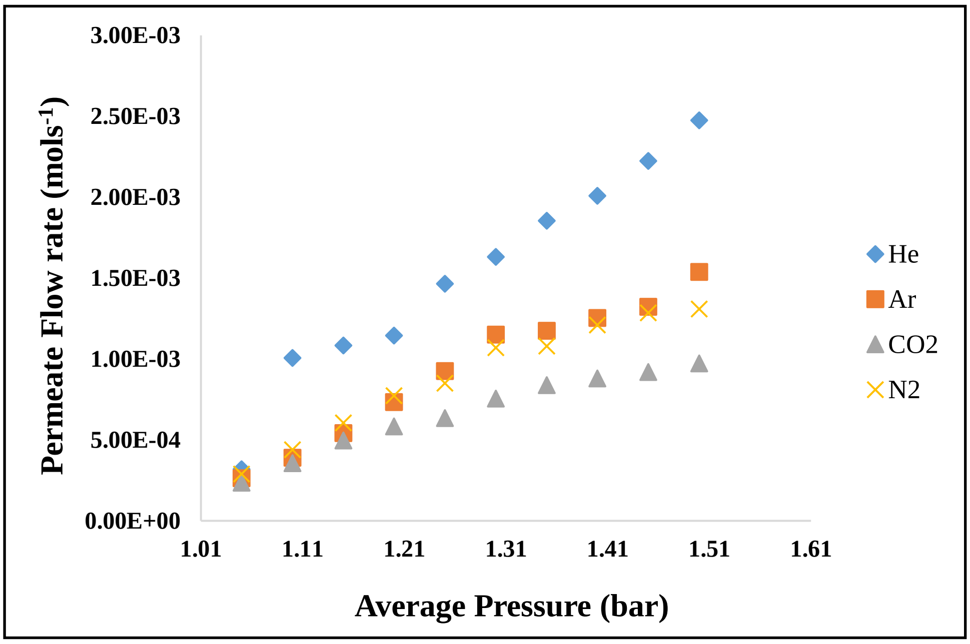

Figure 7.2: Permeate Flow rate against average pressure (bar) for support membrane at the temperature of 333 K.

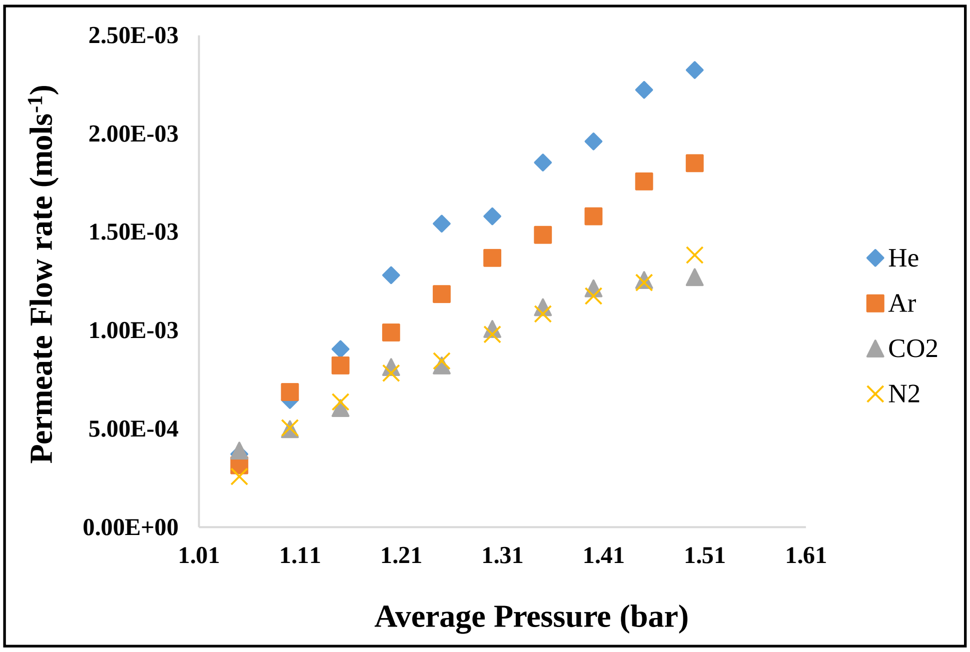

Figure 7.3: Permeate Flow rate against average pressure (bar) for support membrane at the temperature of 353 K.

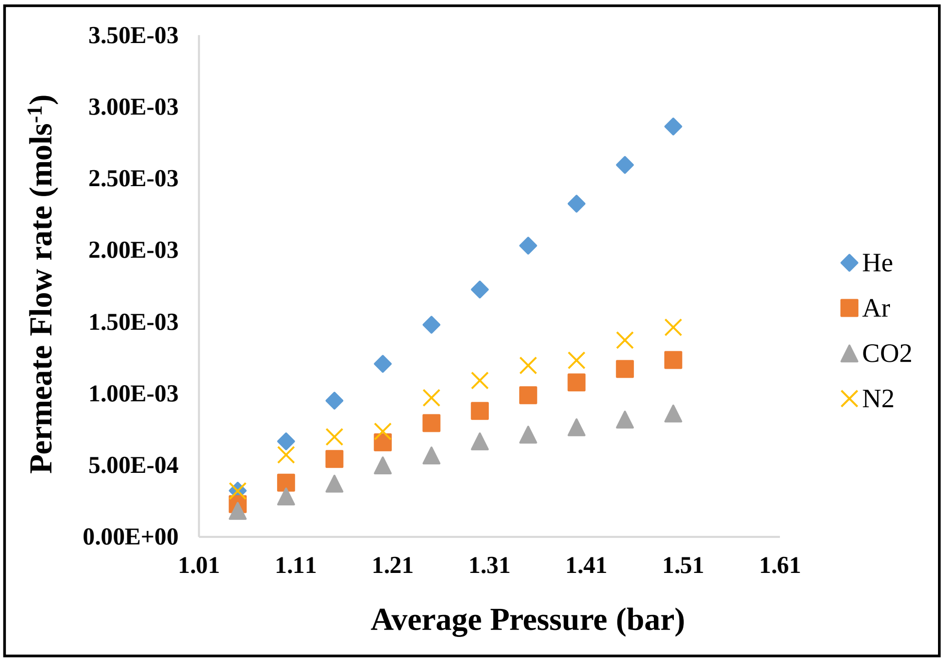

Figure7.4: Permeate Flow rate against average pressure (bar) for support membrane at the temperature of 373 K.

7.1.2 Permeate Flow rate on the dip-coated Membrane at Room Temperature and at different Temperatures.

Figure 7.5-7.8 depicts the relationship between the permeate flow rate of He, N_2, Ar and CO_2 gases against feed gauge pressure for γ-Al_2O_3 silica membrane at the gauge pressure range of 0.10 to 1.00 bar and at temperature of 298 – 413 K. From figure 7.5, it can be seen that He gas demonstrate a significant increase in flow rate with the γ-Al_2O_3 silica membrane at room temperature in contrast to other gases. At 298 K, He gas exhibited a faster permeation between the gauge pressure range of 0.10 – 0.60 bar with the γ-Al_2O_3 silica membrane, however, there was a bit of alteration in the points between the feed gauge pressure of 0.70 – 1.00 bar. Also, at 298 K, CO_2 (44 mol/g) and N_2 (28 mol/g) gas with a higher molecular weight exhibited a lower flow rate than He gas with least molecular weight. This was in accordance with the literature [86]. Helium gas permeation was assumed to be based on Knudsen flow mechanism of transport since this gas exhibited a higher permeation rate with respect to its low molecular weight (4 mol/g) [103,134]. However, Ar (40 mol/g) gas also showed a higher flow rate in contrast N_2 and CO_2. The permeation rate of He and Ar gases in this case were also suggested to be as the result of the surface diffusion process which explain the rate of gas passage through the membrane [95].

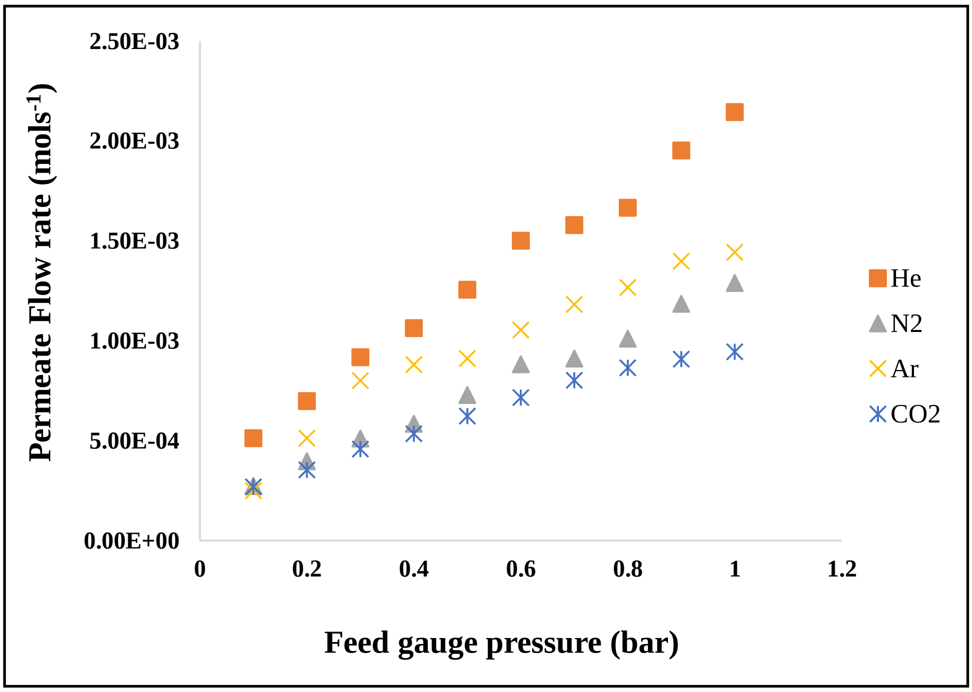

Figure 7.5: Permeate Flow rate against feed gauge pressure (bar) for γ-Al_2O_3 silica membrane at 298 K.

Similarly, from figure 7.6, it was found that the four gases showed a drastic increase in flow rate with respect to pressure drop at 353 after the 1st dip-coating process. Although the flow of the gases was not based on their respective molecular weight, however, after the 1st dip-coating, CO_2 gas which showed the least flow rate at 298 K, was found to exhibit an increase in flow rate in contrast to N_2 gas. In this case, CO_2 (44 mol/g) with a higher molecular weight tends to permeate faster than N_2 (28 mol/g) with least molecular weight which was not still in accordance with the Knudsen diffusion mechanism of gas transport. Also, after the 1st dip-coating, it was observed that Ar (40 mol/g) gas with a heavy molecular weight permeate faster than He (4 mol/g). The order of the gas flow rate with the γ-Al_2O_3 silica membrane after the 1st dip-coating was Ar (40 mol/g) > He (4 mol/g) > CO_2 (mol/g) > N_2 (mol/g). It was suggested that this could be due to sorption process of transport that was in operation after the membrane dip-coating which explained how the gases interact with the surface of the membrane base on the pore size reduction after the silica deposition on the membrane surface [95,99].

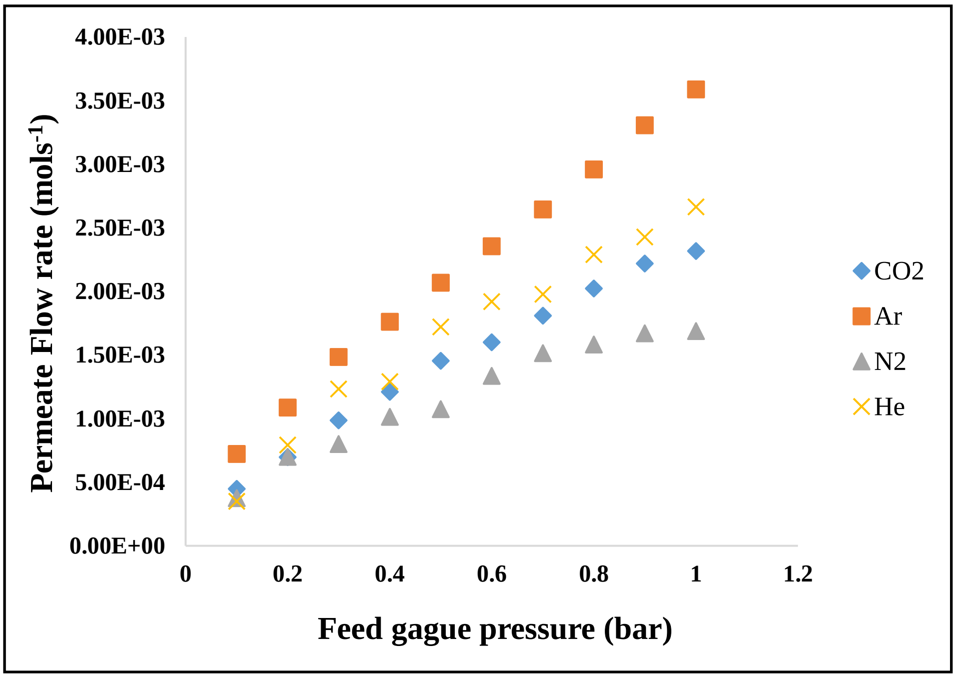

Figure 7.6: Permeate Flow rate against feed gauge pressure (bar) for 1st dip-coated γ-Al_2O_3 membrane at the temperature of 353 K.

Additionally, from figure 7.7, it was found that there was a bit of demarcation in the trend of the flow of the gases after the 2nd dip-coating. From figure 7.7, it was observed that He gas with the least molecular weight still recorded a higher flow rate in contrast to other gases. Though the molecular weight of Ar and N_2 are not close, however, these two gases were observed to permeate at the same rate at 393 K indicating that there could be another mechanism of transport that was in operation. CO_2 was found to exhibit the least flow rate in contrast to other gases at 393 K. It was also observed that between the gauge pressure ranges of 0.10 – 0.40 bar the four gases permeate initially almost at the same rate before deviation of the gases at different level. This was also attributed to the effect of the silica modification. Also, from figure 7.8, it was found that He and Ar gases showed a drastic increase in flow rate at 433 K compared to N_2 and CO_2. After the 3rd dip-coating, it was found that CO_2 gas showed the least flow rate both at 433 K and at 393 K. It was suggested that the silica solution plays a significant effect on the CO_2 permeation. Based on the permeation behaviour of Ar, He, CO_2 and N_2 carrier gas with the α-Al_2O_3 support and γ-Al_2O_3 silica membrane at different feed gauge pressure, room temperature and at different temperatures, He and Ar gas were identified as the suitable carrier gases to couple with GC-MS for the analysis of esterification feed. Other parameters including permeance, flux, effect of kinetic diameter, viscosity of the gases was further determined to further confirm the behaviour of these gases.

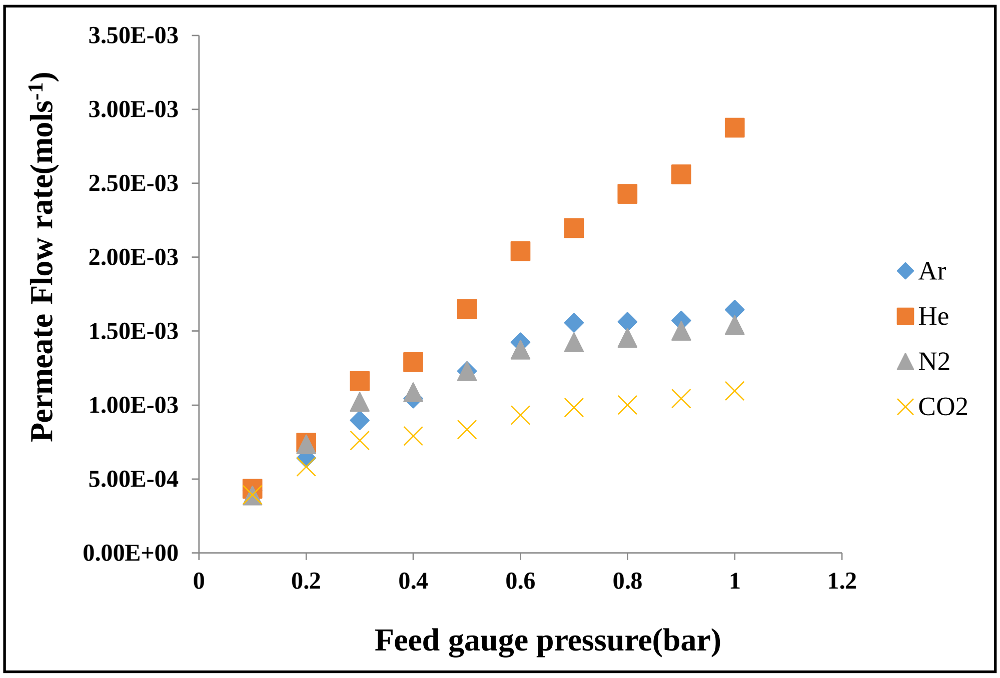

Figure 7.7: Permeate Flow rate against feed gauge pressure (bar) for 2nd dip-coated membrane at the temperature of 120 °C (393 K).

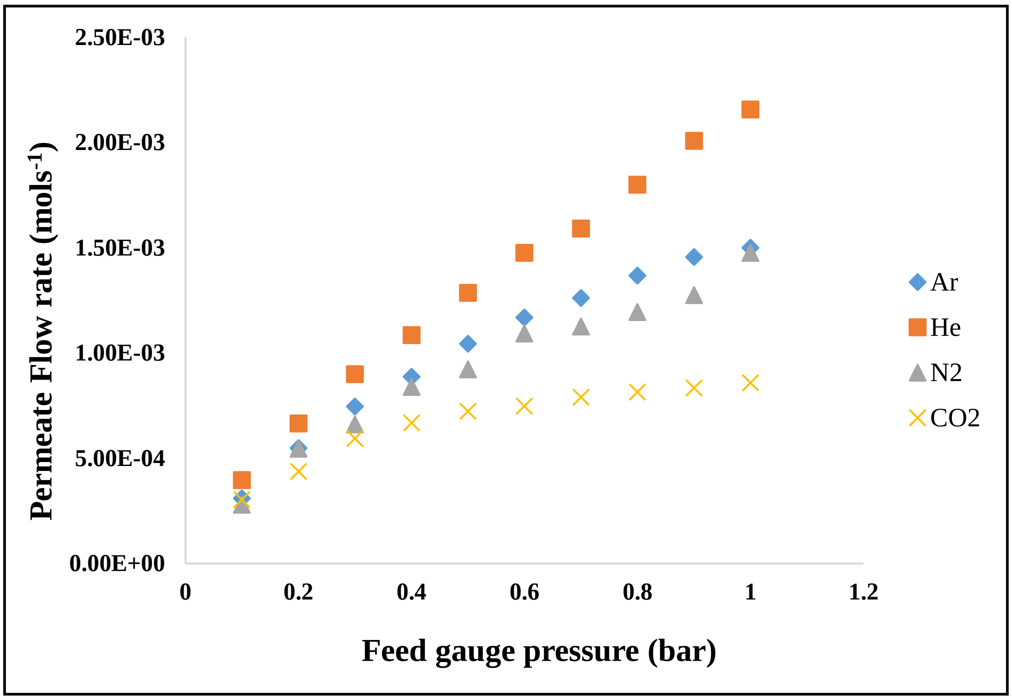

Figure 7.8: Flow rate against feed gauge pressure (bar) for 3rd dip-coated membrane at the temperature of 160 °C (433 K).

7.1.3 Effect of Inlet Feed Pressure on Gas Permeance

Figure 7.9-7.12 presents the relationship between the permeance of He, N_2, Ar and CO_2 gases against feed gauge pressure for the α-Al_2O_3 support membrane at the gauge pressure range of 0.10 to 1.00 bar and at temperature of 298 – 413 K.

The permeance of the four carrier gases was determined using the equation:

$$Q_i = \left(\frac{F_I}{A}\right) \Delta P \ldots\ldots\ldots\ldots\ldots\ldots\ldots\ldots\ldots\ldots\ldots\ldots\ldots\ldots\ldots\ldots(7.1)$$

Where Q_i = permeance (molm^{-2}s^{-1}Pa^{-1}), Fi = gas flow rate (mols^{-1}), A = surface area (m^2) of the membrane and ΔP = pressure difference (Pa) difference between the shell and the tube side [95].

Generally, it observed that the permeance of the gases decreases with increase in gauge pressure at different temperatures as shown in figures 7.9 – 7.12. From figure 7.9, it can be seen that the permeance of the Ar, He, N_2 and CO_2 carrier gases decrease with an increase in feed pressure gauge for the support membrane at 298 K [88]. It was also observed from figure 7.9 that the support membrane exhibited a higher in the range of 2.00 x 10^{-7} to 1.60 x 10^{-6} molm^{-2}s^{-1}Pa^{-1} as shown in table 7.1. However, between the gauge pressure range of 0.20 to 0.40 bar, it was found the permeance of the four gases seems to decrease at the same level however between the feed gauge pressure range of 0.50 to 1.00 bar the gases further decreased differently at 298K.

Table 7.1: Calculated permeance values of Ar, He, N_2 and CO_2 gas for support at different gauge pressure and at 298K

P(bar)	CO_2	Ar	N_2	He
0.10	2.325E-06	3.747E-06	1.943E-06	1.8194E-06
0.20	1.808E-06	2.814E-06	1.816E-06	2.057E-06
0.30	1.704E-06	2.565E-06	1.381E-06	2.129E-06
0.40	1.569E-06	2.282E-06	1.314E-06	1.671E-06
0.50	1.507E-06	2.144E-06	1.115E-06	1.783E-06
0.60	1.382E-06	2.033E-06	1.154E-06	1.659E-06
0.70	1.340E-06	1.957E-06	1.121E-06	1.464E-06
0.80	1.310E-06	1.917E-06	1.025E-06	1.482E-06
0.90	1.277E-06	1.904E-06	9.621E-07	1.397E-06
1.00	1.201E-06	1.859E-06	8.747E-07	1.381E-06

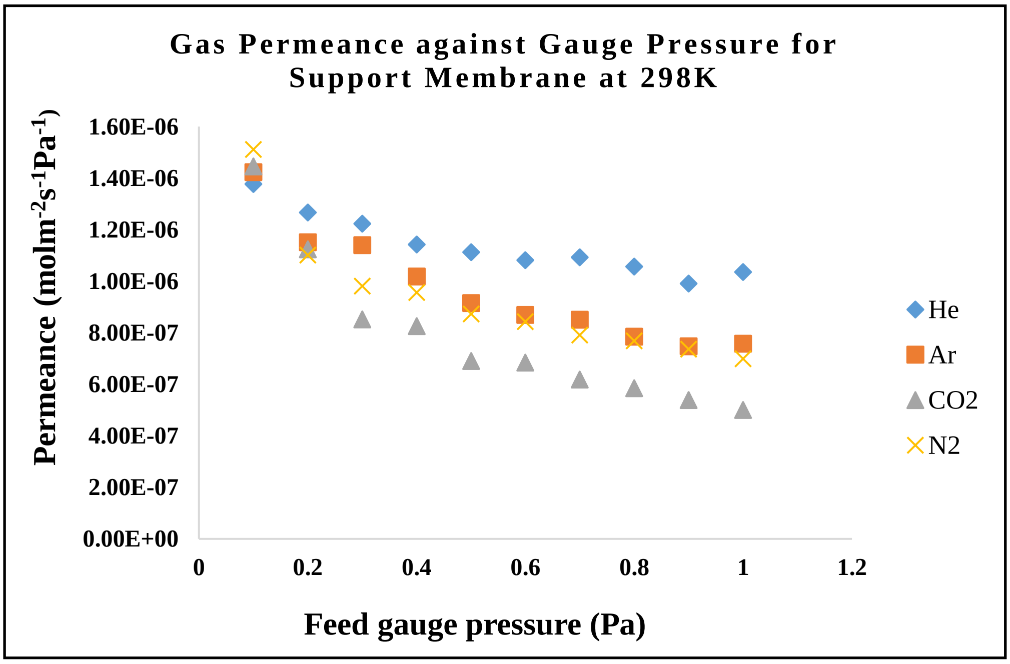

Figure 7.9: Permeance against feed gauge pressure (Pa) for support membrane at room temperature of 298 K.

Similarly, the permeance relationship with feed gauge pressure for He, N_2, Ar and CO_2 was determined at the gauge pressure range of 0.10 to 1.00 bar and at temperature of 298 – 413 K for the 1st, 2nd and 3rd dip-coated γ-Al_2O_3 silica membrane as shown in 7.10, 7.11 and 7.12 respectively. It was found that permeance of the four carrier gases decrease with respect to the feed gauge pressure for the 1st, 2nd and 3rd dip-coated membranes at 353 K, 333K and 413 K respectively which was similar to that of the support membrane. Although the silica membrane showed a reduction with respect to the gauge pressure, it was found that the pattern of gas interaction with the membrane differs after each dip-coating at each gauge pressure. The silica coated membrane exhibited permeance as high as 10^{-7} to 10^{-6} $molm^{-2}s^{-1}Pa^{-1}$ [136] as shown in table 7.2-7.4.

From 7.10, it was found that Ar gas demonstrate a speedily permeance decrease between the gauge pressure of 0.10 – 0.30 bar, but was observed to be stable after 0.40 bar. Although there some alteration in the trend for He gas permeance suggesting some contribution of viscous flow mechanism however, He, CO_2 and N_2 gases were found to permeate almost on the same level at 353 K. Apparently, in figure 7.10, it was observed CO_2, Ar and N_2 gas showed almost the same permeance with respect to gauge pressure. At 0.4 bar–0.50 bar, it was further observed that there was a bit of deviation from the trend line for Helium gas for the 2nd dip-coated membrane at 333 K which was suggested to be as a result of another mechanism of gas transport. Also, in figure 7.11, the ϒ-Al_2O_3 silica coated membrane exhibited almost a similar permeance as that of the 2nd dip-coated membrane although the temperatures weren't the same. He gas showed a sharp decrease between 0.10 – 0.20 bar but subsequently maintained the flow after 0.30 bar at 413 K for the 3rd dipping in figure 7.12. The sharp decrease in permeance for He gas at 413 K was attributed to the mass transfer between the membrane surface and the gas molecule. The order of the gas permeance with respect to the gauge pressure at 413 K is given as He > Ar > N_2 > CO_2 .

Table 7.2: Calculated permeance values of Ar, He, N_2 and CO_2 gas for 1st dip-coated membrane at different gauge pressure and at 353K.

P(bar)	He	Ar	CO_2	N_2
0.10	1.376E-06	1.422E-06	1.446E-06	1.511E-06
0.20	1.266E-06	1.151E-06	1.124E-06	1.101E-06
0.30	1.223E-06	1.139E-06	8.519E-07	9.805E-07
0.40	1.142E-06	1.018E-06	8.250E-07	9.561E-07
0.50	1.112E-06	9.152E-07	6.901E-07	8.720E-07
0.60	1.081E-06	8.693E-07	6.843E-07	8.429E-07
0.70	1.092E-06	8.497E-07	6.174E-07	7.903E-07
0.80	1.056E-06	7.845E-07	5.845E-07	7.677E-07
0.90	9.903E-07	7.475E-07	5.389E-07	7.359E-07
1.00	1.036E-06	7.572E-07	4.996E-07	6.986E-07

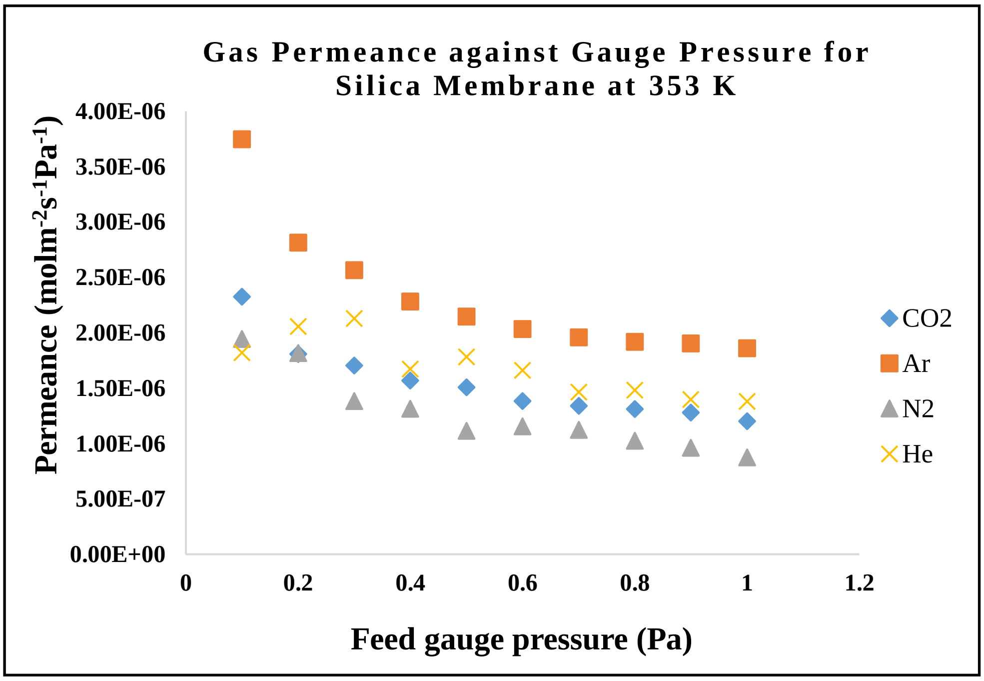

Figure 7.10: Permeance against feed gauge pressure (Pa) for 1st dip-coated membrane at the temperature of 353 K.

Table 7.3: Calculated permeance values of Ar, He, N_2 and CO_2 gas for 2nd dip-coated membrane at different gauge pressure and at 333K.

P(bar)	Ar	He	N_2	CO_2
0.10	2.001E-06	2.787E-06	2.209E-06	1.746E-06
0.20	1.822E-06	2.124E-06	1.608E-06	1.519E-06
0.30	1.599E-06	1.982E-06	1.381E-06	1.396E-06
0.40	1.519E-06	1.843E-06	1.400E-06	1.068E-06
0.50	1.299E-06	1.868E-06	1.275E-06	9.006E-07
0.60	1.347E-06	1.845E-06	1.256E-06	8.128E-07
0.70	1.201E-06	1.690E-06	1.120E-06	7.369E-07
0.80	1.078E-06	1.692E-06	9.980E-07	7.012E-07
0.90	9.925E-07	1.594E-06	9.094E-07	6.430E-07
1.00	8.994E-07	1.551E-06	8.362E-07	5.991E-07

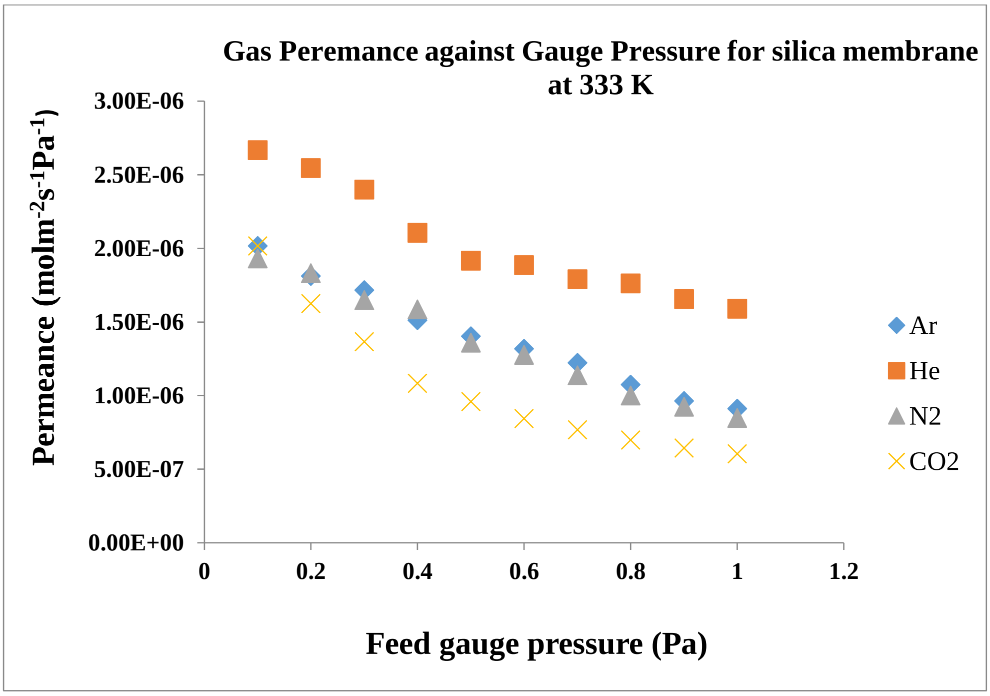

Figure 7.11: Permeance against feed gauge pressure (Pa) for 2nd dip-coated membrane at the temperature of 333 K.

Table 7.4: Calculated permeance values of Ar, He, N_2 and CO_2 gas for 3rd dip-coated membrane at different gauge pressure and at 413K.

P(bar)	Ar	He	N_2	CO_2
0.10	1.6314E-06	1.673E-06	1.415E-06	1.357E-06
0.20	1.193E-06	1.419E-06	1.228E-06	1.129E-06
0.30	1.023E-06	1.563E-06	1.186E-06	8.918E-07
0.40	9.484E-07	1.391E-06	1.024E-06	8.529E-07
0.50	8.505E-07	1.337E-06	9.746E-07	7.517E-07
0.60	7.999E-07	1.374E-06	8.957E-07	6.483E-07
0.70	7.485E-07	1.228E-06	8.189E-07	5.794E-07
0.80	7.219E-07	1.185E-06	7.913E-07	5.272E-07
0.90	6.606E-07	1.151E-06	7.389E-07	4.797E-07
1.00	6.265E-07	1.152E-06	7.413E-07	5.991E-07

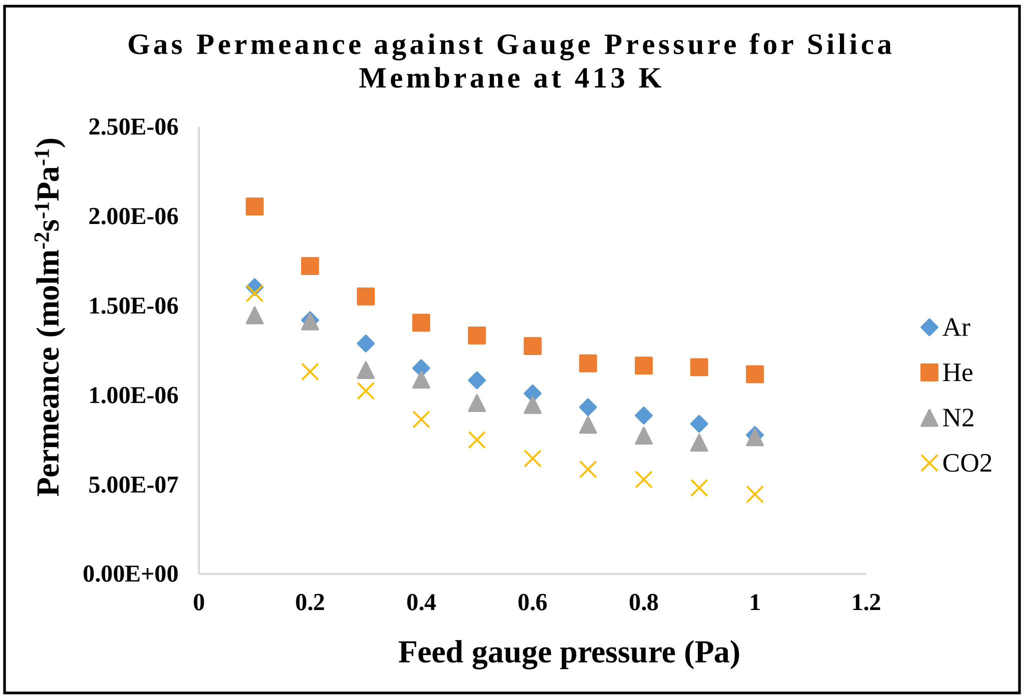

Figure 7.12: Permeance against feed gauge pressure (Pa) for 3rd dip-coated membrane at the temperature of 413 K.

7.1.4 Effect of Kinetic diameter on Gas Permeance

Figure 7.13 – 7.14 depicts the relationship between the permeance (molm^{-2}s^{-1}Pa^{-1}) of the four carrier gas versus gas kinetic diameter (Å) at the feed gauge pressure of 0.30 bar and between the temperature ranges of 298 - 413 K for the alumina support membrane. Generally, the respective kinetic diameter values of the four carrier gas is given as He (2.60 Å), Ar (3.40 Å), N_2 (3.64 Å) and CO_2 (3.30 Å). The result obtained in figure 7.13 shows that He and Ar gases exhibited a higher permeance in contrast to CO_2 and N_2. It was found that N_2 gas has a higher kinetic diameter as shown in Table 7.5.

Table 7.5: Kinetic diameter of Ar, He, CO_2 an N_2 at 298 K and 0.30 bar

Gas molecule	Kinetic Diameter (Å) (137)	Permeance at 0.30 bar (molm^{-2}s^{-1}Pa^{-1})
He	2.60	1.22337E-06
Ar	3.40	1.13984E-06
N_2	3.64	9.80498E-07
CO_2	3.30	8.51992E-07

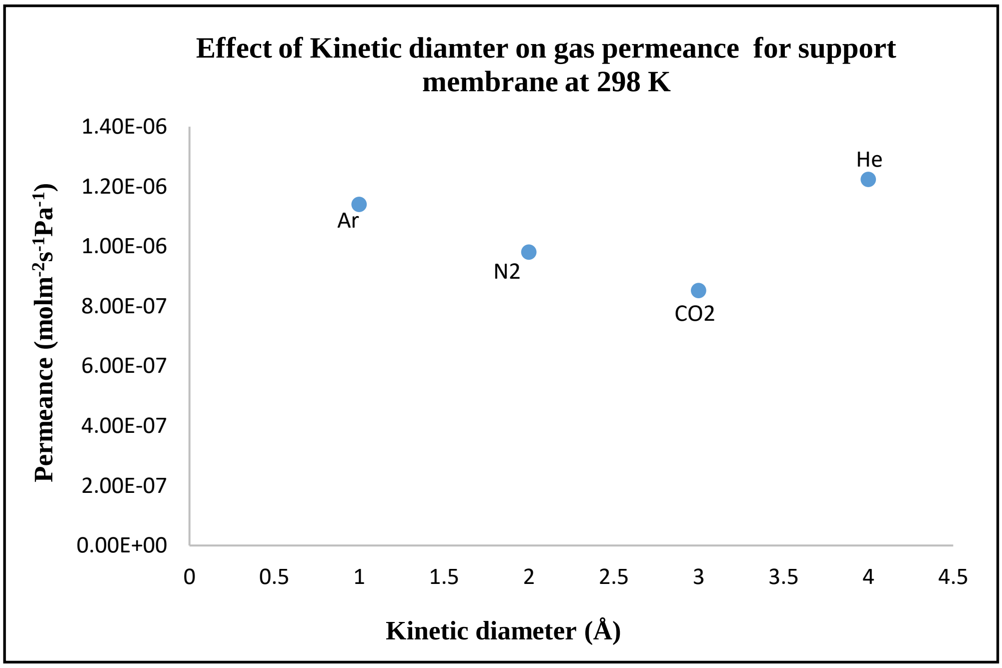

Figure 7.13: Effect of kinetic diameter on gas permeance for the alumina support membrane at 0.30 bar and 298 K.

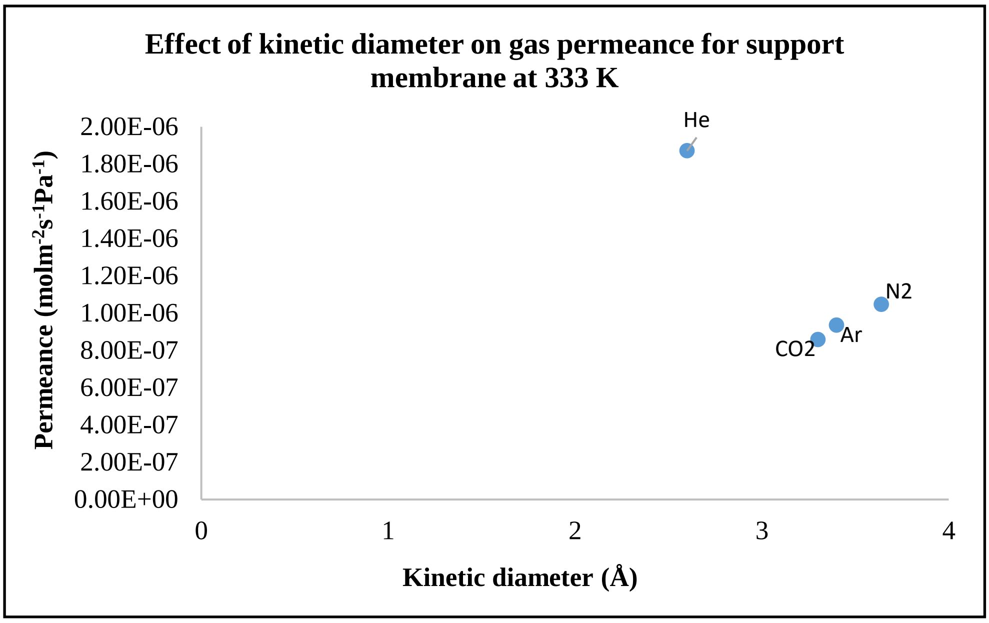

Figure 7.14: Effect of kinetic diameter on gas permeance for the alumina support membrane at 0.30 bar and 333 K.

According to Zornoza et al. [137], for a gas flow through the membrane to be explained by the molecular sieving mechanism of gas transport, the gas molecule with the highest kinetic diameter should have exhibited a lower permeance precisely in the order N_2 (3.64 Å) < Ar (3.40 Å) < CO_2 (3.30 Å) < He (2.60 Å) [137]. However, from the results obtained in figure 7.13, it was found that the reverse was the case. It can be seen that in figure 7.13, N_2 gas with the higher kinetic diameter exhibited a higher permeance for the alumina support membrane at 298 K and at 0.30 bar compared to CO_2 and He with the less kinetic diameter. It was suggested that the gas transport through the alumina support membrane at 0.30 bar and at 298 K was controlled by another mechanism of gas transport. Similarly, the kinetic diameter of the carrier gases with the alumina support membrane was also considered at 333 K at the gauge pressure of 0.30 bar. From figure 7.14, it was observed that the pattern of the gas permeance through the support with respect to the kinetic diameter differs at 333 K. At 333 K, although He gas with the least kinetic diameter still demonstrate a higher permeance followed by N_2, Ar and CO_2, the gas transport in this case was not still in accordance with the molecular sieving mechanism of transport. Also, in figure 7.14, it was also observed that CO_2 gas showed the least permeance for the support membrane at 333 K and 298 K at 0.30 bar. The results were further compared with that of the dip-coated silica membrane at the same operating conditions.

Figure 7.15– 7.18 depicts the relationship between the permeance ($molm^{-2}s^{-1}Pa^{-1}$) of the four carrier gas versus gas kinetic diameter (Å) at the feed gauge pressure of 0.30 bar and between the temperature range of 298 - 419 K for the dip-coated silica membrane.

Table 7.6: Kinetic diameter of Ar, He, CO_2 an N_2 at 333 K and 0.30 bar

Gas molecule	Kinetic Diameter (Å) [137]	Permeance at 0.30 bar ($molm^{-2}s^{-1}Pa^{-1}$)
He	2.60	1.871E-06
Ar	3.40	9.355E-07
N_2	3.64	1.046E-06
CO_2	3.30	8.584E-07

Table 7.7: Kinetic diameter of Ar, He, CO_2 an N_2 at 353 K and 0.30 bar

Gas molecule	Kinetic Diameter (Å) [137]	Permeance at 0.30 bar ($molm^{-2}s^{-1}Pa^{-1}$)
He	2.60	2.129E-06
Ar	3.40	2.565E-06
N2	3.64	1.381E-06
CO2	3.30	1.704E-06

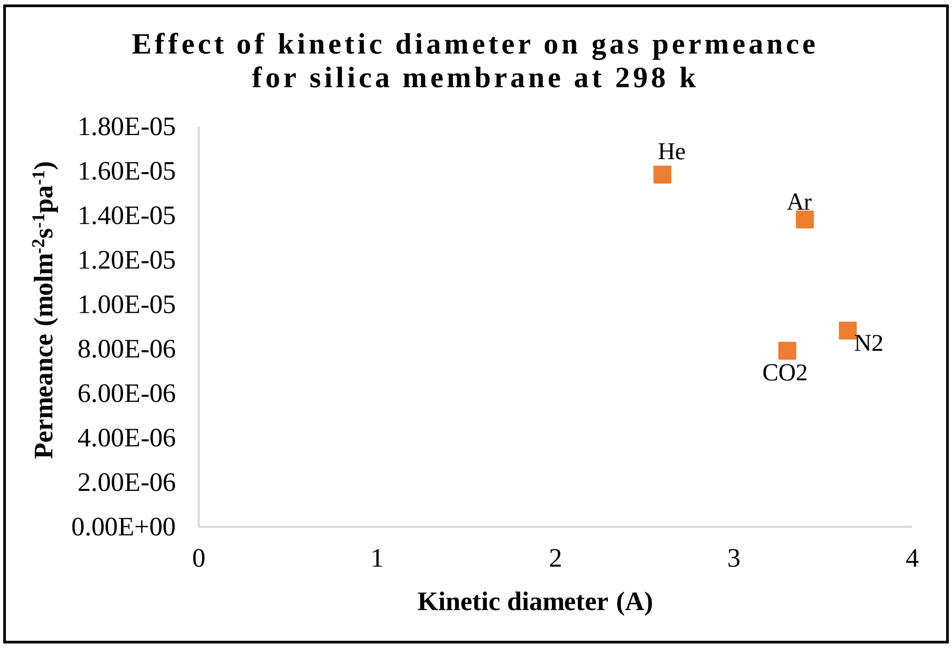

Figure 7.15: Effect of kinetic diameter on gas permeance for the silica coated membrane at 0.30 bar and 298 K.

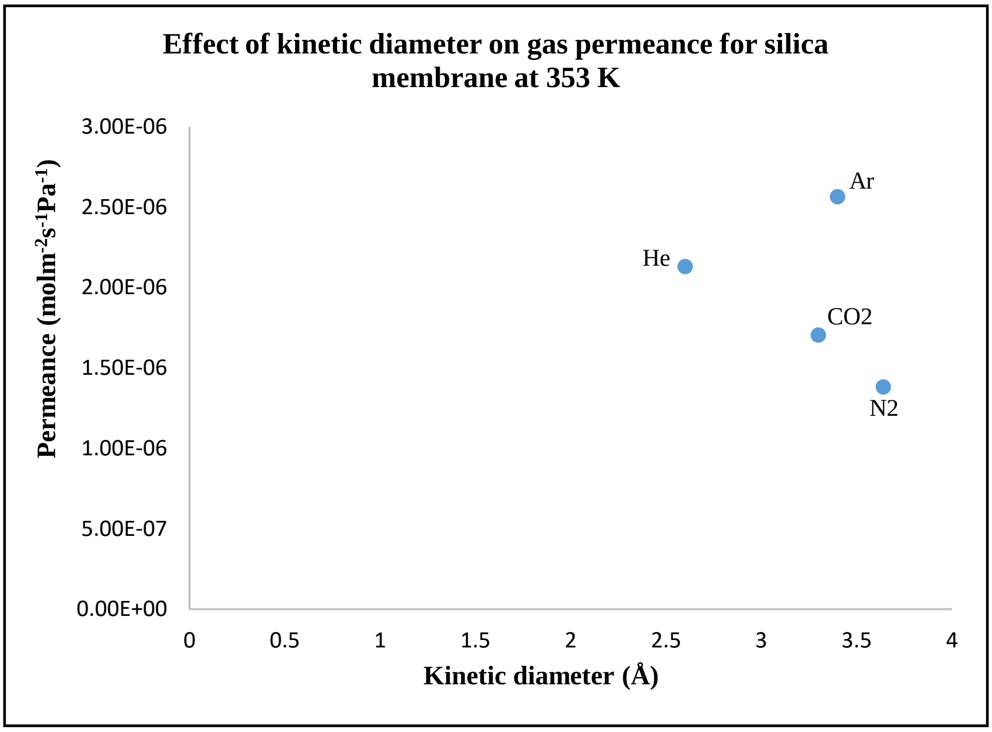

Figure 7.16: Effect of kinetic diameter on permeance for the silica membrane at 0.30 bar and 353 K for 1st dipping.

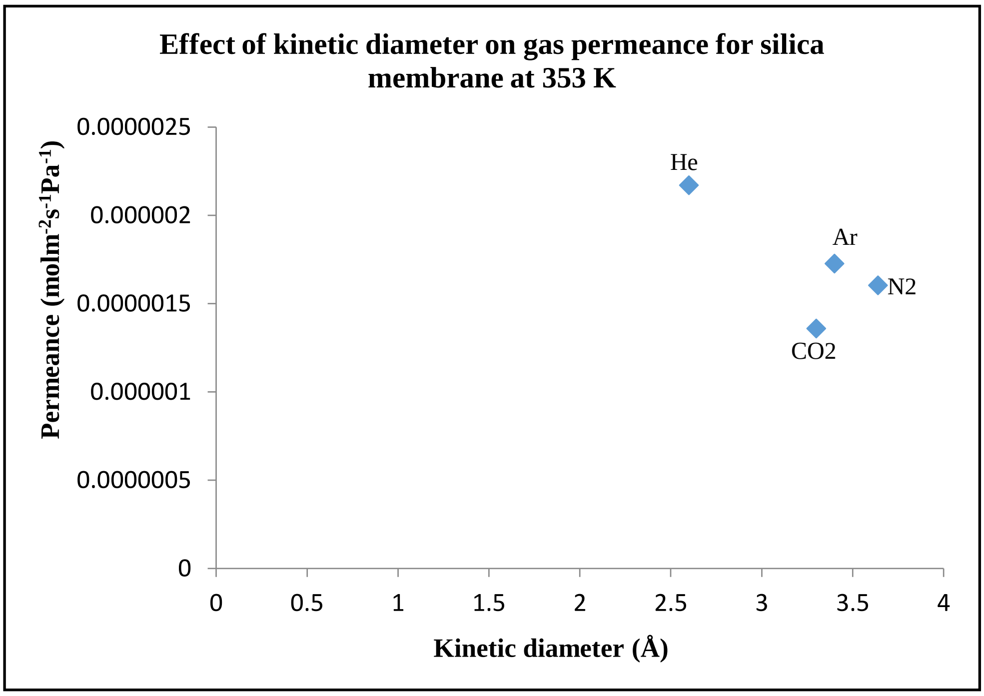

Figure 7.17: Effect of kinetic diameter on permeance for the silica membrane at 0.30 bar and 353 K for 2nd dipping.

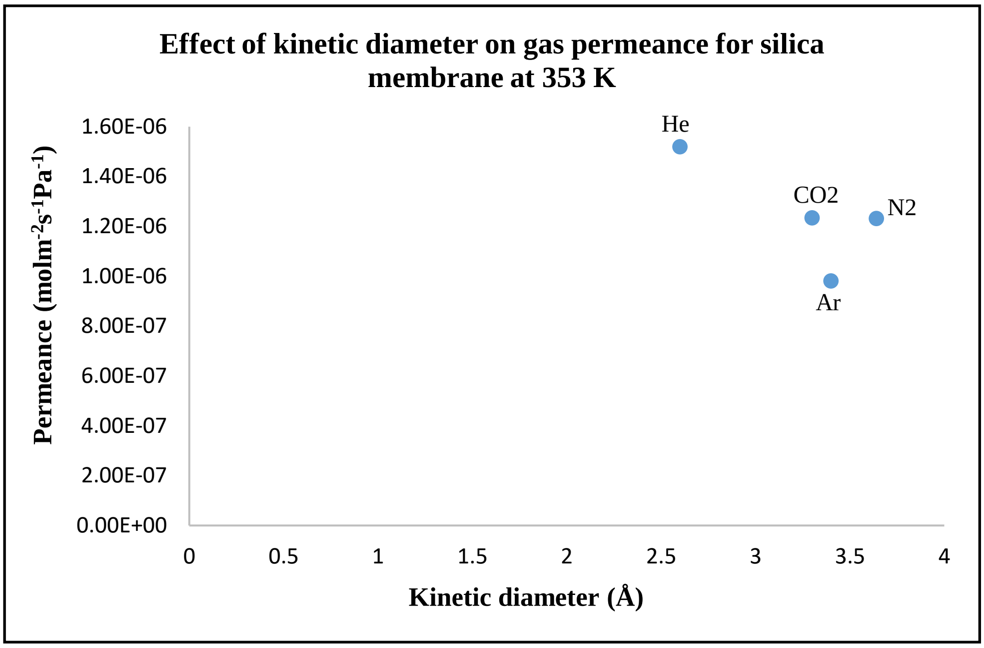

Figure 7.18: Effect of kinetic diameter on permeance for the silica membrane at 0.30 bar and 353 K for the 3rd dipping.

From the results obtained in figure 7.15 and 7.16, it was observed that although the permeance of the four gases measured at 298 K (figure 7.15) and 353 K (figure 7.16) respectively were observed to be in the order He > Ar > N_2 > CO_2 for the dip-coated silica membrane, however, this order of the gas flow through the silica membrane was not exactly based on the order of their respective kinetic diameter the sequential order of the gas kinetic diameter is given as N_2 > Ar > CO_2 > He. It was also found that N_2 with the highest kinetic diameter would have recorded a lower permeance in contrast to CO_2, Ar and He. Also, in figure 7.15 and 7.16, the permeance of He gas would have been close to that of CO_2 rather than Ar and N_2 since their kinetic diameter are close as shown in table 7.8 for the gas flow to be describe by molecular sieving, but the reverse was the case indicating that another mechanism of gas transport was in operation.

Apparently, from the result obtained in figure 7.16, it was observed that at 353 K for the first dip-coated membrane, gases did not follow the expected trend of the ordered of their kinetic diameter. Although N_2 with the highest kinetic diameter exhibited the least permeance with respect to molecular sieving mechanism, Ar gas that should have been next to N_2 was found to be close to He while CO_2 took the place of Ar. With this alteration, it was suggested that the gas flow was not in accordance with the molecular sieving mechanism for the 1st dip-coating membrane. Also, considering the kinetic diameter of the gases at the same temperature (353 K), for the second dip-coated membrane (figure 7.17), it was found that the gases did not still obey the molecular sieving mechanism. Similarly, at 353K, it was observed that the gases followed the same pattern of alteration at this temperature for the 3rd dip-coated membrane in figure 7.18. It was suggested that this could be as a result of the surface diffusion mechanism of transport which explain the interaction of the gases with the silica that was used for the modification of the surface of the membrane [99].

7.1.5 Effect of Molecular weight on Gas Permeance

Figure 7.19 – 7.20 depicts the effect of inverse square root of the gas molecular weight (g/mol) on the permeance ($molm^{-2}s^{-1}Pa^{-1}$) of He, Ar, N_2 and CO_2 between the temperature range of 298 – 433K and at 0.3 bar to determine the relationship between the gas molecular weight and gas permeance. Table 7.8 shows the effect of the gas permeance on the inverse square root of the gas molecular weight at 0.30 bar and 298 K.

Table 7.8: Permeance value, gas molecule and inverse square root of the gas molecular weight for the support membrane at 298 K and 0.30 bar.

Gas molecule	Inverse square root of gas molecular weight (g/mol)	Permeance ($molm^{-2}s^{-1}Pa^{-1}$)
He	4	1.223E-06
Ar	40	1.139E-06
N_2	28	9.805E-07
CO_2	44	8.519E-07

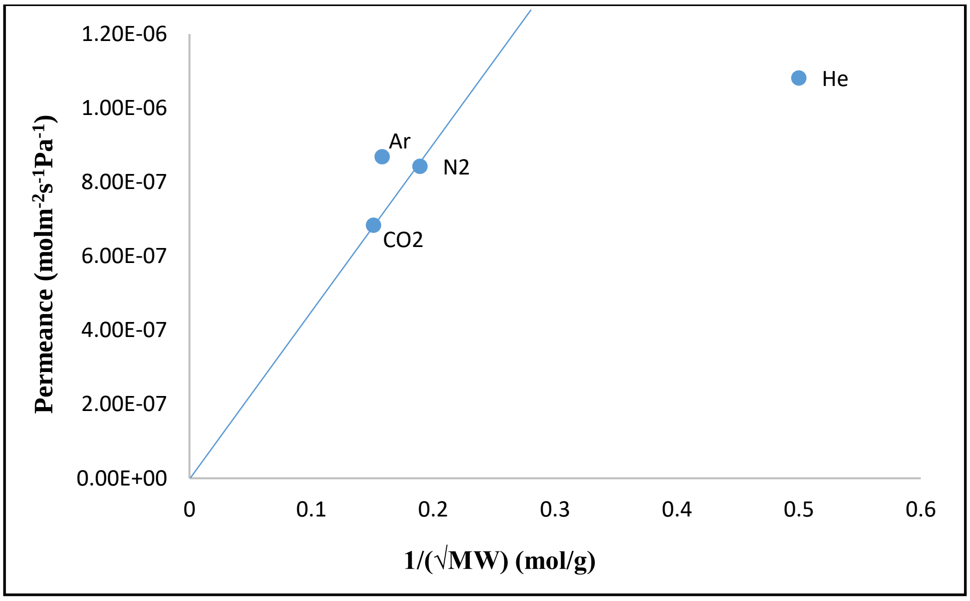

Figure 7.19: Effect of inverse square root of gas molecular weight on permeance for the support membrane at 0.30 bar and 298 K.

According to Araki et al. [138], the linear proportionality of gas permeance on the inverse square root of the gas molecular weight indicate the fact that the gas transport through silica membrane is as the result of Knudsen mechanism of transport [139,86,140]. However, from the results obtained in figure 7.19, it was found that Ar, N_2 and CO_2 gas transport exhibited the linear proportionality of permeance with the inverse square root of the gas molecular weight with except for He gas. It was suggested that the Ar, N_2 and CO_2 gas flow through the membrane were controlled by Knudsen mechanism of gas transport at 298 K for the α-Al_2O_3 support membrane whereas, He gas flow was controlled by another mechanism of gas transport [141]. A similar result was obtained by Barma et al. [140].

Table 7.9: Permeance value, gas molecule and inverse square root of the gas molecular weight for silica coated membrane at 353 K and 0.30 bar

Gas molecule	Inverse square root of gas molecular weight (g/mol) [134]	Permeance ($molm^{-2}s^{-1}Pa^{-1}$)
He	4	2.600E-06
Ar	40	1.396E-06
N_2	28	1.726E-06
CO_2	44	2.165E-06

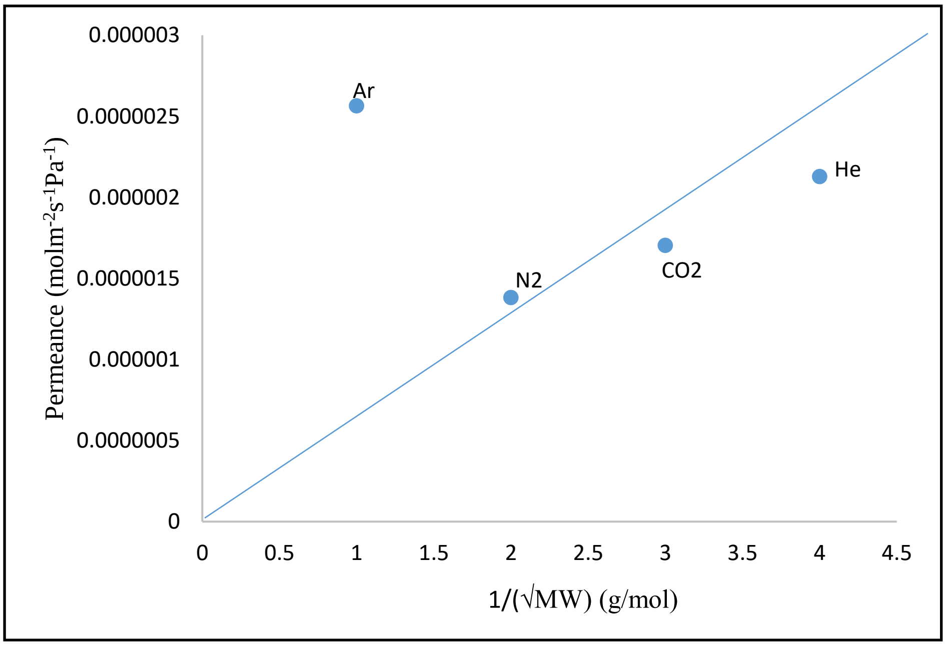

Figure 7.20: Effect of inverse square root of gas molecular weight on permeance for the silica coated membrane at 0.30 bar and 353 K.

Also, at 353 K, the graph of permeance against the inverse square root of the gas molecular weight was obtained for the silica coated membrane. From figure 7.20, it was found that the linear proportionality constant line was obtained between the gases. From figure 7.20, it was found that N_2, He and CO_2 gases showed a linear proportionality relationship with the permeance although the point did not fit exactly to the line of best fit, but they were quite close indicating that N_2, CO_2 and He gas transport occurred mainly due to Knudsen flow mechanism of gas transport [86,103,140]. Also, from figure 7.20, it can be seen that Ar gas clearly deviated from the trend at 353 K at 0.30 bar suggesting that Ar gas did not obey the linear proportionality law with the ϒ-Al_2O_3 silica membrane [142,143]. It was suggested that there could be another mechanism of gas transport that controlled Ar gas flow through the silica membrane. In contrast to the result for the support membrane at 298 K, He gas was found to deviate from the trend but after the support modification, Ar gas showed a deviation from the trend. This indicates that Knudsen flow mechanism through the membrane depend on the interaction of the gases with the pores walls of the membrane.

7.1.6 Effect of Gas Viscosity on Gas Permeance

Figure 7.21 depict the relationship between the respective inverse viscosity (Pas^{-1}) of the gases and the gas permeance ($molm^{-2}s^{-1}Pa^{-1}$) for the α-Al_2O_3 alumina support at 298 K and at 0.30 bar. The viscosity values of the gases as well as their respective permeance values are presented in table 7.10. For a gas flow to be described by the viscous flow mechanism, the flow of the gases through the membrane must be based on the increasing viscosity number [137]. As expected for a viscous flow mechanism, the gases would have permeated in the order Ar (22.90 Pas^{-1}) > He (20.00 Pas^{-1}) > N_2 (17.81 Pas^{-1}) > CO_2 (14.80 Pas^{-1}). From Figure 7.21, it can be seen that the gas transport was not exactly based on their respective viscosity values, although He gas with a higher viscosity showed a slightly higher permeance than CO_2 gas. It was also found that Ar gas with the highest viscosity value as shown in table 7.10, demonstrate a low permeance in contrast to N_2 with a lower viscosity value indicating that the gas flow through the α-Al_2O_3 support membrane at 0.30 bar and at 298 K was not controlled by viscous flow mechanism of gas transport [88]. The order of the gas viscosity was given as He > Ar > N_2 > CO_2.

Table 7.10: Permeance value, gas molecule and inverse viscosity values for Ar, He, CO_2 an N_2 at 298 K and 0.30 bar

Gas molecule	Gas Viscosity (Pas^{-1})	1/Gas Viscosity (Pas^{-1})	Permeance ($molm^{-2}s^{-1}Pa^{-1}$)
He	20.00	0.050	9.805E-07
Ar	22.90	0.044	1.139E-06
N2	17.81	0.056	1.223E-06
CO2	14.80	0.068	8.519E-07

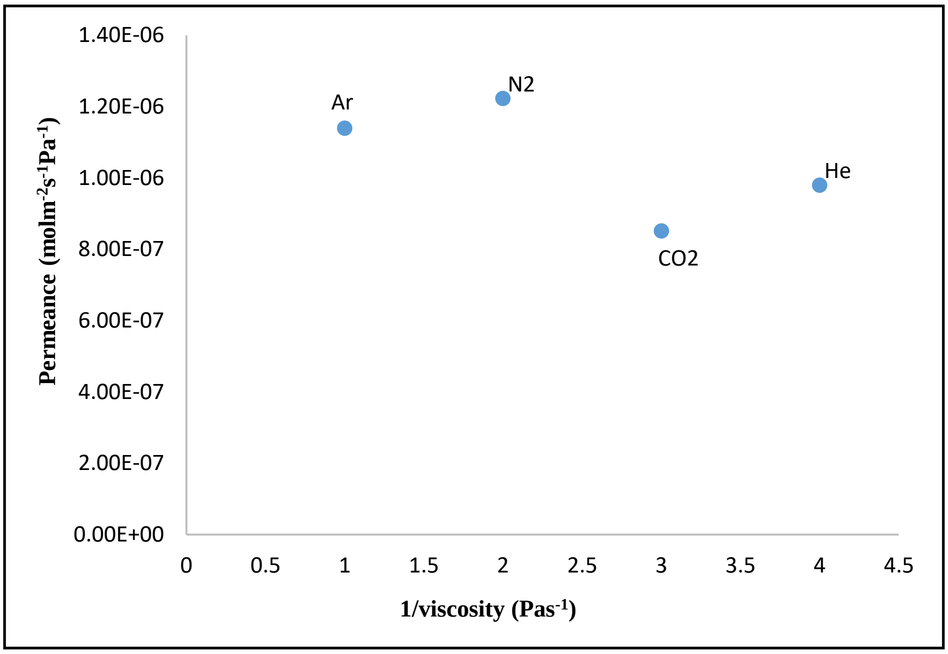

Figure 7.21: Effect of gas viscosity (Pas^{-1}) on gas permeance ($molm^{-2}s^{-1}Pa^{-1}$) for the alumina support membrane at 0.30 bar and 298 K.

Figure 7.22 – 7.24 depict the relationship between the respective inverse viscosity (Pas^{-1}) of the gases and the gas permeance ($molm^{-2}s^{-1}Pa^{-1}$) for the 1st, 2nd and 3rd dip-coated γ-Al_2O_3 silica membrane at 353 K and at 0.30 bar. From figure 7.22, it can be seen that the permeation rate of the gases at first seems to follow the order of their respective mechanism for Ar and He gas at 0.30 bar at 353 K for the 1st dip-coated membrane however, CO_2 with the least viscosity value exhibited a higher permeance in contrast to N_2 with the higher viscosity value as shown in table 7.11. Also, from figure 7.23, it was found that Ar gas with the highest viscosity value as shown in table 7.12, exhibited the lowest permeance in contrast to CO_2 at 0.30 bar and at 353 K for the silica membrane at 2nd dip. It was also found that

although He gas with the highest viscosity value showed a higher permeance than N_2, CO_2, however, N_2 gas still recorded a higher permeance than Ar at 0.30 bar suggesting that the gas flow was not based on the viscous flow mechanism of transport.

Table 7.12: Permeance value, gas molecule and inverse viscosity values for Ar, He, CO_2 an N_2 at 353 K and 0.30 bar for 1st dip-coated membrane.

Gas molecule	Gas Viscosity	1/Gas Viscosity (Pas^{-1})	Permeance ($molm^{-2}s^{-1}Pa^{-1}$)
He	20.00	0.050	2.130E-06
Ar	22.90	0.044	2.560E-06
N2	17.81	0.056	1.380-06
CO2	14.80	0.068	1.700-06

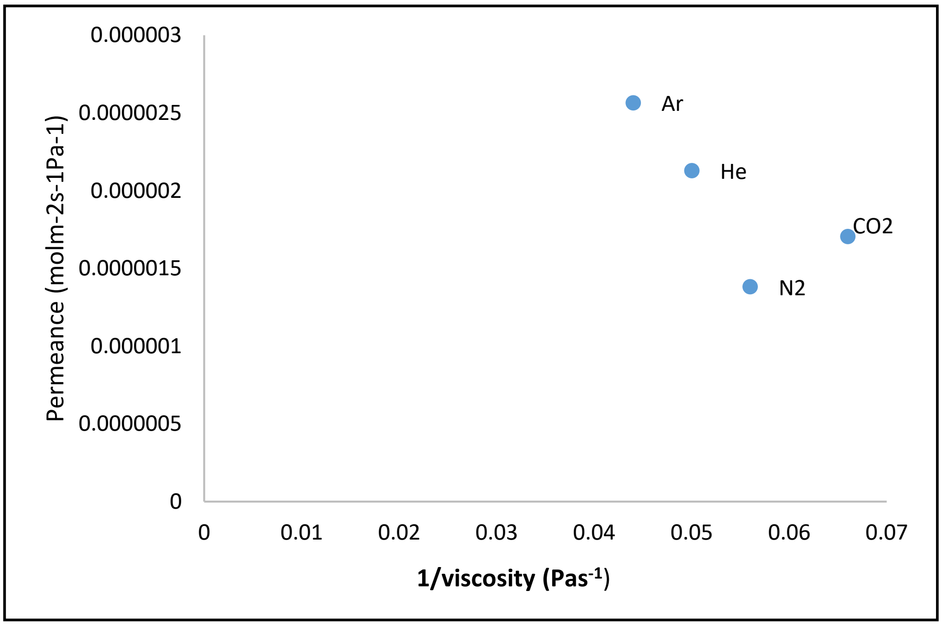

Figure 7.22: Effect of viscosity (Pas^{-1}) on gas permeance ($molm^{-2}s^{-1}Pa^{-1}$) for the silica coated membrane at 0.30 bar and 353 K after 1st dip-coating.

Table 7.12: Permeance value, gas molecule and inverse viscosity values for Ar, He, CO_2 an N_2 at 353 K and 0.30 bar for 2nd dip-coated membrane

Gas molecule	Gas Viscosity	1/Gas Viscosity (Pas^{-1})	Permeance ($molm^{-2}s^{-1}Pa^{-1}$)
He	20.00	0.050	1.520E-06
Ar	22.90	0.044	9.817E-07
N2	17.81	0.056	1.232E-06
CO2	14.80	0.068	1.235E-06

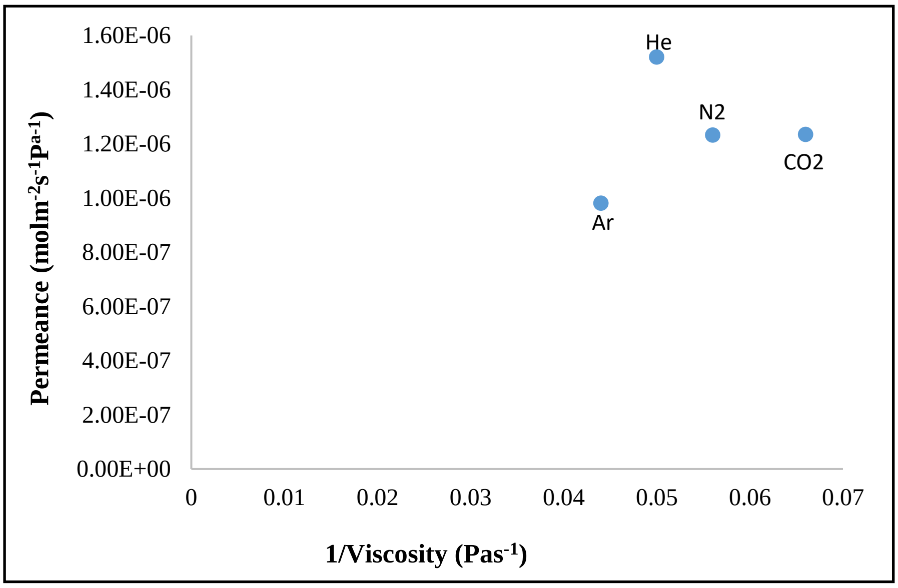

Figure 7.23: Effect of viscosity (Pas^{-1}) on gas permeance ($molm^{-2}s^{-1}Pa^{-1}$) for the silica coated membrane at 0.30 bar and 353 K after 2nd dip-coating.

Similarly, the effect of viscosity (Pas^{-1}) of the four gases as a function of gas permeance ($molm^{-2}s^{-1}Pa^{-1}$) was also investigated for the γ-Al_2O_3 silica membrane after the 3rd dip-coating at 353 K and at 0.30 bar as shown in Figure 7.24. From the results obtained in figure 7.24, it was found that He gas exhibited a higher viscosity value exhibited a permeance for the 3rd dip-coated silica membrane at 0.30 bar and at 353 K in contrast to Ar gas with the highest viscosity value as shown in table 7.13.

Table 7.13: Permeance value, gas molecule and inverse viscosity values for Ar, He, CO_2 an N_2 at 353 K and 0.30 bar for 3rd dip-coated membrane

Gas molecule	Gas Viscosity	1/Gas Viscosity (Pas^{-1})	Permeance ($molm^{-2}s^{-1}Pa^{-1}$)
He	20.00	0.050	2.116E-06
Ar	22.90	0.044	1.559E-06
N2	17.81	0.056	1.305E-06
CO2	14.80	0.068	1.074E-06

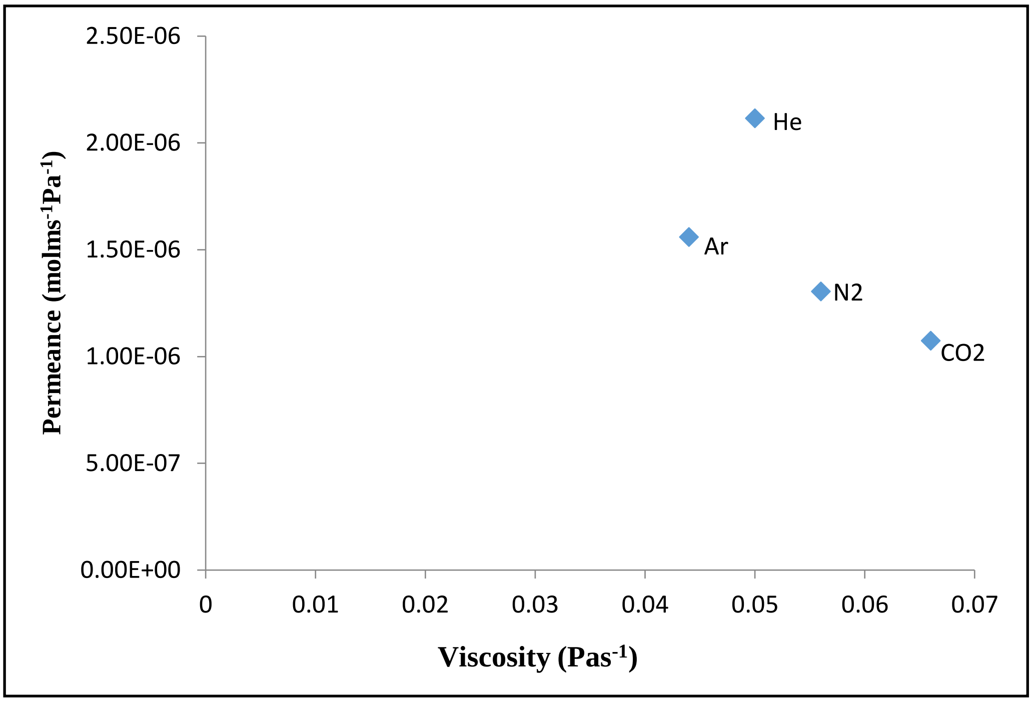

Figure 7.24: Effect of viscosity (Pas^{-1}) on gas permeance ($molm^{-2}s^{-1}Pa^{-1}$) for the silica coated membrane at 0.30 bar and 353 K after the 3rd dip-coating.

7.1.7 Effect of Gas Flux on inlet Gauge Pressure

Figure 7.25 present the relationship between the flux of Ar, He, N_2 and CO_2 gas and gauge pressure for the α-Al_2O_3 support membrane between the gauge pressure range of 0.10 – 1.00 barg and between 298 – 353 K. According to Wall et al. [134], Knudsen flux is dependent on the molecular weight of the permeating gas molecule [134]. From the result obtained in figure 7.25, it was found that the permeate flux increases linearly with an increase in feed gauge pressure for all the gases [144]. From the result obtained in figure 7.25 for the support membrane, it was found that He gas with the least molecular weight exhibited a higher flux with the R^2 value of 0.9957 followed by N_2 gas with 0.9899. It was also found that although CO_2 and Ar gases with a higher molecular weight showed a linearly increases with respect to the feed gauge however, their R^2 square values of 0.9608 and 0.9839 for CO_2 and Ar respectively were found to be a bit lower in contrast to He and N_2 gases [134].

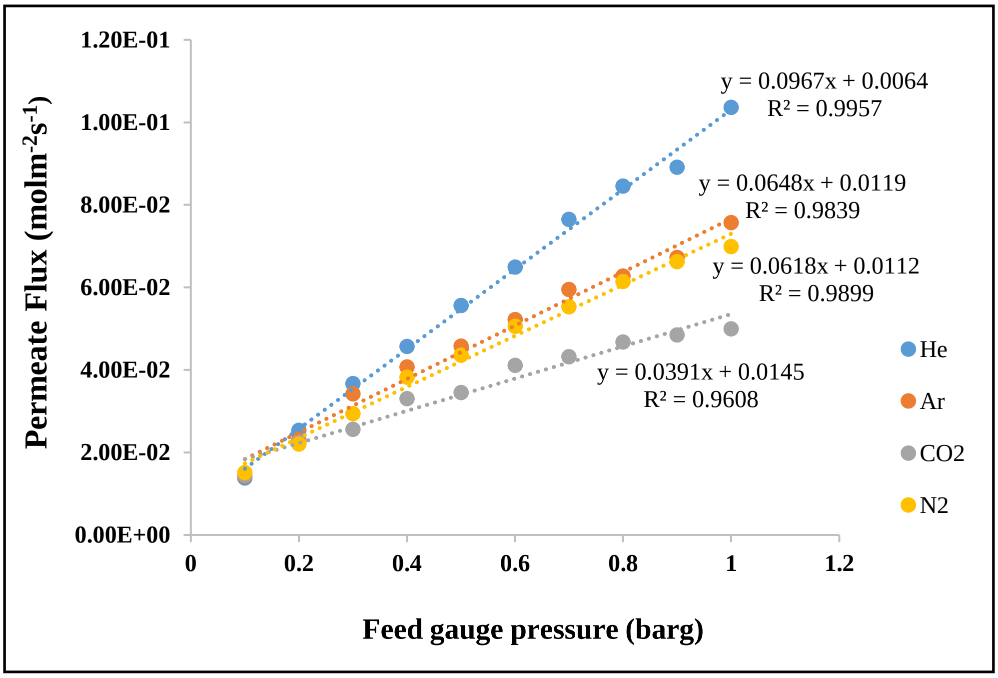

Figure 7.25: Permeate flux against feed gauge pressure (barg) for support membrane at room temperature of 298K.

The gas flux of the dip-coated silica membrane was further investigated 298 K after the modification process in order to compare the behaviour of the gases with the modified membrane in contrast to the support. Figure 7.26 - 7.29 present the relationship between the flux of Ar, He, N_2 and CO_2 gas and gauge pressure for the γ-Al_2O_3 membrane between the gauge pressure range of 0.10 – 1.00 barg and at 298 K after the dip-coating process. From figure 7.26, it can be seen that the gases exhibited a linear increase in flux with the silica membrane with respect to the feed gauge pressure after the modification process. It can be seen that Ar gas increases most followed by CO_2. The heavier molecular weight gases (Ar (40 mol/g) and CO_2 (44 mol/g)) were found to permeate faster than He (4 mol/g) and N_2 (28 mol/g) gases with less molecular weight which was not in accordance as described by Knudsen mechanism as expected. The result was further tested at higher temperature of 353 K for the silica coated membrane. The gases showed a correlation value in the range of 0.9530 – 0.9918.

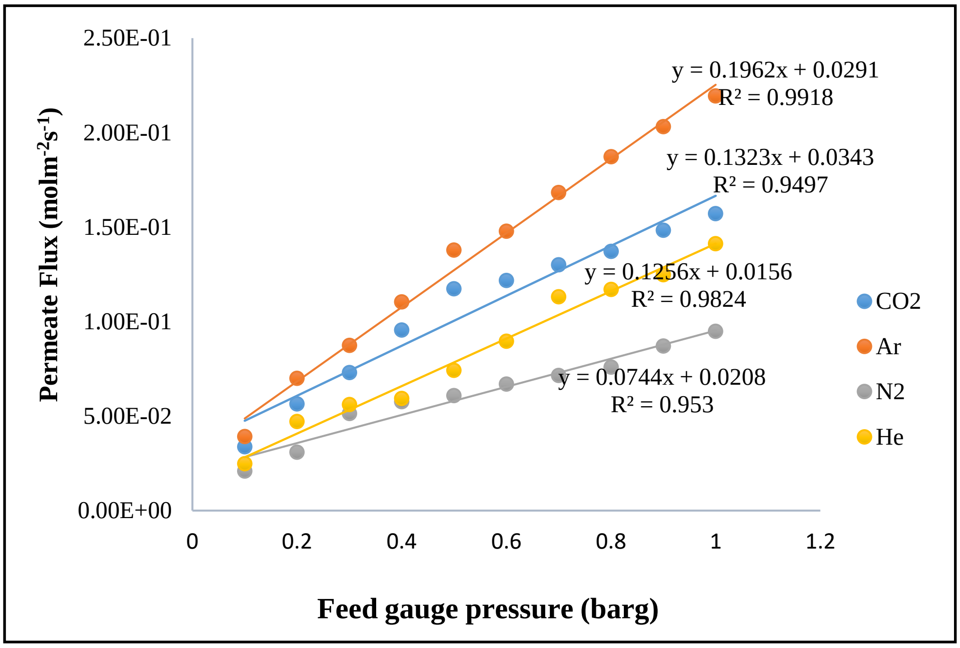

Figure 7.26: Permeate flux against feed gauge pressure (barg) for silica dip-coated membrane at room temperature of 298K.

Figure 7.27 present the relationship between the flux of Ar, He, N_2 and CO_2 gas and gauge pressure for the γ-Al_2O_3 membrane between the gauge pressure range of 0.10 – 1.00 barg and at 353 K after the 1st dip-coating process. From figure 7.27, it was found that Ar gas showed a higher flux followed by He gas. Although the gases did not follow their respective order of the molecular weight, but they all exhibited linear increase in flux with respect to the feed gauge pressure at 353 K. It was also found that at 353 K, the gases showed a good correlation values in the range of 0.9618 – 0.998 K.

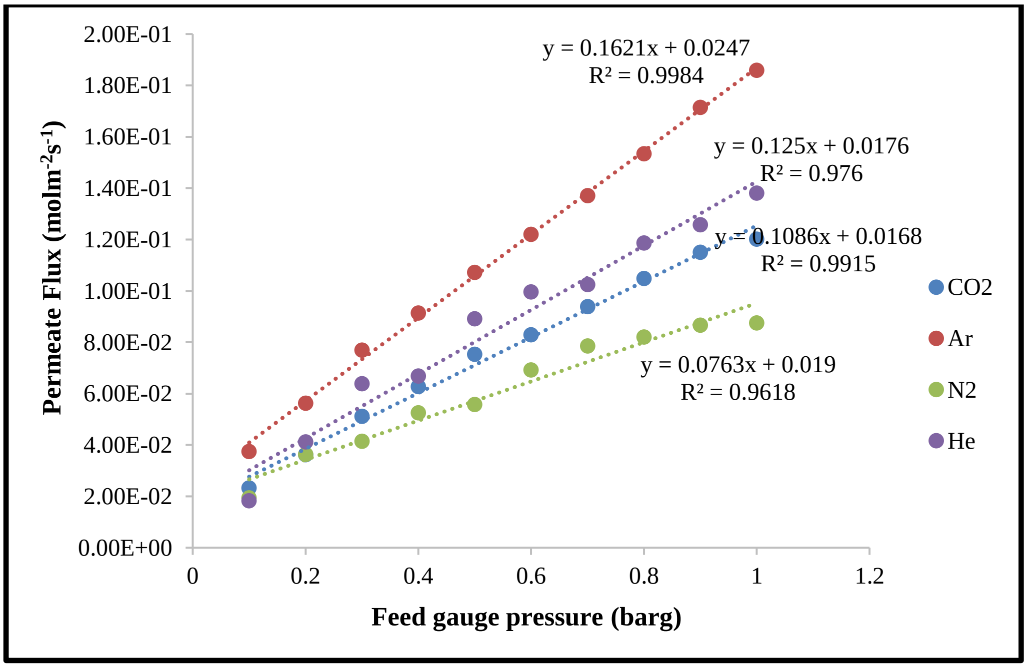

Figure 7.27: Permeate flux against feed gauge pressure (barg) for silica 1st dip-coated membrane at 353 K.

Figure 7.28 – 7.29 present the relationship between the flux of Ar, He, N_2 and CO_2 gas for the γ-Al_2O_3 silica coated membrane at 2nd and 3rd dip between the gauge pressure range of 0.10 –1.00 barg and at the temperatures of 373 K and 353 K respectively. From figure 7.28, it was observed that Helium gas still demonstrate the highest permeation followed by Ar gas after the 2nd dip-coating. Although the gases exhibited a positive slope and intercept, however, the experimental correlation values of the gases were found to be low in the range of 0.8647 – 0.9848. It was also observed that Ar and N_2 gas exhibited the same pattern of flow and as well as the same correlation values at 373 K, although their molecular weight differs. Also, from figure 7.29, it can be seen that He gas showed the highest permeation at the 3rd dip-coating at 353 K followed by N_2 gas. From figure 7.29, it can be seen that the flux of the gases followed their respective molecular weight after the 3rd dip-coating at 353 K which was attributed to Knudsen flow mechanism. However, the correlation values of the gases were found to be in the range of 0.8627 – 0.9836.

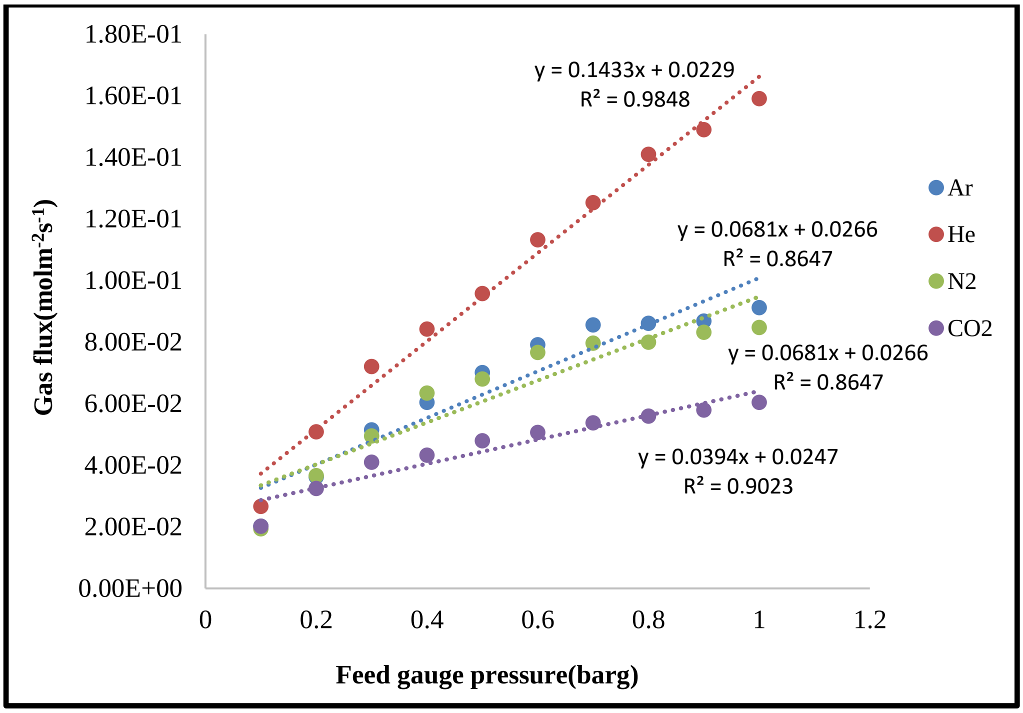

Figure 7.28: Permeate flux against feed gauge pressure (barg) for 2nd dip-coated membrane at room temperature of 373 K.

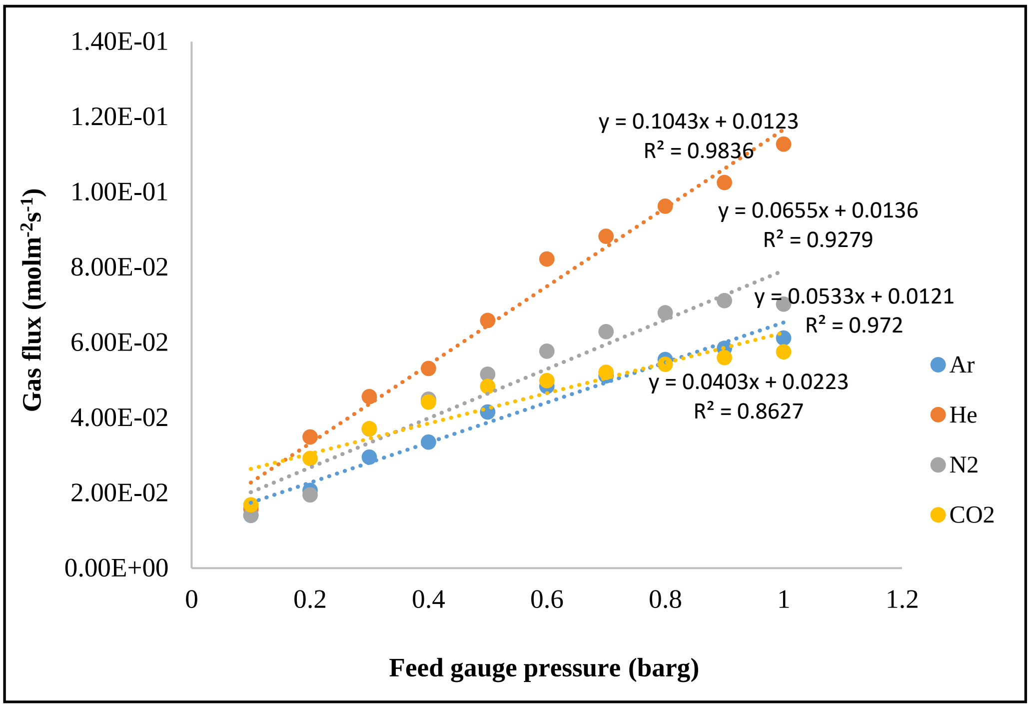

Figure 7.29: Permeate flux against feed gauge pressure (barg) for 3rd dip-coated membrane at room temperature of 353 K.

7.1.7.1 Effect of Helium Flux on inlet Gauge Pressure

Since helium gas exhibited the highest permeation rate, He gas flux was further investigated with respect to the feed gauge pressure to compare the behaviour of the helium carrier gas at different temperatures. Figure 7.30 - 7.35 depicts the flux of Helium gas between the temperature range of 298K to 393K for the support and the silica coated membrane at different dips. From the results obtained in figure 7.30, it can be seen that the flux of the helium gas increases with respect to the feed gauge pressure for both the support and the silica coated membrane which was in accordance with the Knudsen flow mechanism of transport. It can be seen from figure 7.30 that Helium gas exhibited a higher correlation value between the range of 0.9656 – 0.9993 [134]. At 298K and 393K, helium gas demonstrate a correlation value of 0.9957 and 0.9993 respectively. However, at 373K and 333K the gas showed almost a similar correlation values for the support membrane.

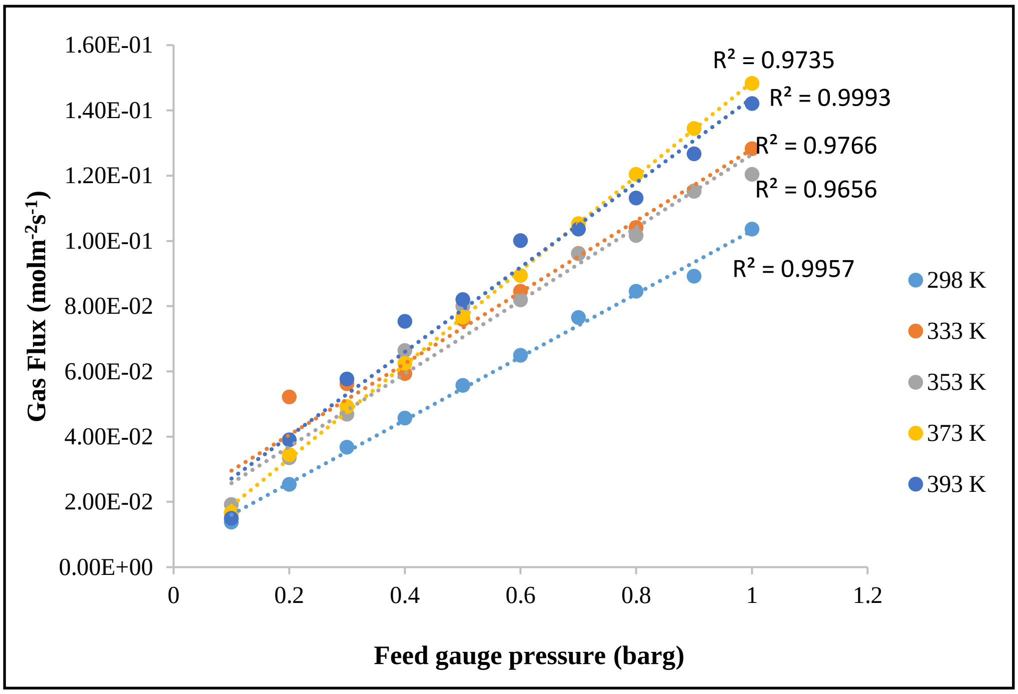

Figure 7.30: Helium flux for support membrane at 298 K -393 K and at gauge pressure range of 0.10 – 1.00 (barg).

Similarly, it was observed that He gas demonstrate the same correlation value of 0.9921 after the 1st, 2nd and 3rd dip-coating for the silica membrane. From figure 7.31 the silica membrane exhibited a good correlation values of 0.9520 – 0.9893 after the 1st dip-coating, 0.9848 – 0.9921 after the 2nd dip-coating and 0.9921-0.9953 after the 3rd coating as shown in figure 7.32 and 7.33 respectively. From the results obtained in figure 7.31-7.33, it was observed from the experimental correlation values that He permeation gas was due to the effect of the silica solution that was used for the modification process.

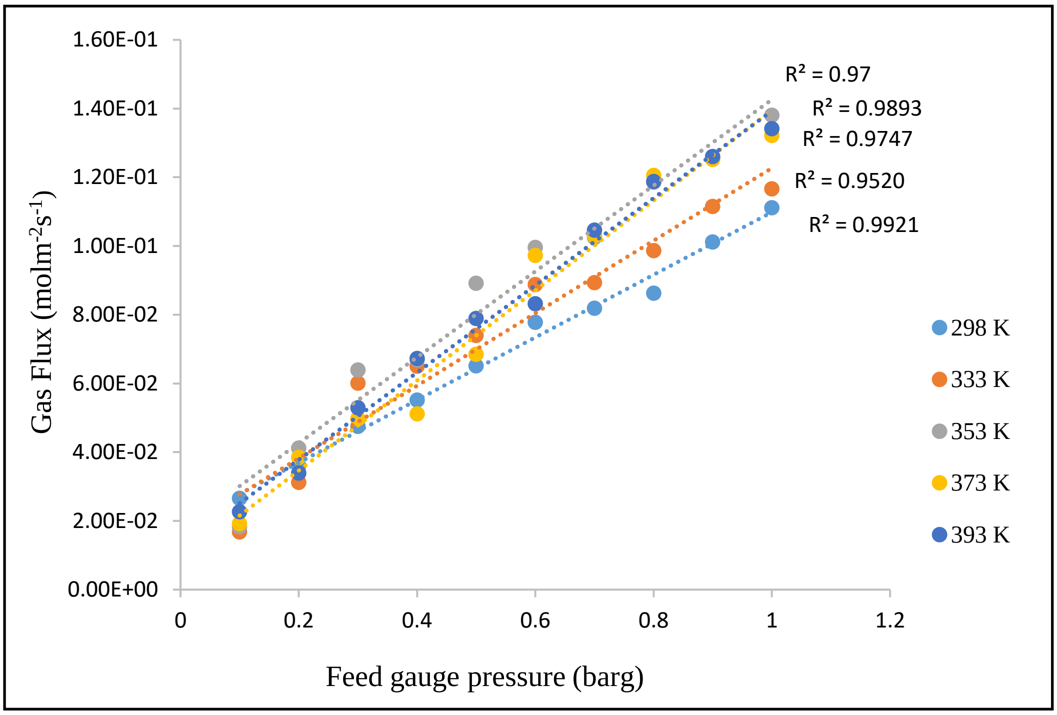

Figure 7.31: Helium flux for 1st silica coated membrane at 298 K -393 K and at different gauge pressure (bar).

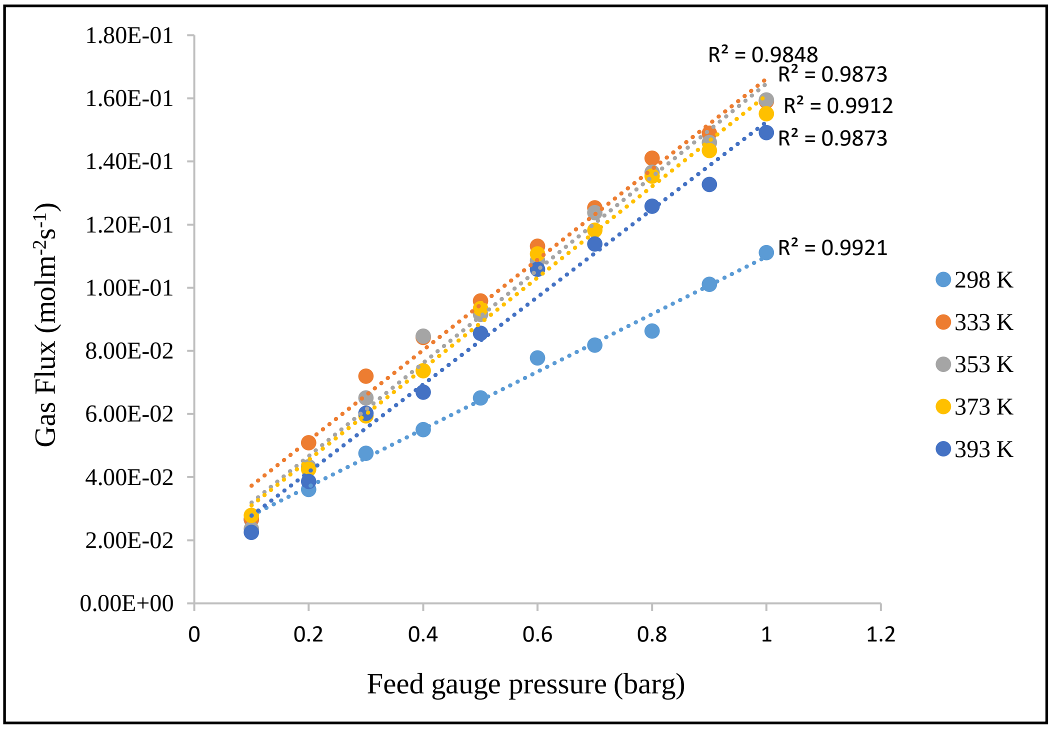

Figure 7.32: Helium flux for 2nd silica coated membrane at 298 K -393 K and at different gauge pressure (bar).

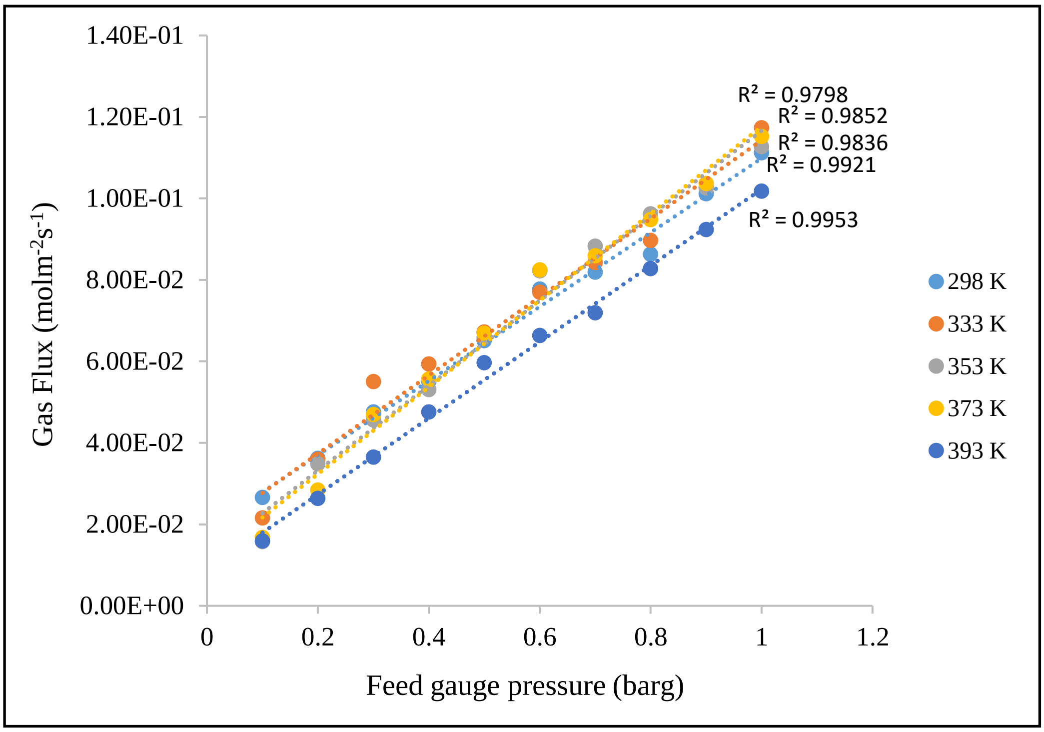

Figure 7.33: Helium flux for 3rd silica coated membrane at 298 K - 393 K and at different gauge pressure (bar).

7.1.8 Effect of Temperature on Gas Permeance

Figure 7.34 shows the influence of tempearture on permeance helium, argon, carbon dioxide and nitrogen gases at the gauge feed pressure of 0.30 bar and the temperature range of 333 -393 K for the support and silica coated membranes. From figure 7.34, it can be seen that the support membrane did not showed dependence of permeance on the temperature at 0.30 bar and at 333 – 393 K. It can be seen that the gases did not exhibit dependence on the temperature at 0.30 bar. It can be seen that between the temperature of 353 K, He gas did not show any dependence with temperature. It was found that CO_2 gas exhibited a similar behaviour as He although at 333K, the CO_2 showed a bit of dependence at 333 K. It was also observed that N_2 gas showed a dependence of permeance on temperature between 333 – 393 K which suggesting that N_2 gas was based on Knudsen mechanism. It was suggest that the non-dependence of the gas permeance was due to the fact that the membrane was not modified. Further investigation was carried out by plotting the graph of tempersture against permeance at the same temperature and gauge pressure.

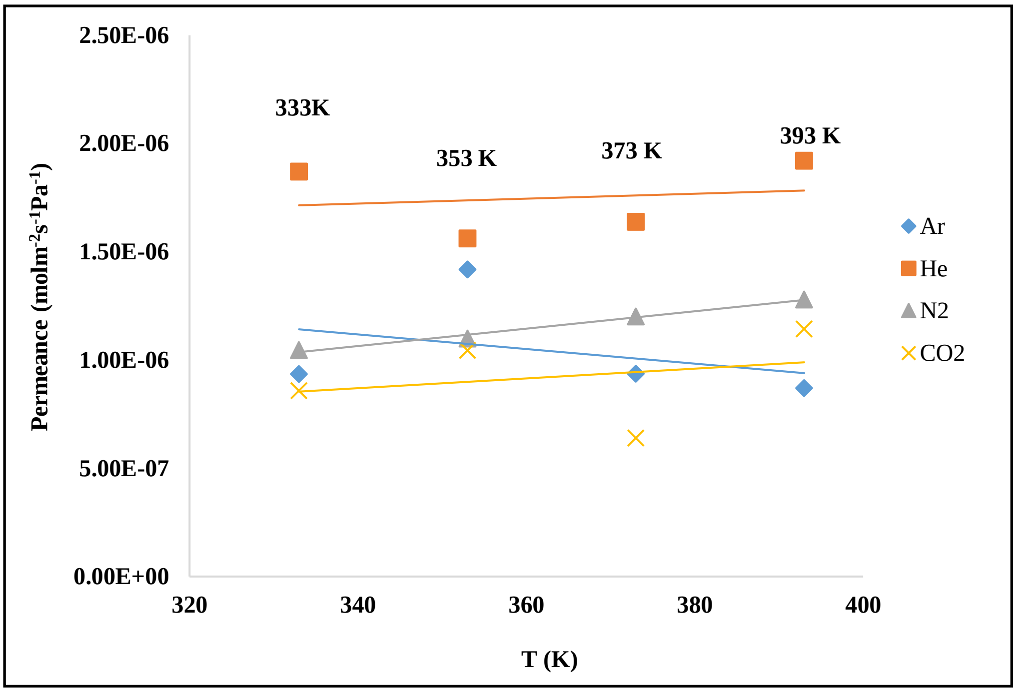

Figure 7.34: Effect of temperature on gas permeance between the temperature range of 333 – 393 K and at 0.30bar for the support.

Figure 7.35 shows the influence of tempearture on permeance helium, argon, carbon dioxide and nitrogen gases at the gauge feed pressure of 0.30 bar and the temperature range of 333 - 393 K for the support and membranes. From the result obtained in figure 7.35, it was found that the dip-coated silica membrane showed a good separation with CO_2 gas 0.30bar and at 333 – 393 K in contrast to other gases. At 353 K, the permeance for N_2 gas drop from 1.50E-6 to 1.30E-6molm^{-2}s^{-1}Pa^{-1} at 0.30 bar whereas He gas showed a slight increase in permeance at 353 K. From the results obtained, it was found that the permeance decraeses with respcet to temperature for the support membrane. It was suggested that the permeance seems to be dependent of the tempeaarture at a lower gauge pressure of 0.30 bar for the silica membrane [143]. It was also suggested that the permeation of the gases is greatly influenced by this temperature (353 K) as the gases permeate through the pores of the support membrane.

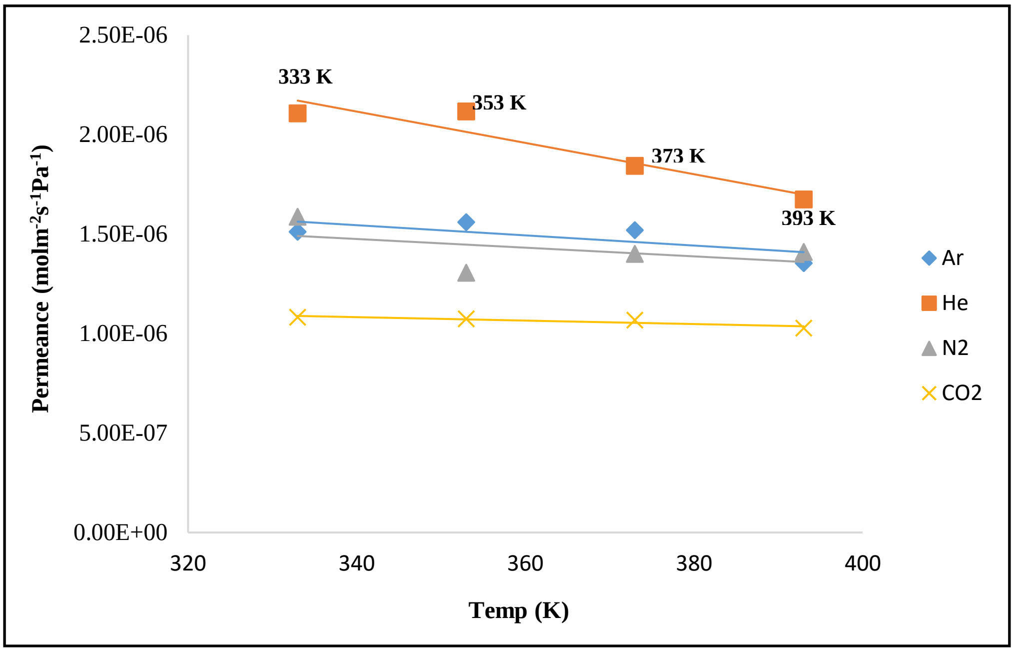

Figure 7.35: Effect of temperature on gas permeance between the temperature range of 333 – 393 K and at 0.30bar for the silica membrane.

7.1.9 Effect of Gas Permeance against Inverse Square root of Temperature

To further investigate the transport mechnaism in the membrane, the gas flux through each membrane was measured as the function of the tempearture. According to Mccool et al. [86], the Kundsen transport predicts a linear dependence of the permeance on the square root of the temperature, as the tempearture increases, the flux or permeance of a given gas molecule should decrease linearly with respect to the square root of the temperature. From the result obtained in figure 7.36, it can be seen that at the temperatures of 373K and 393 K for 0.10 bar and 0.30 bar respectively, Helium gas did not exhibit any dependance on temperature 333K, 393K and 373K, however helium gas exhibited a dependence on temperature with other range of gauge pressure for the support membrane. It was also observed that as the termperature increases the permeance of the He gas was found to decrease in a linear form with respect to the inverse square root of the tempearture [86]. It was suggested that the transport mechanism for He gas at 333K, 393K and 373K was based on the knudsen flow mechanim of gas transport whereas at 373K and 393K, He gas transport was controlled by another mechanim for the support. Further investigation was further carried out for the dip-coated silica membrane for comparison at the same gauge pressure and temperature.

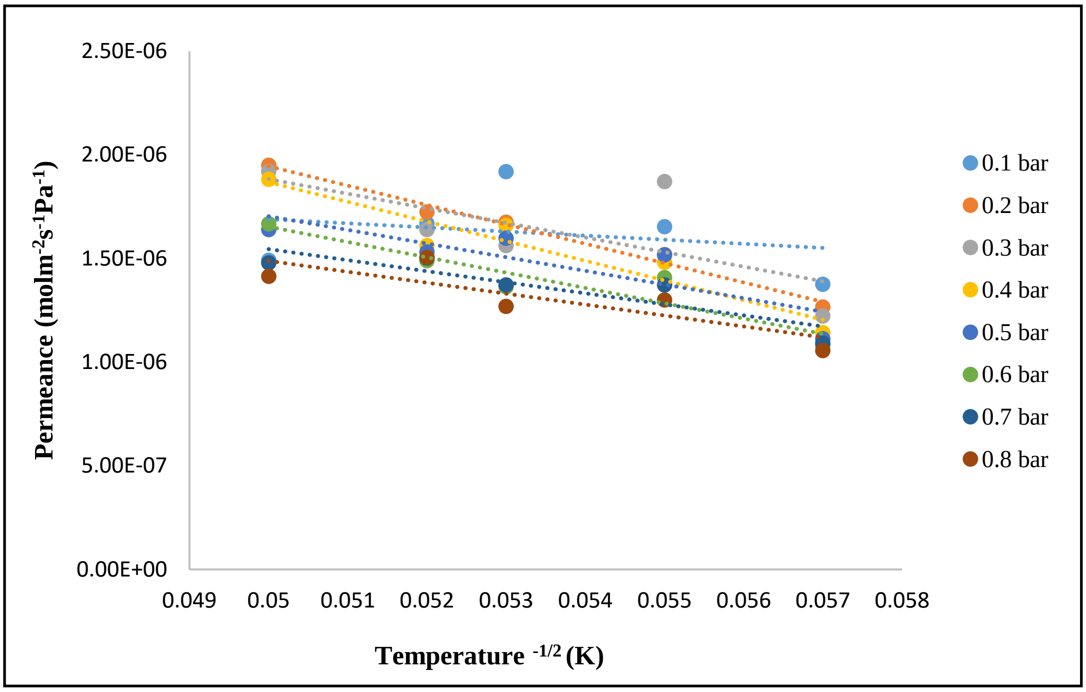

Figure 7.36: Effect of temperature on gas permeance between the temperature range of 333-413 K and at gauge pressure range of 0.10-0.80bar for the support membrane for Helium gas (support).

From the result obtained in figure 7.37, it was found that helium gas exhibited a linear dependence of permeance on the inverse square root of temperature at 298K between the gauge pressure range of 0.20-0.80 bar. It was was also observed that there was a deviation at 0.10 bar at 298K. Also, between the 333 -393K, the gas showed some deviation of permeance from the inverse square root of temperature in contrast to the result obtained for the support membrane. From the results obtained in figure 7.38, it was obsereved that between the gauge pressure range of 0.20 -0.80 bar, Helium gas demonstrates a linear dependence of permeance on the inverse square root of temperature [86]. Also, from figure 7.38, it was found that at 0.10 bar, helium gas did not show any dependence of permeance on the inverse square root of temperature at 333K, 353K, 373, 393 and 413 for the 2nd dip-coating of the silica membrane. It was suggested that there could be another mechanism of transport that was responsible for the gas flow at 0.10bar gauge pressure at the respective temperatures.

Also, the results for the 3rd dip-coated silica membrane was also compared. From the results obtained in figure 7.39, it can be seen that helium gas gas showed a deviation of permeance for the inverse square root of temperature at 333K. However, the non-dependence of permeance on the inverse square root temperature was very obvious for the tempeartures of 373 and 393 K between the gauge pressure range of 0.50-0.80 bar for the 3rd dip-coated membrane.

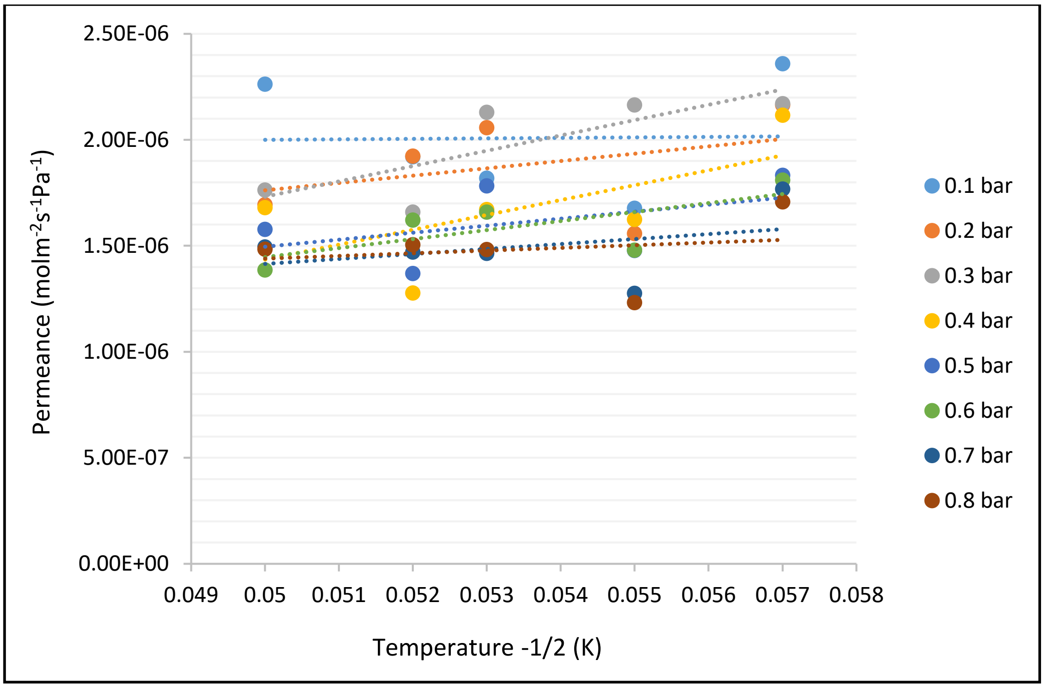

Figure 7.37: Effect of temperature on gas permeance between the temperature range of 333 -413 K and at gauge pressure range of 0.10-0.80bar for the silica coated membrane for Helium gas (1st dip).

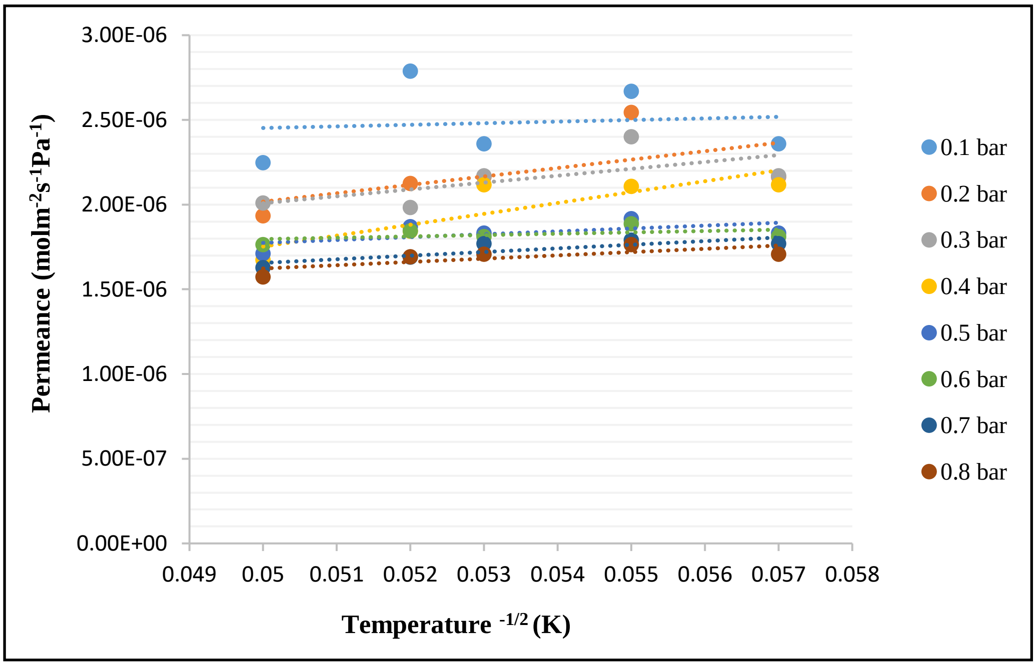

Figure 7.38: Effect of temperature on gas permeance between the temperature range of 333 -413 K and at gauge pressure range of 0.10-0.80bar for the silica coated membrane for Helium gas (2nd dip).

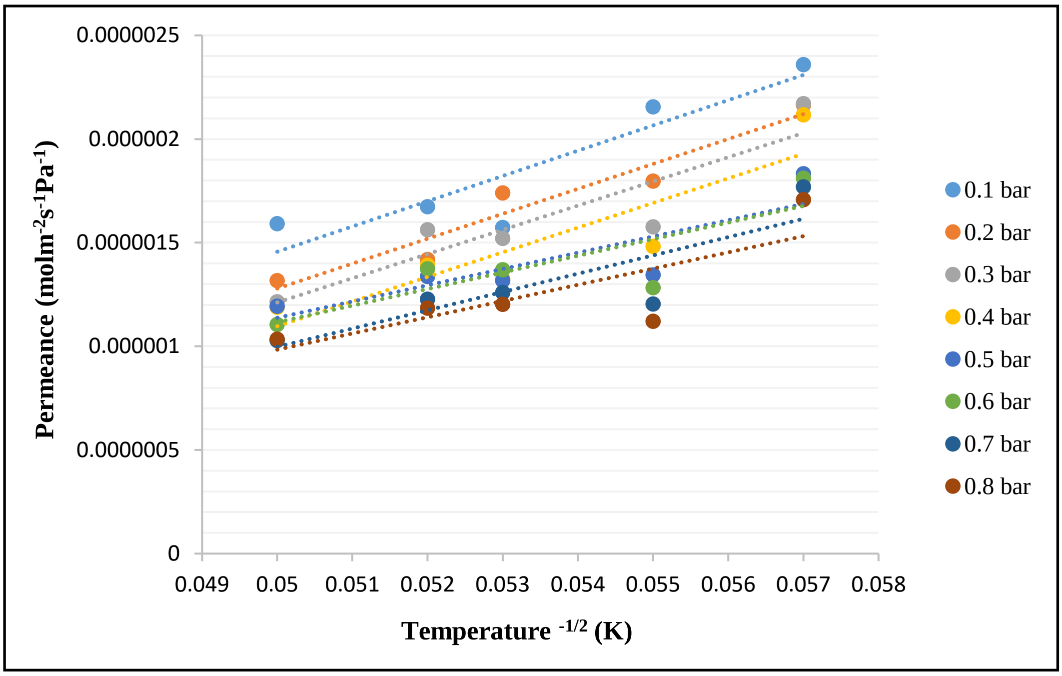

Figure 7.39: Effect of temperature on gas permeance between the temperature range of 333 -413 K and at gauge pressure range of 0.10-0.80bar for the silica coated membrane for Helium gas (3rd dip).

7.1.10 Determination of Activation energy from the temperature relationship with permeance

Figure 7.40 – 7.43 present the the effect tempearture against Permeance (In P) for Ar, He, CO_2 and N_2 gases between the temperature range of 333 - 413 K and at 0.30 bar. The temperature dependent graph was obtained using the arrehius equation (equation 7.2) at the gauge feed pressure of 0.30 bar and the inverse of temperature range of 333 – 413 K for the silica coated membrane. From the temperature plot for the various gases, the activation energy for the transport of the gases were also calculated using equation 7.4 for comparion. Activation energy is the indicator of the barrier for the gases to permeate through the pores of the membrane and this implies that a lower value of the activation energy indicates a lower resistance for the gas transport through the membranes [145]. Table 7.14 depict the calculated activiation energy values for the support and the dip-coated membrane.

Table 7.14: Calculated Activation energy values of the gases with the support and the dip-coated membrane at 0.30 bar between the temperature ranges of 333 – 393 K.

Gases	**Support**	**1st dip**	**2nd dip**	**3rd dip**
He	-4.689 X 10-4	-6.651 X 10-8	-6.600 X 10^{-8}	-4.160 X 10-8
Ar	-2.876 X 10-4	1.660 X 10-7	-2.490 X 10-8	4.990 X 10-9
N_2	0.116 X 10-4	-8.314 X 10-8	-1.660 X 10-8	-3.330 X 10-8
CO_2	-1.097x10-4	-2.490 X 10-8	-7.480 X 10-9	-2.48 X 10-8

From the result obtained and tabulated in table 7.14, it can be seen that Ar, He, CO_2 and N_2 gases exhibited a negative values of activation energy. Also, from the result obtained in figure 7.40 -7.43, it was observed that the calculated activation energy for the four gases with each dip-coated membrane were found to be different based on their adsorption capacities [97]. However, there was a positive activation energy value for N_2 gas, suggesting that this may be due to the effect of the heat of adsorption. It was also found that He ($R^2 = 0.9654$) and Ar ($R^2 = 0.9388$) gases recorded a good linear regession fits suggesting that the gas transport occurred due to Knudsen diffusion in constrast to CO_2 (0.9307) and N_2 (0.9106) gases. From the result obtained in figure 3.58 (Ar gas) and 3.60 (N_2 gas), it was found that the temperature dependence on permeation behaviour with their respective correlation values up to 0.99 for the gases. However, it was observed that N_2 and CO_2 gases showed a bit of deviation at 353 K. The calculated activiation energy for the gases was in good agreement with that reported in the literature by Lee et al. [97].

The activation energy of the gases were calculated using the following equation [97]:

$$Q_i = Q_O \exp\left(\frac{-E_a}{RT}\right) \ldots\ldots\ldots\ldots\ldots\ldots\ldots\ldots\ldots\ldots\ldots\ldots (7.2)$$

Where Q_i = permeance (mol $m^{-2}s^{-1}Pa^{-1}$), Q_O = Arrhenius-type pre–exponential constant (m^2s^{-1}), T= temperature (K), Ea = activation energy (J mol^{-1}) of surface diffusion or heat of adsorption and R= gas molar constant (8.314621 J $mol^{-1}K^{-1}$).

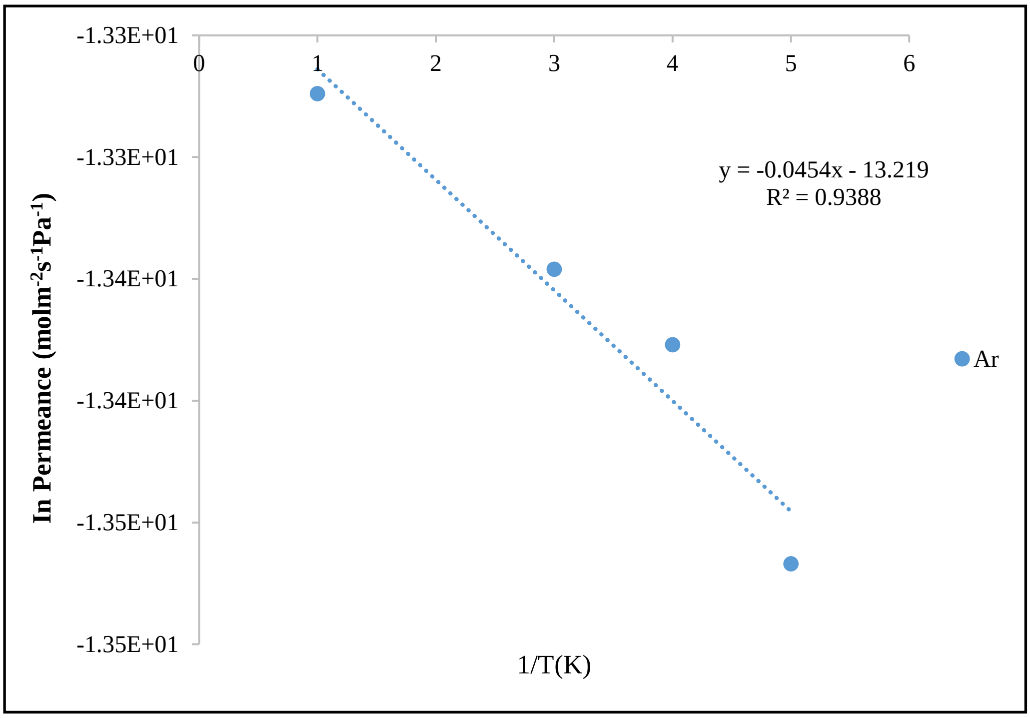

Figure 7.40: Effect of temperature on the gas permeance between the temperature range of 333 - 413 K and at 0.30 bar for Ar gas with the dip-coated membrane.

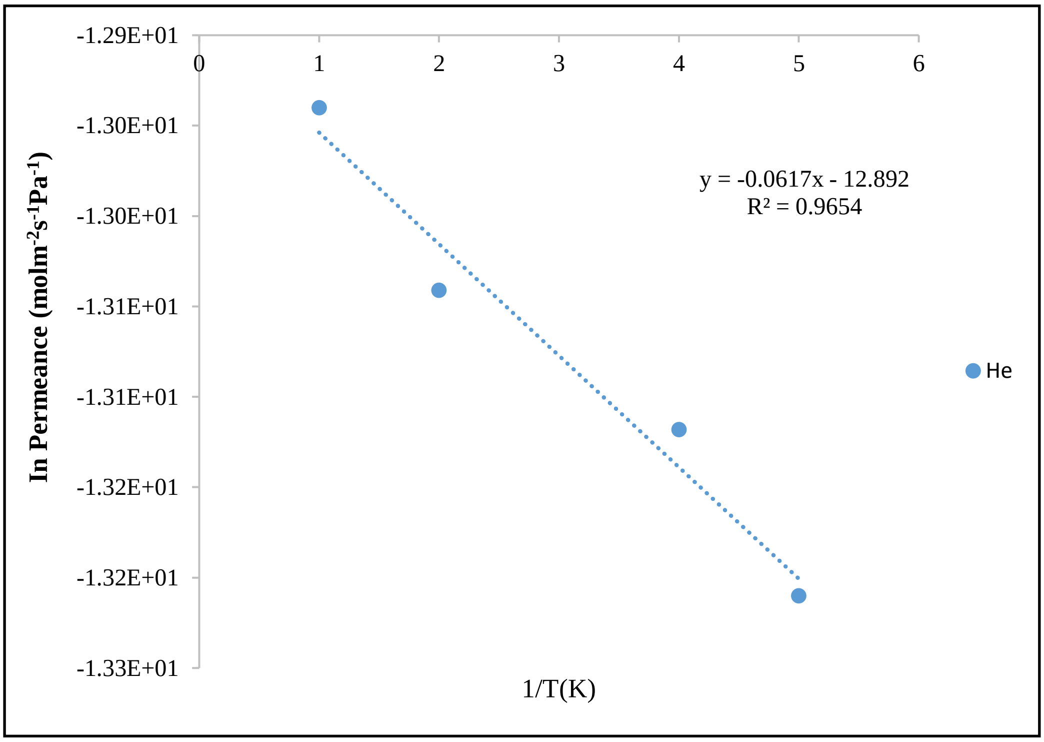

Figure 7.41: Effect of temperature on the gas permeance between the temperature range of 333 - 393 K and at 0.30 bar for He gas with the dip-coated membrane.

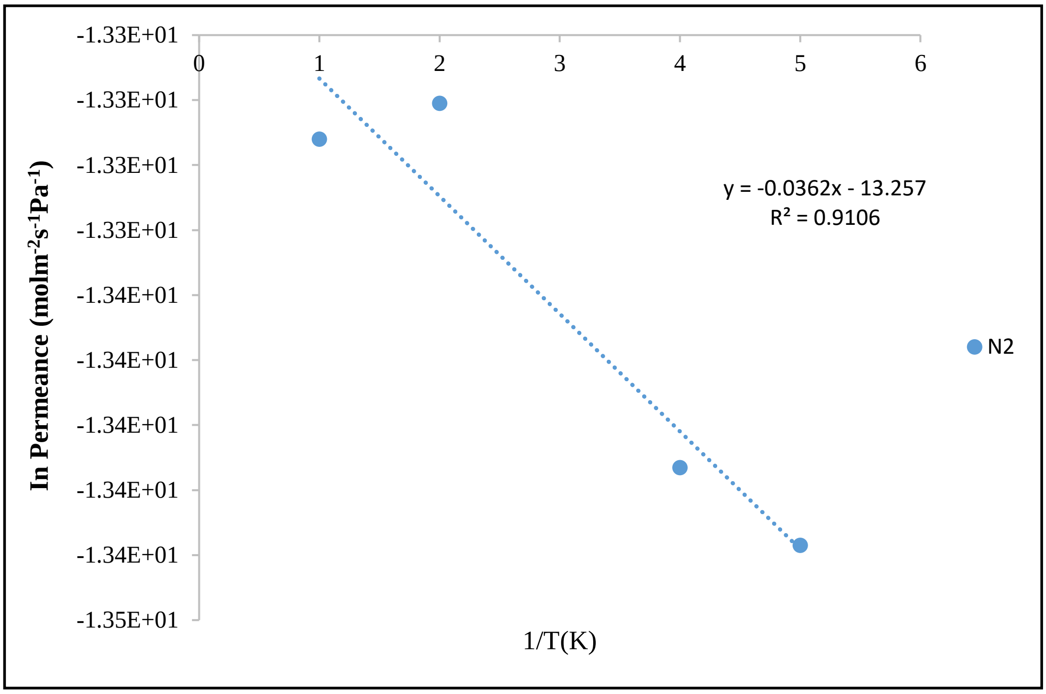

Figure 7.42: Effect of temperature on the gas permeance between the temperature range of 333 – 393 K and at 0.30 bar for N_2 gas with the dip-coated membrane.

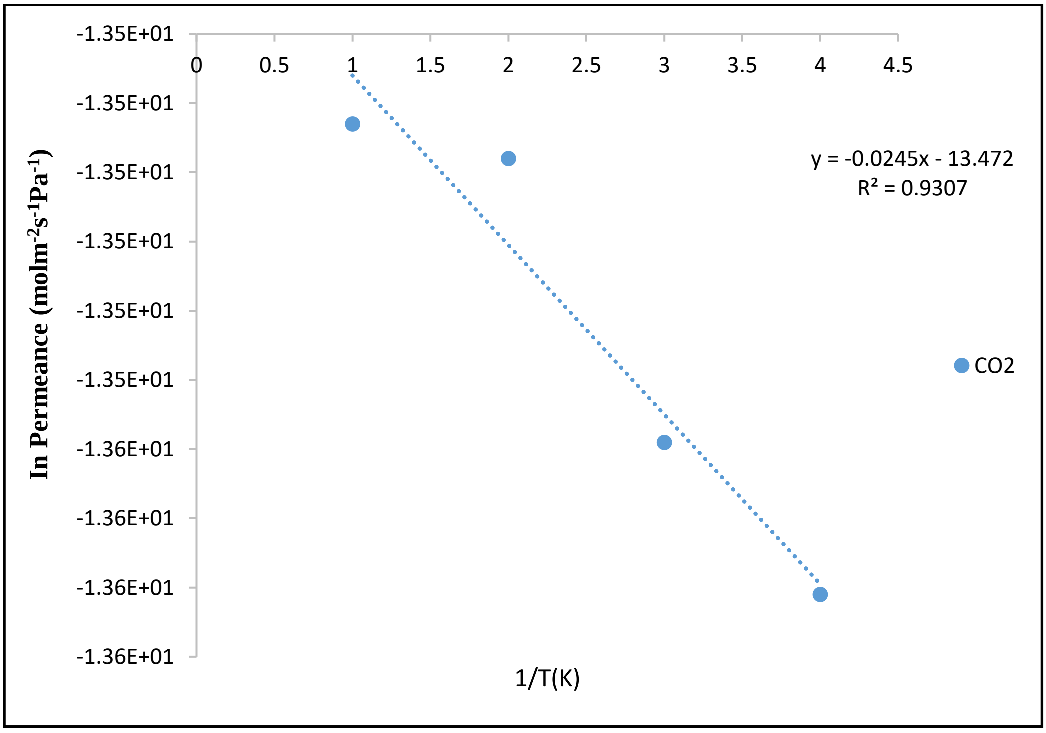

Figure 7.43: Effect of temperature on the gas permeance between the temperature range of 333 – 393 K and at 0.30 bar for CO_2 gas with the dip-coated membrane.

7.1.11 Determination of Membrane Permeability and Thickness

The permeability and thickness of the membrane were also calculated for the dip-coated membrane as shown in table 7.15 and 7.16 respectively. The permeability of the membrane were also calculated by multiplying the thickness values with the permeance of the gases at 0.30 bar gauge pressure and 60 °C. From the result obtained in table 7.15, it can be seen that the permeability of the membrane after the second modification process showed increasing value. It was found that He gas recorded the permeability of 7.44E-08molmm^{-2}s^{-1}Pa^{-1} after the 2nd dip in contrast to other gases. It can be see that the membrane thickness increases with resepct to the dip-coating process. It can be seen that after the 1st dip-coating process, the layer of the coated membrane was found to be 0.031m and after the 2nd dip-coating the membrane thickness was found to 0.035m.

Table 7.15: Gas, Permeability for 1st, 2nd and 3rd dip-coated membranes at 0.30 bar and 60 °C.

	Permeability (molmm^{-2}s^{-1}Pa^{-1})		
	Number of dips		
Gas	**1st**	**2nd**	**3rd**
He	2.82E-08	7.44E-08	5.60E-08
Ar	3.38E-08	5.32E-08	3.40E-08
N_2	1.81E-08	5.11E-08	4.31E-08
CO_2	2.24E-08	4.24E-08	4.31E-08

Table 7.16: Calculated thickness for 1st, 2nd and 3rd dip-coated membranes at 0.30 bar and 60 °C.

Thickness (m)			
Number of dips	**1st**	**2nd**	**3rd**
Calculated values (m)	0.013	0.031	0.035

7.1.12 Determination of Mean free path and pore radius calculation

The membrane pore radius and the mean free path with the gases were also investigated. Figure 7.44 depicts the permeability (molms^{-1}m^{-2}Pa^{-1}) plot of the gases against mean pressure (bar). A straight line equation was obtained from figure 7.44, from the results of the straight line equation, it was assumed that the Knudsen flow (+6E-08) seems to be valid indicating Knudsen mechanism of transport whereas the viscous flow (-5E-08) was very low or approximately zero.

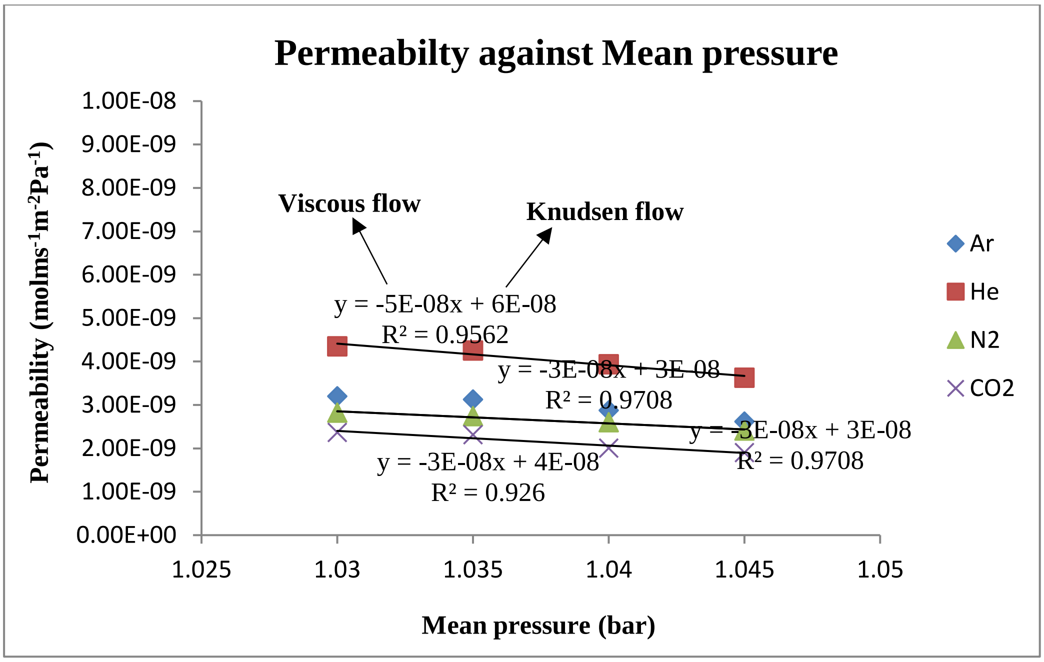

Figure 7.44: Gas Permeability (molms^{-1}m^{-2}Pa^{-1}) against mean pressure (bar).

The straight line equation from the graph (figure 3.63) is written as:

$F = A_o + B_o\, P_m$ ……………………………………………………………………………(7.3)

Where F= permeability (molmm^{-2}s^{-1}Pa^{-1}), A$_o$ = constant representing viscous flow, B$_o$ = constant representing Knudsen flow and Pm = mean pressure (bar) [101]. The membrane pore radius was calculated using the following equation:

$$r_p = \frac{16.Ao.\mu}{3.Bo}\sqrt{\frac{8RT}{\pi M}} \quad \ldots\ldots\ldots\ldots\ldots\ldots\ldots\ldots\ldots\ldots\ldots\ldots\ldots\ldots\ldots\ldots\ldots\ldots(7.4)$$

Where r_p = membrane pore radius (m), B$_o$ = constant representing Knudsen flow from the permeability graph, µ = gas viscosity (Pas^{-1}), M = molecular weight (g/mol), π = 3.142, A$_o$ = constant representing viscous flow from the permeability graph [146].

The mean free path of the membrane was calculated from the following equation:

$$K = \frac{D}{\lambda} \quad \ldots\ldots\ldots\ldots\ldots\ldots\ldots\ldots\ldots\ldots\ldots\ldots\ldots\ldots\ldots\ldots\ldots\ldots\ldots\ldots(7.5)$$

Where K = Knudsen number, D = pore diameter (m) and λ = mean free path (m).

Table 7.17 depicts the gases, calculated membrane pore radius (m) and mean free path (m) [96]. From the results obtained in table 7.17, it was found that the pore radius of the membrane with the four gases was found to be smaller than the mean free path, indicating Knudsen mechanism of transport [78,96,101]. From table 7.17, the results showed that the membrane pore radius with the gases was less than 10nm indicating a free-defect membrane and Knudsen flow as the dominant mechanism of transport [101].

Table 7.17: Calculated values of the membrane pore radius and the mean free path of the four carrier gases with the membrane.

Gas Molecule	Mean free path (λ)m	Pore radius (m)
Ar	3.15 E-04	4.72 E-12
He	3.63 E-04	1.09 E-11
N_2	2.96 E-04	4.45 E-12
CO_2	1.11 E-04	2.22E-12

7.1.13 Effect of CO_2 selectivity over He, N_2 and Ar at different Temperatures

Figures 7.45 - 7.48 shows a plot of the permselectivity of CO_2 over Ar, He, and N_2 for the support and dip-coated silica membrane at the at the gauge pressure range of 0.10 – 1.00 bar at 298 K – 393 K. For the purpose of comparison, Table 7.18 – 7.20 presents a summary of the theoretical selectivity values (ideal Knudsen and theoretical selectivity) and the experimental selectivity values of He, Ar, N_2 and CO_2 gases that were used for the analysis. From the result obtained in figures 7.45, it was found that although the experimental permselectivity value for CO_2/Ar gas exhibited a lower value than the theoretical selectivity at 298K (0.747), 333K (0.918), 353K (0.736) and 373K (0.683), however CO_2/Ar gas showed an increasing value of experimental selectivity at 393K (1.313).

Generally, it was found that the experimental permselectivity values of the CO_2/He and CO_2/N_2 gases with the membrane are greater than the theoretical ideal Knudsen selectivity values as also describe in Table 7.18 except for experimental selectivity of CO_2/N_2 gas at 373K (0.533), which indicate clearly that the support membranes used for the permeation test with the carrier gases are of high quality and exhibited a good separation with the carrier gases which was in accordance with Knudsen flow mechanism. Experimental error bars with 5% error were determined on the graph to further investigate the accuracy of the result. It can be seen that the statistical error bars for the gases showed a good significant value of the experimental data in figure 7.46 – 7.48 respectively.

Table 7.18: Calculated experimental and theoretical selectivity values of the different gas over CO_2 at 0.30 bar and between the temperature range of 298-393K for the support membrane.

Theoretical selectivity		**Experimental Permselectivity**					
At 0.30 bar		**Permeance ratio of CO_2/gases**	**298K**	**333K**	**353K**	**373K**	**393K**
$\alpha_k He/CO_2$	0.30	CO_2/He	0.696	0.459	0.669	0.391	0.595
$\alpha_k Ar/CO_2$	0.95	CO_2/Ar	0.747	0.918	0.736	0.683	1.313
$\alpha_k N_2/CO_2$	0.79	CO_2/N_2	0.869	0.821	1.052	0.533	0.894

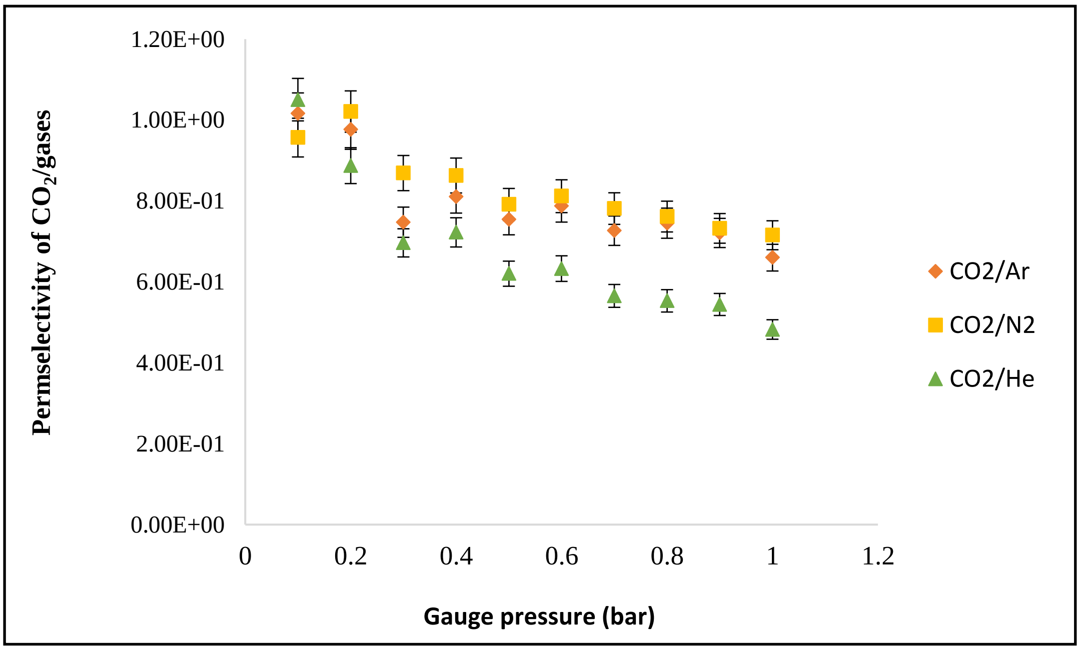

Figure 7.45: Permselectivity of CO_2/gases for support membrane at 353 K.

Similarly, the permselectivity of the gases were also compared with the theoretical ideal selectivity for the silica membrane at different dip-coating. Figure 7.46 - 7.48 depicts the permselectivity of CO_2 over

Ar, He, and N_2 for the 1st, 2nd and 3rd dip-coated silica membrane at the at the gauge pressure range of 0.10 – 1.00 bar at 298 K – 353 K. From figures 7.46 – 7.48, the experimental permselectivity of CO_2 over N_2, Ar and He showed a decrease with respect to the gauge pressure. However, it was found from figure 7.46 and 7.47 that the experimental permselectivity values for CO_2/He and CO_2/N_2 were far above the Knudsen theoretical selectivity after the 1st and 2nd dip-coating as shown in table 7.19 and 7.20. However, the experimental permselectivity value of CO_2/Ar was found to exhibit a drastic decrease as shown in table 7.19 and 7.20 at 298K – 393K after the 1st and 2nd dip-coating. Apparently, from figure 7.48, it can be seen that although experimental permselectivity of CO_2/He and CO_2/N_2 gases were found to be higher than that of the Knudsen theoretical selectivity values at all temperatures. The permselectivity of CO_2/Ar was also found to be higher except at 298K (0.572) and 373K (0.872) after the 3rd dip-coating as shown in table 7.21. It was suggested that after the 1st, 2nd and 3rd dip-coating, the silica membrane demonstrates a good separation with He and N_2 gases indicating Knudsen flow mechanism.

Table 7.19: Calculated experimental and theoretical selectivity values of the different gas over CO_2 at 0.30 bar and between the temperature ranges of 298-393K for 1st dip-coated membrane.

Theoretical selectivity		**Experimental Permselectivity**					
At 0.30 bar		**Permeance ratio of CO_2/gases**	**298K**	**333K**	**353K**	**373K**	**393K**
$\alpha_k He/CO_2$	0.30	CO_2/He	0.499	1.632	0.800	1.216	1.127
$\alpha_k Ar/CO_2$	0.95	CO_2/Ar	0.572	0.651	0.664	0.667	0.747
$\alpha_k N_2/CO_2$	0.79	CO_2/N_2	0.897	2.190	1.233	1.037	1.746

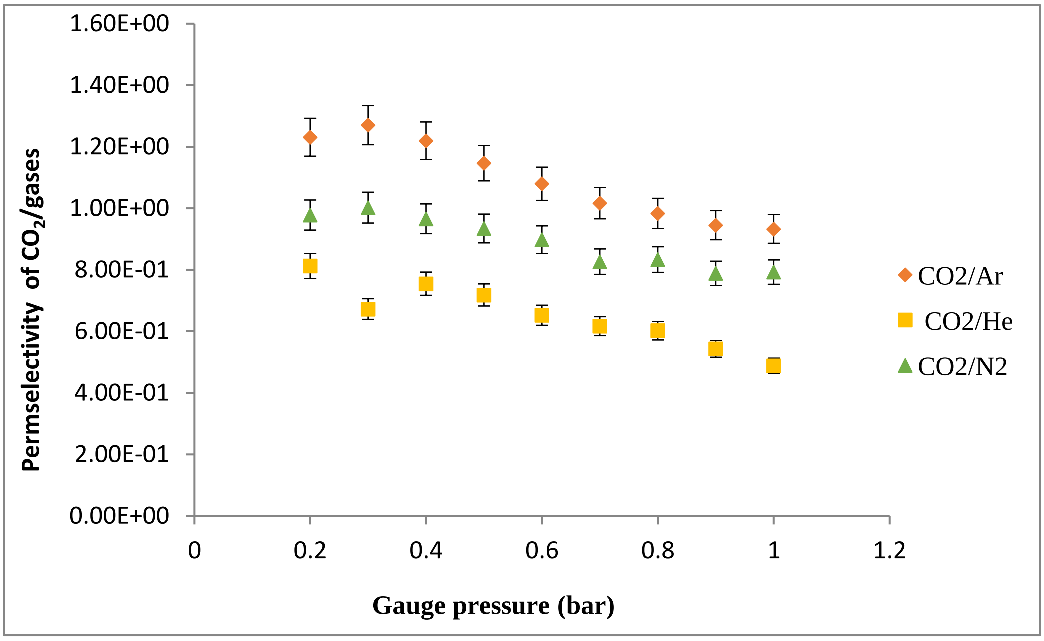

Figure 7.46: Permselectivity of CO_2/gases for the 1st dip-coated membrane at 333 K.

Table 7.20: Calculated experimental and theoretical selectivity values of the different gas over CO_2 at 0.30 bar and between the temperature range of 298-393K for 2nd dip-coated membrane

Theoretical selectivity		**Experimental Permselectivity**					
At 0.30 bar		**Permeance ratio of CO_2/gases**	**298K**	**333K**	**353K**	**373K**	**393K**
$\alpha_k He/CO_2$	0.30	CO_2/He	0.499	0.569	0.626	0.704	0.655
$\alpha_k Ar/CO_2$	0.95	CO_2/Ar	0.572	0.796	0.788	0.873	0.848
$\alpha_k N_2/CO_2$	0.79	CO_2/N_2	0.897	0.829	0.848	1.010	0.744

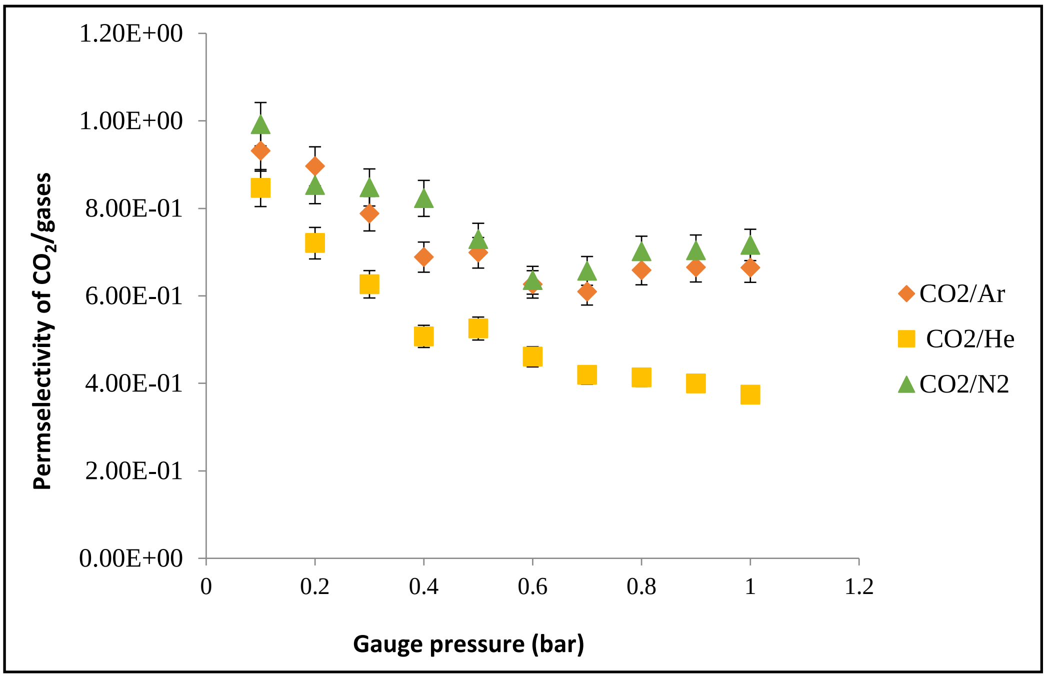

Figure 7.47: Permselectivity of CO_2/gases for 2nd dip-coated membrane at 353 K.

Table 7.21: Calculated experimental and theoretical selectivity values of the different gas over CO_2 at 0.30 bar and between the temperature range of 298-393K for 3rd dip-coated membrane

Theoretical selectivity		**Experimental Permselectivity**					
At 0.30 bar		**Permeance ratio of CO_2/gases**	**298K**	**333K**	**353K**	**373K**	**393K**
$\alpha_k He/CO_2$	0.30	CO_2/He	0.499	0.673	0.812	0.571	0.905
$\alpha_k Ar/CO_2$	0.95	CO_2/Ar	0.572	1.270	1.258	0.872	1.103
$\alpha_k N_2/CO_2$	0.79	CO_2/N_2	0.897	1.002	1.002	0.752	1.079

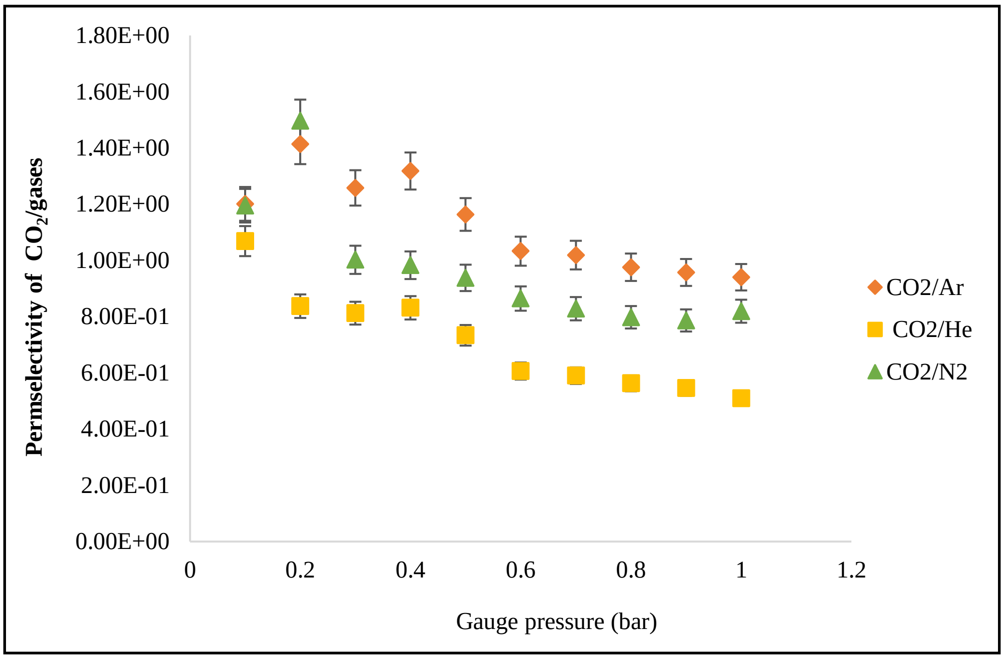

Figure 7.48: Permselectivity of CO_2/gases for the 3rd dip-coated membrane at 353 K.

7.2 Mathematical Modelling

In order to validate the experimental results that were obtained and to further predict results for the parameter that could not be operated under experimental conditions, a mathematical model was developed. Minitab 2016 mathematical model was used to design the graphical plots for the experimental results. The mathematical model was designed to describe different plots including a ‘’scree plot model’’ which considers the gas permeance and flow rate through the support and silica membranes at room and high temperatures with respect of gauge pressure to see the suitability of the gases and compare with the experimental results. The model also put into consideration the Eigen analysis of the correlation matrix i.e how many principal components (PCs) are necessary to describe the experimental data. This model also considers the trend of the gas permeation based on their molecular weight, a ‘’loading plot model’’ which is used to determine the experimental flow rate and feed gauge pressure based on the trend of the gas flow. The loading plot model also explained what proportion of each of the real variable (gases) goes to make up each of the new PCs, and lastly a ‘’score plot model’’ which takes into consideration the permeance, feed gauge pressure and flow rate. This model also describes the grouping of each sample number.

This model also uses the principle components analysis (PCA) which allow the input of the permeance and flow rate variable needed to describe the data. It also gives information about how much variability is describe by each of the principle components. PCA is perform using statistical software of the Minitab 2016. The PCA output from the MiniTAB 2016 model is describe in the results section. This model also put into account different parameters such as temperature and gauge pressure. The model also uses the experimental data as the principal component analysis for the different variables (gases). The comparison of the permeance and flow rate experimental results with that of ‘’scree plot model’’, ‘’loading plot model’’ and ‘’score plot model’’ for the support and dip-coated silica membrane results at 298K and 333K are describe in section 7.2.1.1. Appendix O shows the details of data input from the model. The three models do not consider the different mechanisms of gas transport that is used to explain the permeation of the gas through the pore of the membrane and thus, will have a resulting effect on the accuracy of the generated results from the mathematical model. Due to the nature of the different plots from the model the validation of the experimental results was conducted based on the gas permeation operating parameters including temperature, gauge pressure, each dipping stage, flow rates and permeance. Other parameters are membrane surface area and thickness. Hence the permeance and flow rate values input in the model were the same as that of the experimental values. The plots of the resultant mathematical model were compared with the experimental results. The following parameters for the gas permeation were used to represent the model parameters for achieving the different plots for the mathematical model and were also used for the result interpretation. Table 7.22 shows the model and gas permeation parameters.

Table 7.22: Mathematical Model and Gas Permeation Parameters

Model parameters	**Permeation Parameters**
Sample numbers	-Different gauge pressure (0.1,0.2, 0.3, 0.4, 0.5,0.6,0.7,0.8,0.9,1.0 bar)
PCs	-Experimental results for gases (permeance (molm^{-2}s^{-1}Pa^{-1})/flow rate(mols^{1})
Variables	- Gases (He, Ar, N_2 and CO_2)
Scores	-Calculated values from the experimental results
Eigenvalues	-Calculated values from the experimental results for the respective gas

7.2.1 Comparison of Experimental and Mathematical model results.

7.2.1.1 Permeance vs Gauge Pressure Mathematical Model results for Support and Silica Membrane.

Figure 7.49a-c shows the mathematical model plots of permeance with respect to gauge pressure for the support membrane at 298K and that of dip-coated silica membrane at 333K in figure 7.50a-c. Table 7.23 depict the Eigen analysis for the correlation matrix and the principal components analysis for the four variables (He, Ar, N_2 and CO_2) from the Minitab software. The thickness layer and the effective area for the support and dip-coated membranes were estimated and used for the model. From figure 7.49a and b, it can be see that helium gas permeate faster through the porous ceramic support for both experimental (figure 7.9) and model results. The experimental results fitted well into the model as helium gas with a lower molecular weight demonstrate the highest permeation rate for the support at 298K, although there were some alteration in the trend for CO_2, N_2 and Ar gases in the model results. The model also confirmed the suitability of helium as the carrier gas when coupled with GC-MS (gas chromatograph-mass spectroscopy) for the analysis of esterification product in chapter 4. However, it was also found that the eigenvalue obtained from the principal component analysis (permeance of the gases) decreases with respect to gauge pressure as seen in figure 7.49a for the respective gases. Figure 7.49b shows the loading plot for the variables (gases). This plot explains the contribution of each variables to the first two components (He and Ar with the highest permeation rate).

It can be seen that He, CO_2 and Ar gases demonstrate a positive loading as the gauge pressure increases except for N_2 gas with negative loading suggesting that this could be due to the non-metallic character of N_2 as the non-metallic character of group V elements decreases down then group in the periodic table. The dissimilarity in the trend of the carrier gas permeation for the experimental and mathematical model were suggested to be due to the fact the model does not account for the different mechanisms of gas transport and also due to some form of systematic experimental errors. Figure 7.49c shows the score plot model which explain the grouping of the sample number (gauge pressure). It was found that the samples number were found to be in three different groups with respect to the principal components. It was found that the gauge pressure of 0.1bar, gauge pressure 0.2,0.3,0.4,0.5 bar and gauge pressure 0.6, 0.7,0.8,0.9,1.0 bar appear to be in different groups. The three groups also fall on the positive axis indicating that the gauge pressure increase with decrease in permeance (PCs) for the support at 298K.

Table 7.23 shows the Eigen analysis for the correlation matrix and the principal components analysis for the four variables (He, Ar, N_2 and CO_2). In table 7.23, the first line of the Eigenvalue shows how the variance is distributed between the four PCs with PC1 (He) having a variance of 3.8180, PC2 (Ar) = 0.1166, PC3 (CO_2) = 0.0618 and PC4 (N_2) = 0.0036. It can be seen that PC1 has the highest variance followed by PC2, PC3 and PC4. The second line of the table describe the proportion of the data variation by each PCs whereas the third line shows the cumulative proportion. This suggest that both PC1 and PC2 account for 98.4% of the variable for the data, which further confirm that accuracy of the model. The bottom half of the table depict the coefficients of the principle components. This were also compared with the silica coated membrane.

Table 7.23: Principal Component Analysis: He, Ar, N_2, CO_2 Permeance vs gauge pressure for support.

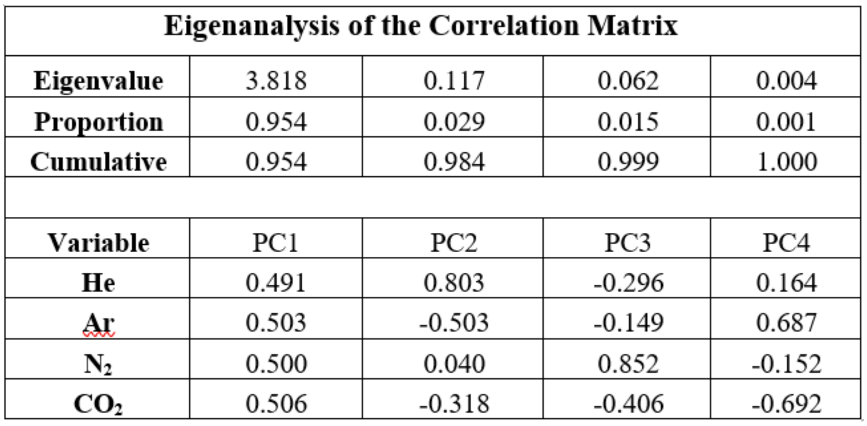

Eigenanalysis of the Correlation Matrix				
Eigenvalue	3.818	0.117	0.062	0.004
Proportion	0.954	0.029	0.015	0.001
Cumulative	0.954	0.984	0.999	1.000
Variable	PC1	PC2	PC3	PC4
He	0.491	0.803	-0.296	0.164
Ar	0.503	-0.503	-0.149	0.687
N_2	0.500	0.040	0.852	-0.152
CO_2	0.506	-0.318	-0.406	-0.692

Scree Plot of He, ..., CO2

Score Plot of He, ..., CO2

Loading Plot of He, ..., CO2

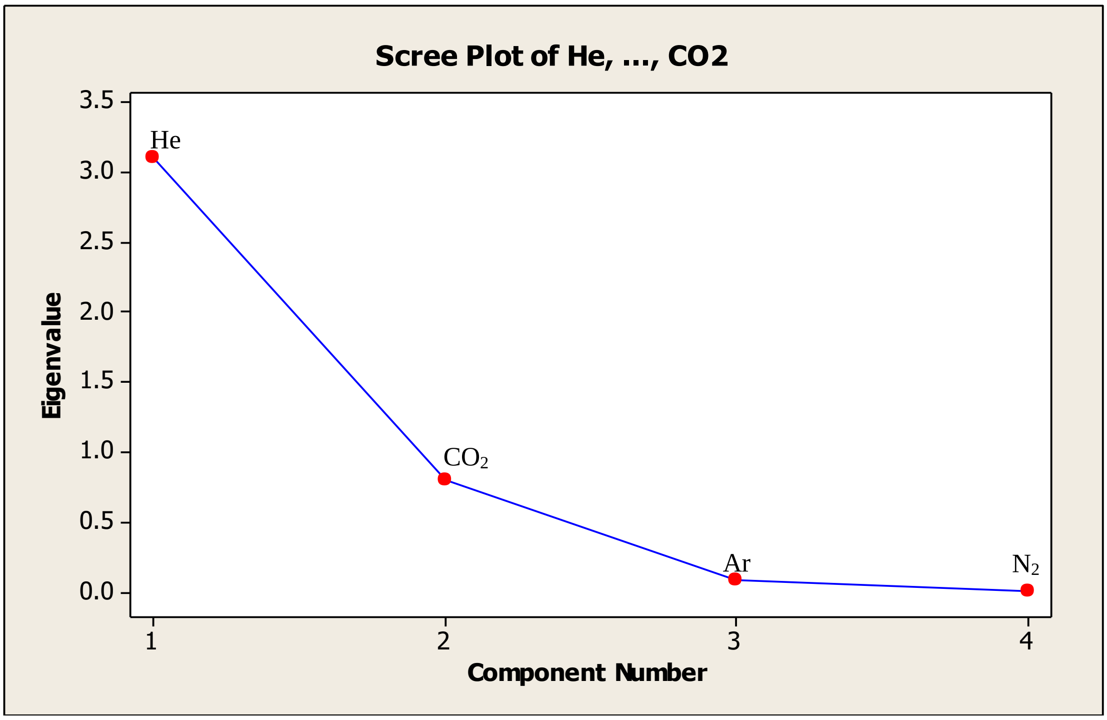

Figure 7.49a: Plot of eigenvalue of gas permeance against gauge pressure for support at 298K.

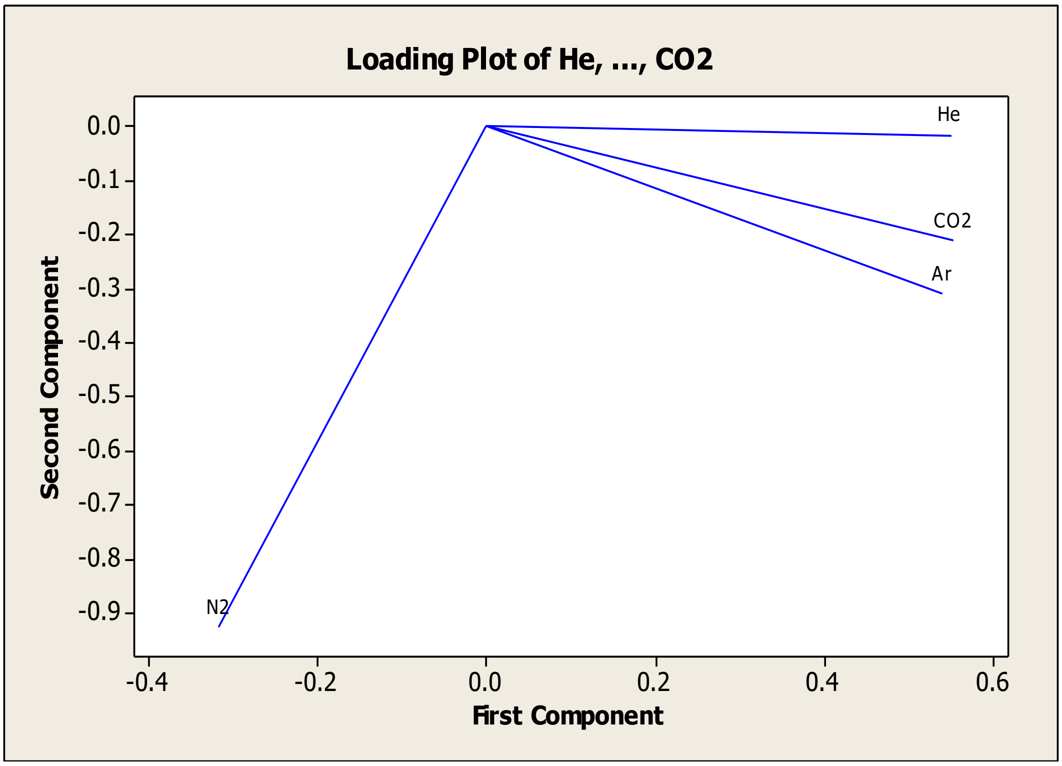

Figure 7.49b: Plot of gas permeance values against gauge pressure for support at 298K.

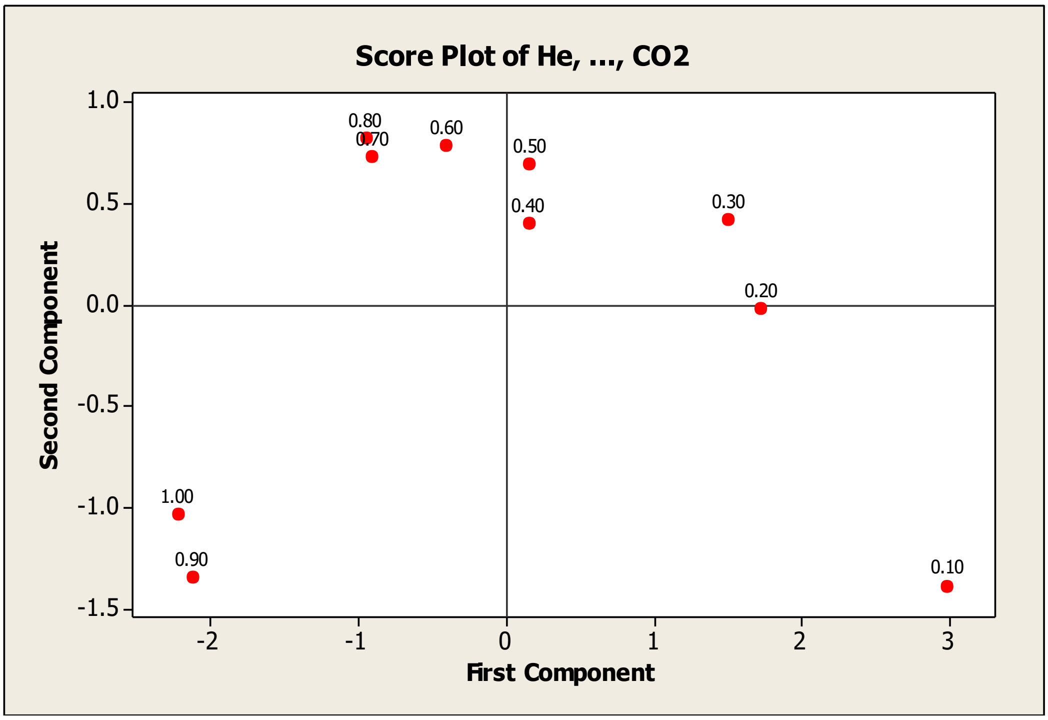

Figure 7.49c: Plot of gas permeance against gauge pressure for support at 298K.

Figure 7.50a-c depict the scree, loading and score plots models for graph of the permeance vs gauge pressure for 1st dip-coated silica membrane. Table 7.24 depict the Eigen analysis of the correlation matrix from the Minitab software which can be seen on the scree plot model for the different variables (gases) with respect to their Eigen values. From figure 7.50a, it can be seen that the model exhibited a similar trend to that of the experimental results (figure 7.10) for the 1st dip-coated silica coated membrane after the at 353K although there was a bit of alteration between Ar and He gases. It can be seen from figure 7.50a that helium and argon exhibited the highest permeation rate followed by CO_2 and N_2 at 353K which was in accordance with the experimental results obtained (figure 7.10), confirming these gases (Helium and Argon) as the suitable carrier gases. The trend of the gas permeation in the model for the silica coated membrane was attributed to the coated substrate on the surface of the membrane as the gases penetrate through the porous media.

It was also suggested that it could be due to systematic error as the model uses the calculated experimental permeance results and only takes into account the trend of the gas permeation without considering the different gas transport mechanisms. Figure 7.50b explain how each of the real variables (different gases) relates to the PCs (permeance results for the gases with respect to gauge pressure). It can be seen from figure 7.50b that He, Ar, N_2 and CO_2 gases were all identified with positive loading with respect to PCs and gauge pressure indicating that the gas permeance decreases with respect to gauge pressure as also as shown on the scree plot. Figure 7.50c shows the score plot model for the grouping of the sample number (gauge pressure) with respect to the PCs (permeance values). It can be seen from figure 7.50 that sample number (gauge pressure) were spited into different group including: 0.1,0.2,0.3,0.4bar, gauge pressure 0.5,0.6,0.7bar and gauge pressure 0.9, 1.0bar appear to be different groups indicating the increasing order of the gauge pressure with respect to the permeance. The similarity of the model with the experimental results for both the support at 298K and the 1st dip-coated silica coated membranes at 353K demonstrates the accuracy of the mathematical model and also validates the results obtained from the experimental analysis. A similar trend was observed for the permeance vs gauge pressure results of the model for 2nd and 3rd dip-coated membrane at 333 and 413 K respectively which also shows a similar trend for the experimental results in figures 7.11 and 7.12 respectively.

Table 7.24 shows the Eigen analysis for the correlation matrix and the principal components analysis for the four variable (He, Ar, N_2 and CO_2). In table 7.24, the first line of the Eigenvalue shows how the variance is distributed between the four PCs with PC1 (He) having a variance of 2.518, PC2 (Ar) = 0.937, PC3 (N_2) = 0.288 and PC4 (CO_2) = 0.257. It can be seen that PC1 has the highest eigenvalue followed by PC2, PC3 and PC4. Table 7.24 also explain that about 86.4% of the variability is demonstrated by the first 2PCs which could indicate the reduction in the pore size of the membrane after the silica modification process in contrast to 98.4% for the support. This also indicate that the silica coating plays a major part in the gas flow. The second line of the table describe the proportion of the variable describe by each PCs whereas the third line shows the cumulative proportion. The bottom half of the table depict the coefficients of the principle components (permeance results for the gases).

Table 7.24: Principal Component Analysis: He, Ar, N_2, CO_2 Permeance vs gauge pressure for silica membrane.

Eigen analysis of the Correlation Matrix				
Eigenvalue	2.518	0.937	0.288	0.257
Proportion	0.629	0.234	0.072	0.064
Cumulative	0.629	0.864	0.936	1.000
Variable	PC1	PC2	PC3	PC4
He	-0.527	0.381	0.718	-0.248
Ar	0.566	0.163	0.051	-0.806
N_2	0.539	-0.323	0.691	0.357
CO_2	0.333	0.851	-0.069	0.401

Scree Plot of He, ..., CO2

Score Plot of He, ..., CO2

Loading Plot of He, ..., CO2

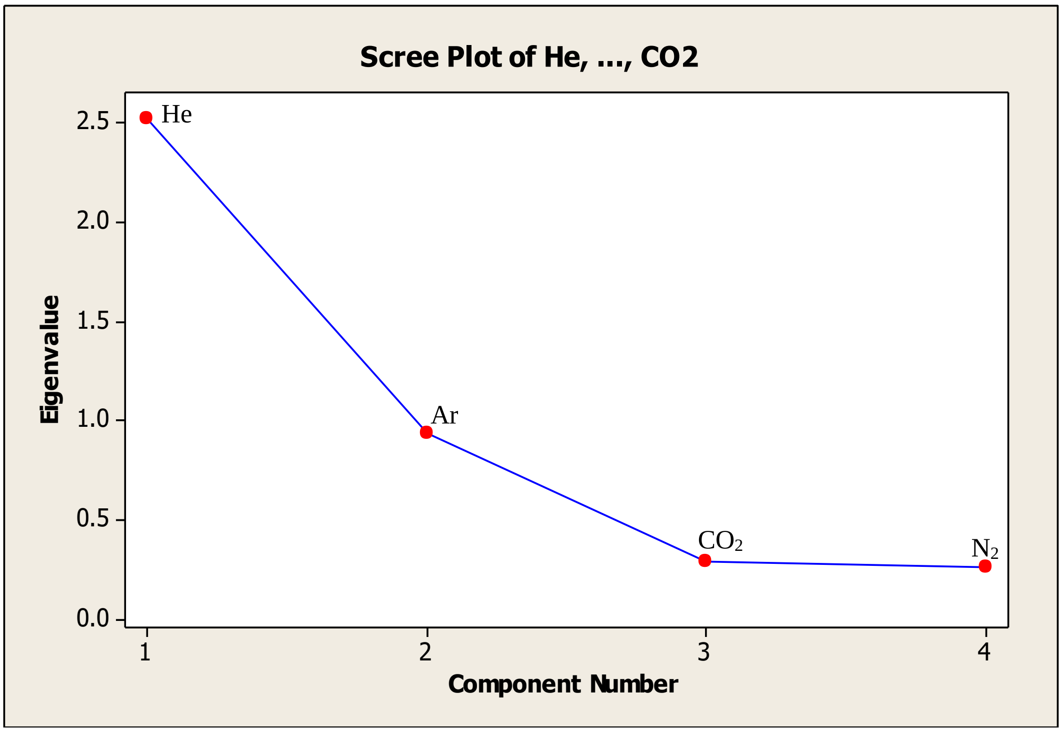

Figure 7.50a: Plot of eigenvalue of gas permeance against gauge pressure for 1st dip-coated at 353 K.

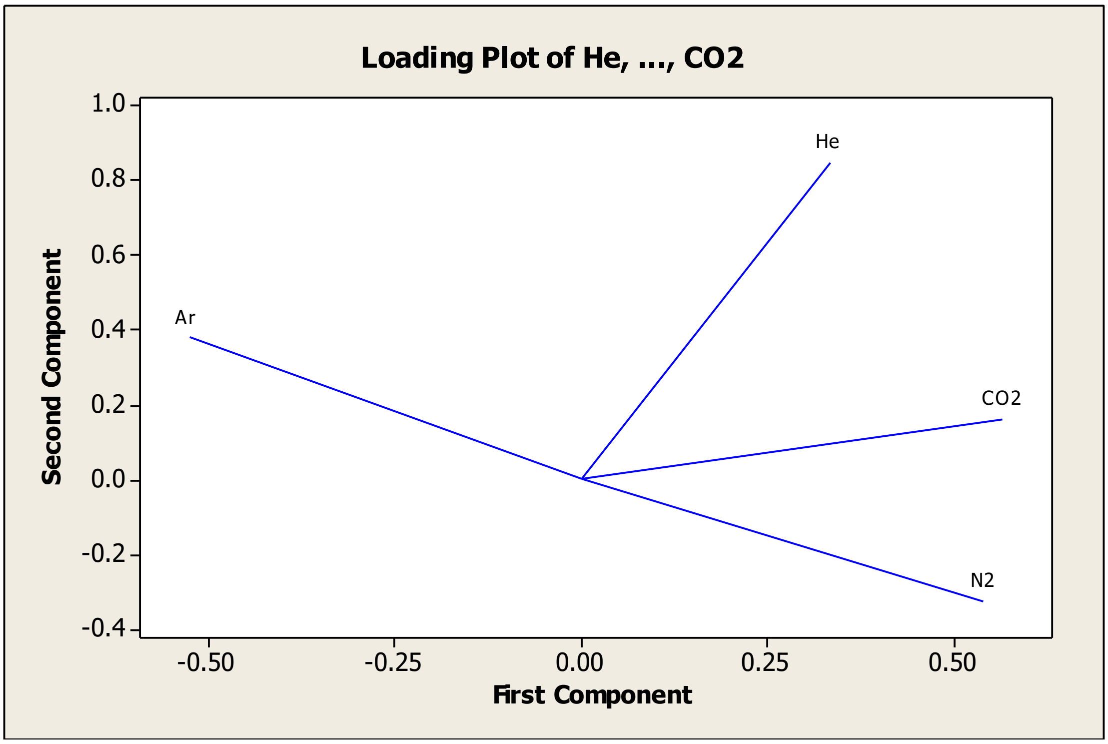

Figure 7.50b: Plot of gas permeance against gauge pressure for 1st dip-coated membrane at 353 K.

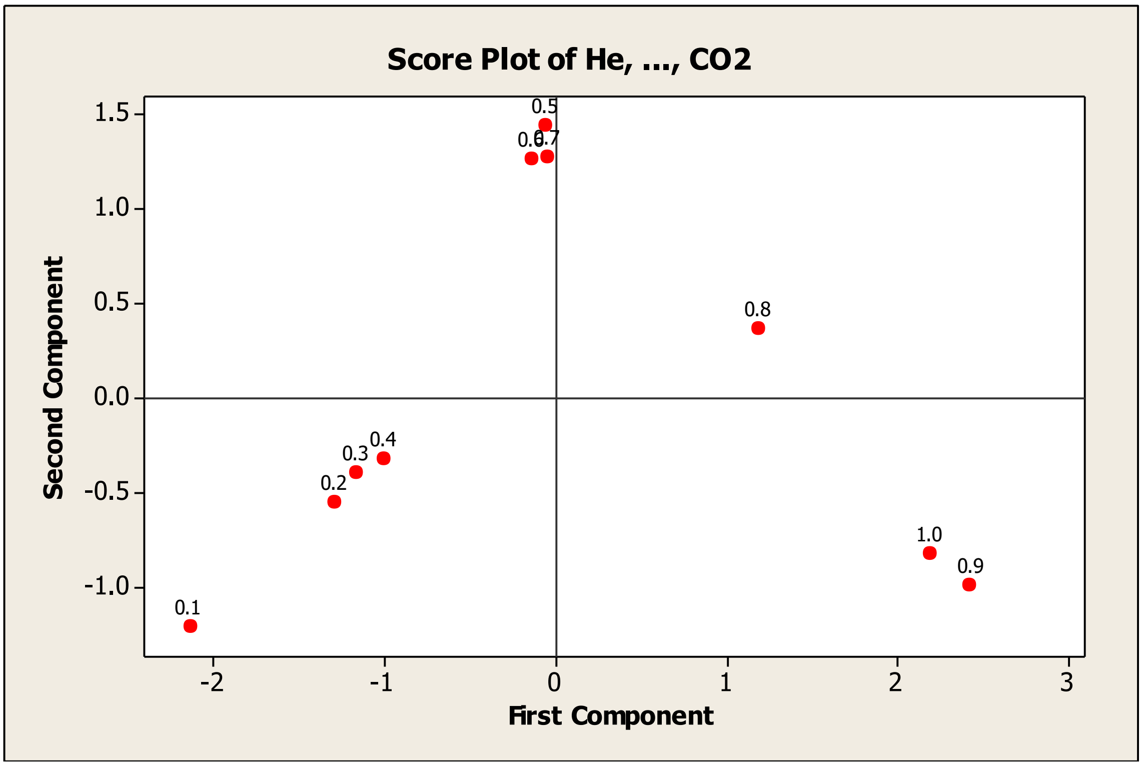

Figure 7.50c: Plot of gas permeance against gauge pressure for 1st dip-coated membrane at 353 K.

7.3 Esterification Reaction Results

7.3.1. Batch Process Esterification of Lactic Acid Feed Conversion

The results of the batch process esterification analysis were determined by comparing the chromatogram of the esterification reaction product with the commercial ethyl lactate solvent [147]. The results for this study are published in Okon et al. [118]. The important of using the commercial available ethyl lactate solvent as the reference solvent was to confirm if the ions that were identified to be the structure of ethyl lactate on the produced esterification product was in accordance with that of the commercial ethyl lactate. Figure 7.51 present the pictorial view of the produced batch process esterification product at the temperatures of 60, 80 and 100 °C. From figure 7.51, it was observed that there was a slight colour change (yellow) for the esterification product in the presence of amberlyst 36 at 60 °C. As the catalyst interact with lactic acid and ethanol when heated at each temperature, the effect of the concentrated reactant solvent with the catalyst result in the colour change of the resin catalysts. Esterification reaction product catalysed by amberlyst 16, 15 and dowex 50W8x at 60 °C at the same temperature exhibited a clear milky colour. Subsequently, at 80 and 100 °C, the esterification product exhibited milky colour which further suggest the fact that amberlyst 36 catalyst is very sensitive when heated at 60 °C. Although the esterification product catalysed by amberlyst 36 exhibited a significant colour change at 60 °C, however, it was observed that the colour change did not affect the chromatogram result obtained from the GC-MS as this catalyst seem to produce a better result when compared to esterification product catalysed by amberlyst 15, 16 and 36 resin catalysts at 60 °C.

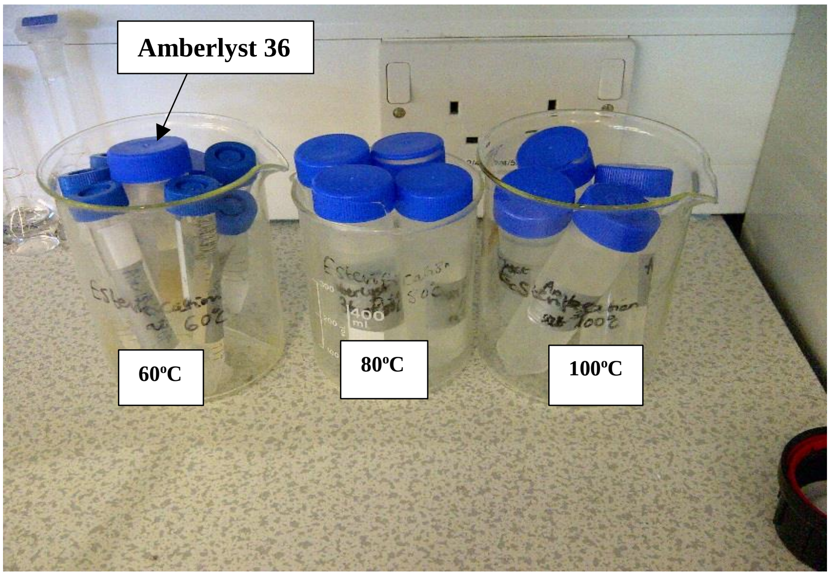

Figure 7.51: Produced esterification product obtained from batch process esterification reaction at 60, 80 and 100 °C.

Figure 7.52 presents NIST spectra the search result of ethyl lactate compound. From the NIST library search of compounds, mass spectra of the compound exhibited ion 45 which was identified to be the structure of ethyl lactate solvent [148].

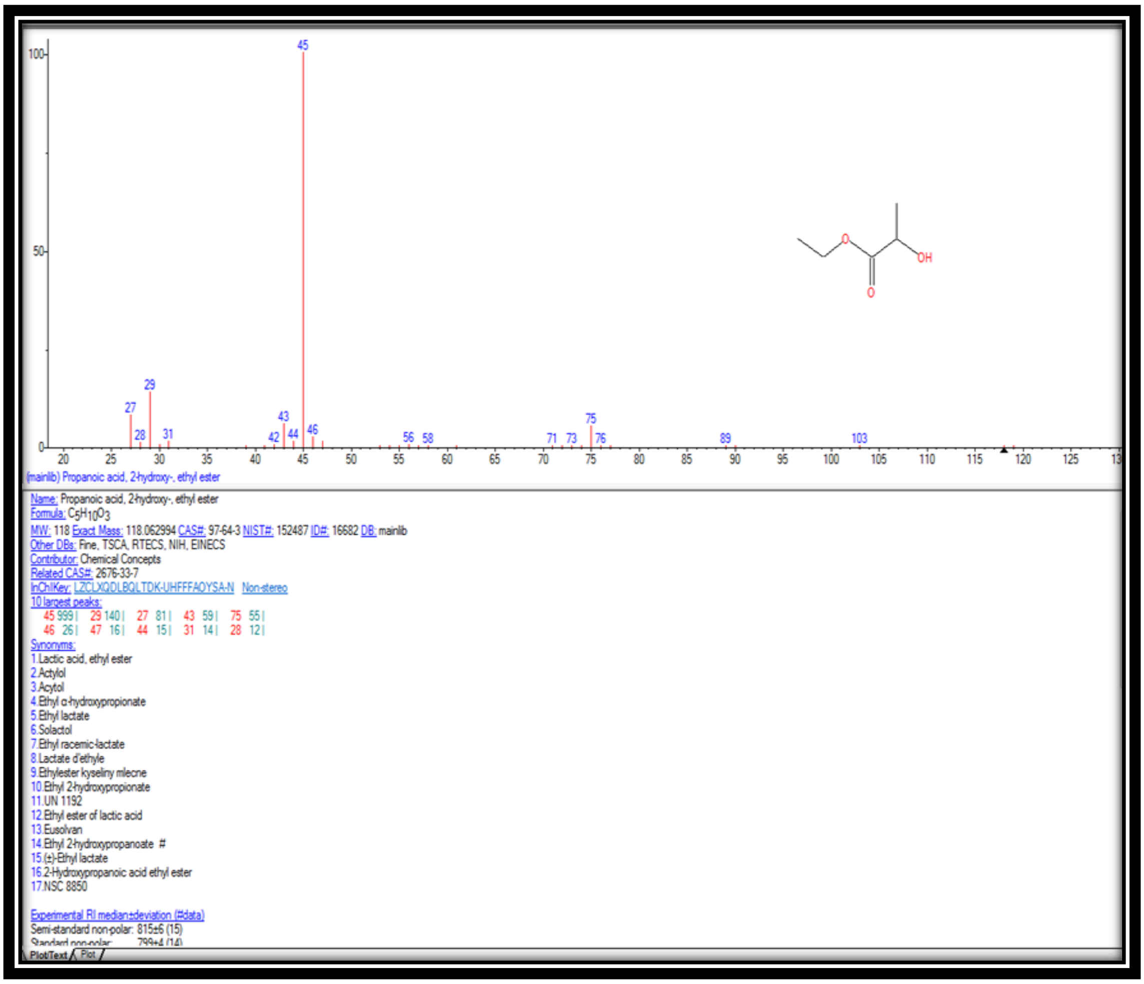

(mainlib) Propanoic acid, 2-hydroxy-, ethyl ester

Name: Propanoic acid, 2-hydroxy-, ethyl ester
Formula: $C_5H_{10}O_3$
MW: 118 Exact Mass: 118.062994 CAS#: 97-64-3 NIST#: 152487 ID#: 16682 DB: mainlib
Other DBs: Fine, TSCA, RTECS, NIH, EINECS
Contributor: Chemical Concepts
Related CAS#: 2676-33-7
InChIKey: LZCLXQDLBQLTDK-UHFFFAOYSA-N Non-stereo
10 largest peaks:
45 999 | 29 140 | 27 81 | 43 59 | 75 55 |
46 26 | 47 16 | 44 15 | 31 14 | 28 12 |
Synonyms:
1.Lactic acid, ethyl ester
2.Actylol
3.Acytol
4.Ethyl α-hydroxypropionate
5.Ethyl lactate
6.Solactol
7.Ethyl racemic-lactate
8.Lactate d'ethyle
9.Ethylester kyseliny mlecne
10.Ethyl 2-hydroxypropionate
11.UN 1192
12.Ethyl ester of lactic acid
13.Eusolvan
14.Ethyl 2-hydroxypropanoate #
15.(±)-Ethyl lactate
16.2-Hydroxypropanoic acid ethyl ester
17.NSC 8850

Experimental RI median±deviation (#data)
Semi-standard non-polar: 815±6 (15)
Standard non-polar: 799±4 (14)

Figure 7.52: GC-MS NIST Library search spectra for ethyl lactate compound.

Figure 7.53 and 7.54a-d depict the chromatogram results of the commercial ethyl lactate and the reaction product in the presence amberlyst 36 (7.54a), amberlyst 16 (7.54b), amberlyst 15 (7.54c) and dowex 50W8x (7.54d) cation-exchange resin catalysts respectively. Table 7.25a-e presents the integration peak list of retention time and peak areas for the commercial ethyl lactate (table 7.25a) and the respective esterification reaction product for amberlyst 36 (table 7.25b), amberlyst 16 (table 7.25c), amberlyst 15 (table 7.25d) and dowex 50W8x (table 7.25e) at 60 ^{o}C. From the chromatogram results, the mass spectra of the reaction product were generated from the highest peak on the chromatogram using GC NIST software program. From the mass spectra of the, ion 45 exhibited the structure of ethyl lactate for both pure commercial ethyl lactate and reaction product as shown in figure 7.53. Comparing the peak area of the commercial ethyl lactate with that of the ester product, it was found that the peak area of the reaction product catalysed by amberlyst 36 was higher than that of the commercial ethyl lactate. It was also observed from the retention time that the ester product eluted (1.521) faster than the commercial ethyl lactate (2.118) which was also attributed to the resin activity. A similar result was also obtained for the esterification of lactic acid feed catalysed by amberlyst 16, amberlyst 15, amberlyst 36 and dowex 50W8x at 80 and 100 ^{o}C.

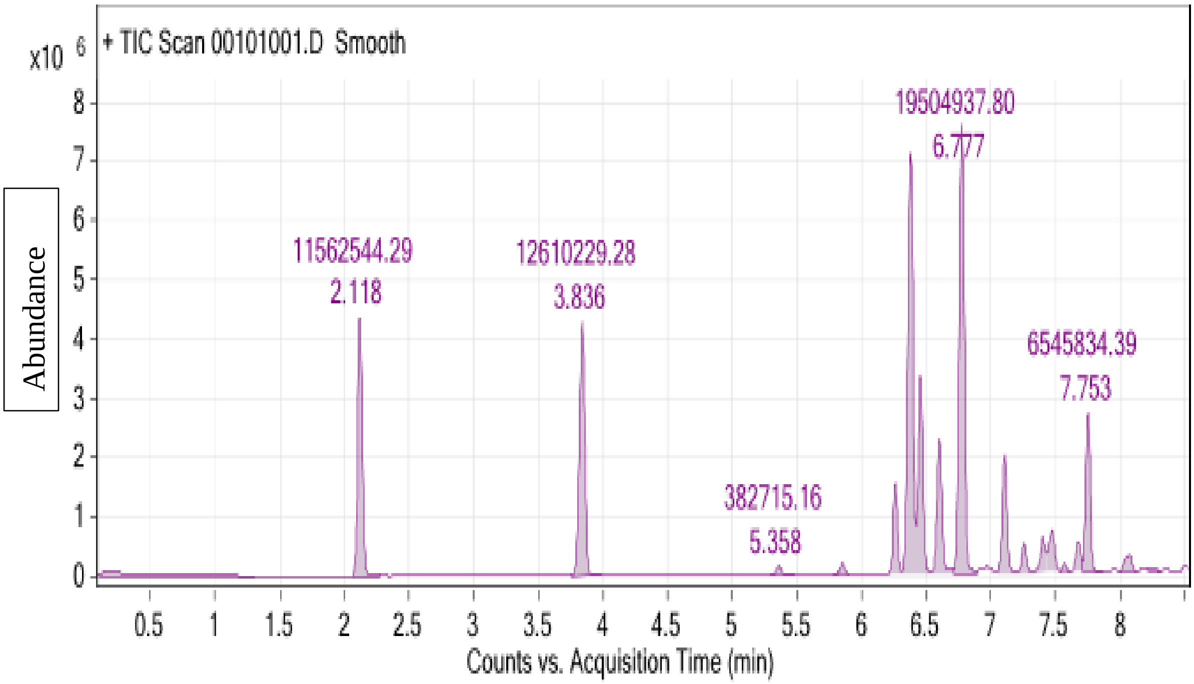

Figure 7.53: GC-MS chromatogram for commercial available ethyl lactate solvent

Table 7.25a: GC-MS Integration peak list for commercial available ethyl lactate solvent.

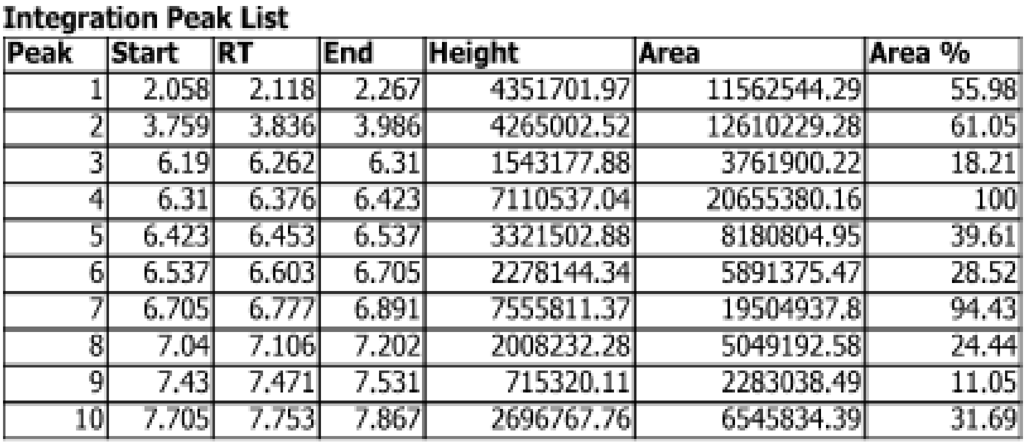

Integration Peak List

Peak	Start	RT	End	Height	Area	Area %
1	2.058	2.118	2.267	4351701.97	11562544.29	55.98
2	3.759	3.836	3.986	4265002.52	12610229.28	61.05
3	6.19	6.262	6.31	1543177.88	3761900.22	18.21
4	6.31	6.376	6.423	7110537.04	20655380.16	100
5	6.423	6.453	6.537	3321502.88	8180804.95	39.61
6	6.537	6.603	6.705	2278144.34	5891375.47	28.52
7	6.705	6.777	6.891	7555811.37	19504937.8	94.43
8	7.04	7.106	7.202	2008232.28	5049192.58	24.44
9	7.43	7.471	7.531	715320.11	2283038.49	11.05
10	7.705	7.753	7.867	2696767.76	6545834.39	31.69

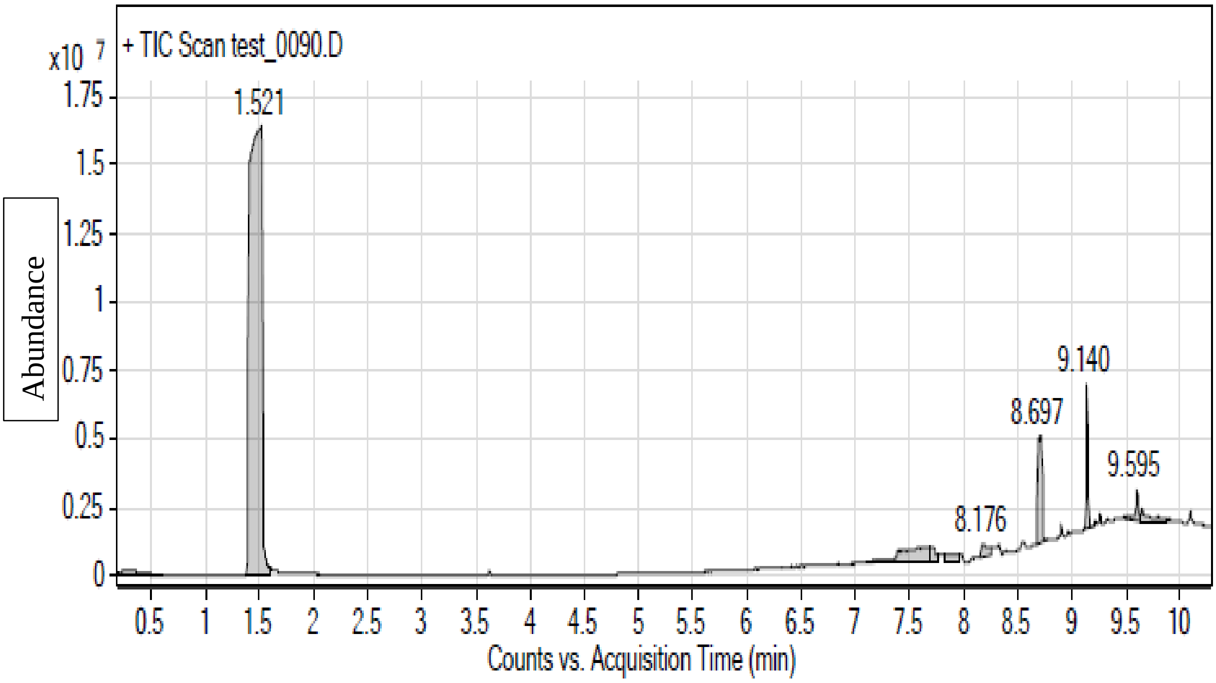

Figure 7.54a: GC-MS chromatogram of lactic acid feed catalysed by amberlyst 36 at 60 ºC

Table 7.25b: GC-MS Integration peak list for lactic acid feed catalysed by amberlyst 36 at 60 ºC.

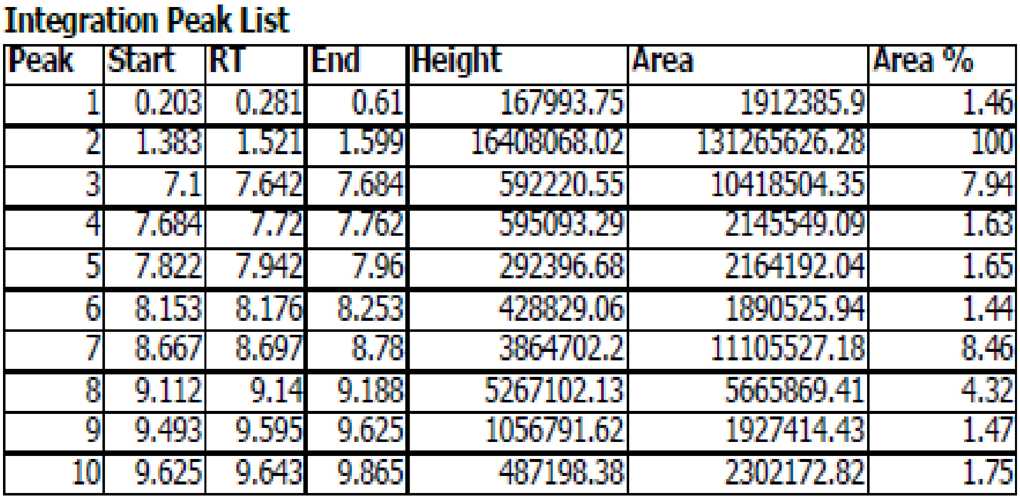

Integration Peak List

Peak	Start	RT	End	Height	Area	Area %
1	0.203	0.281	0.61	167993.75	1912385.9	1.46
2	1.383	1.521	1.599	16408068.02	131265626.28	100
3	7.1	7.642	7.684	592220.55	10418504.35	7.94
4	7.684	7.72	7.762	595093.29	2145549.09	1.63
5	7.822	7.942	7.96	292396.68	2164192.04	1.65
6	8.153	8.176	8.253	428829.06	1890525.94	1.44
7	8.667	8.697	8.78	3864702.2	11105527.18	8.46
8	9.112	9.14	9.188	5267102.13	5665869.41	4.32
9	9.493	9.595	9.625	1056791.62	1927414.43	1.47
10	9.625	9.643	9.865	487198.38	2302172.82	1.75

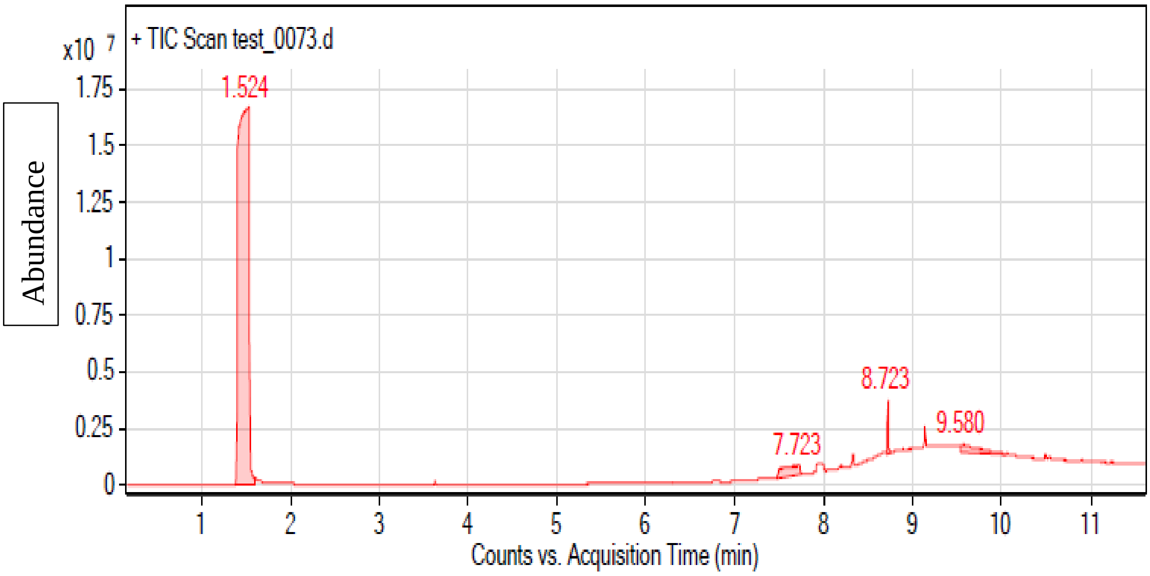

Figure 7.54b: GC-MS Chromatogram of lactic acid feed catalysed by amberlyst 16 at 60 ºC.

Table 7.25c: GC-MS Integration peak list for lactic acid feed catalysed by amberlyst 16 at 60 ºC.

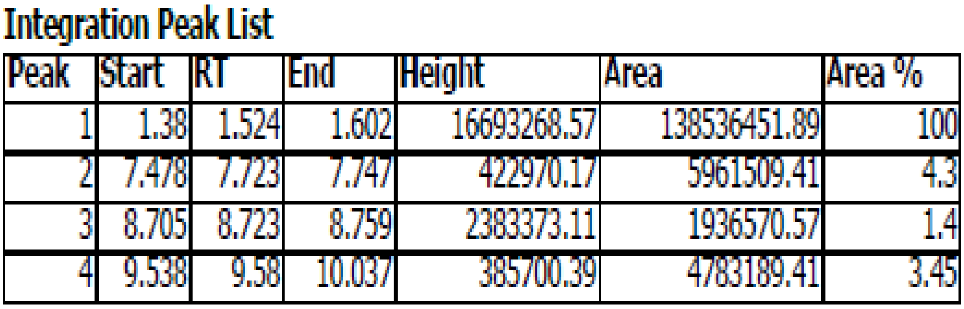

Integration Peak List

Peak	Start	RT	End	Height	Area	Area %
1	1.38	1.524	1.602	16693268.57	138536451.89	100
2	7.478	7.723	7.747	422970.17	5961509.41	4.3
3	8.705	8.723	8.759	2383373.11	1936570.57	1.4
4	9.538	9.58	10.037	385700.39	4783189.41	3.45

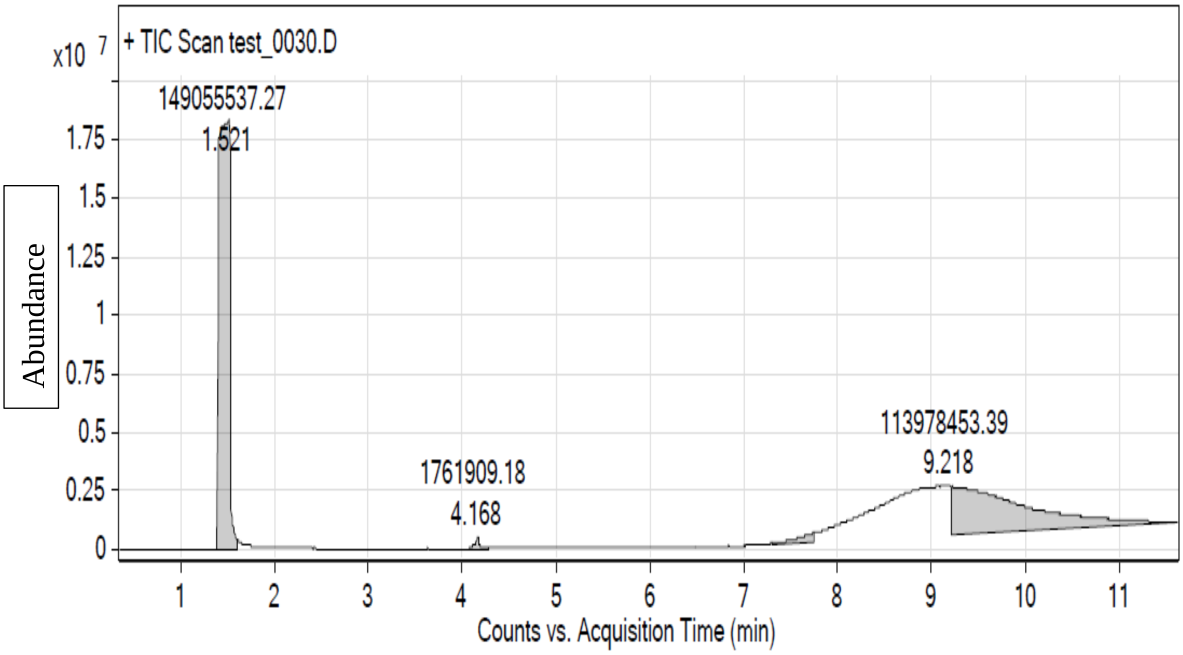

Figure 7.54c: GC-MS Chromatogram of lactic acid feed catalysed by amberlyst 15 at 60 ºC

Table 7.25d: GC-MS Integration peak list for lactic acid feed catalysed by amberlyst 15 at 60 ºC.

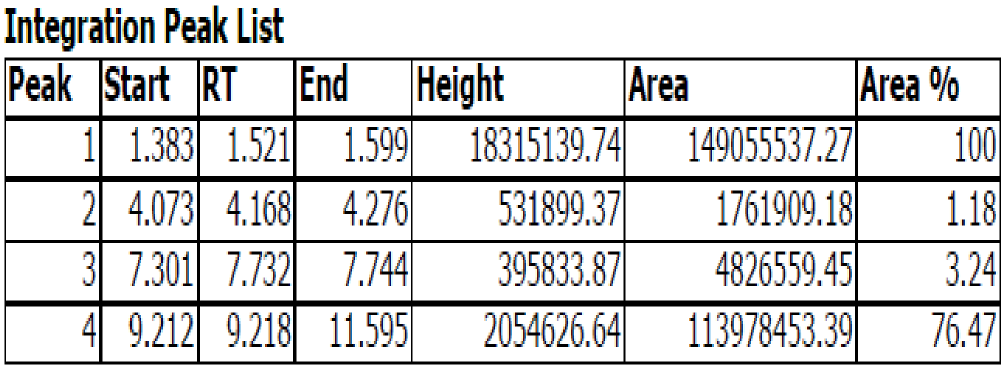

Integration Peak List

Peak	Start	RT	End	Height	Area	Area %
1	1.383	1.521	1.599	18315139.74	149055537.27	100
2	4.073	4.168	4.276	531899.37	1761909.18	1.18
3	7.301	7.732	7.744	395833.87	4826559.45	3.24
4	9.212	9.218	11.595	2054626.64	113978453.39	76.47

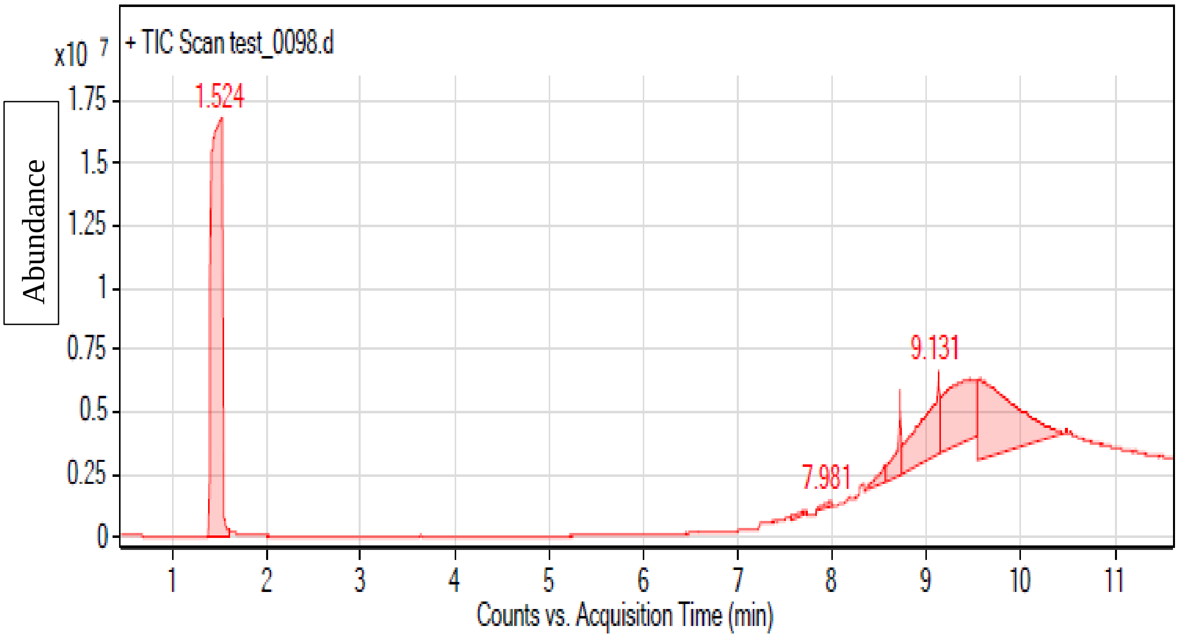

Figure 7.54d: GC-MS chromatogram of lactic acid feed catalysed by dowex 50W8x at 60 ºC.

Table 7.25e: GC-MS Integration peak list for lactic acid feed catalysed by dowex 50x at 60 ºC.

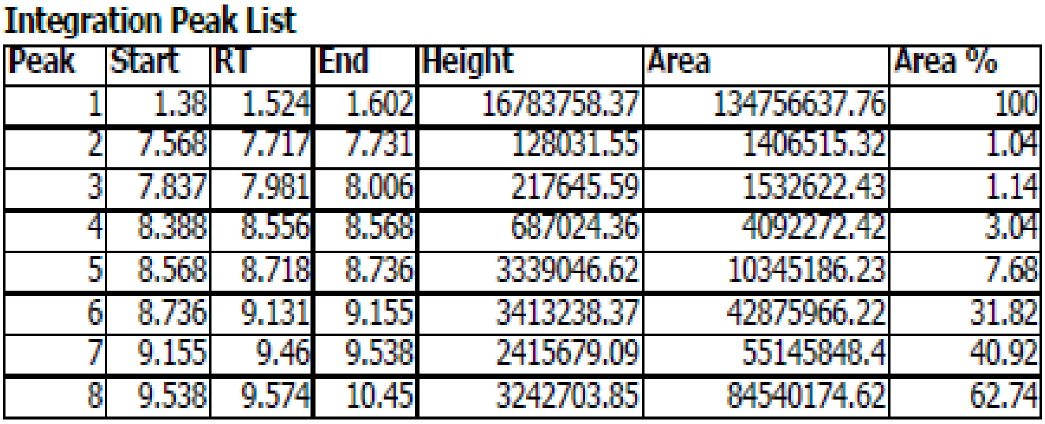

Integration Peak List

Peak	Start	RT	End	Height	Area	Area %
1	1.38	1.524	1.602	16783758.37	134756637.76	100
2	7.568	7.717	7.731	128031.55	1406515.32	1.04
3	7.837	7.981	8.006	217645.59	1532622.43	1.14
4	8.388	8.556	8.568	687024.36	4092272.42	3.04
5	8.568	8.718	8.736	3339046.62	10345186.23	7.68
6	8.736	9.131	9.155	3413238.37	42875966.22	31.82
7	9.155	9.46	9.538	2415679.09	55145848.4	40.92
8	9.538	9.574	10.45	3242703.85	84540174.62	62.74

Figure 7.55 depicts the NIST mass spectra of the ester product catalysed by amberlyst 36 resin at 60 ºC. Table 7.26 shows the description of the different ions and their respective compounds on the mass spectra of amberlyst 36. From Figure 7.55, it can be seen that ion number 45 with the highest peak reflected the structure of the ethyl lactate compound. This was in agreement with the library spectra for the commercial ethyl lactate solvent. Other ions that were found on the spectra include: methyl methanethiosulphonate (43), 2,4-pentanediol (44), methylazoxymthanol acetate (46), hydroxylamine,

o-methyl (53), acetaldehyde, methoxy (56), methylal (58), acetoin (61), formic acid (71), 2,3-butandiol (73) as shown in table 7.26.

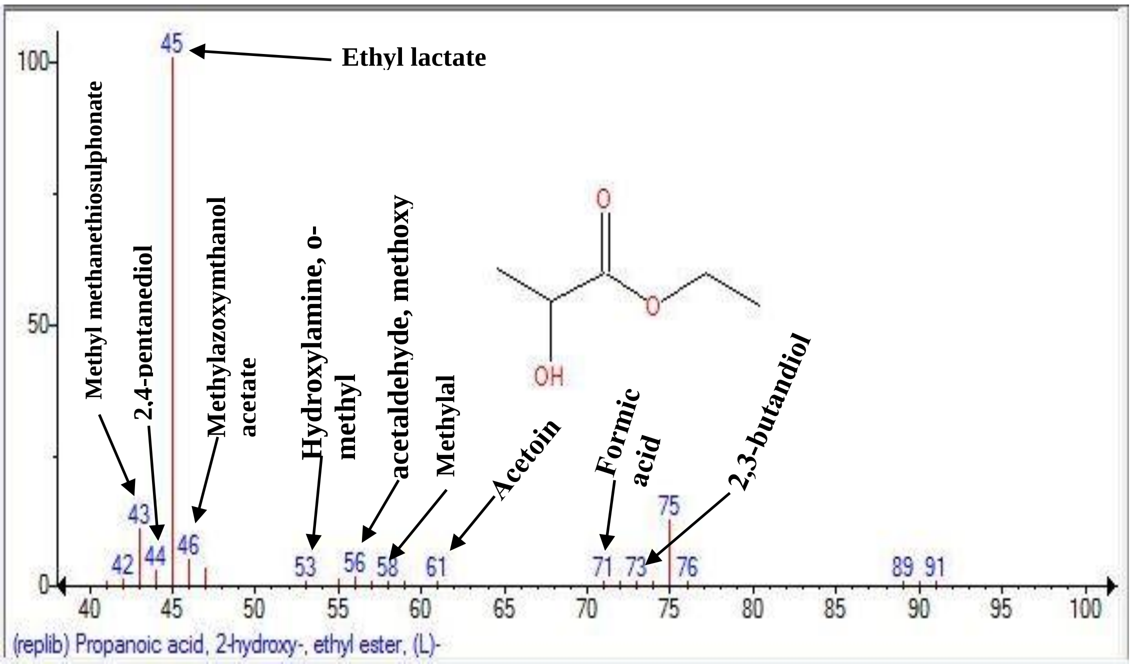

Figure 7.55: Mass spectra of the esterification product catalysed by amberlyst 36 at 60 ºC.

Table 7.26: Retention time, peak area, compound and mass spectra ion extracted from GC-MS chromatogram ester product catalysed with amberlyst 36 at 60 ºC.

Retention time (min)	Peak area (m^2)	Compound	Mass spectra Ion
0.281	1912385.90	Methyl methanethiosulphonate	43
1.521	131265626.28	2,4-pentanediol	44
7.642	10418504.35	Ethyl lactate	45
7.720	2145549.09	Methylazoxymthanol acetate	46
7.942	2164192.04	Hydroxylamine, o-methyl	53
8.176	1890525.94	acetaldehyde, methoxy	56
8.697	11105527.18	Methylal	58

9.140	**5665869.41**	**Acetoin**	**61**
9.959	**1927414.43**	**formic acid**	**71**
9.643	**2302172.82**	**2,3-butandiol**	**73**

7.3.2 Effect of Temperature on Esterification Product Conversion from Batch Process Esterification Analysis.

Figure 7.56 – 7.57 depict the graph of the effect of temperature on lactic acid conversion catalysed with the different cation-exchange resin at the injection concentration of 1.0, 0.5 and 2.0 µg/L. From figure 7.56, it can be seen that the batch process esterification of lactic acid feed catalysed by amberlyst 36 showed a higher conversion 99.2% at 100 °C and 98.9% for both 60 °C and 80 °C. It can also be seen from figure 7.56 that dowex 50W8x also showed a good conversion rate of 98.8% at 1.0µg/L. Also, the lactic acid feed catalysed with amberlyst 36 and dowex 50W8x gave a good conversion rate at 60, 80 and 100 °C in contrast to amberlyst 15 and amberlyst 16 at the same temperatures which confirms the effectiveness of the catalyst. Akbay et al. [149] obtained a similar result for the batch process esterification catalysed with amberlyst 36. Also, from figure 7.56-7.58, the higher conversion rate in the graphs could also represent the shift in the chemical equilibrium to the forward reaction.

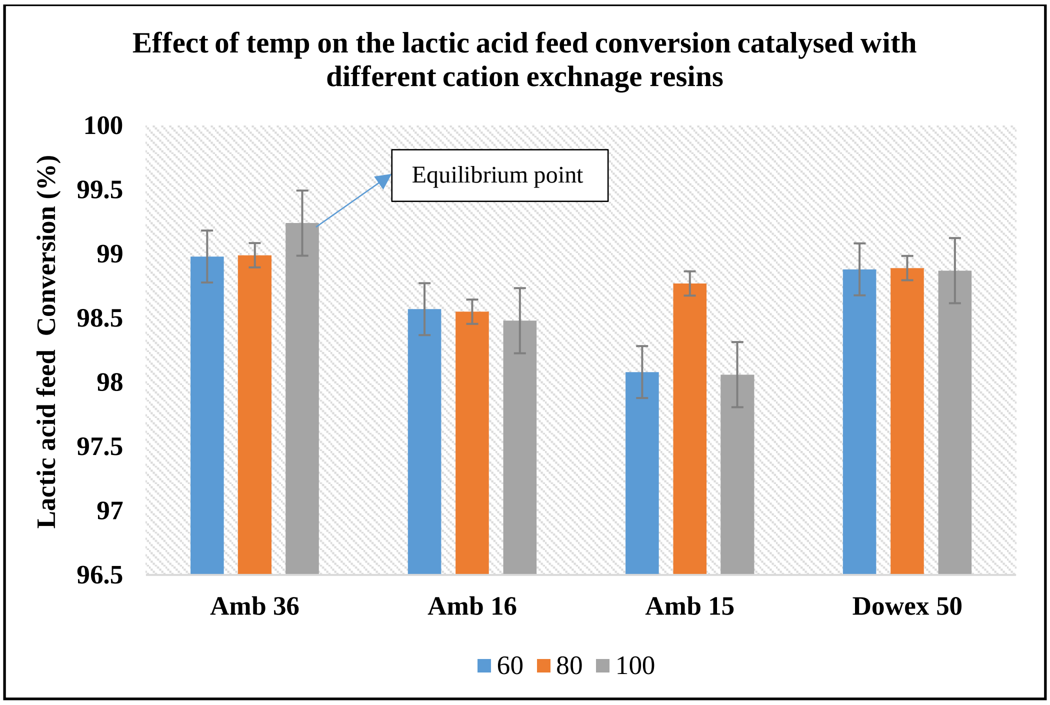

Figure 7.56: Conversion of lactic acid feed catalysed with amberlyst 36, amberlyst 16, amberlyst 15 and dowex 50W8x at different temperatures and at 1.0µg/L.

From figure 7.57, it can be seen that the conversion rate of the lactic acid feed increases with respect to temperature for the lactic acid feed catalysed with amberlyst 36 and dowex50W8x. It was found that although the feed gave a lower conversion of 98.3% at 80 °C for both amberlyst 15 and 16 cation exchange resin, at 60 °C. However, dowex50W8x showed a good conversion of up to 98.7%. It was found that at 60 °C, amberlyst 36, 15 and dowex50W8x showed a good conversion of 99%, 99.4% and 98.6% respectively. At 100 °C, it can be seen that amberlyst 15 demonstrate a conversion of 99.4%.

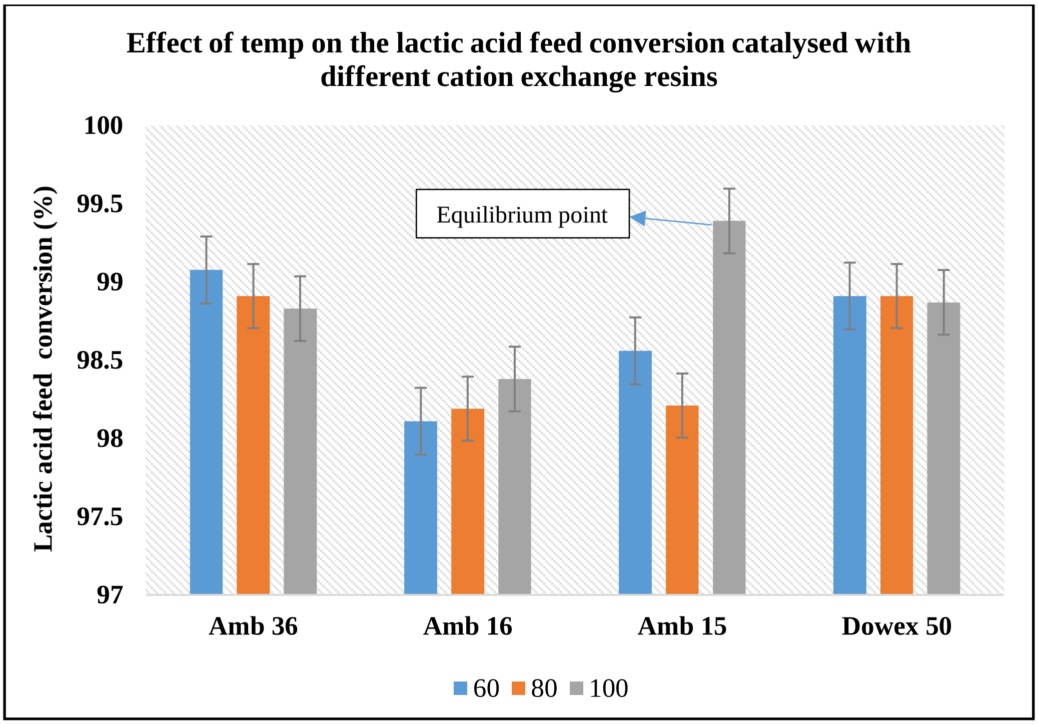

Figure 7.57: Conversion of lactic acid feed catalysed with amberlyst 36, amberlyst 16, amberlyst 15 and dowex 50W8x at different temperatures and at 0.5µg/L.

Also, from figure 7.58, it can be seen that the lactic acid feed catalysed with amberlyst 36 gave a conversion of 99.9% and 98.9% at 80 °C. It was also found that the three temperatures favoured the conversion of the feed catalysed with dowex 50W8x with the highest conversion rate of 98.85% at 60 °C. It was found that the conversion rate of the lactic acid feed catalysed with ambrelyst 15 and 16 were a bit low for the two catalysts at the three temperatures. Amberlyst 36 and dowex 50W8x cation exchange resin exhibited a good conversion and can also with stand the effect of temperature at the concentration of 2.0µg/L. It was also found that at 80 °C, the conversion of the lactic acid feed catalysed with amberlyst 15 was very low (97.9%).

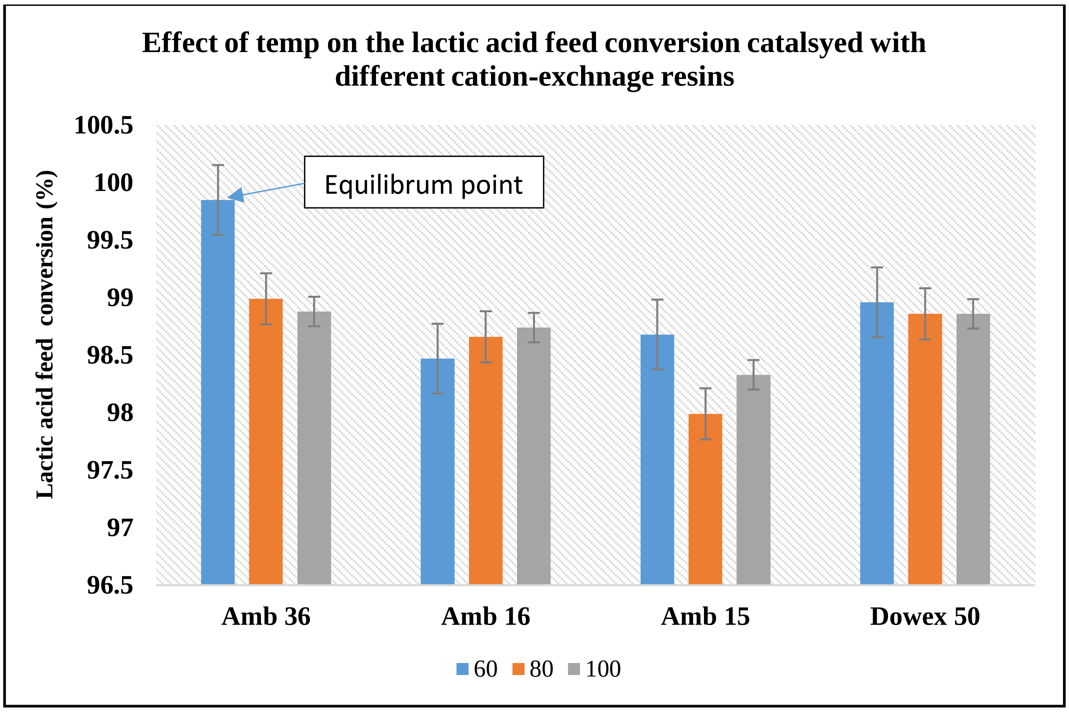

Figure 7.58: Conversion of lactic acid feed catalysed with amberlyst 36, amberlyst 16, amberlyst 15 and dowex 50W8x at different temperatures and at 2.0µg/L.

7.3.3 Effect of Concentration on Lactic acid feed Conversion from the Batch Process Esterification Analysis.

Figure 7.59– 7.62 shows a plot of the lactic acid feed conversion (%) against the injection concentration (µg/L). From figure 7.59, it can be seen that the injection concentration also affects the conversion of the feed. It was found that at lower concentration, the ester product catalysed with amberlyst 36 showed a conversion of 99% at 60 and 100 °C. It was found that at 1.0µg/L, the feed also exhibited a good conversion (97.9%) at 80 °C. From figure 7.60, conversion rate of the feed catalysed with amberlyst 16 was found to increase with respect to the concentration. At 2.0µg/L of injection concentration, the lactic acid feed gave a conversion rate of 98.9% at 100 °C whereas at 1.0µg/L, the conversion of the feed increases as the temperature decrease whereas at 2.0µg/L, the concentration of the lactic acid feed increases with respect to temperature. The lactic acid product catalysed with amberlyst 16, exhibited a lower conversion of 98.2% at 60 °C and at 0.5µg/L. Also, it can be seen in figure 7.59–7.62 that the experimental percentage error determined for the batch process analysis of the lactic acid feed exhibited a better correlation of the graphs. From figure 7.61, at 0.1µg/L, the lactic acid feed catalysed with amberlyst 15 exhibited a conversion of 99.7% at 80 °C. At 0.1, 0.5 and 2.0µg/L the lactic acid feed exhibited a high conversion of 99.8%, 99.4% and 99.5% at 60, 80 and 100 °C respectively. It was observed that the conversion of the lactic acid feed catalysed with amberlyst 15 at different temperatures for the different injection concentrations demonstrate a low conversion for the lactic acid feed.

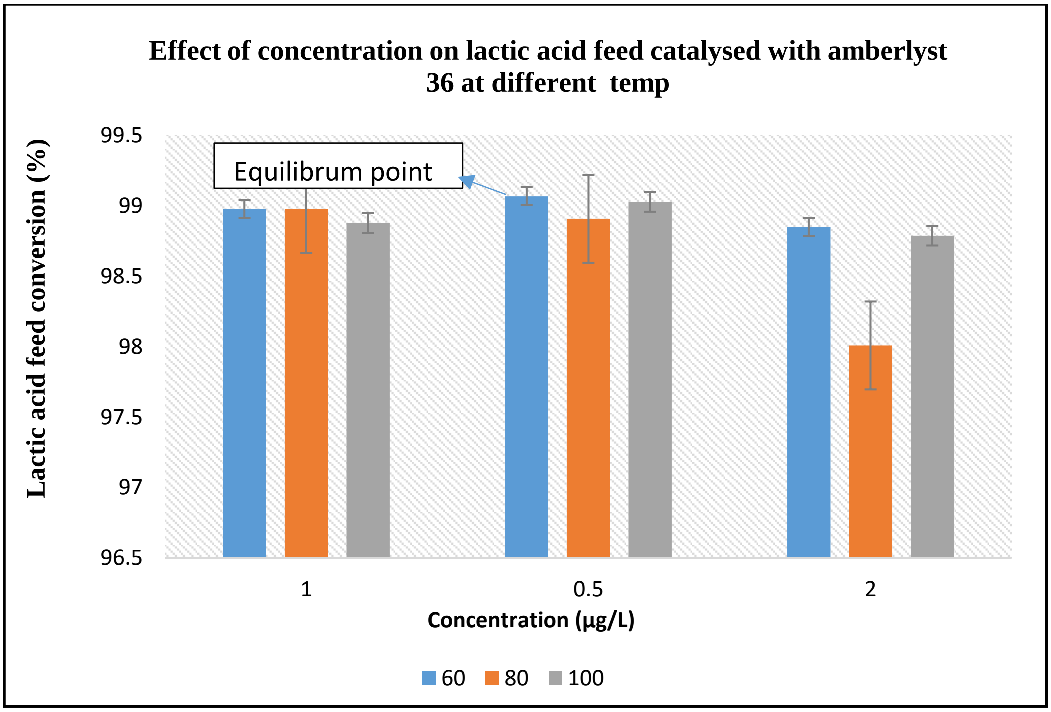

Figure 7.59: Effect of temperature on lactic acid feed conversion catalysed with amberlyst 36 at different injection concentrations.

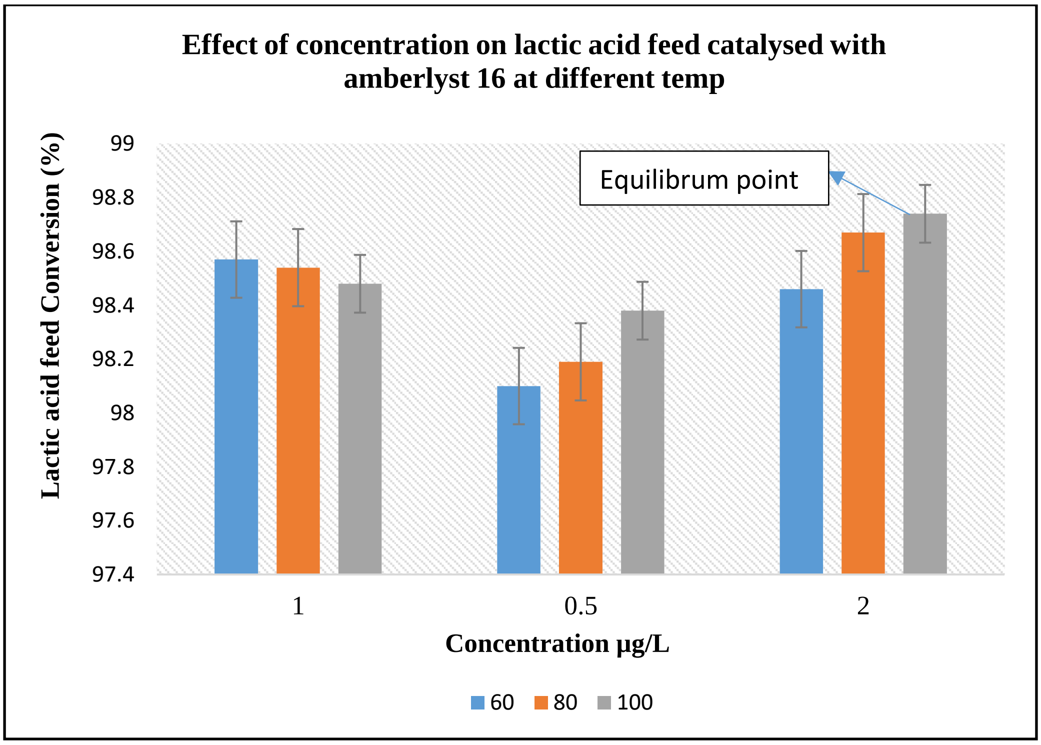

Figure 7.60: Effect of temperature on lactic acid feed Conversion catalysed with amberlyst 16 at different injection concentrations.

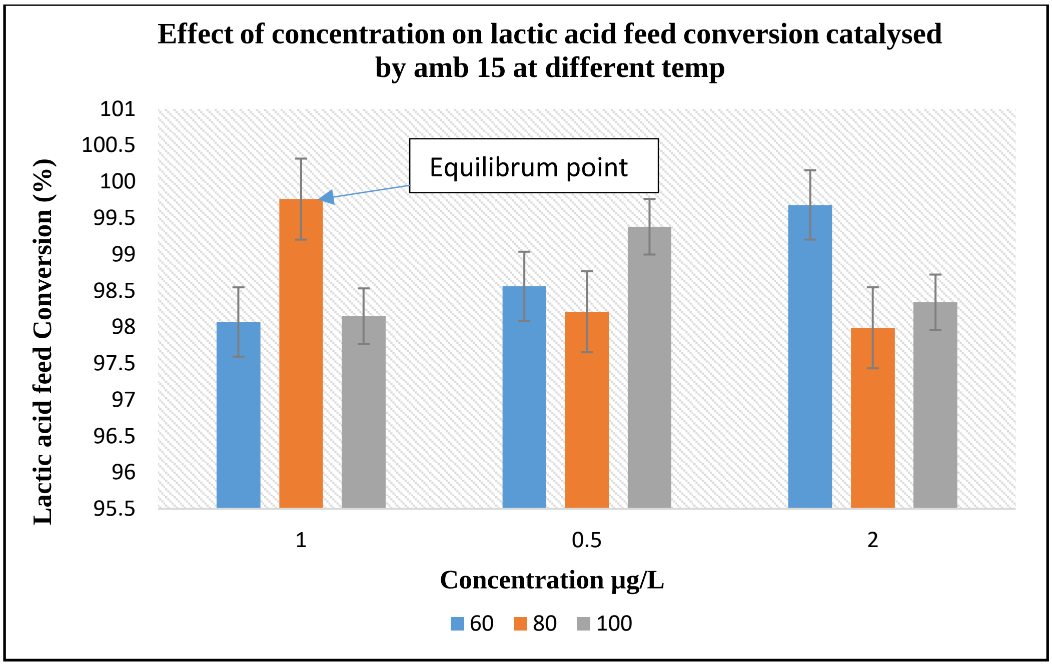

Figure 7.61: Effect of temperature on lactic acid feed conversion catalysed with amberlyst 15 at different injection concentrations.

Similarly, figure 7.62 depict the graph of the lactic acid feed conversion against the concentration at different temperatures. From figure 7.62, it can be seen that lactic acid feed catalysed by dowex50W8x resin showed a conversion rate of 98.96 at 60 °C at 0.2µg/L conc. However, at 0.5µg/L it was also found that the lactic acid feed also exhibits a conversion of 98.9% and 98.89% at 80 and 60 °C respectively. Kumar et al. [150] obtained a conversion of up to 84.3% from the esterification of carboxylic acid with methanol to produce the resulting ester.

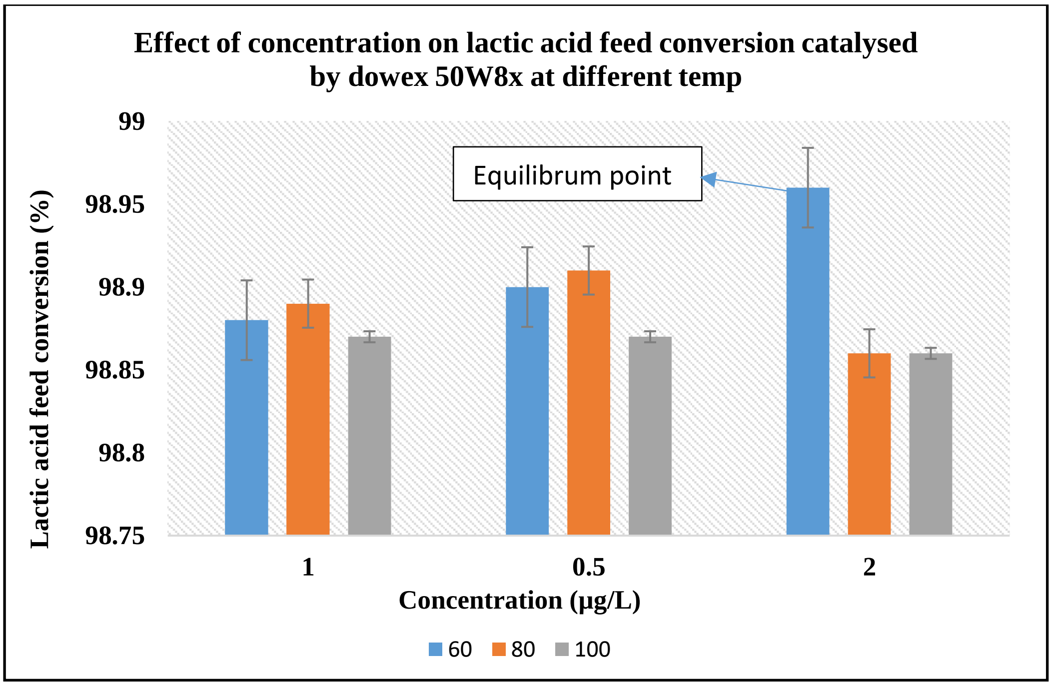

Figure 7.62: Effect of temperature on lactic acid feed Conversion catalysed with dowex50W8x at different injection concentrations.

7.3.4: Esterification reaction using Resin Catalysts attached to Cellulose Acetate Membrane at different Temperatures.

This section explained the results obtained from the esterification reaction involving lactic acid and ethanol by impregnating cellulose acetate membrane with the cation-exchange resin catalysts. In this section the percentage conversion of the lactic acid feed from the esterification analysis catalysed with cellulose acetate membrane and the different cation-exchange resin that were deposited on the surface of the membrane was determine. The result for this study is published in Okon et al. [125].

7.3.4.1 Effect of Temperature on Lactic Acid Feed Conversion.

According to Martin et al. [151], at low temperature, water permeance of a polymeric membrane vary over a wide range from $3x10^{-10}$ to $3x10^{-6}$ $mols^{-1}m^{-2}Pa^{-1}$, strongly depending on the type of polymeric membrane. From the conversion rate result, it was suggested that the cellulose acetate membrane could exhibit permeability in the same range as described by Martin et al. [151] since it successfully shifted the chemical equilibrium to produce higher conversion of the ester product. Figure 7.63– 7.65 shows the graph of the conversion rate of lactic acid feed catalysed with amberlyst 16, amberlyst 15, amberlyst 36 and dowex 50W8x impregnated with cellulose acetate membrane at $0.30Lmin^{-1}$. Table 7.27 shows the calculated percentage conversion of the esterification reaction product with the cellulose acetate membrane attached to the different cation-exchange resins at 60, 80 and 100 ^{o}C and at $0.30Lmin^{-1}$. From the results of the spectra obtained from the GC-MS analysis of the esterification process, the conversion of the esterification product was calculated to determine the percentage conversion of the produced esterification product. Also, from figure 7.63-7.65, the higher conversion rate in the graphs could also represent the shift in the chemical equilibrium to the forward reaction as shown with the arrow.

Table 7.27: Calculated Percentage Conversion of the Lactic Acid Feed Conversion using Cellulose Acetate Membrane attached to amberlyst 36, 16, 15 and dowex 50W8x resins at 60 °C and at 0.30Lmin^{-1}.

Cellulose acetate/resins	Lactic acid feed Conversion (%)
Cellulose acetate/amberlyst 36	99.998
Cellulose acetate/amberlyst 16	99.988
Cellulose acetate/amberlyst 15	99.866
Cellulose acetate/dowex 50W8x	99.887

From these results obtained in figure 7.63 – 7.65, the percentage conversion of the lactic acid feed was also obtained to be in the range of 98 - 100% by measuring the concentration of the commercial ethyl lactate with that of the obtained with respect to the flow rate of the sweep gas which was used on the permeate side of the reactor. From figure 7.63, it can be seen that the conversion of the lactic acid feed increases with respect to the temperature. Amberlyst 36 attached to cellulose acetate membrane gave a conversion of the lactic acid feed of upto 100% at 0.30Lmin^{-1}. It was also found from figure 7.63 that amberlyst 36, amberlyst 15, dowex 50W8x and amberlyst 16 showed a higher conversion of upto 100% at 80 and 100 °C in contrast to 60 °C. It was also found that ester product conversion of the catalyst attached to cellulose acetate membrane was found to be low at 60 °C for all the catalyst at 0.30Lmin^{-1}. This result was in good agreement with a similar work by Chandane et al. [65] and Sharma et al. [147], From the results obtained, it was also found that the experimental percentage error determine fitted well to the graphs.

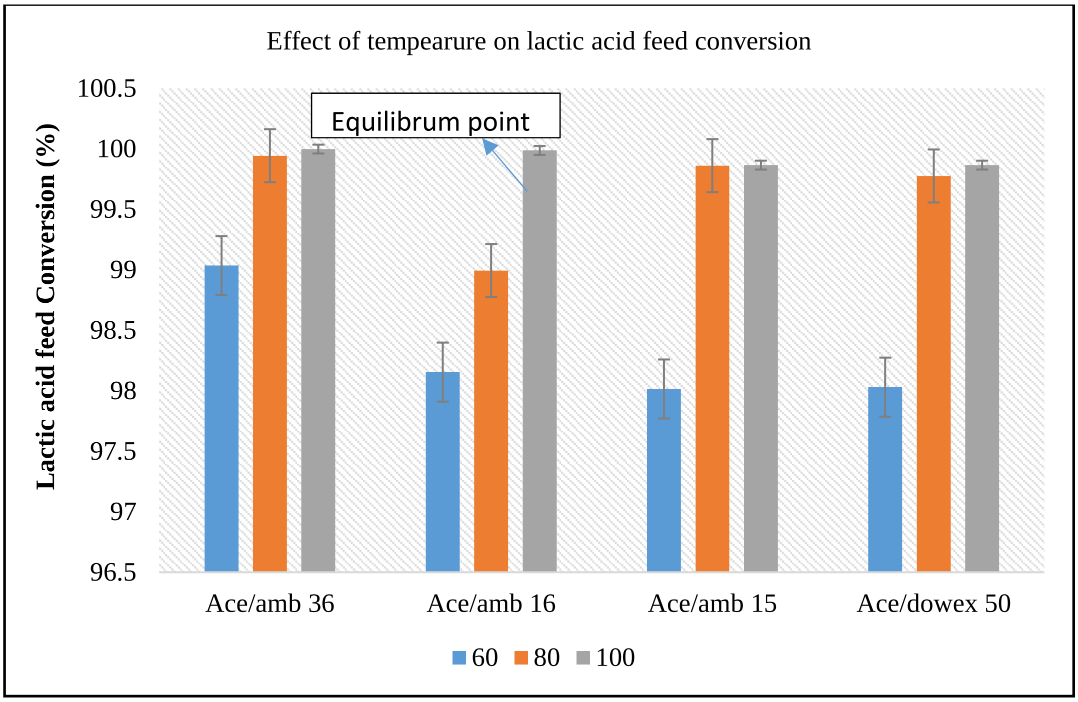

Figure 7.63: Conversion of lactic acid feed catalysed with amberlyst 36, amberlyst 16, amberlyst 15, dowex 50W8x attached to cellulose acetate membrane at 60, 80 and 100 °C and at 0.30Lmin^{-1}.

Similarly, from figure 7.64, it was found that at 0.40Lmin^{-1}, the amberlyst 36 and dowex50W8x attached to cellulose acetate membrane showed a good conversion rate (100%) of the lactic acid feed at 60, 80 and 100 °C at 0.40Lmin^{-1} in contrast to amberlyst 16 and amberlyst 15. It was also observed that although amberlyst 16 attached to cellulose acetate membrane exhibited a 100% conversion of the lactic acid feed, however the 60 and 80 °C, the conversion of the lactic acid feed was found to be 98.5% and 99% respectively. Also, from figure 7.64, it can also be seen that amberlyst 15 attached to cellulose acetate membrane also demonstrate a 100% conversion at 80 and 100 °C in contrast to 60 °C at 0.40Lmin^{-1}. Pighin et al. [152] carried out the synthesis of ethyl lactate from triose sugars via catalysts impregnation method and obtained a conversion of 68% yield of ethyl lactate. Also, in figure 7.65, it was found that the lactic acid feed conversion catalysed with amberlyst 36 and amberlyst 16 attached to cellulose acetate membrane exhibited a conversion of upto 100% at 80 and 100 °C at the flow rate of 0.50Lmin^{-1}. It was found that the catalysts also exhibited a 99.8 and 99.7% conversion for amberlyst 36 and 16 catalysts at 60 °C. Also, from figure 7.66, it was found that amberlyst 15 and dowex 50W8x catalysts exhibited the same conversion rate of 99.8% at 80 and 100 °C. However, it was also observed that the lactic acid feed exhibited low conversion value of 98% at 60 °C for the both catalysts. It was also suggested that at 0.50Lmin^{-1} permeate flow rate, the conversion of the lactic acid feed increases with respect to the temperature. This result is in good agreement with literature findings [153].

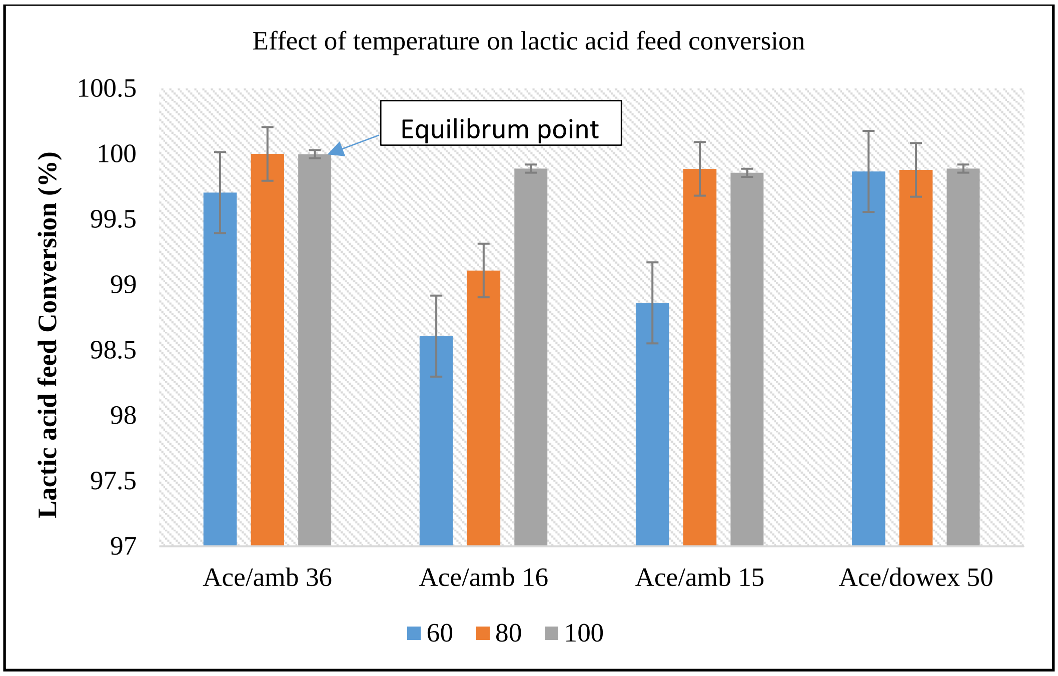

Figure 7.64: Conversion of lactic acid feed catalysed with amberlyst 36, amberlyst 16, amberlyst 15, dowex 50W8x attached to cellulose acetate membrane at 60, 80 and 100 ºC and at 0.40Lmin^{-1}.

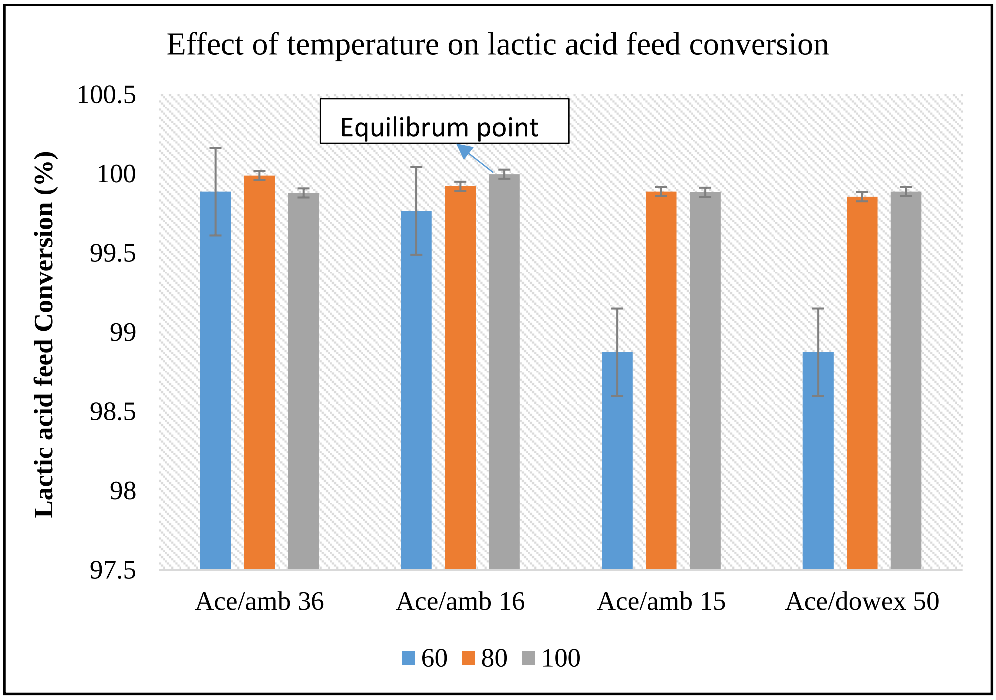

Figure 7.65: Conversion of lactic acid feed catalysed with amberlyst 36, amberlyst 16, amberlyst 15, dowex 50W8x attached to cellulose acetate membrane at 60, 80 and 100 ºC and at 0.50Lmin^{-1}.

7.3.4.2 Effect of Permeate Flow rate on Lactic acid feed Conversion.

Figure 7.66 – 7.69 depict the graph of the permeate flow rate on the lactic acid feed conversion catalysed with amberlyst 36, amberlyst 16, amberlyst 15 and dowex 50W8x attached to cellulose acetate membrane at 0.30, 0.40 and 0.50Lmin^{-1}. From the result in figure 7.66 – 7.69, it was found that generally the flow rate has a little effect on the conversion of the lactic acid feed. From figure 7.66, it was found that at 60 ^{o}C, the lactic acid feed catalysed with amberlyst 36 attached to cellulose acetate membrane exhibited a conversion of upto 99.6% and 99.8% with an increase in flow rate. At 80 ^{o}C it was found that the lactic acid feed exhibited almost the same conversion rate for the three flow rates. It was also found that at 100 ^{o}C the lactic acid feed conversion was found to be higher at 0.30 and 0.40 Lmin^{-1} (99.9%) in contrast to the feed conversion of the flow rate of 0.50 Lmin^{-1}. A similar result was also obtained in figure 7.67 for lactic acid feed conversion of amberlyst 16 and dowex 50W8x attached to cellulose acetate membrane at the permeate flow rate of 0.30, 0.40 and 0.50 Lmin^{-1} with lactic acid feed conversion of 97.8% at 0.30Lmin^{-1} for amberlyst 16 at 60^{o}C.

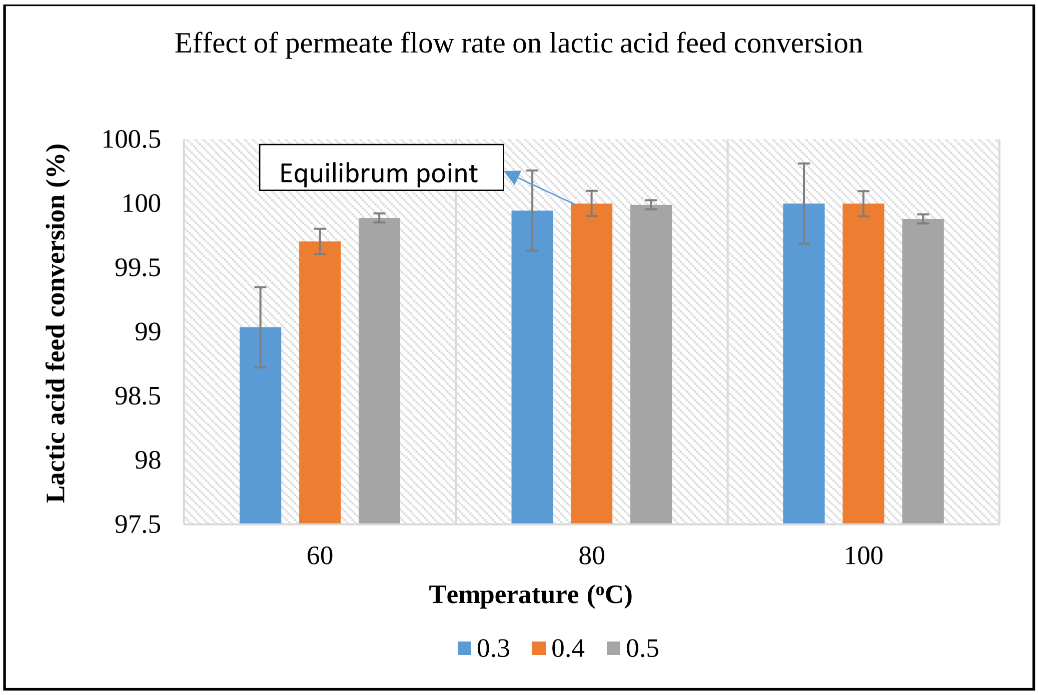

Figure 7.66: Effect of permeate flow rate on lactic acid feed conversion catalysed with amberlyst 36 attached to cellulose acetate membrane at 0.30, 0.40 and 0.50Lmin^{-1}.

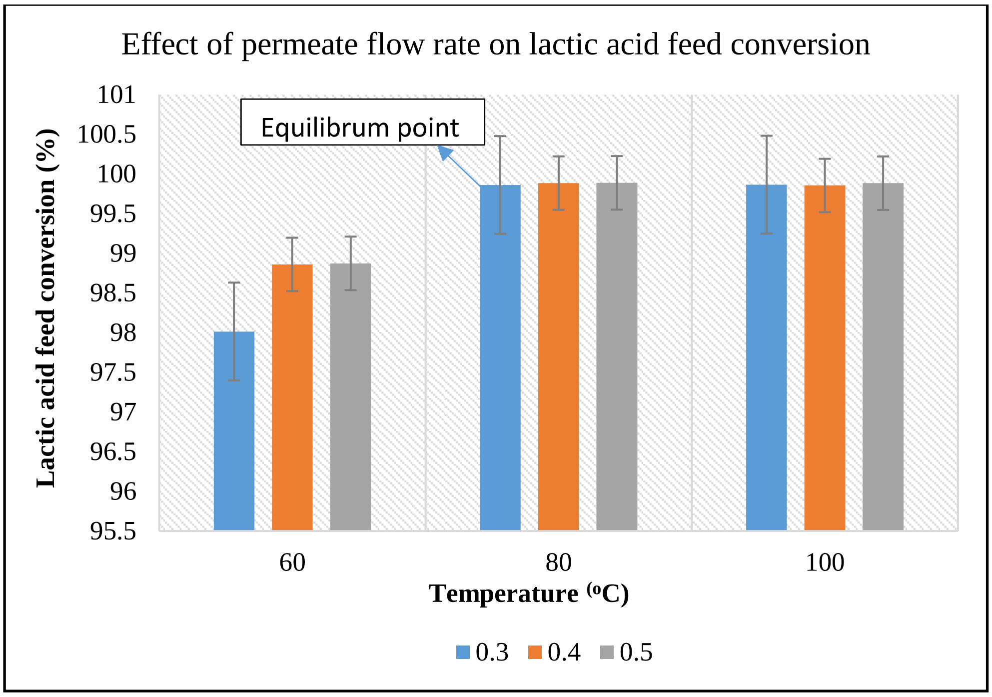

Figure 7.67: Effect of permeate flow rate on lactic acid feed conversion catalysed with amberlyst 16 attached to cellulose acetate membrane at 0.30, 0.40 and 0.50Lmin^{-1}.

Also, from figure 7.68, it was found that the conversion rate for the lactic acid feed catalysed with amberlyst 15 attached to cellulose acetate membrane demonstrate a good conversion rate of 99.8% at the permeate flow rate of 0.50Lmin^{-1} and at 60, 80 and 100 ºC in contrast to the conversion rate at 0.30 and 0.40Lmin^{-1} permeate flow rate. It was suggested that the permeate flow rate was dependent on the esterification temperature as the lactic acid feed gave a good conversion at higher permeate flow rate. From figure 7.69, it can be seen that lactic acid flow rate demonstrates upto 99.9% conversion at 80 ºC and at 0.40Lmin^{-1}. It was also found that a conversion rate of 99.7 and 99.8% were also obtained at the same temperature for the flow rate of 0.30 and 0.50 Lmin^{-1} respectively. However, at 60 ºC, it was found that the lactic acid feed conversion rate catalysed with dowex50W8x decreases with respect to the flow rate with the highest percentage conversion of 98.9% at 0.50 Lmin^{-1}.

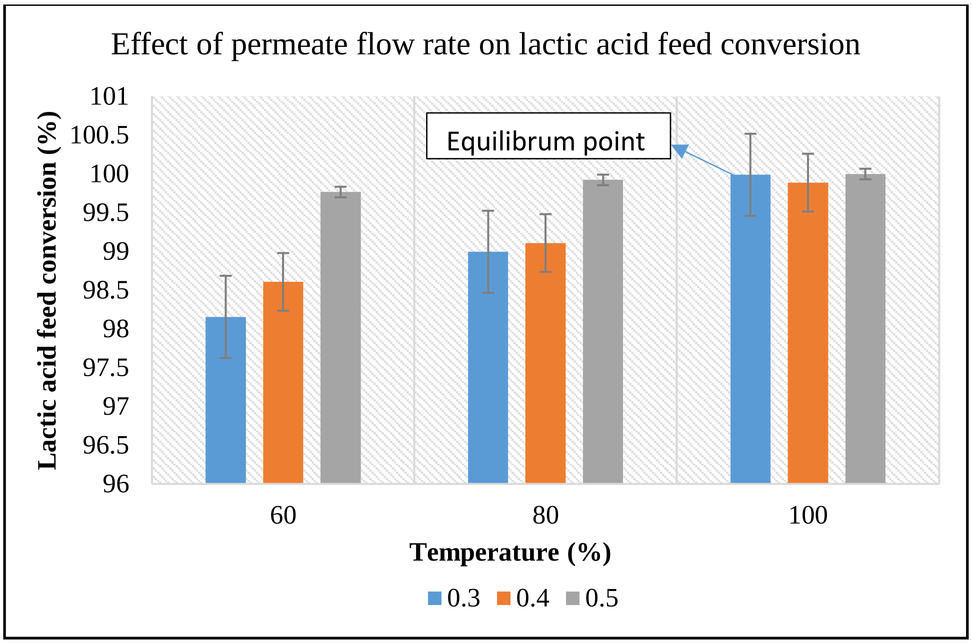

Figure 7.68: Effect of permeate flow rate on lactic acid feed conversion catalysed with amberlyst 15 attached to cellulose acetate membrane at 0.30, 0.40 and 0.50Lmin^{-1}.

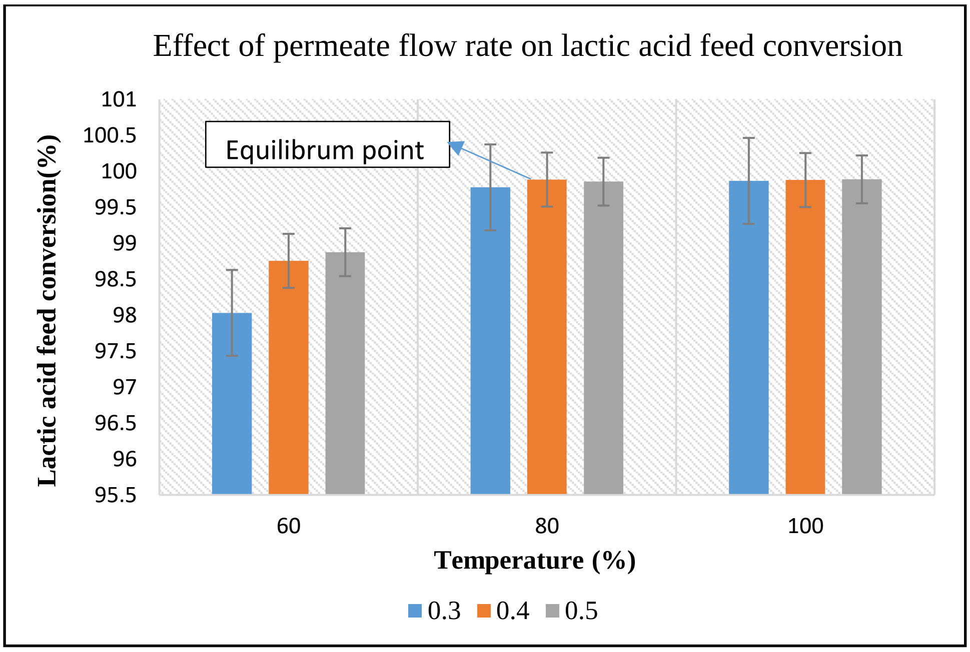

Figure 7.69: Effect of permeate flow rate on lactic acid feed conversion catalysed with dowex50W8x attached to cellulose acetate membrane at 0.30, 0.40 and 0.50Lmin^{-1}.

7.3.5 Observations for the Two Methods

The comparison between batch process and process intensification methods were perform to determine the suitable method for the esterification reaction process. From the result obtained for the batch process esterification, it was found that both the temperature and injection concentration play a part in the conversion of the esterification product. It was found that the temperature of the esterification product is favourable for some of the cation exchange resin catalysts. Batch process esterification catalysed with amberlyst 36 and dowex 50W8x showed a higher conversion of the ester product in contrast to amberlyst 15 and 16 cation-exchange resin. From the observation for the experiments, it was found that attaching cation-exchange resin catalysts to cellulose acetate membrane and using a sweep carrier gas on the permeate side of the separator helps in the equilibrium shift to the forward reaction for the selective removal of the water resulting in a higher conversion of the lactic acid feed.

It was also observed that attaching amberlyst 36 and amberlyst 16 cation-exchange resin with cellulose acetate membrane gave a higher conversion of the lactic acid feed in contrast to amberlyst 15 and dowex 50W8x. Rathod et al. [154] employ the process intensification of esterification of lactic acid and iso-propoanol and observed that lactic acid feed was increased from its equilibrium value of 51 – 86%. It was observed that the process intensification by pervaporation could enhance the conversion of lactic acid feed for production of ethyl lactate. This was also observed in a similar work by Khudsange et al. [153]. It was also confirmed that the process intensification gave a better conversion rate of 100% for the lactic acid feed in contrast to the batch process esterification [155]. From the results obtained from the two esterification reaction processes, it was confirmed that attaching cation-exchange resin catalysts to cellulose acetate membrane and using a carrier gas on the permeate side of the reactor help to shift the chemical equilibrium to the forward reaction hence resulting in a higher conversion of the lactic acid feed in contrast to the batch process.

7.3.6 Investigation of the Effect of Esterification Parameters

The different parameters involved in the batch process esterification including the effect of reaction temperature, catalysts type, catalyst performance were investigated thus:

7.3.6.1 Effect of Temperature for Batch Process Esterification

The effect of the temperature was also analysed during the esterification process. Different temperatures were used for the esterification process and the choice of selecting the temperature was based on the literature. Review has shown that temperature above 120 °C will cause sealing problems [156]. Temperature positively affects the endothermic reaction between lactic acid and ethanol due to Arrhenius equation in the sense that temperature increases the reaction rate of the solvent as it penetrates through pores of the catalysts [156]. During the catalysts cleaning before the batch esterification reaction, amberlyst 36 and dowex 50Wx8 showed a higher activity in contrast to amberlyst 16. The increasing other of the catalytic activity was dowex 50Wx8 > amberlyst 36. The temperatures of the different experiment were carried out at 60, 80 and 100 ^{o}C to determine the effect of the temperature on the different catalyst.

7.3.6.2 Catalysts Performance during batch esterification

The effect of the performance of the different cation exchange resins were also evaluated during the esterification process at different temperatures. During the process it was observed that amberlyst 15 resin catalysts reacted very fast when in contact with the lactic acid and ethanol in contrast to other catalysts. Although the result of the esterification reaction product of this catalyst showed a lower retention time when analysed with GC-MS, the reaction of this catalyst with the reactant liquid reveal a higher catalytic effect with a stronger active site in contrast to other catalyst and as such cannot withstand a higher temperature above 120 ^{o}C. The order of the cation exchange resin performance with the reactant solvent during the esterification process was amberlyst 15 > dowex 50W8x > amberlyst 16 > amberlyst 36.

7.3.6.3 Catalyst Types

The different type of the catalysts used for the batch process was strong cation-exchange resin catalyst with the sulphonic acid functional group (SO_3H) [157]. The structure of this catalyst comprises of styrene-divinyl benzene and strong acidic catalysts as described by the manufacturers (Sigma Aldrich, UK).

7.3.6.4 Effect of Mass Transfer Resistance

The batch process esterification reaction was carried out between the stirring time range of 400 – 800rpm (rotation per minutes) to study the mass transfer resistance. According to Nie at al. [158], the effect of external mass transfer diffusion limitation between the liquid components and the resin catalysts can be avoided by increasing the agitation time of the esterification reaction. During the batch esterification process, it was observed that when the stirring process was increase above 800 rpm, there were no noticeable changes in the rate of the reaction. However, the stirring time was found to be stable above 400rpm [118]. Thus, the esterification process at different temperatures of 60, 80 and 100 ^{o}C was further conducted within agitation speed range of 400 – 800 rpm with 800 rpm at the highest agitation time to ensure that there is no existing mass transfer between the catalyst and the solvent liquid and also to avoid the breakage of the cation-exchange resin at higher rpm [147]. From the results obtained in figure 7.70, it was observed that the solvent concentration increases with an increase in agitation time (sec) [118,157].

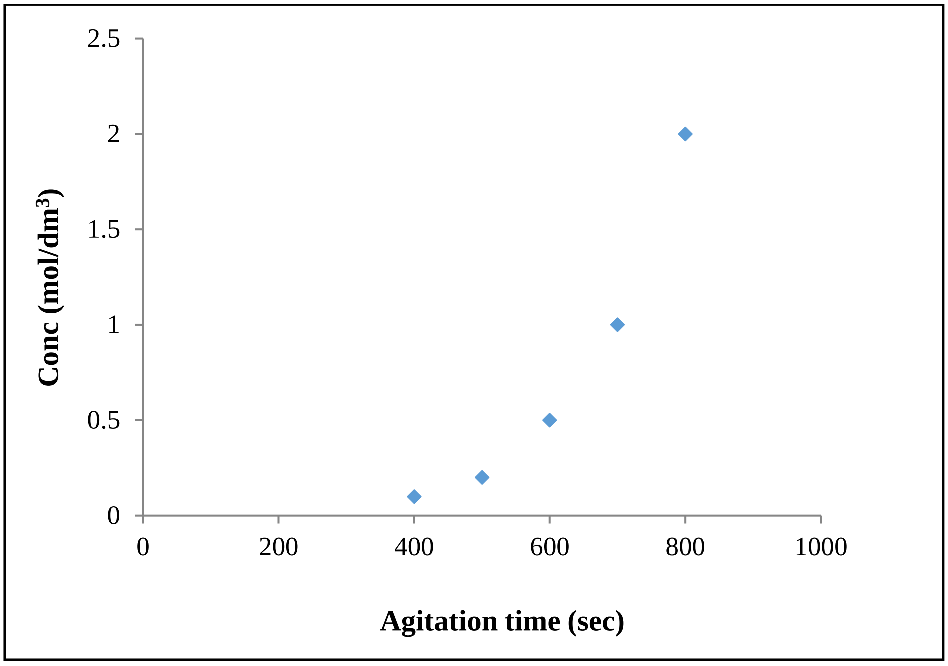

Figure 7.70: Concentration (mol/dm^3) against agitation time (sec).

7.3.6.5 Catalyst Loading

During esterification reaction, it was observed that the esterification reaction involves the donation of a proton from the sulphonic acid group to the carboxylic acid, when acid ionic exchange resins are used as catalysts, the active site on the catalysts is the sulphonic group (SO_3H) that the hydrogen ion with the components involved in the reaction adsorbed on the resin surface [159-160]. Generally, the higher the amount of catalysts used for the esterification reaction, the higher the reaction rate at which the reaction equilibrium is obtained. The different catalyst was loaded at each temperature and at 60 ^oC, 80 ^oC and 100 ^oC. During the washing of the catalyst, dowex50x and amberlyst 15 hydrogen were found to react most with the lactic acid and ethanol in contrast to amberlyst 36 and amberlyst 15 cation exchange resins. This was attributed to the increase in the number of active sites on the catalyst as the reactant solvent penetrate through the pores of the catalyst. The catalyst loading varied in mole ratio form 1:2 to 2:3 wt%. The higher the catalyst loading, the faster the equilibrium was reached due to the increasing number of acid sites available for the reaction to take place.

7.4 Results for the Identification of the Adsorption Components.

The library spectra of compounds which was provided by the School of Pharmacy and Life Sciences (RGU) was used for the interpretation of the FTIR results. Figure 7.71 shows the pictorial view of the FTIR infrared library spectra of compounds.

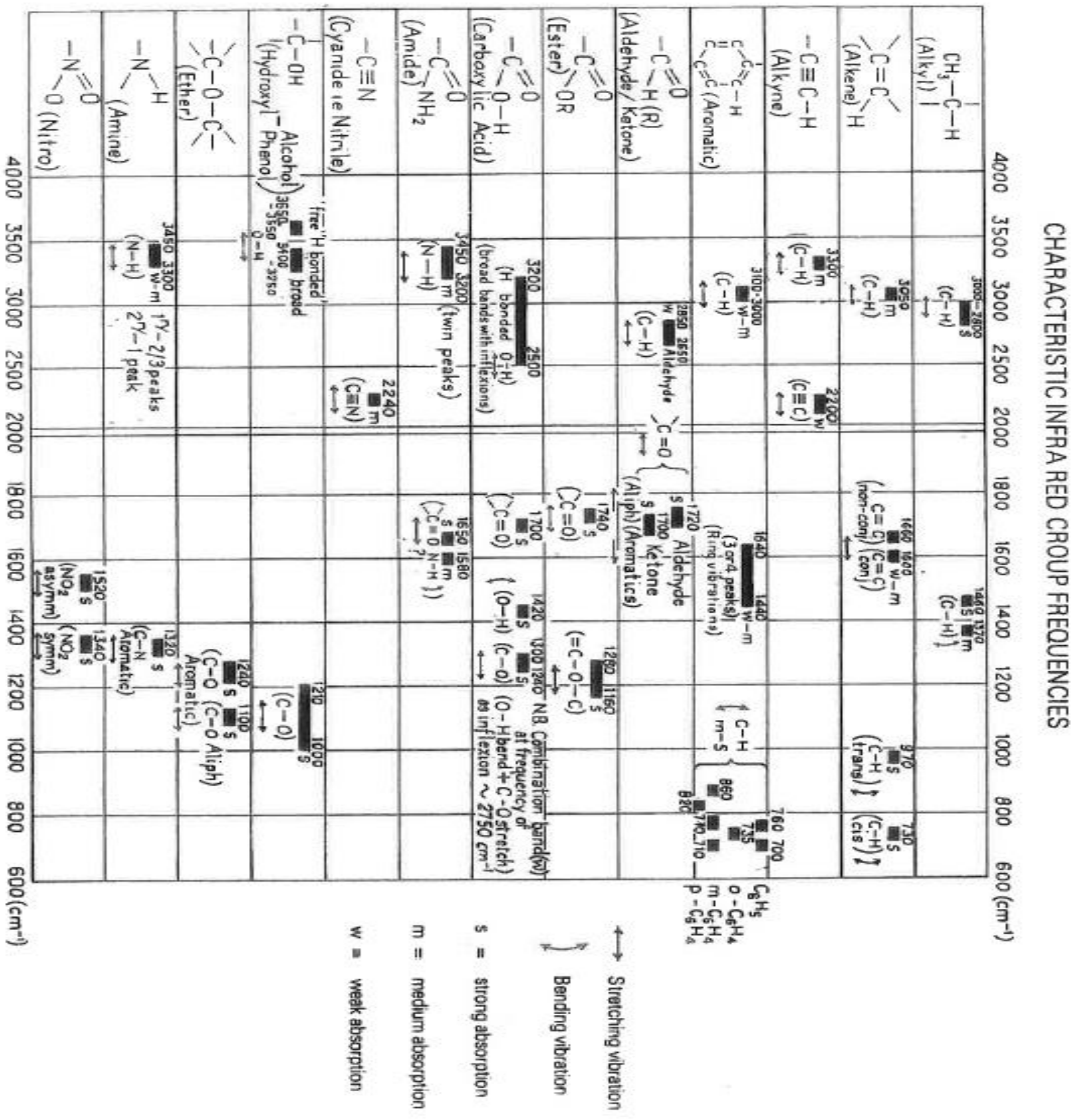

Figure 7.71: Pictorial view of the infrared library spectra of compounds that was used as reference for the FTIR-ATR results interpretation [127].

7.4.1 FTIR-ATR of Fresh Cation-exchange Resins before Esterification.

Figure 7.72 (a-b) present the FTIR-ATR spectrum of the percentage transmittance (%) against the wavelength (cm^{-1}) for the fresh commercial available cation-exchange resins before esterification reaction at different temperatures. The wavenumbers and their respective functional groups were extracted from the different spectra for each temperature. The cation exchange resins were found to be associated with different functional groups with absorptions including: strong (s), weak (w) and medium (m) absorption bands. From figures 7.72a-b, it was found that the small peaks at 2925.49 cm^{-1} and 2921.26 cm^{-1} for amberlyst 15 (7.72a) and amberlyst 36 (7.72b) respectively are due to C-H stretching vibration bonds with a strong absorption on the surface of the resin catalysts. It can also be seen from figure 7.72a-b that the wavenumber at 1123.61cm^{-1} (amberlyst 36) and 1123.25 cm^{-1} (amberlyst 15) were found to correspond to C-O group with a strong absorption strength, whereas the bands at 1414.09 cm^{-1} (amberlyst 36) and 1414.09 cm^{-1} (amberlyst 15) were found to associate with O-H with strong absorption. The C-H, O-H and the C-O functional groups were suggested to arise from the styrene functional group that makes up the structure of the fresh cation-exchange resins catalysts. A similar result was obtained for amberlyst 16 and dowex 50W8x. These results were compared with the FTIR spectra of the liquid sample after esterification at the same reaction temperatures.

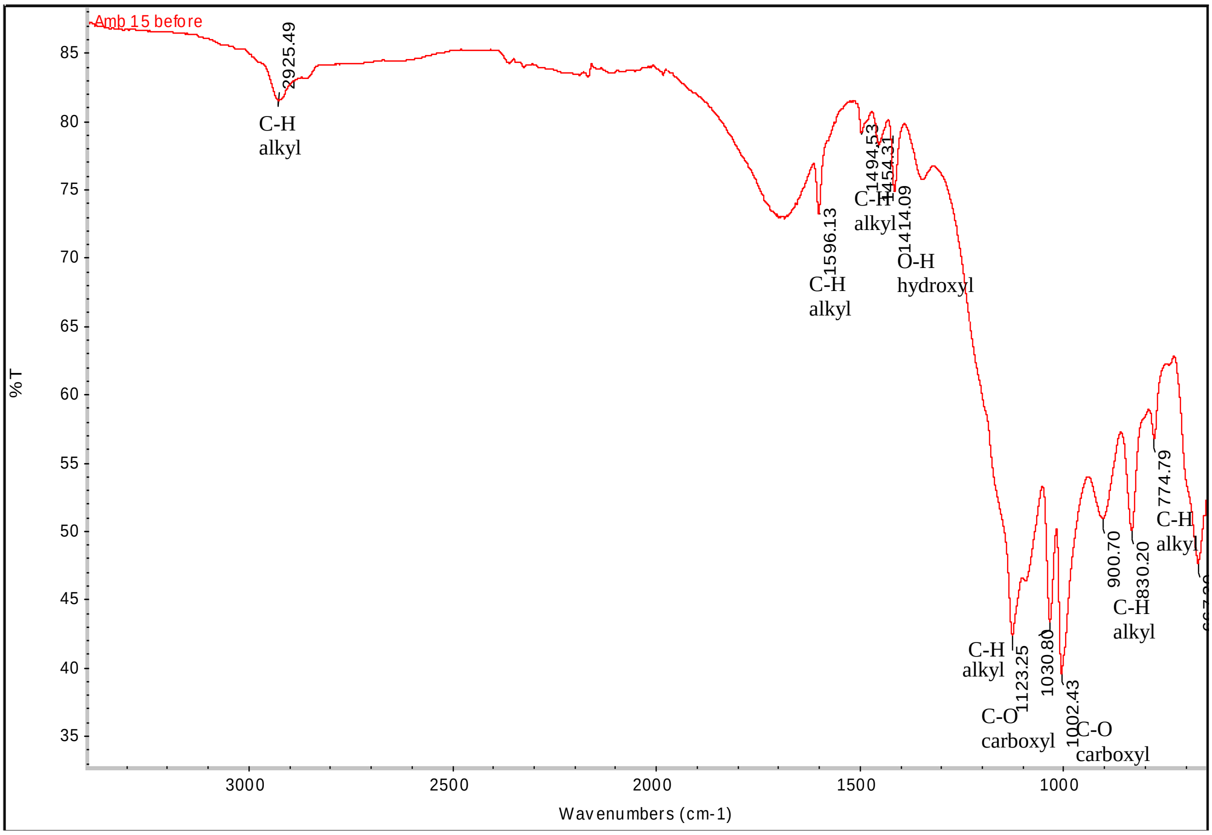

Figure 7.72a: FTIR spectra of amberlyst 15 before esterification reaction.

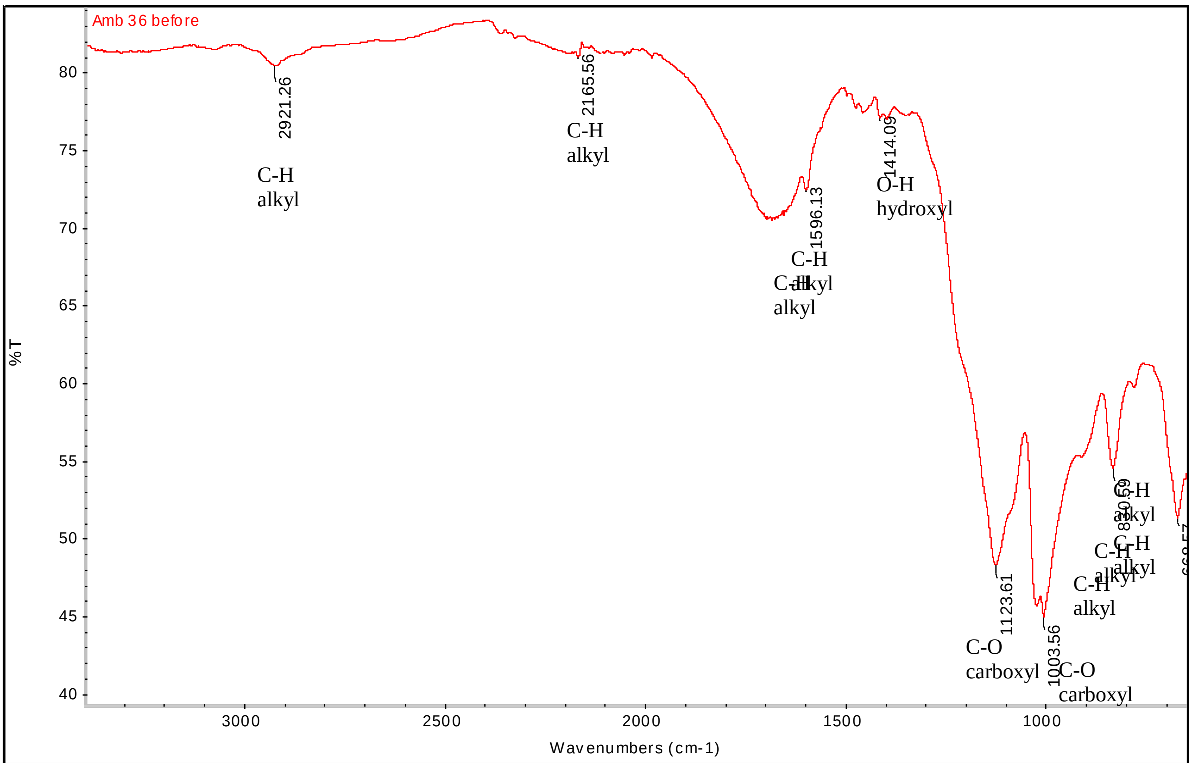

Figure 7.72b: FTIR spectra of amberlyst 36 before esterification reaction.

7.4.2 FTIR-ATR of Cation-exchange Resins after Esterification reaction at 60 °C.

Figure 7.73a-b present the FTIR-ATR spectrum of the percentage transmittance (%) against the wavelength (cm^{-1}) for the esterification product catalysed by the amberlyst 15 (7.73a) and amberlyst 36 (7.73b) cation-exchange resin catalysts at 60 °C. From figure 7.73a, it was observed that the four cation-exchange resins exhibited a wavelength in the range of 2936.07 – 2929.72 cm^{-1} which was attributed to symmetric and asymmetric stretching vibration of C-H functional group [4,9]. Also, from figure 7.73b, it was found that the esterification feed catalysed by amberlyst 36 exhibited a band at round 1594.02 cm^{-1}. This was attributed to the stretching vibration of C-H and C=C functional groups. Also, the C-O stretching vibration bond at 1031.17 (7.73a) and 1003.41 cm^{-1} (7.73b) also possess a sharp band. The bands between 1123 – 1700 cm^{-1} was attributed to the benzene ring vibrations [161]. From figure 7.73a-b, it was suggested from the reoccurrence of C-O group originated from the structure of ethanol and C-H, O-H and C=O from the structure of lactic acid reactant solvents, it was suggested that it could be ethanol and lactic acid that adsorbed most on the surface of the resin catalyst. Zhang et al. [4] obtained a similar result although.

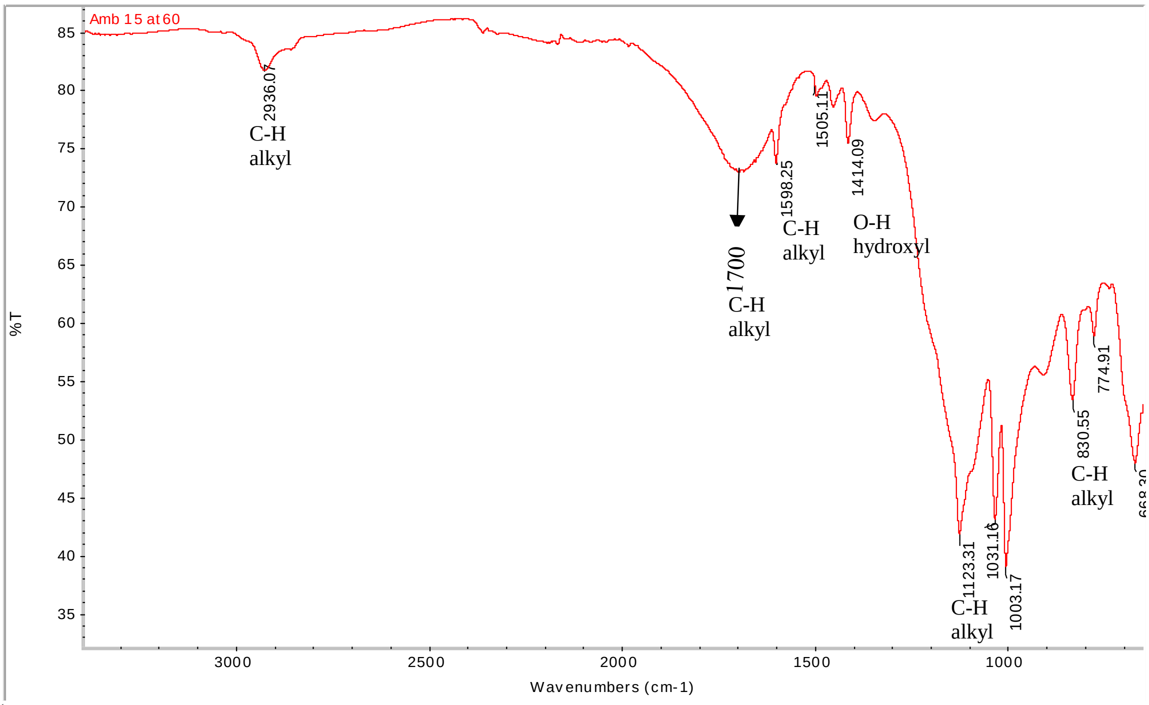

Figure 7.73a: FTIR spectra of esterification reaction product catalysed by amberlyst 15 after esterification reaction at 60 ºC.

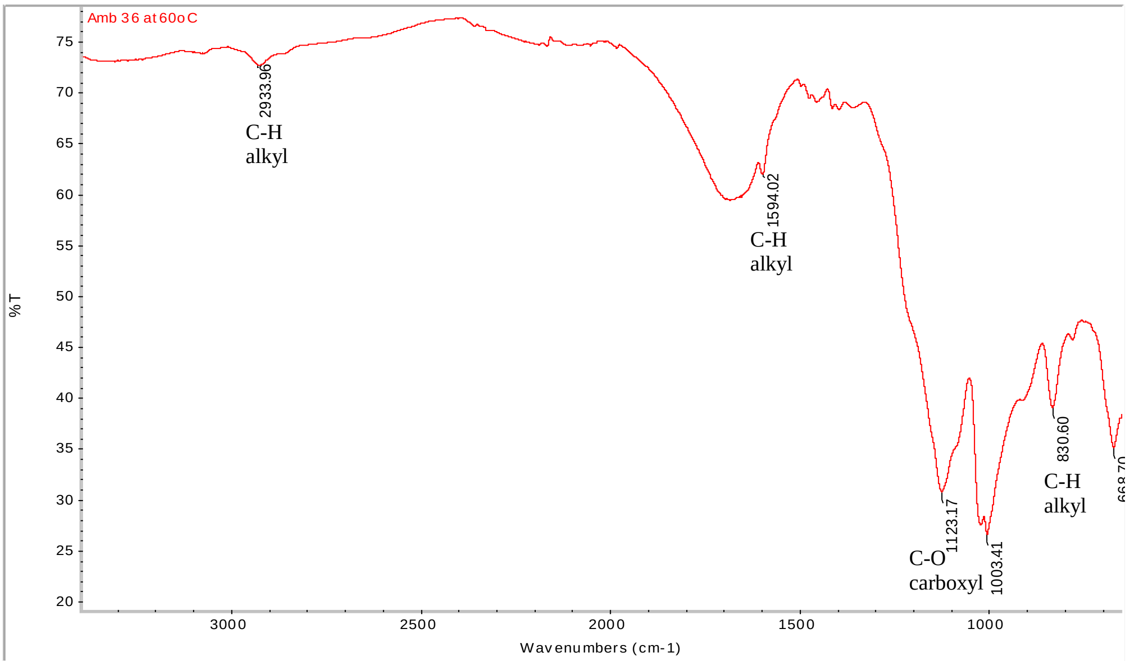

Figure 7.73b: FTIR spectra of esterification reaction product catalysed by amberlyst 36 after esterification reaction at 60 ºC.

7.4.3 FTIR Results for fresh Support and Silica Tubular Membranes.

Figure 7.74a-b present the FTIR of the support (7.74a) and that of silica membrane (7.74b) after the dip-coating process. From figures 7.74a-b, it can be seen that the support membrane exhibited 3 bands on the spectra while the silica coated membrane exhibited upto 5 bands. From Figure 7.74a, it was found that the band at 2335.07 indicated the C-H functional group while the band at 2167.34 and 1977.73 showed the presence of C=O and functional group. It was suggested that the C=O functional groups indicate that these could be due to the alumina oxide in the original support. From Figure 7.74b, it was found that the band at 2356.07 indicated the C-H functional group while the bands at 2165.58 and 1257.44 were attributed to the stretching vibration of C=O and C-O functional groups respectively. Also, the bands at 1088.10 and 1011.89 depicts C-O functional group.

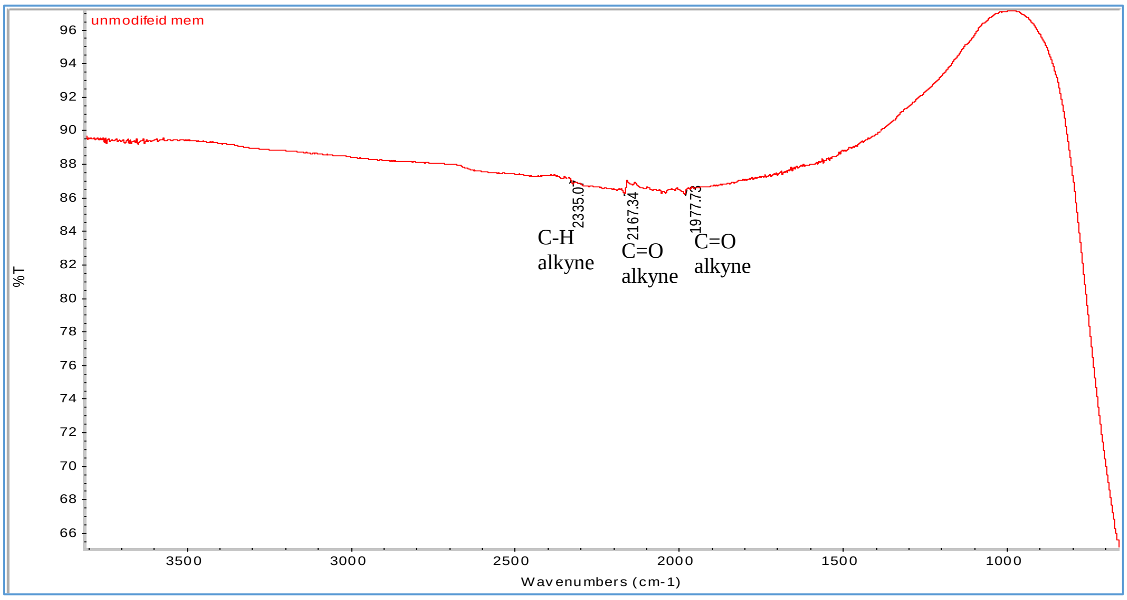

Figure 7.74a: FTIR for unmodified support membrane.

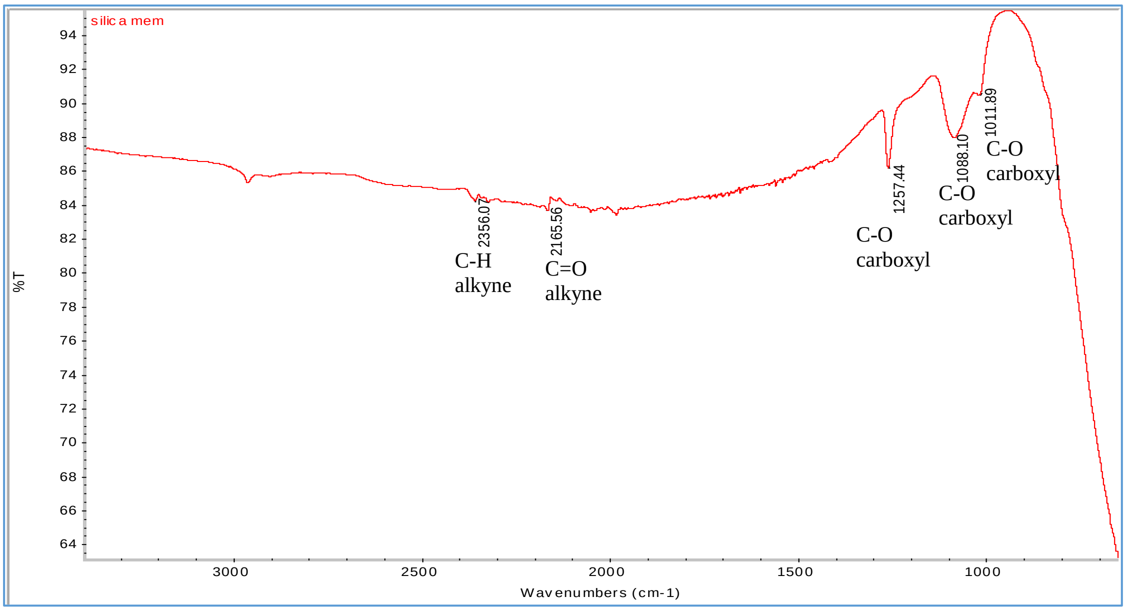

Figure 7.74b: FTIR for silica coated membrane.

7.4.4 Mathematical Model based Langmuir-Hinshelwood Model for Esterification Reaction Mechanism

The Langmuir model was used to explain the reaction mechanisms for the adsorption components on the surface of the resin catalyst. The results were compared with the literature [4,133]. For example, some authors have argued that it is water and ethyl lactate that adsorbed most on the surface of the resin catalysts, while some argued that it is lactic acid and ethanol [4]. From the FTIR-ATR analysis of identified functional groups, ethanol and lactic acid were suggested to adsorbed most on the surface of the resins. It was suggested that the Langmuir-Hinshelwood model could best described the adsorption of components with the strongest adsorption strength on the surface of the resin catalysts, as well as also giving a good fit of behaviour of the resin catalyst employed in the batch process esterification involving lactic acid and ethanol using kinetic correlation of experimental data in comparison to other kinetic methods [162-163]. A similar result was reported in Miao et al. [133].

7.4.4.1 Reaction kinetics using Langmuir Hinshelwood model (LH)

According to Zhang et al 2004 [4], heterogeneous reaction can be presented with many models including LM, ER (Eley-Rideal) and pseudo-homogenous (PH) models. Among them, LH model seems to be more appropriate for describing the esterification kinetics [15]. From the FTIR results, it was suggested that the reoccurrence of C-O, O-H group originated from the structure of ethanol and C-H, and C=O from the structure of lactic acid reactant solvents, it was suggested that it could be ethanol and lactic acid that adsorbed most on the surface of the resin catalysts and were further tested using a simplified mechanism of the Langmuir Hinshelwood model as thus:

$$\mathrm{LA + S \Longleftrightarrow LA - S.} \tag{7.6}$$
$$\mathrm{E + S \Longleftrightarrow E - S.} \tag{7.7}$$

$$\mathrm{E - S + LA - S \Longleftrightarrow LA + S - E + S.} \tag{7.8}$$

$$\mathrm{EL - S \Longleftrightarrow EL + S.} \tag{7.9}$$

$$\mathrm{W - S \Longleftrightarrow W + S.} \tag{7.10}$$

Where LA = Lactic Acid, E = Ethanol, EL = Ethyl Lactate, W = Water and S = Vacant site on catalyst surface [4]. Therefore, the LH model which describes the reaction rate as initial molar amount of lactic acid and water in the esterification process could be written as shown in equation 7.11:

$$\boldsymbol{r = \frac{n_{LA,0}}{W}\left(\frac{dx}{dt}\right)} \tag{7.11}$$

Where r = reaction rate, $^{n}LA,o$ = initial molar concentration of Lactic acid, W= water and dx/dt = time esterification process. From equation 6, the reaction rate constant (k) involving the esterification parameters (lactic acid, ethanol, ethyl lactate and water) can be written as shown in equation 7.12:

$$\mathbf{K} = \boldsymbol{\frac{a_{LA}a_E - a_{EL}a_W}{(1+k_W a_W + k_E a_E + k_{LA}a_{LA} + k_{EL}a_{EL})2}} \tag{7.12}$$

Where k = reaction rate constant, LA = lactic acid, W = water and EL = Ethyl lactate, E = ethanol.

The adsorption coefficient (i) as well as the equilibrium constant (Keq) of the esterification parameters in the esterification reaction can be written using the equation 7.13:

$$\boldsymbol{k_i = \frac{c_i - s}{a_i\ c_s},\ K_{eq} = \left(\frac{a_{EL}\ x\ a_W}{a_{LA}\ x\ a_E}\right)eq} \tag{7.13}$$

Where $n_{LA,0}$= initial molar concentration of lactic acid, k = represent the reaction rate constant, k_i = adsorption coefficient, C_s = the concentration of vacant site on catalyst surface, C_i – s = the concentration of component i on the catalyst surface, a_i = the activity for component (i), a = catalytic activity and K_{eq} = the reaction equilibrium constant.

Although ethanol and water were identified as the most adsorbed components on the surface of the resin catalysts, lactic acid was also suspected to also adsorb on the surface of the resins. However, two mechanisms of the Langmuir model were tested in order to determine which one of these was more suitable to describe the adsorption components.

For mechanism ‘’A’’, it was assumed that ethanol and water adsorbed much stronger than other components in the esterification solution and as such, the adsorption of lactic acid and ethyl lactate were ignored. Whereas for mechanism ‘’B’’, it was assumed that water and lactic acid adsorbed most on the surface of the catalysts and as such ethanol and ethyl lactate were ignored. In both mechanisms, the denominator of the equations (7.12 and 7.13) were used to explain the adsorption parameters. The kinetic equations for the two mechanisms (A and B) were written by combining equation 7.12 and 7.13. In the A mechanism, it was assumed that water and ethanol adsorbed on the surface of the resin catalysts as in the denominator of equation 7.14.

$$\boldsymbol{r = k\ \frac{a_{LA}a_E - \frac{a_{EL}a_W}{keq}}{(1{+}k_W a_W{+}k_E a_E)2}} \tag{7.14}$$

Where r = reaction rate, k = rate constant, ^{a}W=water, ^{a}LA = lactic acid, ^{a}EL= ethyl lactate, Keq = the reaction equilibrium constant, k_W = rate constant for water, k_E = rate constant for ethanol.

In comparison to the first mechanism, in the second mechanism it was assumed that water and lactic acid adsorbed most in the second mechanism as shown in the denominator of equation 7.15.

$$\boldsymbol{r = k\ \frac{a_{LA}a_E - \frac{a_{EL}a_W}{keq}}{(1{+}k_W a_W{+}\ k_{LA} a_{LA})2}} \tag{7.15}$$

Where r = reaction rate, k = rate constant, ^{a}W=water, ^{a}LA = lactic acid, ^{a}EL= ethyl lactate, Keq = the reaction equilibrium constant, k_W = rate constant for water, k_E = rate constant for ethanol. In both A and B mechanisms, three parameters were considered for evaluation at a constant reaction temperature. In mechanism A, the parameters include: k, k_W and k_E whereas for B mechanism, the corresponding parameters are k, k_W and k_{LA}.

From the results obtained for the esterification reaction involving lactic acid and ethanol and the corresponding catalysts, LH model was chosen among the different heterogeneous approaches based on results found in the literature for this type of reaction [15]. Overall, these results further confirmed

Langmuir model as the fitted model for the description of the adsorption components on the surface of the cation-exchange resins. This model was based on a similar work by Zhang et al. [4].

7.4.5 ^{1}HNMR Results for the Identification of Organic Compounds

The results of the esterification feed from the NMR experiments was determined based on the structure of the reactant solvent to determine the connectivity of the bond and also to further validate the FTIR-ATR results. The NMR library spectra of compounds was used for the results interpretation. Figure 7.75 shows the pictorial view of the NMR library spectra of compounds that was used for the results interpretation.

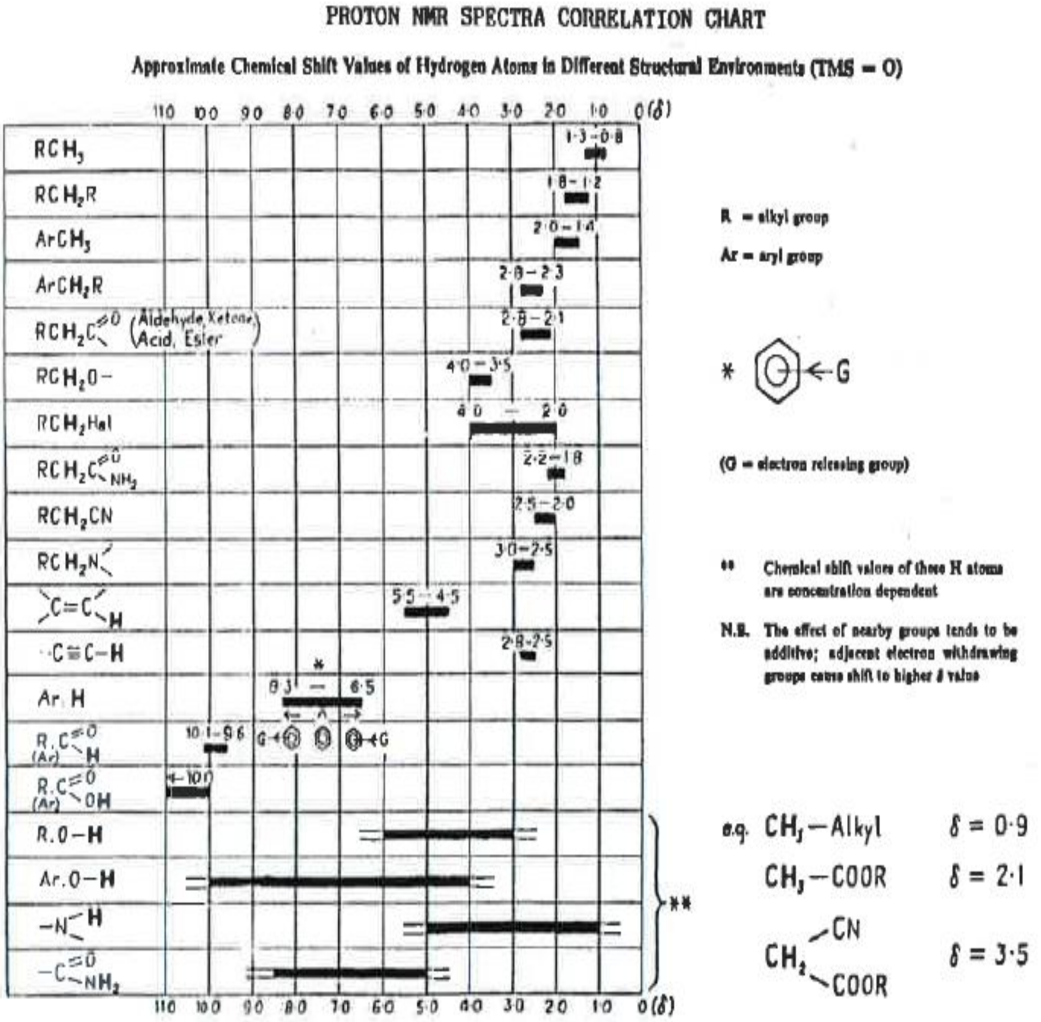

Figure 7.75: Pictorial view of the NMR library spectra of compounds [127].

Figure 7.76 depicts the ^{1}H NMR spectra for the lactic acid feed catalysed by amberlyst 36 cation-exchange resin catalysts at 60 °C. From figure 7.76, it was found that the ^{1}H NMR spectra of the feed exhibited the chemical shift in the range of 1.00 – 5.0 ppm. It was found that there were 5 groups of peaks at 1.2ppm, 3.0ppm, 4.2ppm and 5.1ppm on the spectra indicating that there are 5 type of hydrogens i.e 2 x CH_3, 2 x CH_3 and 1 x CH_2 (4 methyl and 1 methylene group). It was observed from figure 7.76 that there was a smaller peak at a chemical shift of 5.0ppm which was attributed to the shielding effect (peak at upper field e.g 5ppm with respect to 10ppm) [127]. From the spectra, it was found that for the structure of the ethyl lactate, there was a quartet bond from the methylene function group (CH_2) and a triplet bond from the alkyl functional group (CH_3). The distance between the quartet (1H) and the double (3H) in the structure of lactic acid which was used as the reactant solvent, was due to the deshielding effect from the groups because this structure is an aromatic compound. The demarcation between the two peaks were due to the transfer of magnetization between the functional groups. From the library spectra of organic compounds for NMR interpretations (figure 7.76), the chemical shift at 3.81 was suggested to indicate the presence of RCH_2OH and RCH_2OR (the presence of a carboxyl and hydroxyl groups) which was said to arise from the structure of the lactic acid and the ethanol groups. The shift at 1.00ppm was attributed to the primary alkyl group (RCH_3) with triplet bond. The fall within the range of 1.0 to 5.0ppm was because of the fact that there was aryl hydrogen present in the structure (C-H). Also, from the result obtained in figure 7.76, it was found that the characteristic peak of carboxylic (-COOH) proton observed at 3.0ppm and a triple of α-CH3 proton at 4.2ppm and 5.1ppm respectively. The two peaks at 4.2 ppm and 3.0 ppm were the distinct peaks for the confirmation of ethyl esters present in the lactic acid feed sample. This result corresponds to a similar work by Zuriarrain et al. [164].

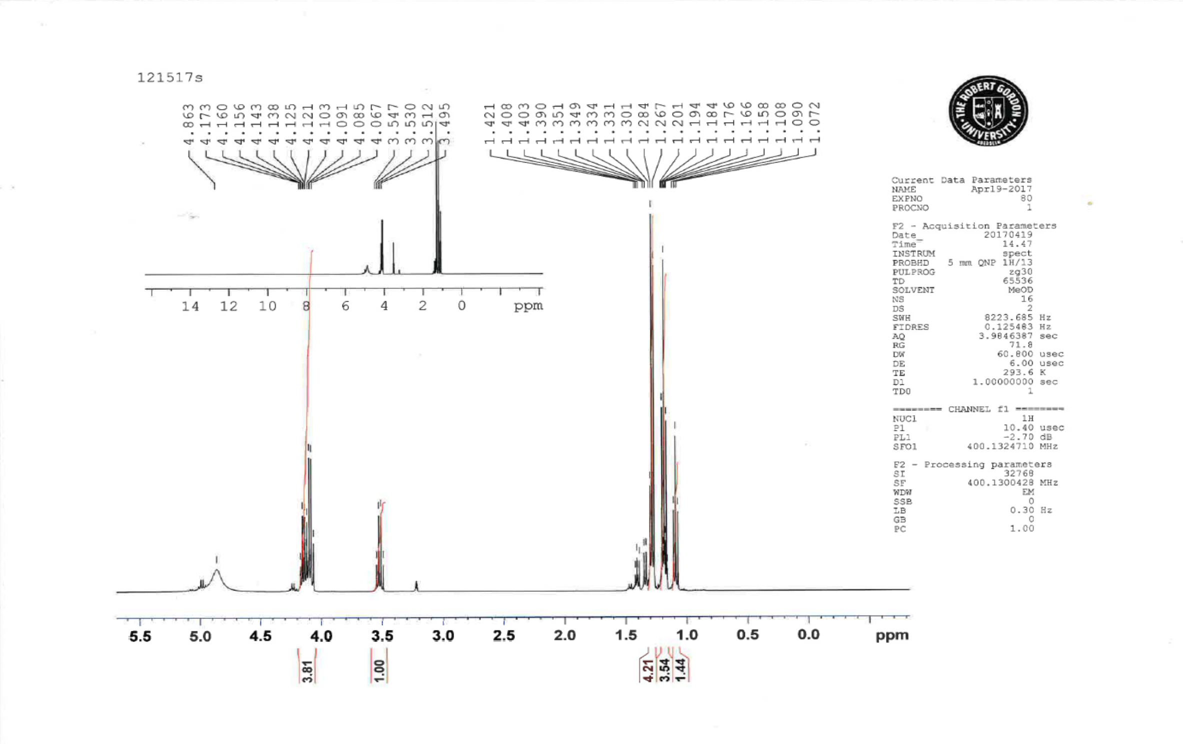

```
Current Data Parameters
NAME              Apr19-2017
EXPNO                     80
PROCNO                     1

F2 - Acquisition Parameters
Date_               20170419
Time                   14.47
INSTRUM                spect
PROBHD    5 mm QNP 1H/13
PULPROG                 zg30
TD                     65536
SOLVENT                 MeOD
NS                        16
DS                         2
SWH                 8223.685 Hz
FIDRES              0.125483 Hz
AQ                 3.9846387 sec
RG                      71.8
DW                    60.800 usec
DE                      6.00 usec
TE                     293.6 K
D1                1.00000000 sec
TD0                        1

======== CHANNEL f1 ========
NUC1                      1H
P1                     10.40 usec
PL1                    -2.70 dB
SFO1             400.1324710 MHz

F2 - Processing parameters
SI                     32768
SF               400.1300428 MHz
WDW                       EM
SSB                        0
LB                      0.30 Hz
GB                         0
PC                      1.00
```

Figure 7.76: Scanned copy of result for ^{1}H NMR Spectrum of batch process esterification product catalysed with amberlyst 36 @ 60 °C.

7.5: Results of Membrane and Resins Characterisation using SEM-EDAX and Liquid Nitrogen Adsorption.

7.5.1 Effect of Thermal Stability of Resin catalyst

The thermal stability of the cation-exchange resin catalysts was also evaluated by examining the surface morphology of both the commercial available resin sample and the cation-exchange resin heated at different temperatures of 60, 80 and 100 °C. From the SEM result obtained, amberlyst 15 cation-exchange resin have been identified to have a very low thermal stability implying that it cannot withstand the effect of high temperature [165]. It was also observed that amberlyst 15 exhibited less thermal stability and less resistance at the temperature of 60˚C indicating that it can break easily at higher temperature. However, amberlyst 16, 36, and dowex 50W8x were found to be more stable.

7.5.2 Effect of Mechanical stability of Resin catalyst

According to Nemec et al. 2005 [65] amberlyst 15 catalyst does not really possess high mechanical stability, however, it is commercially available in particle form. From the SEM result, it was found that amberlyst 15 catalyst showed a less mechanical effect by breaking easily when in contact with the reactant solvent. It was also observed that this catalyst cannot withstand the applied forces of high concentrations of lactic acid from the esterification reaction.

7.5.3 SEM/EDAX Characterisation of the Cation-exchange Resin before Esterification Process.

Figures 7.77(a-d), present the SEM images of the fresh commercial resin catalysts. It can be seen that the surfaces of amberlyst 16 (a), amberlyst 36 (b) and dowex 50xw8 (c) showed a very smooth surface indicating that the resin catalysts were defect-free. A similar result was obtained by Zhang et al. [4]. Before the esterification reaction, the fresh catalyst was expected to show a smooth surface. From figure 7.77d, it was observed that amberlyst 15 exhibited small cracks on the surface in contrast to other catalysts. This Marginal defect observed on the surface of the commercial amberlyst 15 would probably have originated from the sulphonic acid group (SO_3H) in which solid catalyst is made up of thereby indicating a strong catalytic effect [72]. This results for this study are published in Okon et al. [130-131]. The results of the SEM images of the resin catalysts obtained in figure 7.77(a-d) was compared with the results of the cation-exchange resin after the esterification reactions. This was in good agreement with a similar result obtained in the literature [161,120,166,].

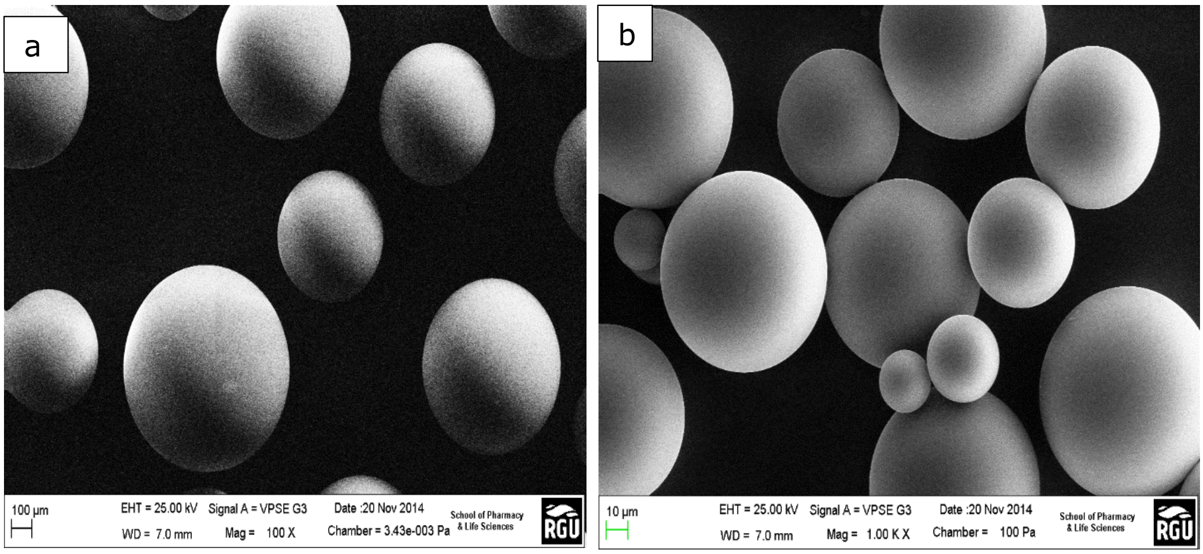

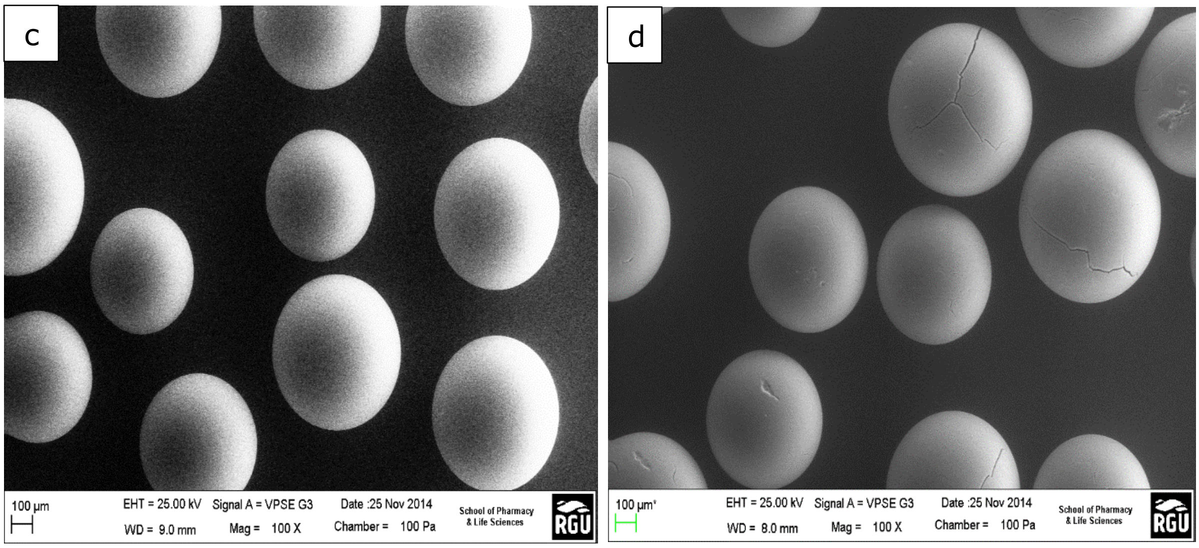

Figure 7.77a-d: SEM morphology of amberlyst 16 (a), dowex 50W8x (b), amberlyst 36 (c) and amberlyst 15 (d) before esterification reaction.

7.5.3.1 EDAX of Fresh Cation exchange resin before Esterification Reaction

The elemental composition of the resin catalysts were also analysed using EDAX and the spectrum is shown in figure 7.78(a-b) and were compared with the EDAX of the resin catalysts after the esterification reaction. Table 7.28a-b shows the elemental composition of the resin with respect to the EDAX spectra. Generally, from Figure 7.78(a-b), it was observed that the EDAX of the resin catalyst consists of different elements such as oxygen (O), carbon (C), aluminium (Al) and sulphur (S). It can be seen from figure 7.78 (a-b), that sulphur (S) exhibited the highest peak on all the spectra in contrast to other elements which is attributed to the sulfonic acid functional group from the chemical structure of the resin catalysts. It was also observed that amberlyst 15 (a) and amberlyst 36 (c) resin catalysts possesses the same element (S, C and O) on their spectra. From table 7.28a-b, it was observed that total atomic weight percent (%) in each spectra of the resin catalysts was found to be 100%, although out of the 100% the different elements comprises of a certain percentage. It can also be seen from table 7.28a-b that carbon possesses a higher weight percentage for all the spectra. It was found that amberlyst 15 and 36 exhibited a higher carbon weight percent of 60.40% (table 7.28a) and 51.75% (table 7.28b) respectively. A similar result was obtained for amberlyst 16 and dowex 50W8x before esterification reaction.

Table 7.28a: Amberlyst 15 EDAX analysis before esterification process

Element	**Weight (%)**	**Atomic (%)**
Carbon (C K)	60.40	81.09
Oxygen (O K)	10.59	10.68
Sulphur (S K)	16.37	8.23
Total	87.36	100.00

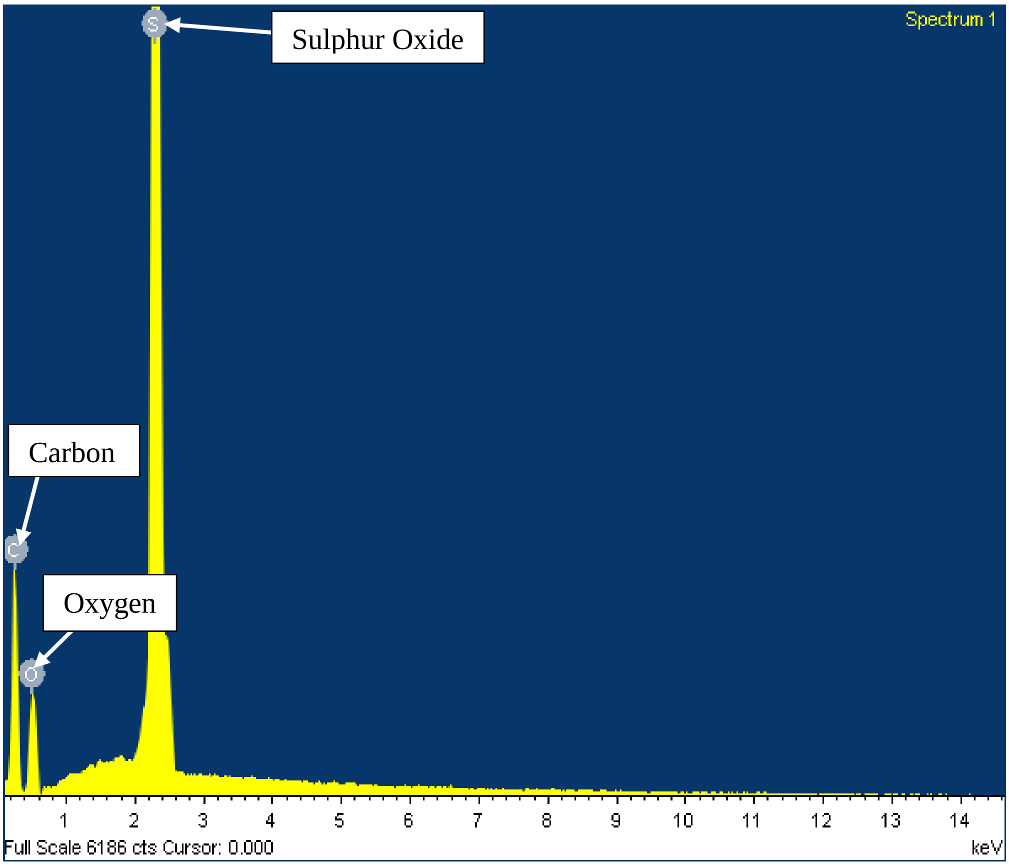

Figure 7.78a: EDAX spectra for Amberlyst 15 fresh commercial resin catalysts before esterification reaction.

Table 7.28b: Amberlyst 36 EDAX analysis before esterification process

Element	**Weight (%)**	**Atomic (%)**
Carbon (C K)	51.75	75.34
Oxygen (O K)	12.73	13.91
Sulphur (S K)	19.70	10.74
Total	84.19	100.00

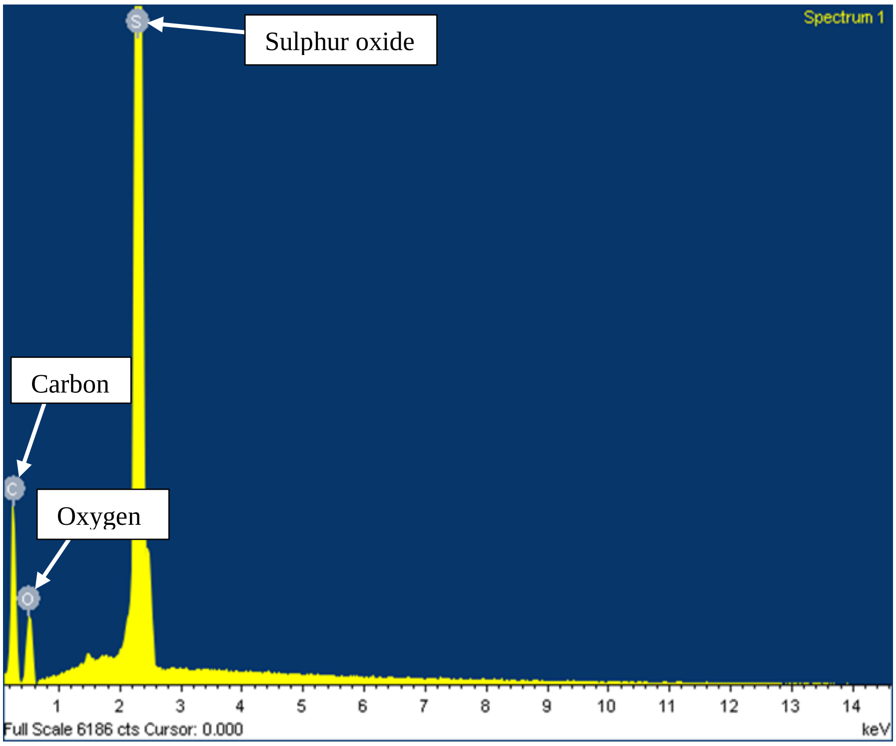

Figure 7.78b: EDAX spectra for amberlyst 36 fresh commercial resin catalysts before esterification reaction.

7.5.4 SEM Characterisation of the Cation-exchange Resin after Batch Esterification Process at 60 °C.

Figure 7.79a-d depicts the SEM micrograph of the amberlyst 16 (7.79a), amberlyst 15 (7.79b), amberlyst 36 (7.79c) and dowex 50W8x (7.79d) resin catalysts after the esterification process at 60 °C. From the SEM results in figure 7.79a-d, it was observed that the pore size of amberlyst 16 (a) and dowex 50W8x (d) resin catalysts showed a reduction in size after the esterification process compared to their SEM surface morphology before the esterification process. It was observed that the pore size reduction was very obvious for dowex 50W8x suggesting the non-stability of the catalysts at 60 °C. However, amberlyst 36 (c) were found to exhibit a bigger pore size with a clear surface with no crack indicating that it can withstand the effect of high temperature and is also suitable for equilibrium limitation process. Although amberlyst 16 (a) also exhibit a clear surface, there were some tiny evidence of perturbation on the surface. It can also be seen that there was a serious crack on the surface image of amberlyst 15 (b) with a reduction on the pore size for dowex 50W8x (d) in contrast to their surface morphology before the esterification process. These changes were suggested to be as the result of the effect of temperature and high concentration of lactic acid on the resins catalysts during the esterification process.

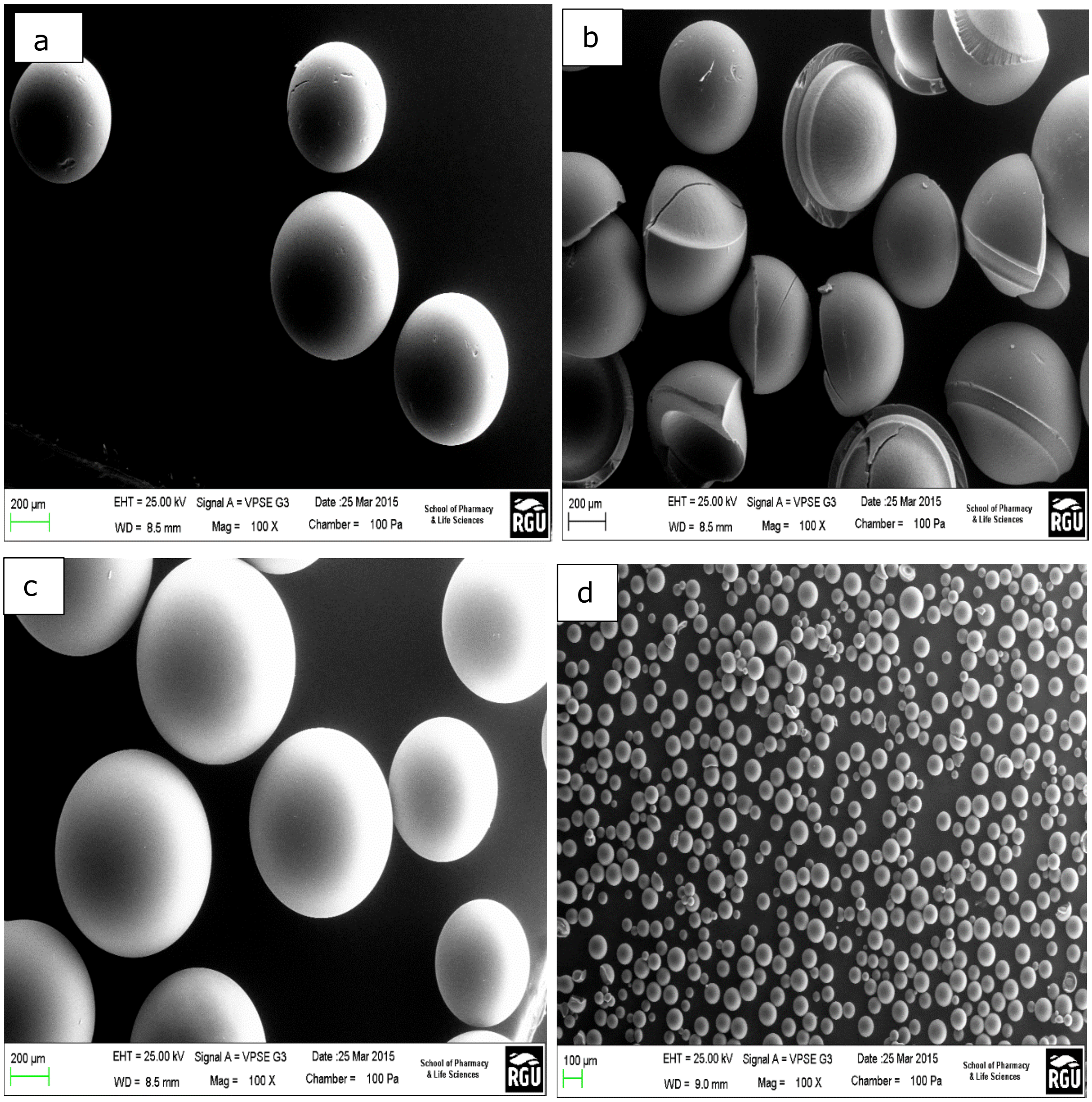

Figure 7.79a-d: SEM morphology of amberlyst 16 (a), amberlyst 15(b), amberlyst 36 (c)and dowex 50W8x (d)after esterification reaction at 60 °C

7.5.4.1 EDAX of Cation-exchange resin After Esterification Reaction at 60 °C.

The EDAX method was used to determine the elemental composition of the cation-exchange resin catalysts after the esterification process at 60 °C. Figure 7.80a-b present the EDAX spectra of amberlyst 36 (7.80a) and amberlyst 15 (7.80b) resin catalysts after esterification at 60 °C. The weight percentage and the atomic percentage of the different elements are also presented in table 7.29a-b. The it can be clearly seen from the EDAX of the resins (figure 7.29a-b), that there was an even distribution of the different elements including sulphur (S), aluminium (Al), carbon (C) and oxygen (O) [161] in the cation-exchange resins after esterification at 60 °C. It was observed that sulphur exhibited the highest peak in all the spectra (Figure 7.29a-b). In contrast to the EDAX of the catalysts before esterification, an additional peak was observed for sulphur in the EDAX of the catalysts after esterification at 60 °C. Although the EDAX of the resin catalysts after the esterification reaction at 60 °C exhibited the same element as the EDAX of the resin catalysts before esterification process, however, it was observed that there was an increase in the weight percent (%) of the different elements after the esterification reaction at 60 °C. It was also found that the weight percent of carbon on amberlyst 36 was found to be 101.86 while the weight percent of carbon for amberlyst 15 was 90.38 at 60 °C, in contrast to the weight percent of the same catalysts before the esterification process. A similar results were obtained for amberlyst 16 and dowex 50W8x.

Table 7.29a: Amberlyst 36 EDAX analysis after batch esterification reaction at 60°C

Element	**Weight (%)**	**Atomic (%)**
C K	101.86	69.57
O K	41.24	21.15
Al K	1.68	0.51
S K	34.28	8.77
Total	179.06	100.00

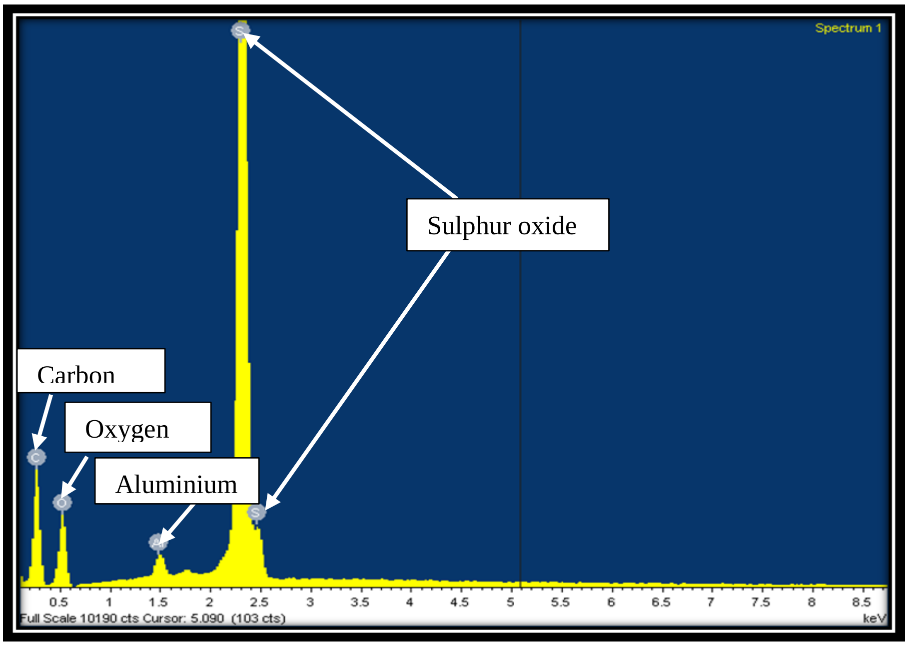

Figure 7.80a: EDAX of amberlyst 36 resin catalysts after esterification reaction at 60 ºC.

Table 7.29b: Amberlyst 15 EDAX analysis after esterification reaction at 60ºC.

Element	Weight (%)	Atomic (%)
C K	90.38	74.66
O K	29.83	18.50
S K	22.09	6.84
Total	142.31	100.00

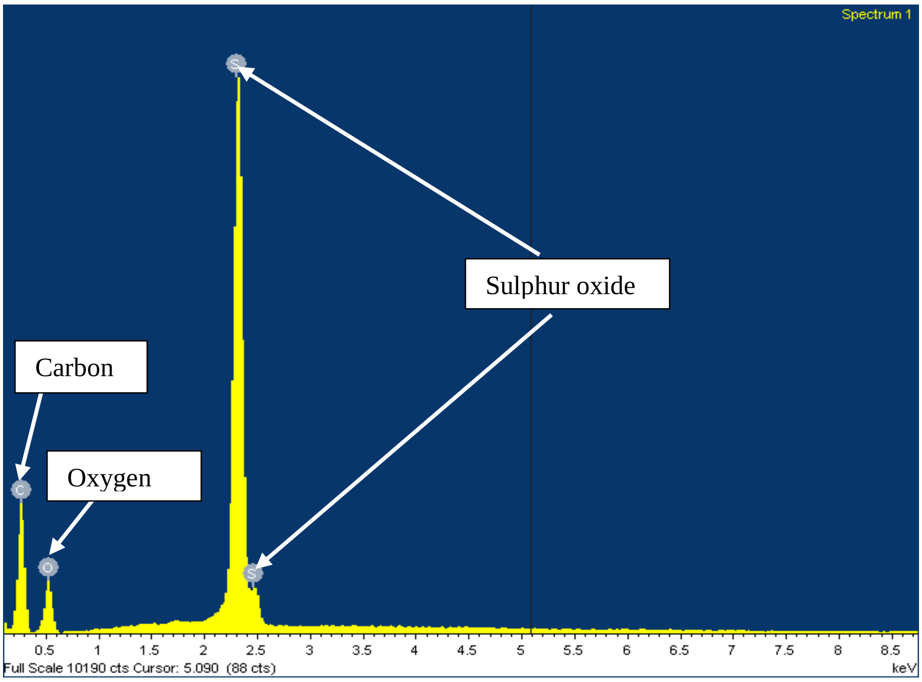

Figure 7.80b: EDXA of the amberlyst 15 resin catalysts after esterification reaction at 60 °C.

7.5.5 SEM/EDAX Results for Support Membranes

Figure 7.81a-c present the SEM surface micrograph of the inner (7.81a), outer (7.81b) and the cross section (7.81c) of the tubular membrane. From the SEM surface morphology of the α-Al_2O_3 support membrane, it was found that there were no noticeable cracks on the inner surface image (7.81a) of the support membrane before the dip-coating process indicating that the membrane was crack free confirming an excellent pore structure for the carrier gas permeation analysis with the membrane sample [84]. A similar result was also obtained by Jin et al. [87] for α-Al_2O_3 support membrane before the dip-coating process [15]. From figure 7.81b, it was also observed that there was some tiny crystal on the surface which could indicate the dispersed of alumina coating on the outer surface image of the support membrane. It was also observed on the cross-sectional image (figure 7.81c) that the support composes of an α-Al_2O_3 layer of 0.4μm in size. These results were further compared with the SEM micrograph of the membrane after the silica dip-coating process.

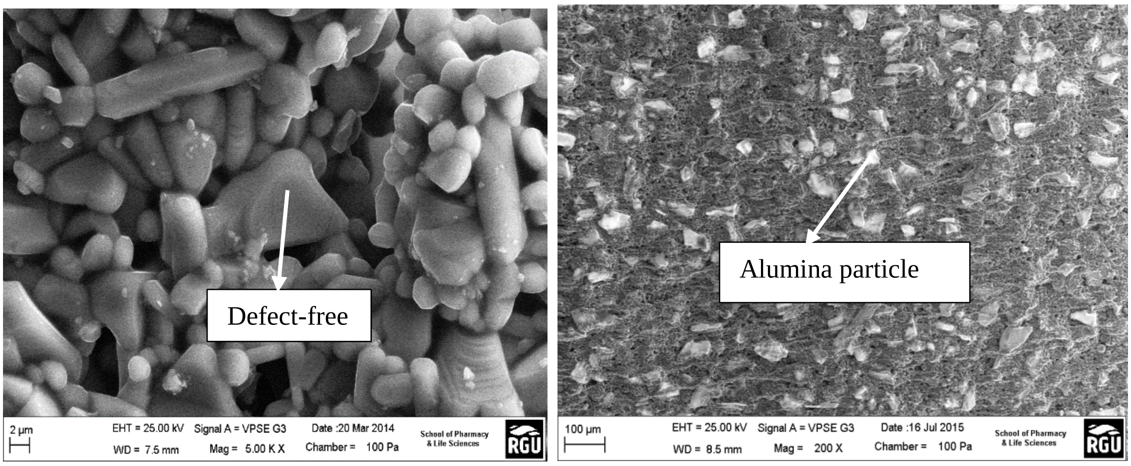

(a) Inner surface of support (b)outer surface of support

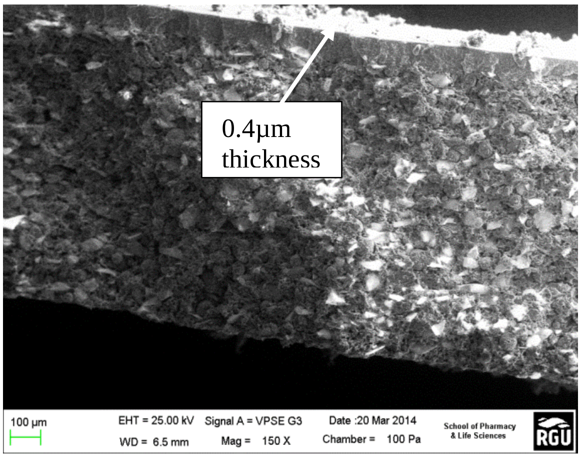

(c) Cross section

Figure 7.81a-c: SEM micrograph of the inner (a), outer (b) and cross sectional (c) surface of the support membrane before the dip-coating process.

Figure 7.82 present the EDAX of the support sample. From figure 7.82, it was observed that the material for the support sample consists of different elements including carbon (C), titanium (Ti), aluminium (Al) and oxygen (O) [15],[76]. It was also found that the Al, Ti and O exhibited a higher peak on the spectra indicating that the fresh commercial available membrane support was coated with different layer including Al_2O_3 [16] and TiO_2 which are suggested as the major materials that was used for the manufacture of the membrane support. The weight and atomic percentage of the different elements were also determined from the EDAX results. It was observed that Al, Ti and oxygen exhibited the highest weight and atomic percent as shown in table 7.30. It was found that Al exhibited 43.04 wt% with the respective atomic % of 19.83. However, oxygen showed the weight percent of 42.62 wt% with the 58.79 atomic %. Although Ti was found to exhibit a higher peak on the EDAX spectra, however, the weight percentage composition was found to be less than (9.46%) that of Al which confirmed that the fresh support composed of a higher amount of Al_2O_3 compared to TiO_2.

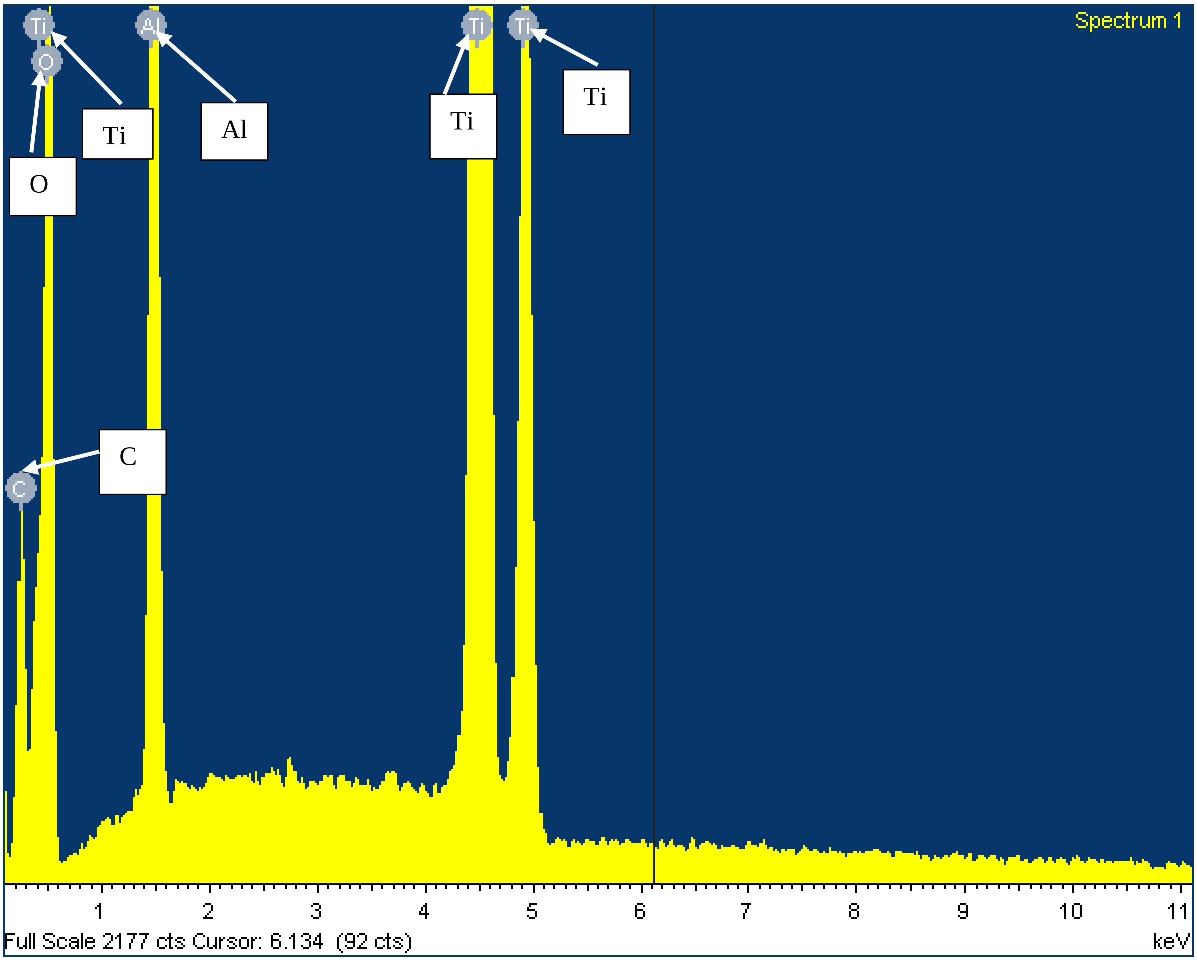

Figure 7.82: EDXA of the membrane support outer surface before the dip-coating process.

Table 7.30: Support EDAX analysis before the dip-coating process

Element	**Weight (%)**	**Atomic (%)**
C K	4.88	3.99
O K	42.62	58.79
Al K	43.04	19.83
Ti K	9.46	17.39
Total	100	100

7.5.6 SEM-EDAX of the Dip-coated Silica Membrane

Figure 7.83a-c present the SEM surface image of the dip-coated membrane. From the results obtained in figure 7.83a-c, it was found that there was a great difference between the support surface image and the surface image of the dip-coated silica membrane. From the result obtained for the inner surface image (figure 7.83a), it was observed that there was a whitish particle on the surface indicating the effect of the silica layer in which the membrane was coated with. Although the membrane showed a crystalline surface, there was no noticeable crack on the surface indicating that the layer was free from defect. It was also observed that there was a deposition of the SiO_2 particles on top of the α-Al_2O_3 support layer. A similar result was also observed by McCool et al. [86].

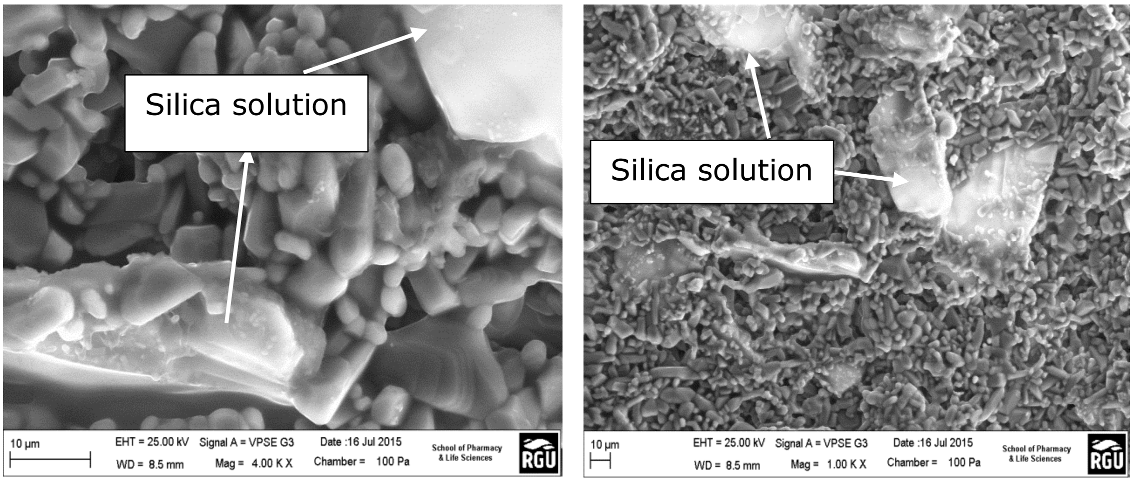

(a) Inner surface of support (b) Outer surface of support

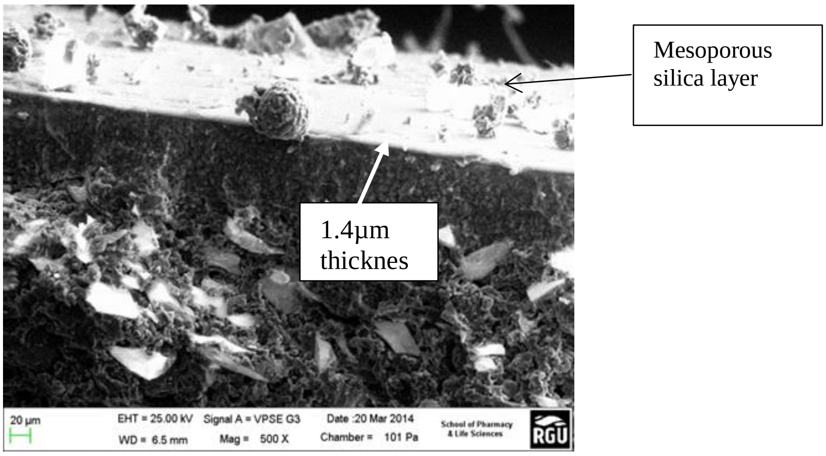

(c) Cross section

Figure 7.83: SEM surface micrograph of the inner (a), outer (b) and cross section (c) of silica membrane after the dip-coating process.

The sample analysis was further carried out using EDAX to identify the component of the different layer that was distributed on the membrane surface. Figure 7.84 shows the EDAX micrograph of the dip-coated membrane. From figure 7.84, it was found that the EDAX results obtained showed that the elemental composition of the dip-coated silica membrane consists of elements such as silicon (Si), titanium (Ti), oxygen (O), carbon (C), chlorine (Cl) and Aluminum (Al) [84]. However, Al and Si showed a higher concentration in contrast to other elements as shown in table 7.31. It also observed that

Si exhibited a higher weight percent value of 32.21% with the respective atomic percent of 19.9%. Although Si and Al exhibited almost the same peak height on the spectra, however, the percentage weight of Si was found to be higher than that of Al. This could indicate that the commercial available support was initially coated with Al_2O_3 and TiO_2 and subsequently coated with SiO_2. A similar result was obtained study by Tomita et al. [144]. From the EDAX result it was found that the higher weight percentage of Si, O and C in the membrane confirms that the silica layer was successful formed on the porous of the alumina support.

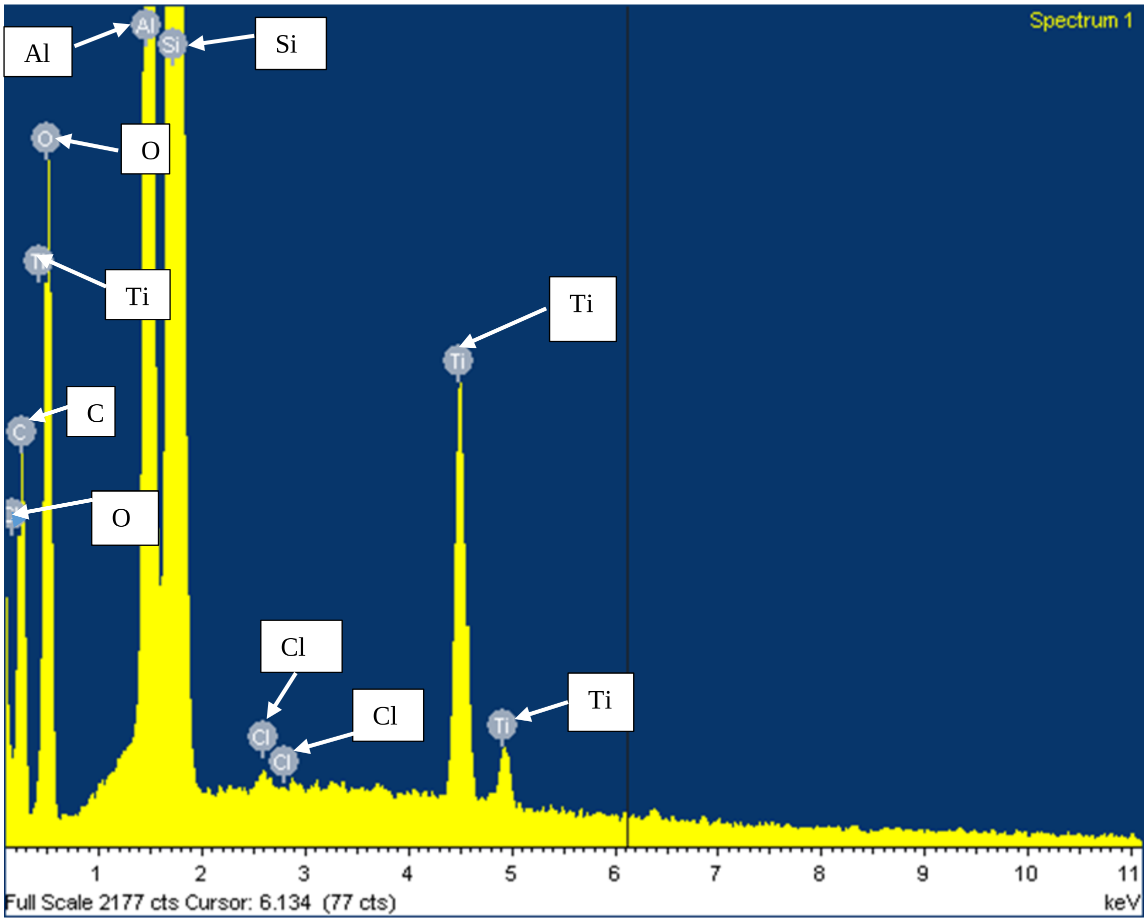

Figure 7.84: EDXA spectra of the dip-coated membrane

Table 7.31: Silica membrane EDAX analysis after the dip-coating process

Element	Weight (%)	Atomic (%)
C K	31.97	46.17
O K	26.74	28.99
Al K	5.81	3.74
Si K	32.21	19.90
Cl K	0.08	0.04
Ti K	3.20	1.16
Total	100.01	100.00

7.5.7 SEM/EDAX for Flat Sheet Cellulose Acetate Membrane

Figure 7.85 a and b present the SEM micrograph of the fresh cellulose acetate membrane before process intensification while figure 7.85c and d depicts the SEM micrograph of cellulose acetate/resin cross section and outer surface after esterification reaction. From figure 7.85a, it can be seen that the surface image of the cellulose membrane showed a cleared image for the fresh commercial acetate membrane indicating that the membrane was defect-free. After the esterification process (figure 7.85b), it could be seen that there some tiny particles which could indicate an even distribution of the reactant solvent deposited on the surface of the membrane sample. In figure 7.85c and d, the boundary layer between the catalytic and the separation layer can be clearly seen.

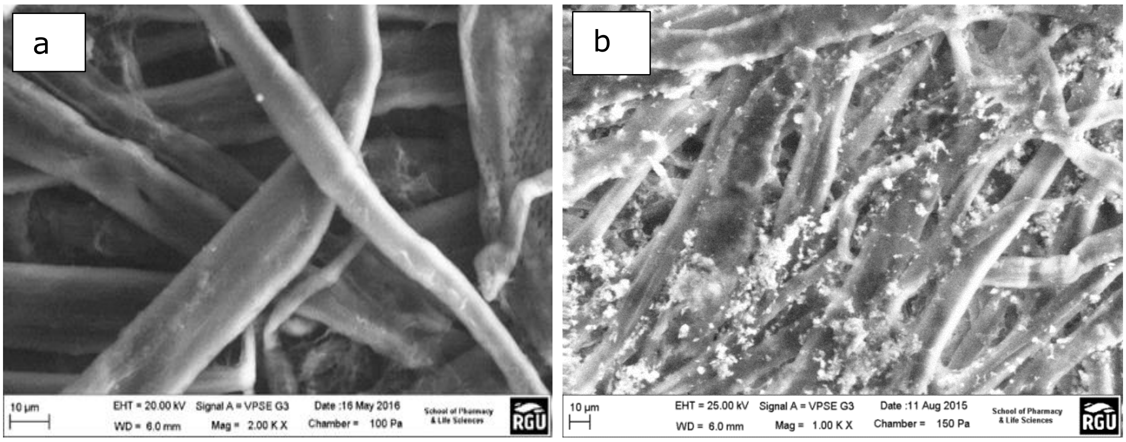

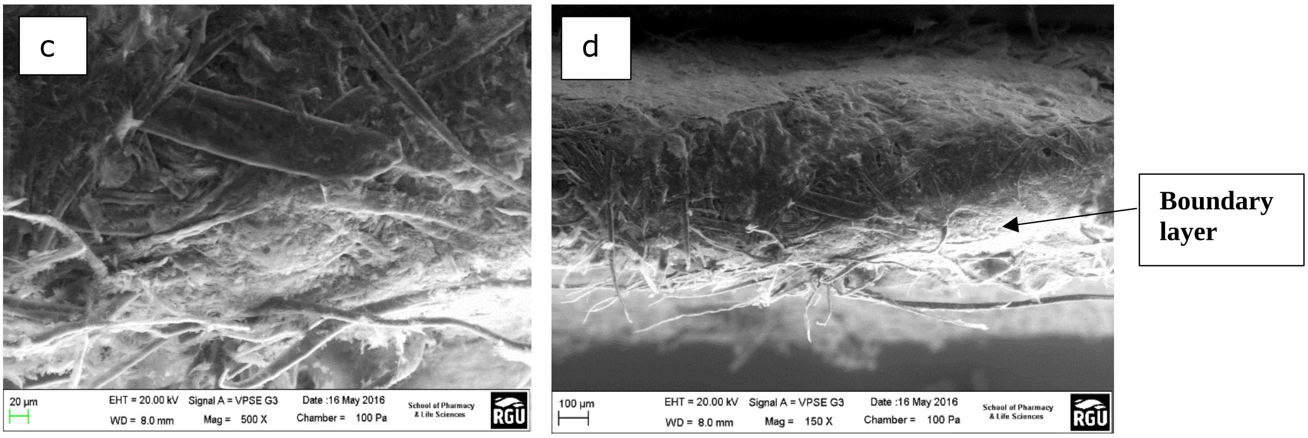

Figure 7.85: Surface image of the cellulose acetate before (a) and after (b) attached to cation-exchange and surface image of the cellulose acetate/membrane after esterification reaction (c and d).

The EDAX method was further used to confirm the presence of compounds on the surface of the cellulose acetate membrane. From figure 7.86a and b shows the EDAX of the cellulose acetate membrane before (a) and after (b) the esterification process. From figure 7.86a, the EDAX of the membrane before esterification consist of the different elements including calcium (Ca), Oxygen (O), carbon (C), and Silicon (Si) as shown in table 7.32a-b. From figure 7.86b, it was observed that after the process intensification, the cellulose acetate membrane exhibited different elements on the structure including calcium (Ca), Oxygen (O), carbon (C), silicon (Si) and Aluminium (Al) as shown in table 7.32a-b.

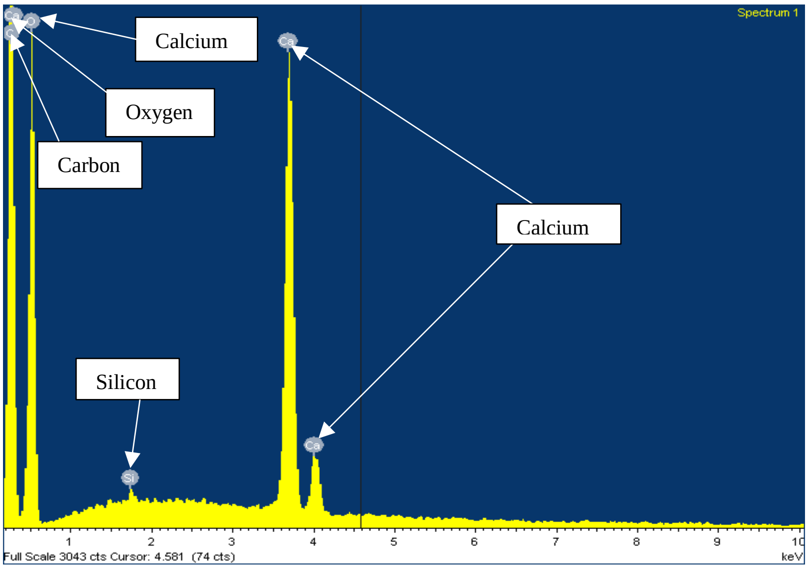

Figure 7.86a: EDAX spectra of the cellulose acetate membrane before esterification process.

Table 7.32a: Cellulose acetate EDAX analysis before the process intensification

Element	Weight (%)	Atomic (%)
C K	39.71	48.73
O K	52.31	48.19
Si K	0.27	0.09
Ca K	7.38	2.73
Total	100	100

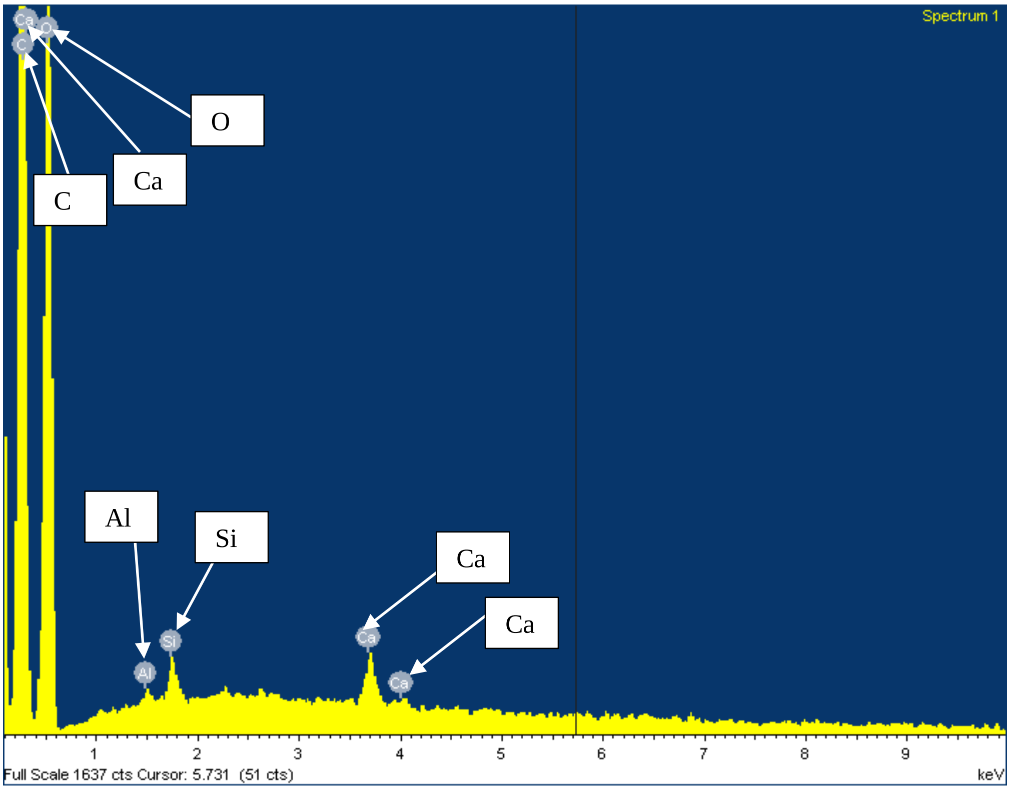

Figure 7.86b: EDXA spectra of the cellulose acetate membrane after esterification process.

Table 7.32b: Cellulose acetate EDAX analysis after the process intensification

Element	Weight (%)	Atomic (%)
C K	46.39	53.88
O K	52.27	45.57
Al K	0.13	0.07
Si K	0.39	0.19
Ca K	0.82	0.29
Total	100.00	100.00

7.6 Results of Cation-exchange resin and Membrane Characterisation using Liquid Nitrogen Adsorption-desorption Method.

7.6.1 Liquid Nitrogen Adsorption of Tubular Silica Membrane

Figures 7.87a-d shows the BET and BJH isotherm for the support while figure 7.88a-d shows the BET and BJH isotherms for the silica membrane. From the result obtained in 7.87a, it was observed that the surface area of the support was low (0.206 m^2/g), in contrast to the dip-coated membranes (0.253 m^2/g) as shown in table 7.33. It was assumed that there could have been a weak interaction between the adsorbing gas molecule and the support thereby resulting in a low surface area [95],[129]. According to Lee et al. [87], the adsorption isotherm shows various types based on the pore structure of the porous material. The result of the BET isotherm for the support in Figure 7.87a showed a flat curve with no hysteresis for both adsorption (red line) and desorption (blue line) indicating a type III isotherm from the IUPAC classification of BET adsorption isotherm [97].

Figure 7.88a, presents the BET isotherms of the silica membranes. It was found that the BET isotherms for the dip-coated membranes was in good agreement with the type IV and V isotherm which is characteristic of a mesoporous structure with hysteresis loop [82]. Lee et al. [97] obtained a similar result. Also, from figure 7.88a, it can be seen that there was an expansion in the hysteresis loop of the membrane after the 1st dip-coated process similar to the type IV isotherm. It was suggested that this may be due to the capillary condensation formation in the mesoporous as the amount of adsorption increases sharply at an elevated temperature [97,82]. Figure 7.87c and 7.88c shows the plot of the amount of the gas adsorbed (volume at STP (cc/g)) against the relative pressure (P/P_o). After the dip-coating process, the membrane pore diameter was expected to reduce in order to allow the selective transport of the gas molecule across the membrane [87]. From figure 7.87c and 7.88c, it was observed that the pore diameter of the membrane did not reduce accordingly as shown in figure 7.88d. Although the pore diameter did not reduce as expected, the obtained values still indicated a characteristic feature of a mesoporous classification with a pore diameter in the range of 2-50 nm [71,97].

Table 7.33: BET and BJH values for the support and 1st silica membranes at 77 K.

Fragment (Number of dips)	BET Surface area (m^2/g)	BJH Pore diameter(nm)	Pore Volume (cc/g)	Slope	Intercept
unmodified	0.206	4.175	0.002	15554.123	1.357*E+03
1st dip-coating	0.253	4.180	0.006	5852.337	7.933*E+03

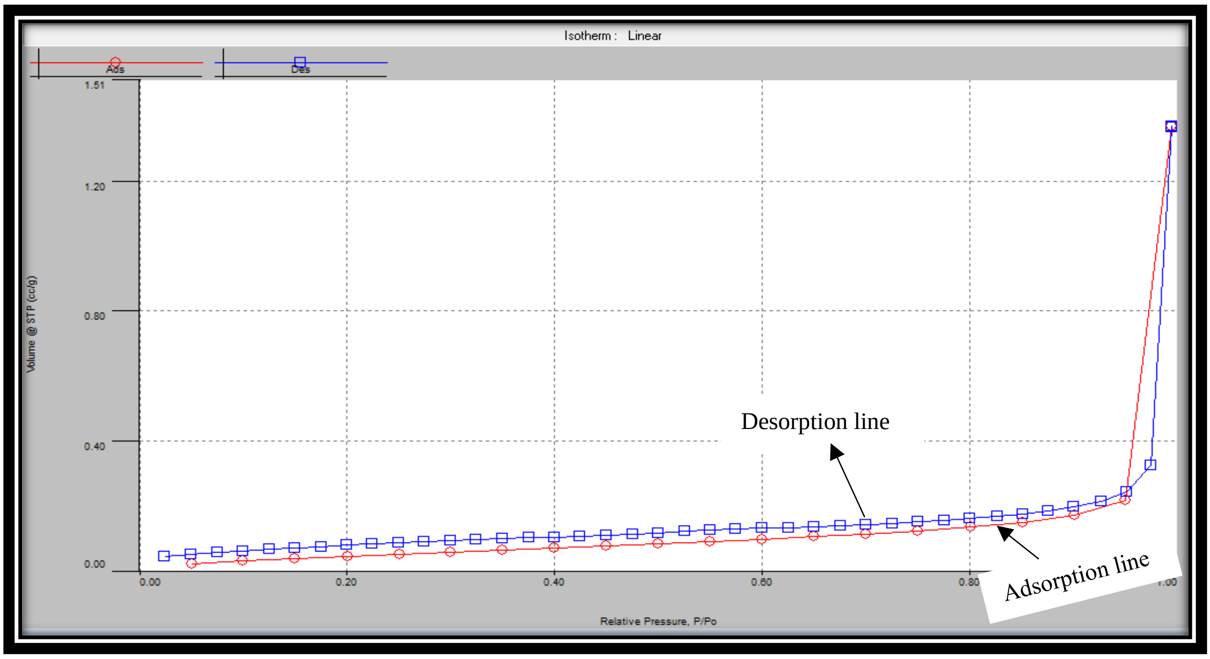

Figure 7.87a: BET isotherm for the fresh support membrane at 77 K.

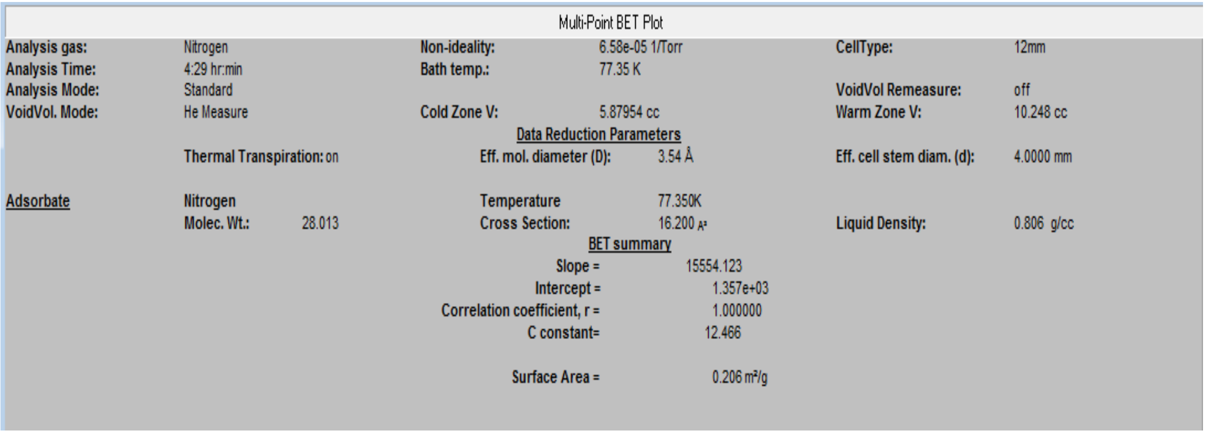

```
                                   Multi-Point BET Plot
Analysis gas:      Nitrogen                Non-ideality:    6.58e-05 1/Torr     CellType:            12mm
Analysis Time:     4:29 hr:min             Bath temp.:      77.35 K
Analysis Mode:     Standard                                                     VoidVol Remeasure:   off
VoidVol. Mode:     He Measure              Cold Zone V:     5.87954 cc          Warm Zone V:         10.248 cc
                                          Data Reduction Parameters
                   Thermal Transpiration: on    Eff. mol. diameter (D):  3.54 Å   Eff. cell stem diam. (d):  4.0000 mm

Adsorbate          Nitrogen                     Temperature          77.350K
                   Molec. Wt.:      28.013      Cross Section:       16.200 Å²    Liquid Density:      0.806  g/cc
                                          BET summary
                                        Slope =                 15554.123
                                    Intercept =                     1.357e+03
                     Correlation coefficient, r =                  1.000000
                                   C constant=                    12.466

                                 Surface Area =                    0.206 m²/g
```

Figure 7.87b: BET description for support membrane.

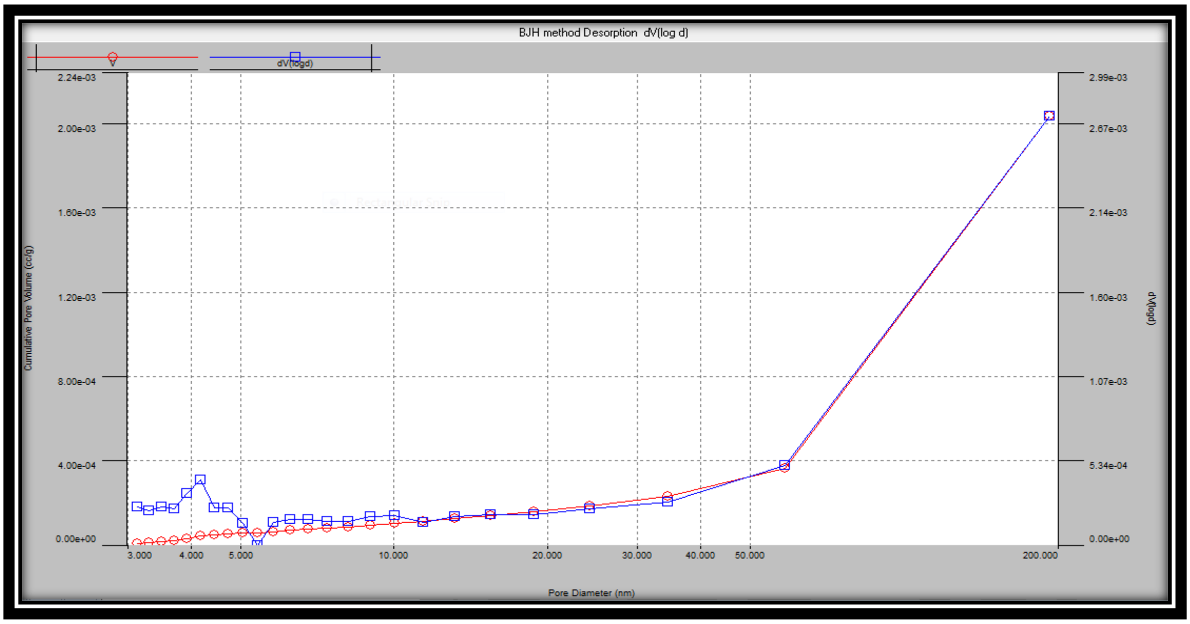

Figure 7.87c: BJH curve for the support at 77 K.

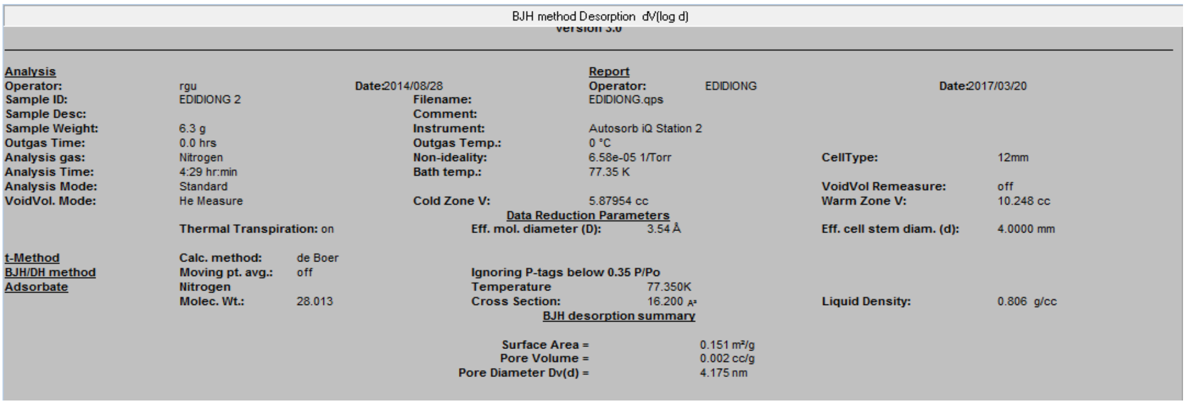

```
                              BJH method Desorption  dV(log d)
                                        version 3.0
_______________________________________________________________________________________
Analysis                                                 Report
Operator:          rgu           Date:2014/08/28         Operator:       EDIDIONG              Date:2017/03/20
Sample ID:         EDIDIONG 2           Filename:        EDIDIONG.qps
Sample Desc:                            Comment:
Sample Weight:     6.3 g                Instrument:      Autosorb iQ Station 2
Outgas Time:       0.0 hrs              Outgas Temp.:    0 °C
Analysis gas:      Nitrogen             Non-ideality:    6.58e-05 1/Torr       CellType:              12mm
Analysis Time:     4:29 hr:min          Bath temp.:      77.35 K
Analysis Mode:     Standard                                                    VoidVol Remeasure:     off
VoidVol. Mode:     He Measure           Cold Zone V:     5.87954 cc            Warm Zone V:           10.248 cc
                                            Data Reduction Parameters
                   Thermal Transpiration: on    Eff. mol. diameter (D):   3.54 Å    Eff. cell stem diam. (d):  4.0000 mm

t-Method           Calc. method:    de Boer
BJH/DH method      Moving pt. avg.: off         Ignoring P-tags below 0.35 P/Po
Adsorbate          Nitrogen                     Temperature            77.350K
                   Molec. Wt.:      28.013      Cross Section:         16.200 Å²    Liquid Density:       0.806  g/cc
                                                 BJH desorption summary

                                           Surface Area =            0.151 m²/g
                                            Pore Volume =            0.002 cc/g
                                     Pore Diameter Dv(d) =           4.175 nm
```

Figure 7.87d: BJH description for support membrane.

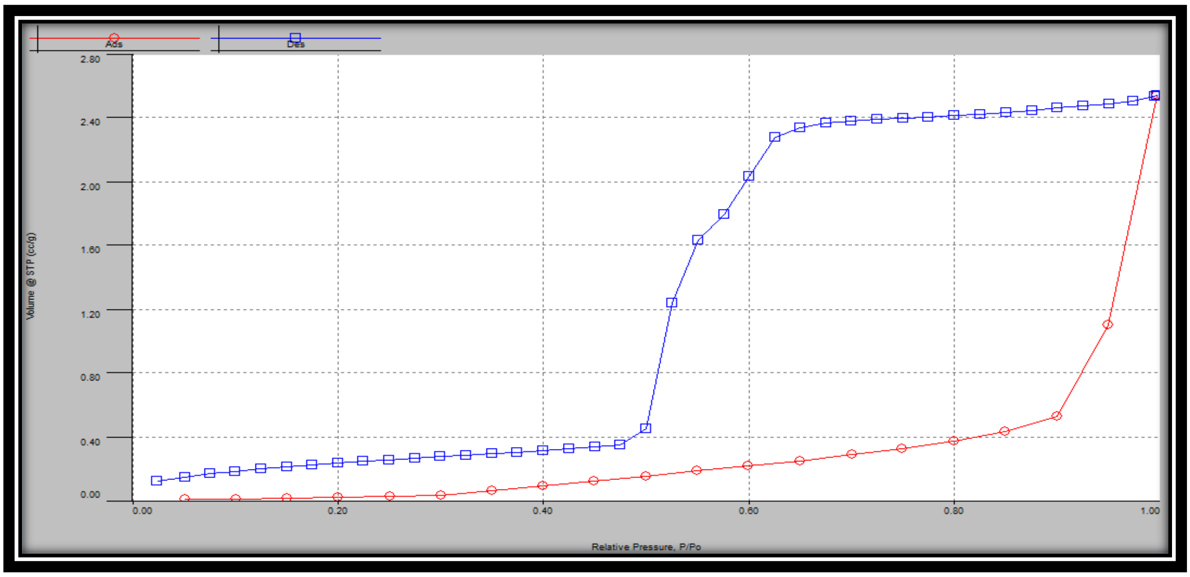

Figure 7.88a: BET isotherm for silica membrane at 77 K at 1st dip-coated membrane

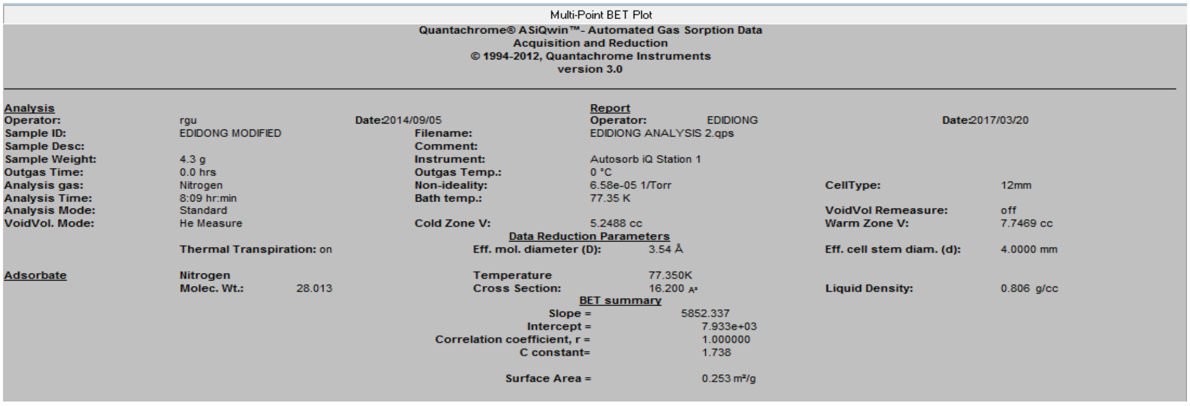

```
                                   Multi-Point BET Plot
                 Quantachrome® ASiQwin™- Automated Gas Sorption Data
                               Acquisition and Reduction
                        © 1994-2012, Quantachrome Instruments
                                      version 3.0

Analysis                                                   Report
Operator:            rgu                  Date:2014/09/05  Operator:      EDIDIONG                      Date:2017/03/20
Sample ID:           EDIDONG MODIFIED     Filename:        EDIDIONG ANALYSIS 2.qps
Sample Desc:                              Comment:
Sample Weight:       4.3 g                Instrument:      Autosorb iQ Station 1
Outgas Time:         0.0 hrs              Outgas Temp.:    0 °C
Analysis gas:        Nitrogen             Non-ideality:    6.58e-05 1/Torr    CellType:                 12mm
Analysis Time:       8:09 hr:min          Bath temp.:      77.35 K
Analysis Mode:       Standard                                                 VoidVol Remeasure:        off
VoidVol. Mode:       He Measure           Cold Zone V:     5.2488 cc          Warm Zone V:              7.7469 cc
                                              Data Reduction Parameters
                     Thermal Transpiration: on  Eff. mol. diameter (D):  3.54 Å   Eff. cell stem diam. (d):  4.0000 mm

Adsorbate            Nitrogen                   Temperature          77.350K
                     Molec. Wt.:      28.013    Cross Section:       16.200 A²    Liquid Density:           0.806  g/cc
                                                   BET summary
                                                Slope =              5852.337
                                            Intercept =                 7.933e+03
                             Correlation coefficient, r =               1.000000
                                           C constant=                  1.738

                                         Surface Area =                 0.253 m²/g
```

Figure 7.88b: BET description for 1st dip-coated membrane.

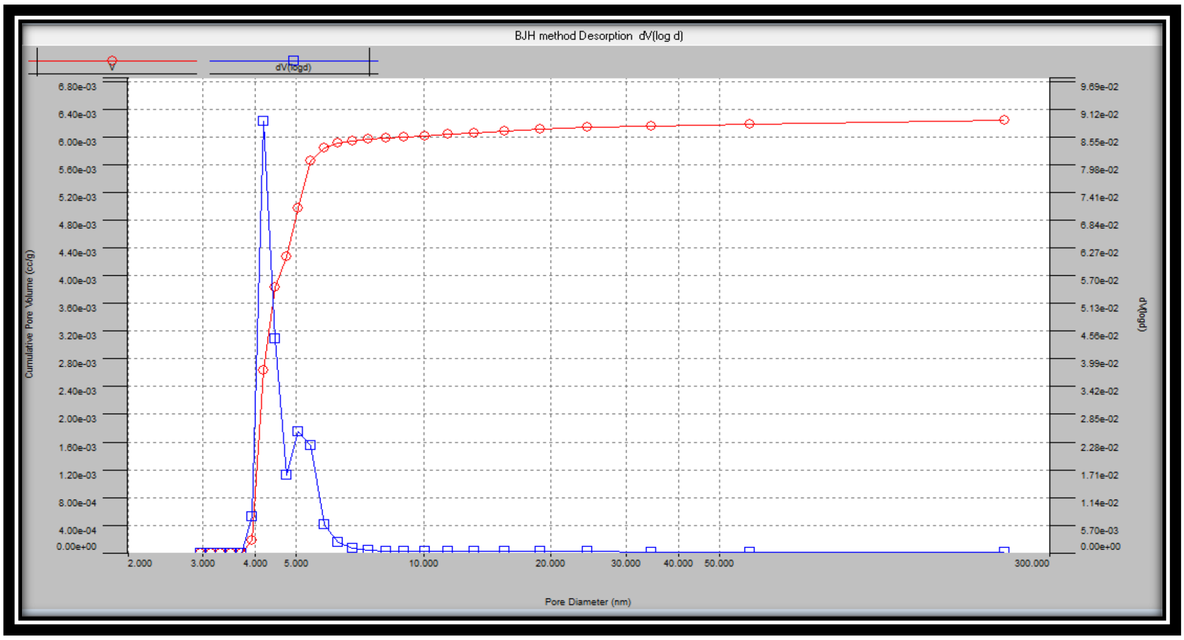

Figure 7.88c: BJH curve for 1st dip-coated silica membrane at 77 K.

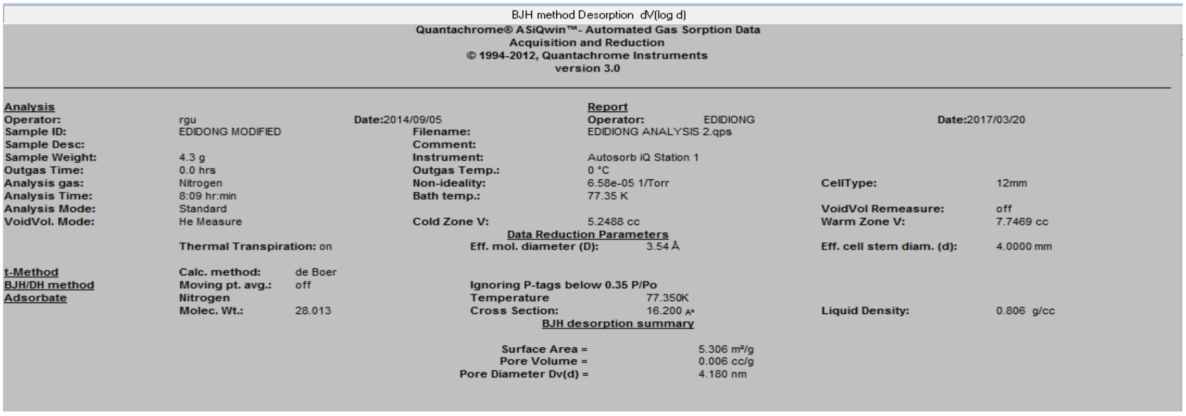

```
                                        BJH method Desorption  dV(log d)
                          Quantachrome® ASiQwin™- Automated Gas Sorption Data
                                        Acquisition and Reduction
                                © 1994-2012, Quantachrome Instruments
                                              version 3.0
________________________________________________________________________________________________________

Analysis                                                          Report
Operator:          rgu                  Date:2014/09/05           Operator:         EDIDIONG                 Date:2017/03/20
Sample ID:         EDIDONG MODIFIED          Filename:            EDIDIONG ANALYSIS 2.qps
Sample Desc:                                 Comment:
Sample Weight:     4.3 g                     Instrument:          Autosorb iQ Station 1
Outgas Time:       0.0 hrs                   Outgas Temp.:        0 °C
Analysis gas:      Nitrogen                  Non-ideality:        6.58e-05 1/Torr        CellType:               12mm
Analysis Time:     8:09 hr:min               Bath temp.:          77.35 K
Analysis Mode:     Standard                                                              VoidVol Remeasure:      off
VoidVol. Mode:     He Measure                Cold Zone V:         5.2488 cc              Warm Zone V:            7.7469 cc
                                                       Data Reduction Parameters
                   Thermal Transpiration: on     Eff. mol. diameter (D):     3.54 Å      Eff. cell stem diam. (d):  4.0000 mm

t-Method           Calc. method:      de Boer
BJH/DH method      Moving pt. avg.:   off        Ignoring P-tags below 0.35 P/Po
Adsorbate          Nitrogen                      Temperature                 77.350K
                   Molec. Wt.:        28.013     Cross Section:              16.200 A²   Liquid Density:         0.806  g/cc
                                                         BJH desorption summary

                                                   Surface Area =               5.306 m²/g
                                                   Pore Volume =                0.006 cc/g
                                              Pore Diameter Dv(d) =             4.180 nm
```

Figure 7.88d: BJH description for 1st dip-coated silica membrane at 77 K.

7.6.2 Liquid Nitrogen Adsorption of the Cation-exchange Resin Catalysts

Figure 7.89a-d and 7.90a-d presents the BET plots of the amount of gas adsorbed (volume at STP (cc/g)) against the relative vapour pressure (P/Po) and BJH plots of cumulative pore volume (cc/g) against relative pressure (P/Po) for amberlyst 36 and amberlyst 15. Table 7.34 present the BET and BJH summary of the cation-exchange resin catalysts. From the results obtained, it was found that the resin catalysts exhibited a very high surface area and pore volume for some cation-exchange resins as shown in table 7.34. It was also found that the BET of amberlyst 15 (Fig 7.89a-b) showed a flat curve with little hysteresis on the surface while amberlyst 36 (Fig 7.90a-b) exhibited of hysteresis loop on the curves. Although the BET of the resin catalysts showed a flat and hysteresis curve on the surface, it was observed that the material possessed a characteristic feature of a type IV isotherm because of the capillary condensation in the mesoporous region (2-50nm) [136, 161]. The increasing order of the BET surface area of the resin catalysts was amberlyst 36 (20.171 m^2/g) > amberlyst 16 (16.994 m^2/g) > amberlyst 15 (14.302 m^2/g) > dowex 50W8x (0.497m^2/g). From figure 7.89c-d, it was found that amberlyst 15 resin catalysts also exhibited a very higher pore diameter in contrast to amberlyst 36 (figure 7.90c-d). The obtained results for the cation-exchange resins catalysts were found to be in accordance with the IUPAC classification of mesoporous materials as described in the literature [133].

Table 7.34: BET surface area, BJH pore volume, slope and intercept for the different cation-exchange resin catalysts.

Catalysts (cation-exchange resin)	BET Surface area (m^2/g)	BJH Pore diameter (nm)	Pore Volume (cc/g)	Slope	Intercept
Amberlyst 15	14.302	33.839	0.137	381.995	-1.385*E-02
Amberlyst 16	16.994	3.932	0.037	-42.002	2.469*E+02
Amberlyst 36	20.171	3.320	0.125	522.42	1.607*E-01
Dowex 50W8x	0.497	3.708	0.004	11309.297	-4.261*E-03

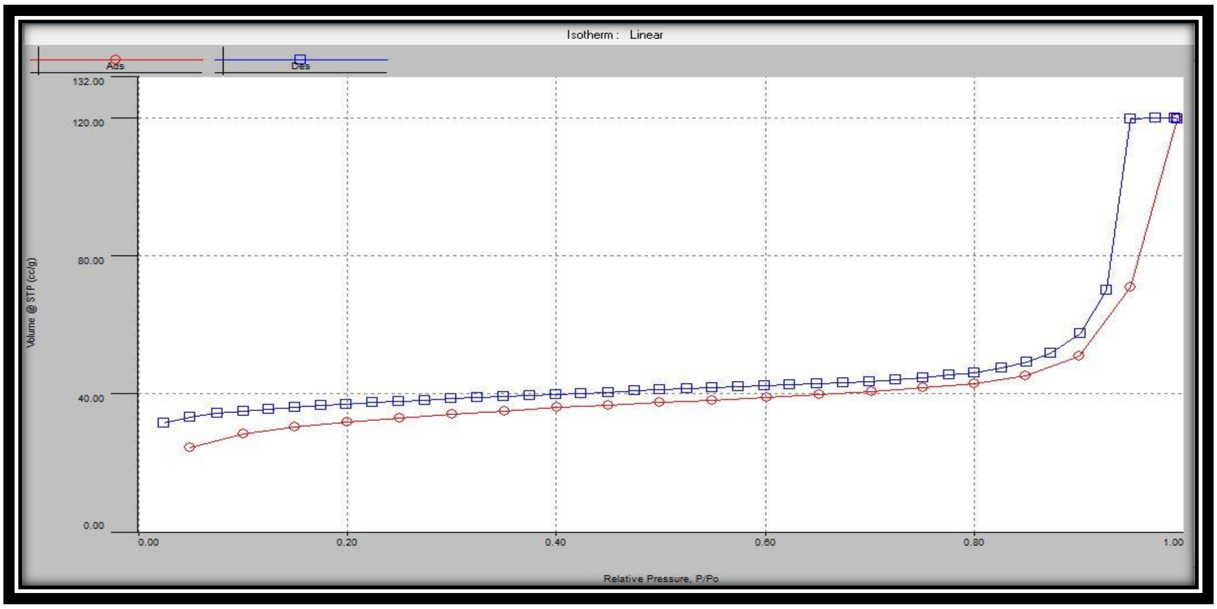

Figure 7.89a: BET isotherm for amberlyst 15 at 77 K.

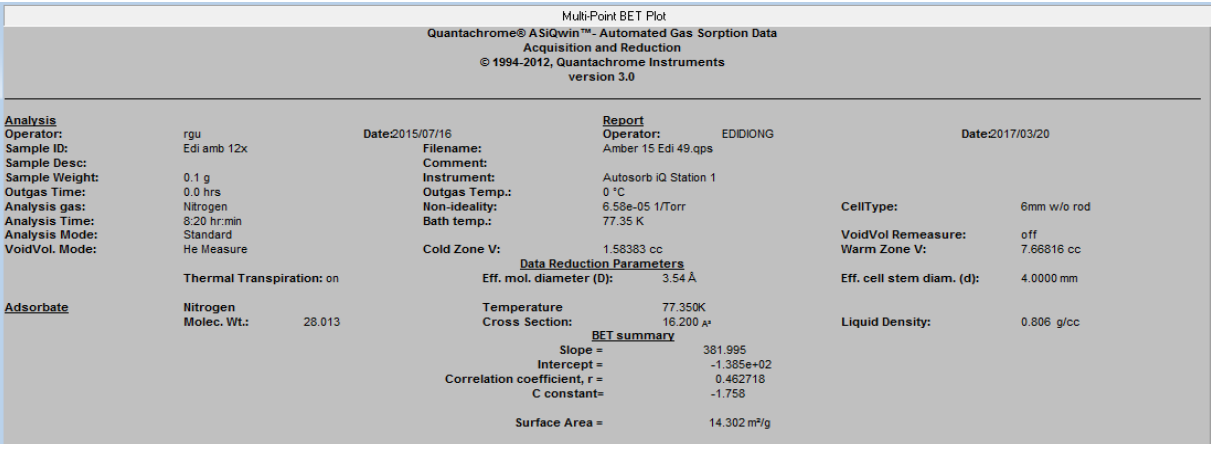

```
                                   Multi-Point BET Plot
                   Quantachrome® ASiQwin™- Automated Gas Sorption Data
                                 Acquisition and Reduction
                          © 1994-2012, Quantachrome Instruments
                                        version 3.0

Analysis                                                  Report
Operator:          rgu              Date:2015/07/16       Operator:       EDIDIONG                    Date:2017/03/20
Sample ID:         Edi amb 12x            Filename:       Amber 15 Edi 49.qps
Sample Desc:                              Comment:
Sample Weight:     0.1 g                  Instrument:     Autosorb iQ Station 1
Outgas Time:       0.0 hrs                Outgas Temp.:   0 °C
Analysis gas:      Nitrogen               Non-ideality:   6.58e-05 1/Torr         CellType:            6mm w/o rod
Analysis Time:     8:20 hr:min            Bath temp.:     77.35 K
Analysis Mode:     Standard                                                       VoidVol Remeasure:   off
VoidVol. Mode:     He Measure             Cold Zone V:    1.58383 cc              Warm Zone V:         7.66816 cc
                                              Data Reduction Parameters
                   Thermal Transpiration: on   Eff. mol. diameter (D):  3.54 Å    Eff. cell stem diam. (d):  4.0000 mm

Adsorbate          Nitrogen                    Temperature              77.350K
                   Molec. Wt.:     28.013      Cross Section:           16.200 A²  Liquid Density:     0.806  g/cc
                                                     BET summary
                                                 Slope =               381.995
                                             Intercept =                -1.385e+02
                              Correlation coefficient, r =               0.462718
                                            C constant=                 -1.758

                                          Surface Area =               14.302 m²/g
```

Figure 7.89b: BET description for amberlyst 15 at 77 K.

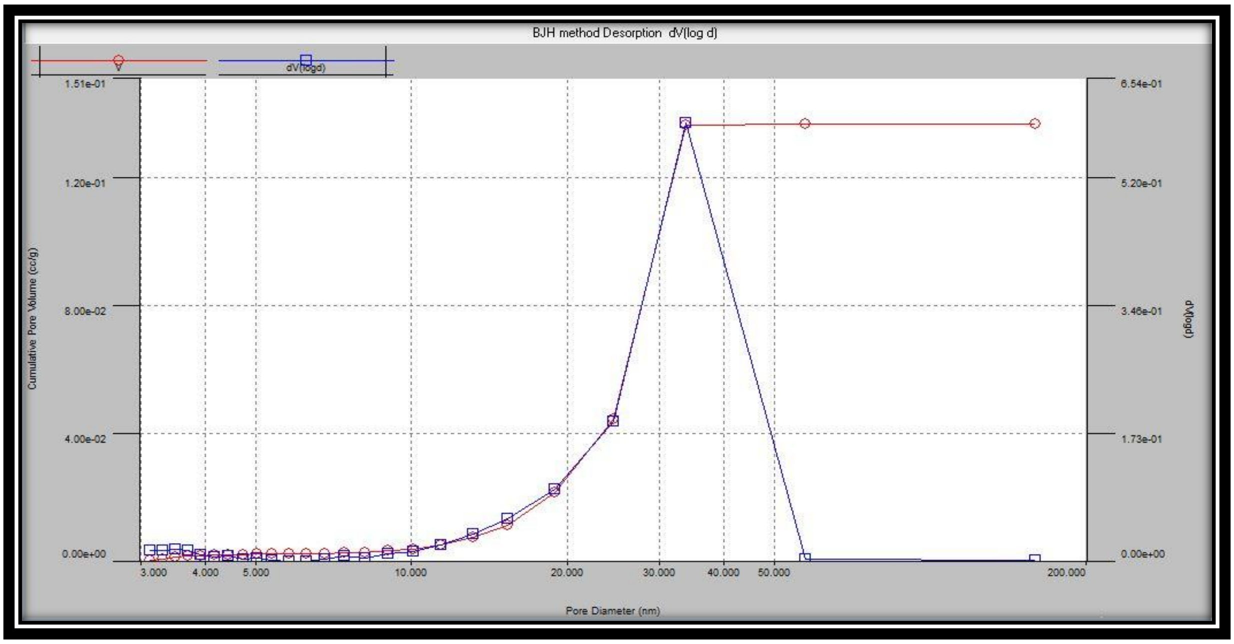

Figure 7.89c: BJH curve for amberlyst 15 at 77 K.

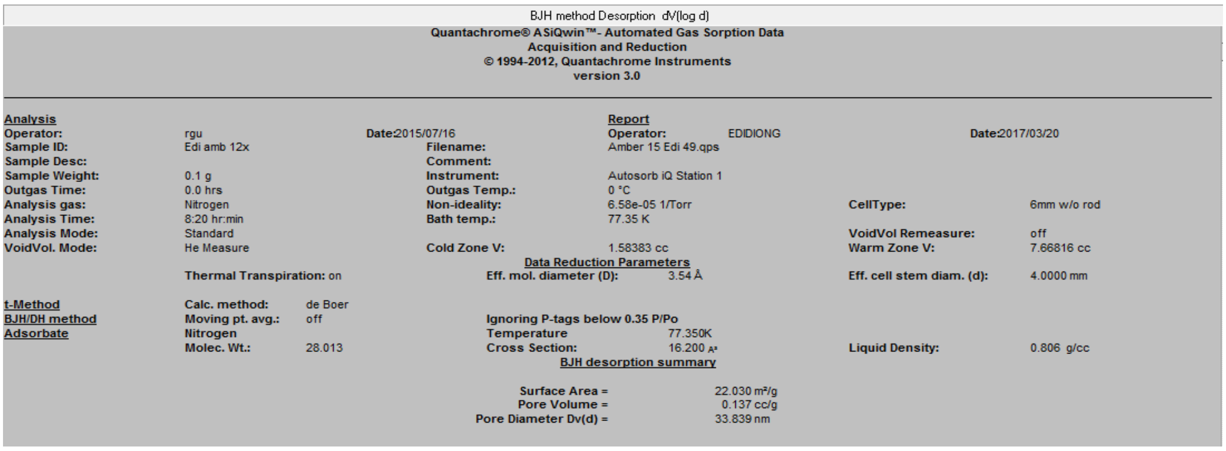

```
                                BJH method Desorption  dV(log d)
                   Quantachrome® ASiQwin™- Automated Gas Sorption Data
                                 Acquisition and Reduction
                          © 1994-2012, Quantachrome Instruments
                                        version 3.0

Analysis                                                  Report
Operator:          rgu              Date:2015/07/16       Operator:       EDIDIONG                    Date:2017/03/20
Sample ID:         Edi amb 12x            Filename:       Amber 15 Edi 49.qps
Sample Desc:                              Comment:
Sample Weight:     0.1 g                  Instrument:     Autosorb iQ Station 1
Outgas Time:       0.0 hrs                Outgas Temp.:   0 °C
Analysis gas:      Nitrogen               Non-ideality:   6.58e-05 1/Torr         CellType:            6mm w/o rod
Analysis Time:     8:20 hr:min            Bath temp.:     77.35 K
Analysis Mode:     Standard                                                       VoidVol Remeasure:   off
VoidVol. Mode:     He Measure             Cold Zone V:    1.58383 cc              Warm Zone V:         7.66816 cc
                                              Data Reduction Parameters
                   Thermal Transpiration: on   Eff. mol. diameter (D):  3.54 Å    Eff. cell stem diam. (d):  4.0000 mm

t-Method           Calc. method:   de Boer
BJH/DH method      Moving pt. avg.: off        Ignoring P-tags below 0.35 P/Po
Adsorbate          Nitrogen                    Temperature              77.350K
                   Molec. Wt.:     28.013      Cross Section:           16.200 A²  Liquid Density:     0.806  g/cc
                                                   BJH desorption summary

                                          Surface Area =               22.030 m²/g
                                           Pore Volume =                0.137 cc/g
                                   Pore Diameter Dv(d) =               33.839 nm
```

Figure 7.89d: BJH description for amberlyst 15 at 77 K.

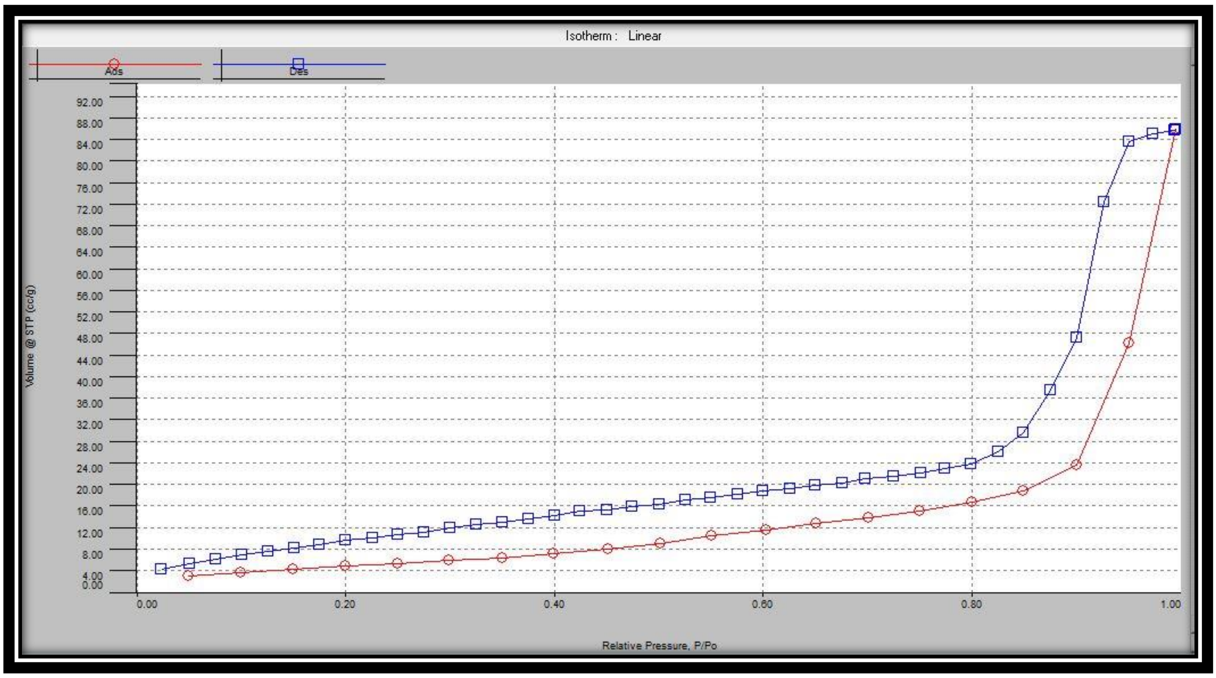

Figure 7.90a: BET isotherm for amberlyst 36 at 77 K.

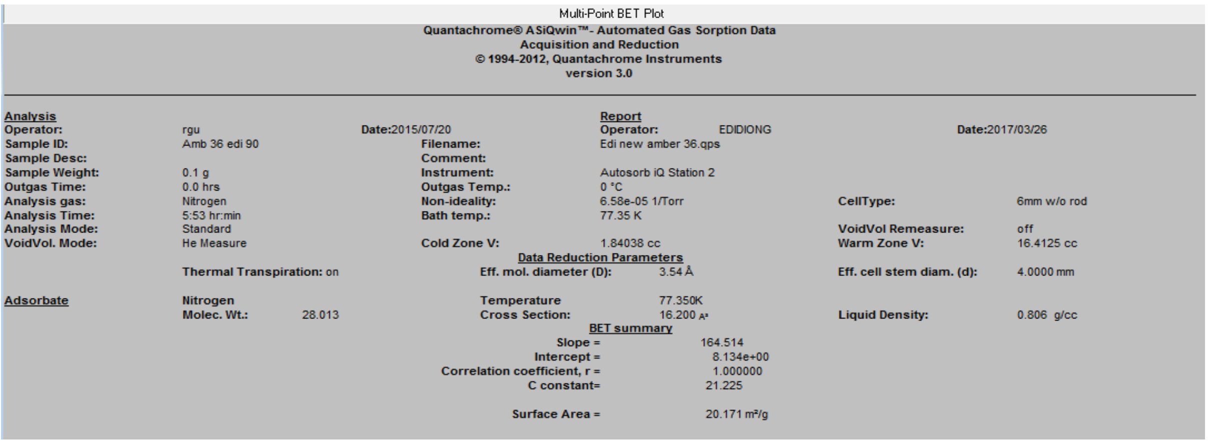

```
                                              Multi-Point BET Plot
                          Quantachrome® ASiQwin™- Automated Gas Sorption Data
                                         Acquisition and Reduction
                                 © 1994-2012, Quantachrome Instruments
                                                version 3.0

Analysis                                                    Report
Operator:          rgu              Date:2015/07/20         Operator:      EDIDIONG                        Date:2017/03/26
Sample ID:         Amb 36 edi 90         Filename:          Edi new amber 36.qps
Sample Desc:                             Comment:
Sample Weight:     0.1 g                 Instrument:        Autosorb iQ Station 2
Outgas Time:       0.0 hrs               Outgas Temp.:      0 °C
Analysis gas:      Nitrogen              Non-ideality:      6.58e-05 1/Torr          CellType:                   6mm w/o rod
Analysis Time:     5:53 hr:min           Bath temp.:        77.35 K
Analysis Mode:     Standard                                                          VoidVol Remeasure:          off
VoidVol. Mode:     He Measure            Cold Zone V:       1.84038 cc               Warm Zone V:                16.4125 cc
                                               Data Reduction Parameters
                   Thermal Transpiration: on     Eff. mol. diameter (D):   3.54 Å    Eff. cell stem diam. (d):   4.0000 mm

Adsorbate          Nitrogen                      Temperature               77.350K
                   Molec. Wt.:      28.013       Cross Section:            16.200 A²  Liquid Density:            0.806  g/cc
                                                     BET summary
                                                Slope =              164.514
                                            Intercept =                8.134e+00
                           Correlation coefficient, r =                1.000000
                                           C constant=               21.225

                                        Surface Area =               20.171 m²/g
```

Figure 7.90b: BET description for amberlyst 36 at 77 K.

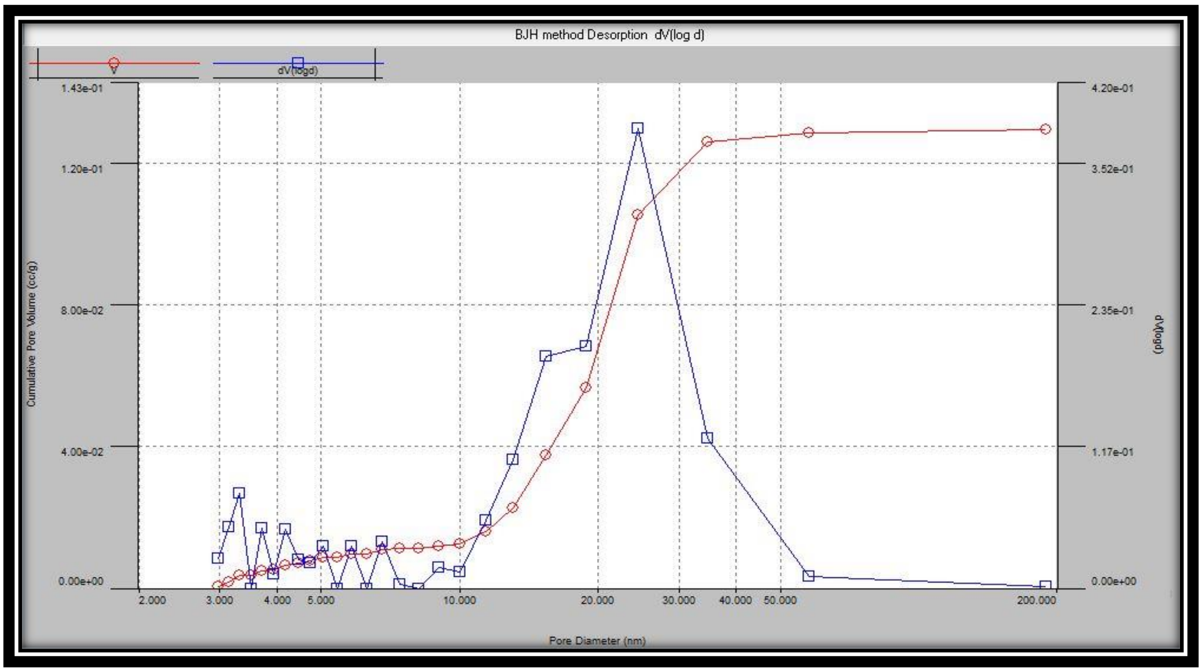

Figure 7.90c: BJH curve for amberlyst 36 at 77 K.

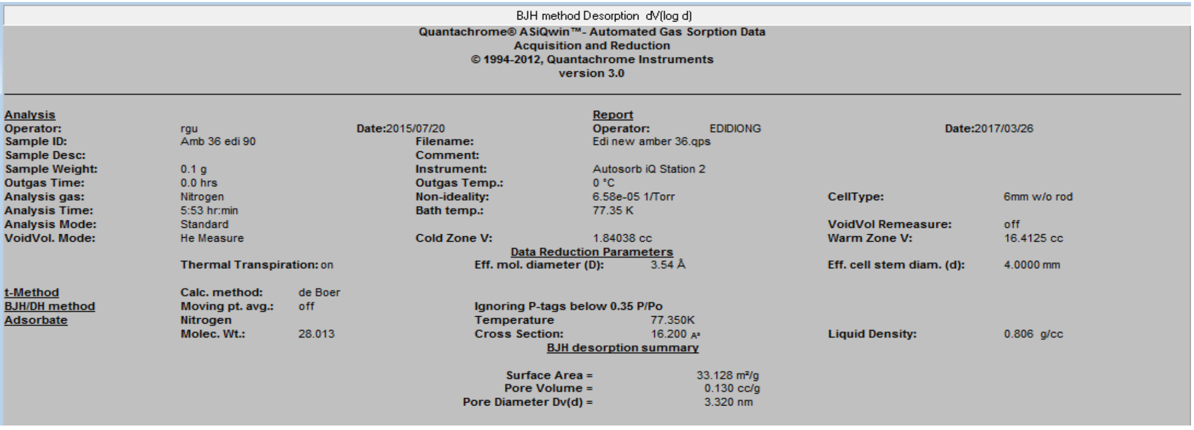

Quantachrome® ASiQwin™- Automated Gas Sorption Data
Acquisition and Reduction
© 1994-2012, Quantachrome Instruments
version 3.0

Analysis
Operator: rgu **Date:**2015/07/20
Sample ID: Amb 36 edi 90
Sample Desc:
Sample Weight: 0.1 g
Outgas Time: 0.0 hrs
Analysis gas: Nitrogen
Analysis Time: 5:53 hr:min
Analysis Mode: Standard
VoidVol. Mode: He Measure
Thermal Transpiration: on

Report
Operator: EDIDIONG **Date:**2017/03/26
Filename: Edi new amber 36.qps
Comment:
Instrument: Autosorb iQ Station 2
Outgas Temp.: 0 °C
Non-ideality: 6.58e-05 1/Torr
Bath temp.: 77.35 K
Cold Zone V: 1.84038 cc

CellType: 6mm w/o rod
VoidVol Remeasure: off
Warm Zone V: 16.4125 cc

Data Reduction Parameters
Eff. mol. diameter (D): 3.54 Å
Eff. cell stem diam. (d): 4.0000 mm

t-Method **Calc. method:** de Boer
BJH/DH method **Moving pt. avg.:** off
Ignoring P-tags below 0.35 P/Po
Adsorbate **Nitrogen**
Temperature 77.350K
Molec. Wt.: 28.013
Cross Section: 16.200 Å²
Liquid Density: 0.806 g/cc

BJH desorption summary

Surface Area = 33.128 m²/g
Pore Volume = 0.130 cc/g
Pore Diameter Dv(d) = 3.320 nm

Figure7.90d: BJH description for amberlyst 36 at 77 K.

7.7 Results Validation

In other to validate the results that were obtained, a number of parameters were put into considerations. Errors due to the measurement of the sample were considered when measuring the sample before the degassing analysis. It could be that sample was not accurately measured or some of the additional error may occur due to the weighing balance. It could also be that the sample was not well degassed or crushed before the analysis. Also, the discrepancy in the BET and BJH results could be due to a small particle of the silica solution was deposited on the membrane surface during the modification process. However, instrumental error were also considered in terms of the set temperatures during the degassing i.e if the dewar comes down while the sample is still running or the dry inert gases used for the sample degassing process could also finish while the sample is still degassing, then this can also contribute to error during the experiment which could affect the results. However, human error was also considered as this could also affect the obtained result during the experimental analysis. Also, the uniformity of the coating plays a significant effect on the carrier gas permeation performance with the membrane. A more uniformly coated and crystalline finish was obtained for the silica membrane from the dip-coated method. The silica membrane demonstrate the highest helium flux after the 2nd and 3rd dipping in contrast to the 1st dip-coated membrane. However, other factors such as the presence of leaks from graphite seals and loose bolts/nuts from the stainless membrane reactor during the permeation tests experiment may also have contributed to the high helium flux after the 2nd and 3rd dipping. During the course of this work, it was also observed that it is very important to fix the graphite seals at both ends of the membrane and replace them periodically. Also, when the membrane reactor is removed from the experimental rig, the inside of the reactor must be cleaned properly such that no particles are left which could alter the placement of the membrane in the reactor. Also, there is need to properly install the membrane reactor on the permeation test rig and tighten the bolts and nuts appropriately as loose nuts and bolts could result in gas leaks.

During the process intensification, it was also observed that it is important to place the O-rings rubber gasket first on top of the membrane on the downward compartment of the stainless steel separator before covering the core holder and the upper compartment of the reactor to avoid any leakage on the separator. Also, it was found that it is very important to carefully tighten the nuts through each point on the stainless steel reactor as loose nuts could also cause the condensation of the reactant solvent during the experiment. Also, there is need to properly cover the openings of the reactor and then condenser with cork/glass stopper during the batch process esterification experiment as this could cause solvent evaporation.

Also, it was also noted that it was observed that it was important to measure a tiny little amount of solvents for injection through the GC-MS as the instrument was very sensitive and measure samples as tiny as in ppm (part per million). If the concentration was larger than expected, it could lead to error in the result interpretation as it will result in broaden peaks. Also, the sample valves were carefully cleaned before any analysis as the leftover solvent could contribute to error in the results interpretation. Also, there is need to properly install the column and septa on the GC and tighten the column nuts and bolts carefully as loose nuts/septa may cause leakage on the GC-MS during sample analysis. During NMR analysis it was observed that it was important to carefully dissolve the lactic acid feed with a suitable deuterated solvent before the analysis on the NMR instrument to avoid solvent signal as this could affect the result. Also, it necessary to also dry the excess ethanol using rota evaporator to obtain the pure lactic acid feed before the analysis on NMR instrument as this could cause a problem on the instrument.

CHAPTER 8

8.0 Conclusion and Recommendation for Future Work

8.1 Conclusion

The shift in the thermodynamic chemical equilibrium for the selective removal of water from esterification reaction for a higher conversion of the lactic acid feed using inorganic/organic membranes and catalysts has been widely accepted as a possible option. However, it is still early days to propose that the challenges in using cellulose acetate membranes and cation-exchange resin catalysts for solving thermodynamic equilibrium limitation problems in esterification reaction has been fully addressed and investigated. The major difficulty in cation-exchange resins is how to select a heat resistant and mechanically stable catalyst that is cost effective, reusable, environmentally friendly, higher conversion of the lactic acid feed and the ability to withstand the high concentration of the reactant solvents used. The choice of a water permeable cellulose acetate membrane for chemical equilibrium shift has also posed a major challenge in esterification reaction processes. Also, the selection of a suitable carrier gas that could be compatible with GC for the lactic acid feed conversion analysis has also been a major challenge. The summary of the conclusions in this study is given below:

1) The carrier gas transport properties, preparation and characterisation of inorganic, organic membranes and cation-exchange resin for lactic acid applications was achieved. The rate of transport of the carrier gas through the membrane was described by Knudsen flow mechanism of transport with some contribution of viscous and surface diffusion mechanisms. The characterisation of the cation-exchange resin and membrane was performed using different analytical techniques including SEM/EDAX, FTIR-ATR, ^{1}HNMR, Liquid nitrogen physisorption and GC-MS.

2) The permeation test of the carrier gas with membrane was carried out for both the support and silica membrane to determine the flow mechanisms and the behaviour of the tubular membrane with carrier gases before esterification reaction. The silica membrane modification was achieved using the sol-gel dip-coating method. The permeation experiment with the silica membrane was carried out between the temperatures of 333 – 413 K. The silica membrane exhibited a linear flux in the range of 0.8866 – 0.9873 indicating viscous flow mechanism. The gas permeance decreases with respect to temperature. The silica membrane exhibited a linear dependence with the inverse square root of the gas molecular weight confirming Knudsen flow mechanism. However, He gas were identified as the most suitable carrier gas for the analysis of EL using GC-MS. The experimental results were further tested on a mathematical model

(Minitab 2016) which the results fitted well into the model with helium gas exhibiting the highest variance values of 3.8180 and 2.518 for both support and silica membranes respectively confirming Helium as the suitable carrier gas.

3) The characterisations of cation-exchange resins and membrane have been investigated using SEM/EDAX before and after esterification. The SEM of the resin catalysts disclosed a defect-free surface for the fresh commercial resin catalysts, before the esterification process exception of amberlyst 15, while the EDAX spectra of the resin before the esterification process indicated the presence of sulphur with the highest peak on the spectra. Amberlyst 36, amberlyst 16 and dowex 50W8x were found to be the most effective, low cost, stable and efficient catalysts. The EDAX of the resins after the esterification process showed different elements on the spectra including sulphur, aluminium, oxygen and carbon. Also, the SEM of the support membrane demonstrate a clear surface before the dip-coating process indicating a crack-free image with an excellent pore structure. EDAX of the support consists of different elements including carbon (C), titanium (Ti), aluminium (Al) and oxygen (O) whereas the EDAX of the dip-coated silica membrane consists of elements such as silicon (Si), titanium (Ti) and oxygen (O).

4) The FTIR-ATR analysis of the resin catalysts detected C=O and O=H functional groups which confirms the presence of ethanol and lactic acid as the strongest components on the surface of the resin catalysts. From the FTIR-ATR analysis, it was also found that Langmuir Hinshelwood model was the best fitted model that could best describe the esterification reaction process. The nuclear magnetic resonance (NMR) was also used to further investigate the bond connectivity for the lactic acid feed. The ^{1}HNMR analysis showed different functional groups and the different bond connectivity including CH, COOH, OH, CH_2 and CH_3 for singlet, quartet and triplet bonds which was suggested to occur from the reactant solvents.

5) The process intensification of resins catalysts attached to cellulose acetate membrane for the selective removal of water from the reaction mixture to enhanced ethyl lactate conversion was also obtained. The result of the conversion rate of the lactic acid feed showed that by employing the process intensification for esterification reaction, the conversion rate of the lactic acid feed substantially increased from 99.86% to 100% at 80 and 100 ^{o}C respectively confirming the effectiveness of the process. The mass spectra of the esterification product was identified to be that of ethyl lactate and was in accordance with that of the commercial ethyl lactate.

6) Developing a membrane and tested the membrane with different gases and found helium to be selective with the membrane, identification of helium being an expensive inert gas as a suitable carrier gas from the gas transport experiments and employing helium gas for esterification

reaction to shift the chemical equilibrium for improve yield of the ester product with the GC-MS which also uses helium as a carrier and detector gas.

8.2 Recommendation

The GC-MS results obtained identified amberlyst 36 and 16 as the most suitable catalysts for the esterification process and could be recommended for industrial purposes. The present work would also like to recommend helium and argon as the most suitable carrier gases for the analysis of the esterification reaction feed with GC-MS. Also, water permeable cellulose acetate membrane is recommended as the suitable membrane in solving the equilibrium limitation problems in esterification reactions because this membrane is obtained from carbohydrate which is also obtained from biomass product and is also classified as green solvent. Also, since reaction and separation occurred in one stream in the separator, it was difficult to put the resin catalysts through the tubular membrane reactor. But in the flat sheet separator, reaction and separation takes place in one single unit.

8.3 Future Work

This study detailed some achievements based on the results that were obtained from various experimental analysis that were performed. However, research is a continuous process and certain areas of this work will form the basis for future work as thus:

1) To investigate the compression/fatigue strength of the cation exchange resin catalyst using Intron technique and compared the result at different temperatures with the results of the present study. It would be beneficiary for future work to focus on using thermogravimetric analysis (TGA), x-ray diffraction methods to determine the spectra and the absorption angle on the surface of the resin catalysts and membrane and to compare their behaviour with FTIR-ATR and liquid nitrogen adsorption methods.
2) To investigate the metal composition in the membrane sample at low concentration using ICP-MS (Inductive coupled plasma-mass spectrometry) method and compare the results for support and silica membrane.
3) To use methanol and acetone as diluting solvents to dilute the lactic acid feed after esterification reaction to reduce the concentration of the solvent before injecting to the GC-MS and compare the chromatogram to the present work which uses ethanol as the diluting solvent. Since the present study has identified helium as the most suitable carrier gas from the permeation test with membrane, and this gas was coupled with the GC-MS for the analysis of lactic acid feed which ethyl lactate was confirmed. Future work should consider the use of other carrier gases

including hydrogen, air and oxygen to test their suitability with the tubular membrane to see if there would be any different in the flow rate and also incorporate this gases in analysis of lactic acid feed with GC-FID/GC-TCD (Gas chromatograph-flame ionisation detector/gas chromatograph-thermal conductivity detector) and compare the conversion rate results with the present work.

4) Future work can also investigate on the water permeance of the ester product with the cellulose acetate membrane as well as the thickness of the membrane.
5) Further carrier gas transport tests should be carried out with both the support and the silica membrane to evaluate the performance of the gases.
6) To deposit the cation exchange resin catalyst on a stainless steel tubular membrane reactor and investigate the effect of the esterification parameters in contrast to the flat sheet separator.
7) To use mathematical model such as MATLAB to analysis the experimental data to further test the permeation rate of He and Ar gases and compare with the present work. This present work should serve as the foundation and reference point for other studies relating to conversion of the lactic acid feed in esterification reaction process of carboxylic acid and ethanol affected by thermodynamic equilibrium limitation problems.

9.0 REFERENCES

[1] Vu DT, Lira CT, Asthana NS, Kolah AK, Miller DJ. Vapor-liquid equilibria in the systems ethyl lactate ethanol and ethyl lactate water. *Journal of Chemical & Engineering Data.* 2006; 51(4):1220-1225.

[2] Cannilla C, Bonura G, Frusteri F. Potential of Pervaporation and Vapor Separation with Water Selective Membranes for an Optimized Production of Biofuels—A Review. Catalysts. 2017; 7(6):187.

[3] Liu Y, Lotero E, Goodwin Jr JG. Effect of water on sulfuric acid catalyzed esterification. *Journal of Molecular Catalysis A: Chemical.* 2006; 245(1):132-140.

[4] Zhang Y, Ma L, Yang J. Kinetics of esterification of lactic acid with ethanol catalyzed by cation-exchange resins. *Reactive and Functional Polymers.* 2004; 61(1):101-114.

[5] Li W, Liu W, Xing W, Xu N. Esterification of Acetic Acid and n-Propanol with Vapor Permeation Using NaA Zeolite Membrane. *Industrial & Engineering Chemistry Research.* 2013; 52(19):6336-6342.

[6] Armor J. Overcoming equilibrium limitations in chemical processes. *Applied Catalysis A: General.* 2001; 222(1):91-99.

[7] de Paiva, Eduardo Jose Mendes, Sterchele S, Corazza ML, Murzin DY, Wypych F, Salmi T. Esterification of fatty acids with ethanol over layered zinc laurate and zinc stearate–Kinetic modeling. *Fuel.* 2015; 153:445-454.

[8] Sert E, Buluklu AD, Karakuş S, Atalay FS. Kinetic study of catalytic esterification of acrylic acid with butanol catalyzed by different ion exchange resins. *Chemical Engineering and Processing: Process Intensification.* 2013; 73(0):23-28.

[9] Kaur K, Wanchoo RK, Toor AP. Sulfated iron oxide: A proficient catalyst for esterification of butanoic acid with glycerol. *Industrial & Engineering Chemistry Research.* 2015; 54(13):3285-3292.

[10] Ugur Nigiz F, Durmaz Hilmioglu N. Green solvent synthesis from biomass based source by biocatalytic membrane reactor. *International Journal of Energy Research.* 2015; .

[11] Khajavi S, Jansen JC, Kapteijn F. Application of a sodalite membrane reactor in esterification—Coupling reaction and separation. *Catalysis Today.* 2010; 156(3):132-139.

[12] Benedict DJ, Parulekar SJ, Tsai S. Esterification of lactic acid and ethanol with/without pervaporation. *Industrial & Engineering Chemistry Research.* 2003; 42(11):2282-2291.

[13] Engin A, Haluk H, Gurkan K. Production of lactic acid esters catalyzed by heteropoly acid supported over ion-exchange resins. *Green Chemistry.* 2003; 5(4):460-466.

[14] Altıokka MR, Çıtak A. Kinetics study of esterification of acetic acid with isobutanol in the presence of amberlite catalyst. *Applied Catalysis A: General.* 2003; 239(1):141-148.

[15] Delgado P, Sanz MT, Beltrán S. Kinetic study for esterification of lactic acid with ethanol and hydrolysis of ethyl lactate using an ion-exchange resin catalyst. *Chemical Engineering Journal.* 2007; 126(2):111-118.

[16] Han Y, Lv E, Ma L, Lu J, Chen K, Ding J. Coupling membrane pervaporation with a fixed-bed reactor for enhanced esterification of oleic acid with ethanol. *Energy Conversion and Management.* 2015; 106:1379-1386.

[17] Lunelli BH, De Morais ER, Maciel MRW, Filho R. Process Intensification for Ethyl Lactate Production Using Reactive Distillation. *Chem Eng Trans.* 2011; 24:823-828.

[18] Osorio-Pascuas OM, Santaella MA, Rodriguez G, Orjuela A. Esterification Kinetics of Tributyl Citrate Production Using Homogeneous and Heterogeneous Catalysts. *Industrial & Engineering Chemistry Research.* 2015; 54(50):12534-12542.

[19] Stanford JP, Soto MC, Pfromm PH, Rezac ME. Aqueous phase hydrogenation of levulinic acid using a porous catalytic membrane reactor. Catalysis Today. 2016; 268:19-28.

[20] Buchaly C, Kreis P, Górak A. Hybrid separation processes—Combination of reactive distillation with membrane separation. *Chemical Engineering and Processing: Process Intensification.* 2007; 46(9):790-799.

[21] Aparicio S, Halajian S, Alcalde R, García B, Leal JM. Liquid structure of ethyl lactate, pure and water mixed, as seen by dielectric spectroscopy, solvatochromic and thermophysical studies. *Chemical Physics Letters.* 2008; 454(1):49-55.

[22] Pereira CS, Pinho SP, Silva VM, Rodrigues AE. Thermodynamic equilibrium and reaction kinetics for the esterification of lactic acid with ethanol catalyzed by acid ion-exchange resin. *Industrial & Engineering Chemistry Research.* 2008; 47(5):1453-1463.

[23] Lomba L, Giner B, Zuriaga E, Gascón I, Lafuente C. Thermophysical properties of lactates. *Thermochimica Acta.* 2014; 575(0):305-312.

[24] Aparicio S, Alcalde R. The green solvent ethyl lactate: an experimental and theoretical characterization. *Green Chemistry.* 2009; 11(1):65-78.

[25] Paninho AB, Nunes AVM, Paiva A, Najdanovic-Visak V. High pressure phase behavior of the binary system (ethyl lactate + carbon dioxide). *Fluid Phase Equilibria.* 2013; 360(0):129-133.

[26] Pereira CS, Silva VM, Rodrigues AE. Fixed bed adsorptive reactor for ethyl lactate synthesis: Experiments, modelling, and simulation. *Separation Science and Technology*. 2009; 44(12):2721-2749.

[27] Delgado P, Sanz MT, Beltrán S. Pervaporation study for different binary mixtures in the esterification system of lactic acid with ethanol. Separation and Purification Technology. 2008; 64(1):78-87.

[28] Peña-Tejedor S, Murga R, Sanz MT, Beltrán S. Vapor–liquid equilibria and excess volumes of the binary systems ethanol ethyl lactate, isopropanol isopropyl lactate and n-butanol n-butyl lactate at 101.325 kPa. Fluid Phase Equilibria. 2005; 230(1):197-203.

[29] Asthana N, Kolah A, Vu DT, Lira CT, Miller DJ. A continuous reactive separation process for ethyl lactate formation. *Organic process research & development.* 2005; 9(5):599-607.

[29] Sundmacher K, Kienle A. *Reactive distillation: status and future directions.* : John Wiley & Sons; 2006.

[31] Zeng Z, Cui L, Xue W, Chen J, Che Y. Recent Developments on the Mechanism and Kinetics of Esterification Reaction Promoted by Various Catalysts. *Chemical kinetics, InTech.* 2012; .

[32] Tanaka K, Yoshikawa R, Ying C, Kita H, Okamoto K. Application of zeolite T membrane to vapor-permeation-aided esterification of lactic acid with ethanol. *Chemical Engineering Science.* 2002; 57(9):1577-1584.

[33] Tanaka K, Yoshikawa R, Ying C, Kita H, Okamoto K. Application of zeolite membranes to esterification reactions. *Catalysis Today.* 2001; 67(1):121-125.

[34] Okamoto K, Yamamoto M, Noda S, Semoto T, Otoshi Y, Tanaka K, et al. Vapor-permeation-aided esterification of oleic acid. *Industrial & Engineering Chemistry Research.* 1994; 33(4):849-853.

[35] Dange P, Sharma A, Rathod V. Synthesis of Methyl Butyrate Using Heterogeneous Catalyst: Kinetic Studies. Catalysis Letters. 2014; 144(9):1537-1546.

[36] Toor AP, Sharma M, Thakur S, Wanchoo RK. Ion-exchange Resin Catalyzed Esterification of Lactic Acid with Isopropanol: a Kinetic Study. *Bulletin of Chemical Reaction Engineering & Catalysis.* 2011; 6(1).

[37] Pereira CS, Silva VM, Rodrigues AE. Ethyl lactate as a solvent: Properties, applications and production processes–a review. *Green Chemistry.* 2011; 13(10):2658-2671.

[38] Buonomenna M, Bae J. Membrane processes and renewable energies. Renewable and Sustainable Energy Reviews. 2015; 43:1343-1398.

[39] Clark JH, Budarin V, Deswarte FEI, HardyCurrent address: Royal Society of Chemistry, Jeffrey J. E., House B, Piccadilly, et al. Green chemistry and the biorefinery: a partnership for a sustainable future. Green Chemistry. 2006; 8(10):853.

[40] Ren J. *Biodegradable poly (lactic acid): synthesis, modification, processing and applications.* : Springer; 2011.

[41] Wang Y, Tashiro Y, Sonomoto K. Fermentative production of lactic acid from renewable materials: recent achievements, prospects, and limits. *Journal of bioscience and bioengineering.* 2015; 119(1):10-18.

[42] Datta R, Henry M. Lactic acid: recent advances in products, processes and technologies—a review. *Journal of Chemical Technology and Biotechnology.* 2006; 81(7):1119-1129.

[43] Joglekar H, Rahman I, Babu S, Kulkarni B, Joshi A. Comparative assessment of downstream processing options for lactic acid. *Separation and purification technology.* 2006; 52(1):1-17.

[44] Pereira CS, Rodrigues AE. Ethyl Lactate Main Properties, Production Processes, and Applications. Alternative Solvents for Natural Products Extraction. : Springer; 2014. p. 107-125.

[45] Pal P, Sikder J, Roy S, Giorno L. Process intensification in lactic acid production: A review of membrane based processes. *Chemical Engineering and Processing: Process Intensification.* 2009; 48(11):1549-1559.

[46] Li W, Zhang X, Xing W, Jin W, Xu N. Hydrolysis of ethyl lactate coupled by vapor permeation using polydimethylsiloxane/ceramic composite membrane. *Industrial & Engineering Chemistry Research.* 2010; 49(22):11244-11249.

[47] Cardona CA, Sánchez ÓJ. Fuel ethanol production: process design trends and integration opportunities. *Bioresource technology.* 2007; 98(12):2415-2457.

[48] Julbe A, Farrusseng D, Guizard C. Porous ceramic membranes for catalytic reactors—overview and new ideas. *Journal of Membrane Science.* 2001; 181(1):3-20.

[49] Ju IB, Lim H, Jeon W, Suh DJ, Park M, Suh Y. Kinetic study of catalytic esterification of butyric acid and n-butanol over Dowex 50Wx8-400. Chemical Engineering Journal. 2011; 168(1):293-302.

[50] Ali SH, Merchant SQ. Kinetic study of Dowex 50 Wx8-catalyzed esterification and hydrolysis of benzyl acetate. *Industrial & Engineering Chemistry Research.* 2009; 48(5):2519-2532.

[51] Bamunusingha B, De Silva E, Gunasekera M. Performance of ion exchange resin as solid catalyst for the esterification of acetic acid with ethanol. *Journal of the National Science Foundation of Sri Lanka.* 2016; 44(1).

[52] Liu W, Tan C. Liquid-phase esterification of propionic acid with n-butanol. Industrial & Engineering Chemistry Research. 2001; 40(15):3281-3286.

[53] Bozek-Winkler E, Gmehling J. Transesterification of methyl acetate and n-butanol catalyzed by Amberlyst 15. *Industrial & Engineering Chemistry Research.* 2006; 45(20):6648-6654.

[54] Farebrother AJ, Meijer AJ, Clary DC, Fisher AJ. Formation of molecular hydrogen on a graphite surface via an Eley–Rideal mechanism. *Chemical Physics Letters.* 2000; 319(3):303-308.

[55] Ju IB, Lim H, Jeon W, Suh DJ, Park M, Suh Y. Kinetic study of catalytic esterification of butyric acid and n-butanol over Dowex 50Wx8-400. Chemical Engineering Journal. 2011; 168(1):293-302.

[56] Liu W, Tan C. Liquid-phase esterification of propionic acid with n-butanol. Industrial & Engineering Chemistry Research. 2001; 40(15):3281-3286.

[57] QU Y, PENG S, WANG S, ZHANG Z, WANG J. Kinetic Study of Esterification of Lactic Acid with Isobutanol and< i> n</i>-Butanol Catalyzed by Ion-exchange Resins. Chinese Journal of Chemical Engineering. 2009; 17(5):773-780.

[58] de la Iglesia Ó, Mallada R, Menéndez M, Coronas J. Continuous zeolite membrane reactor for esterification of ethanol and acetic acid. Chemical Engineering Journal. 2007; 131(1):35-39.

[59] JagadeeshBabu P, Sandesh K, Saidutta M. Kinetics of esterification of acetic acid with methanol in the presence of ion exchange resin catalysts. Industrial & Engineering Chemistry Research. 2011; 50(12):7155-7160.

[60] Figueiredo, Katia Cecilia de Souza, Salim VMM, Borges CP. Synthesis and characterization of a catalytic membrane for pervaporation-assisted esterification reactors. Catalysis Today. 2008; 133:809-814.

[61] Kuzminska M, Backov R, Gaigneaux EM. Behavior of cation-exchange resins employed as heterogeneous catalysts for esterification of oleic acid with trimethylolpropane. Applied Catalysis A: General. 2015; .

[62] Dange P, Sharma A, Rathod V. Synthesis of Methyl Butyrate Using Heterogeneous Catalyst: Kinetic Studies. Catalysis Letters. 2014; 144(9):1537-1546

[63] Mekala M, Thamida SK, Goli VR. Pore diffusion model to predict the kinetics of heterogeneous catalytic esterification of acetic acid and methanol. Chemical Engineering Science. 2013; 104:565-573.

[64] Ismail AF, Khulbe KC, Matsuura T. *Gas Separation Membranes.* : Springer; 2015.

[65] Chandane VS, Rathod AP, Wasewar KL. Coupling of In-situ Pervaporation for the Enhanced Esterification of Propionic Acid with Isobutyl Alcohol over Cenosphere based Catalyst. *Chemical Engineering and Processing: Process Intensification.* 2017; .

[66] Labropoulos A, Athanasekou C, Kakizis N, Sapalidis A, Pilatos G, Romanos G, et al. Experimental investigation of the transport mechanism of several gases during the CVD post-treatment of nanoporous membranes. *Chemical Engineering Journal.* 2014; 255:377-393.

[67] Clarizia G. Strong and weak points of membrane systems applied to gas separation. *Chem Eng Trans.* 2009; 17:1675-1680.

[68] Van Gestel T, Buchkremer HP. Processing of Nanoporous and Dense Thin Film Ceramic Membranes. *The Nano-Micro Interface: Bridging the Micro and Nano Worlds.* 2015; :431-458.

[69] Westermann T, Melin T. Flow-through catalytic membrane reactors—Principles and applications. *Chemical Engineering and Processing: Process Intensification.* 2009; 48(1):17-28.

[70] Jiang H, Meng L, Chen R, Jin W, Xing W, Xu N. A novel dual-membrane reactor for continuous heterogeneous oxidation catalysis. *Industrial & Engineering Chemistry Research.* 2011; 50(18):10458-10464.

[71] Li K. *Ceramic membranes for separation and reaction.* : John Wiley & Sons; 2007.

[72] Nemec D, van Gemert R. Performing esterification reactions by combining heterogeneous catalysis and pervaporation in a batch process. Industrial & Engineering Chemistry Research. 2005; 44(25):9718-9726.

[73] Peters T, Fontalvo J, Vorstman M, Keurentjes J. Design directions for composite catalytic hollow fibre membranes for condensation reactions. Chemical Engineering Research and Design. 2004; 82(2):220-228.

[74] Jafar JJ, Budd PM, Hughes R. Enhancement of esterification reaction yield using zeolite A vapour permeation membrane. *Journal of Membrane Science.* 2002; 199(1):117-123.

[75] Collazos HF, Fontalvo J, Gómez-García MÁ. Design directions for ethyl lactate synthesis in a pervaporation membrane reactor. *Desalination and Water Treatment.* 2013; 51(10-12):2394-2401.

[76] Bai C, Jia M, Falconer JL, Noble RD. Preparation and separation properties of silicalite composite membranes. Journal of Membrane Science. 1995; 105(1):79-87.

[77] Mulder M. *Basic Principles of Membrane Technology Second Edition.* : Kluwer Academic Pub; 1996.

[78] Pandey P, Chauhan R. Membranes for gas separation. *Progress in Polymer Science.* 2001; 26(6):853-893.

[79] Smart S, Beltramini J, Diniz da Costa JC, Katikaneni SP, Pham T. 9 - Microporous silica membranes: fundamentals and applications in membrane reactors for hydrogen separation. In: Basile A, editor. *Handbook of Membrane Reactors.* : Woodhead Publishing; 2013. p. 337-369.

[80] JIANG H, MENG L, CHEN R, JIN W, XING W, XU N. Progress on Porous Ceramic Membrane Reactors for Heterogeneous Catalysis over Ultrafine and Nano-sized Catalysts. *Chinese Journal of Chemical Engineering.* 2013; 21(2):205-215.

[81] Guizard C, Princivalle A. Preparation and characterization of catalyst thin films. *Catalysis Today.* 2009; 146(3):367-377.

[82] Smart S, Liu S, Serra JM, Diniz da Costa JC, Iulianelli A, Basile A. 8 - Porous ceramic membranes for membrane reactors. In: Basile A, editor. Handbook of Membrane Reactors. : Woodhead Publishing; 2013. p. 298-336.

[83] Ismail AF, David L. A review on the latest development of carbon membranes for gas separation. *Journal of Membrane Science.* 2001; 193(1):1-18.

[84] Tsai C, Tam S, Lu Y, Brinker CJ. Dual-layer asymmetric microporous silica membranes. *Journal of Membrane Science.* 2000; 169(2):255-268.

[85] Ju X, Huang P, Xu N, Shi J. Influences of sol and phase stability on the structure and performance of mesoporous zirconia membranes. *Journal of Membrane Science.* 2000; 166(1):41-50.

[86] McCool BA, Hill N, DiCarlo J, DeSisto WJ. Synthesis and characterization of mesoporous silica membranes via dip-coating and hydrothermal deposition techniques. Journal of Membrane Science. 2003; 218(1–2):55-67.

[87] Zhu J, Fan Y, Xu N. Modified dip-coating method for preparation of pinhole-free ceramic membranes. Journal of Membrane Science. 2011; 367(1):14-20.

[88] Okon E, Shehu H, Gobina E. Novel Application of Gas Transport Properties with Ceramic Membrane for VOC Emission and Lactic Acid Esterification. *European Journal of Engineering and Technology Vol.* 2014; 2(2).

[89] Criscuoli A, Basile A, Drioli E. An analysis of the performance of membrane reactors for the water–gas shift reaction using gas feed mixtures. *Catalysis Today.* 2000; 56(1):53-64.

[90] Ye P, Grahn M, Korelskiy D, Hedlund J. Efficient separation of N2 and he at low temperature using MFI membranes. AIChE Journal. 2016; 62(8):2833-2842.

[91] Sunarso J, Hashim S, Lin Y, Liu S. Membranes for helium recovery: An overview on the context, materials and future directions. Separation and Purification Technology. 2016; .

[92] Donald J. Bowe, "Helium Recovery and Recycling Makes Good Business Sense," Industrial Heating (2004), pp. 79-81. http://wwvv.airproducts.com/NR/rdonlyres/F9D0CAA5-2A67-413B-A71F-54C72CD46E67/0/ IHHeRecoveryArticlefinal.pdf.

[93] Ruthven DM. Diffusion through Porous Media: Ultrafiltration, Membrane Permeation and Molecular Sieving. 2009; .

[94] Coronas J, Santamarıa J. Catalytic reactors based on porous ceramic membranes. *Catalysis Today*. 1999; 51(3):377-389.

[95] Lee D, Oyama ST. Gas permeation characteristics of a hydrogen selective supported silica membrane. *Journal of Membrane Science*. 2002; 210(2):291-306.

[96] Sidhu PS, Cussler E. Diffusion and capillary flow in track-etched membranes. *Journal of Membrane Science*. 2001; 182(1):91-101.

[97] Lee H, Yamauchi H, Suda H, Haraya K. Influence of adsorption on the gas permeation performances in the mesoporous alumina ceramic membrane. *Separation and Purification Technology*. 2006; 49(1):49-55.

[98] Phattaranawik J, Jiraratananon R, Fane A. Effect of pore size distribution and air flux on mass transport in direct contact membrane distillation. *Journal of Membrane Science*. 2003; 215(1):75-85.

[99] Marković A, Stoltenberg D, Enke D, Schlünder E, Seidel-Morgenstern A. Gas permeation through porous glass membranes: Part II: Transition regime between Knudsen and configurational diffusion. *Journal of Membrane Science*. 2009; 336(1):32-41.

[100] Ohwoka A, Ogbuke I, Gobina E. Performance of pure and mixed gas transport in reconfigured hybrid inorganic membranes Pt.2. *Membrane Technology*. 2012; 2012(7):7-9.

[101] Benito JM, Conesa A, Rubio F, Rodríguez MA. Preparation and characterization of tubular ceramic membranes for treatment of oil emulsions. *Journal of the European Ceramic Society*. 2005; 25(11):1895-1903.

[102] Singh RP, Way JD, McCarley KC. Development of a model surface flow membrane by modification of porous vycor glass with a fluorosilane. *Industrial & Engineering Chemistry Research*. 2004; 43(12):3033-3040.

[103] Javaid A. Membranes for solubility-based gas separation applications. Chemical Engineering Journal. 2005; 112(1):219-226.

[104] Basu A, Akhtar J, Rahman M, Islam M. A review of separation of gases using membrane systems. Petroleum Science and Technology. 2004; 22(9-10):1343-1368.

[105] Nguyen QT, M'Bareck CO, David MO, Métayer M, Alexandre S. Ion-exchange membranes made of semi-interpenetrating polymer networks, used for pervaporation-assisted esterification and ion transport. *Materials Research Innovations.* 2003; 7(4):212-219.

[106] Y. Lim S, Park B, Hung F, Sahimi M, T. Tsotsis T. *Design issues of pervaporation membrane reactors for esterification.* 2002ID: 271348.

[107] Morigami Y, Kondo M, Abe J, Kita H, Okamoto K. *The first large-scale pervaporation plant using tubular-type module with zeolite NaA membrane.* 2001ID: 271948.

108] Gobina E. *Apparatus and method for separating gases.* 2006; .

[109] Gobina E. *Apparatus and method for separating gases.* 2007; .

[110] De Vos RM, Verweij H. Improved performance of silica membranes for gas separation. Journal of Membrane Science. 1998; 143(1):37-51.

[111] Lin Y. Microporous and dense inorganic membranes: current status and prospective. *Separation and Purification Technology.* 2001; 25(1):39-55.

[112] Han HH, Ryu SH, Nakao S, Lee YT. Gas permeation properties and preparation of porous ceramic membrane by CVD method using siloxane compounds. Journal of Membrane Science. 2013; 431(0):72-78.

[113] Gitis V, Rothenberg G. Ceramic Membranes: New Opportunities and Practical Applications. : John Wiley & Sons; 2016.

[114] Okon E, Shehu H, Gobina E. Evaluation of the performance of α-alumina nano-porous ceramic composite membrane for esterification applications in petroleum refinery. Catalysis Today.

[115] Poshusta JC, Noble RD, Falconer JL. Temperature and pressure effects on CO< sub> 2</sub> and CH< sub> 4</sub> permeation through MFI zeolite membranes. *Journal of Membrane Science.* 1999; 160(1):115-125.

[116] Coutinho FM, Souza RR, Gomes AS. Synthesis, characterization and evaluation of sulfonic resins as catalysts. *European Polymer Journal.* 2004; 40(7):1525-1532.

[117] Jogunola O, Salmi T, Wärnå J, Mikkola J. Kinetic and diffusion study of acid-catalyzed liquid-phase alkyl formates hydrolysis. *Chemical engineering science.* 2012; 69(1):201-210.

[118] Edidiong O, Habiba S and Gobina E. Batch Process Esterification of Lactic Acid Catalysed by Cation-exchange Resins for the Production of Environmental-friendly Solvent. *Proceedings of the World Congress on Engineering and Computer Science*; 2015.

[119] Santos-Barbosa J, Lee ST, Cook D, Gardner DR, Viana LH, Ré N. A Gas Chromatography-Mass Spectrometry (GC-MS) Method for the Detection and Quantitation of Monofluoroacetate in Plants Toxic to Livestock. *Journal of Agricultural and Food Chemistry.* 2017;.

[120] Komoń T, Niewiadomski P, Oracz P, Jamróz ME. Esterification of acrylic acid with 2-ethylhexan-1-ol: Thermodynamic and kinetic study. *Applied Catalysis A: General.* 2013; 451:127-136.

[121] CHRISTIAN, G. D., 2004. Analytical Chemistry. 6th ed. John Wiley and Sons. Pte Ltd, Singapore.

[122] Santos F, Galceran M. Modern developments in gas chromatography–mass spectrometry-based environmental analysis. *Journal of Chromatography A.* 2003; 1000(1):125-151.

[123] Nigiz FU, Hilmioglu ND. Simultaneous separation performance of a catalytic membrane reactor for ethyl lactate production by using boric acid coated carboxymethyl cellulose membrane. Reaction Kinetics, Mechanisms and Catalysis. :1-19.

[124] Kwon SJ, Song KM, Hong WH, Rhee JS. Removal of water produced from lipase-catalyzed esterification in organic solvent by pervaporation. Biotechnology and bioengineering. 1995; 46(4):393-395.

[125] Okon E, Shehu H, Gobina E. Novel esterification reaction from biomass product by coupled acetate membrane and catalysts for ethyl lactate separation. International Journal of Hydrogen Energy. 2017.

[126] Hubadillah SK, Harun Z, Othman MHD, Ismail A, Salleh WNW, Basri H, et al. Preparation and characterization of low cost porous ceramic membrane support from kaolin using phase inversion/sintering technique for gas separation: Effect of kaolin content and non-solvent coagulant bath. *Chemical Engineering Research and Design.* 2016; 112:24-35.

[127] School of Pharmacy and Life Sciences, 2017. Laboratory Manual. The Robert Gordon University, Aberdeen, Scotland, UK.

[128] Karimi S, Korelskiy D, Mortazavi Y, Khodadadi AA, Sardari K, Esmaeili M, et al. High flux acetate functionalized silica membranes based on in-situ co-condensation for CO2/N2 separation. Journal of Membrane Science. 2016; 520:574-582.

[129] Weidenthaler C. Pitfalls in the characterization of nanoporous and nanosized materials. *Nanoscale.* 2011; 3(3):792-810.

[130] Okon E, Shehu H and Gobina E. Characterisation of Inorganic Composite Ceramic Membrane for Lactic Acid Esterification Processes. *Advanced Materials Research*: Trans Tech Publ; 2015. p. 99-102.

[131] Okon Edidiong, Mohammed NasirKajama, Habiba Shehu, Ngozi Nwogu and Edward Gobina. Surface area analysis and gas transport properties with inorganic ceramic membranes. *International Journal of Current Research. Vol. 6, Issue, 11, pp.9569-9575, November, 2014.*

[132] Vospernik M, Pintar A, Berčič G, Batista J, Levec J. Potentials of Ceramic Membranes as Catalytic Three-Phase Reactors. *Chemical Engineering Research and Design.* 2004; 82(5):659-666.

[133] Miao S, Shanks BH. Mechanism of acetic acid esterification over sulfonic acid-functionalized mesoporous silica. Journal of Catalysis. 2011; 279(1):136-143.

[134] Wall Y, Braun G, Brunner G. Gas transport through ceramic membranes under super-critical conditions. *Desalination.* 2010; 250(3):1056-1059.

[135] Kanellopoulos NK. Recent advances in gas separation by microporous ceramic membranes. : Elsevier; 2000.

[136] Xomeritakis G, Naik S, Braunbarth C, Cornelius CJ, Pardey R, Brinker C. Organic-templated silica membranes: I. Gas and vapor transport properties. *Journal of Membrane Science.* 2003; 215(1):225-233.

[137] Zornoza B, Casado C, Navajas A. Chapter 11 - Advances in Hydrogen Separation and Purification with Membrane Technology. In: Diéguez LMGAM, editor. *Renewable Hydrogen Technologies.* Amsterdam: Elsevier; 2013. p. 245-268.

[138] Araki S, Mohri N, Yoshimitsu Y, Miyake Y. Synthesis, characterization and gas permeation properties of a silica membrane prepared by high-pressure chemical vapor deposition. *Journal of Membrane Science.* 2007; 290(1):138-145.

[139] Amanipour M, Safekordi A, Ganji Babakhani E, Zamaniyan A, Heidari M. Effect of synthesis conditions on performance of a hydrogen selective nano-composite ceramic membrane. *International Journal of Hydrogen Energy.* 2012; 37(20):15359-15366.

[140] Barma S, Mandal B. Synthesis and characterization of ordered mesoporous silica membrane: Role of porous support and gas permeation study. *Microporous and Mesoporous Materials.* 2015; 210:10-19.

[141] Okon E, Kajama MN, Gobina E. Gas Permeation on Silica Membrane for Lactic Acid Esterification Applications. *Journal of Energy.* 2014; 1(5):265-269.

[142] Lee D, Zhang L, Oyama S, Niu S, Saraf RF. Synthesis, characterization, and gas permeation properties of a hydrogen permeable silica membrane supported on porous alumina. Journal of Membrane Science. 2004; 231(1):117-126.

[143] Okon E, Shehu H, Kajama M, Nwogu N, Orakwe I and Edward G. Cation-Exchange Resin Characterisation and Carrier Gas Performance with Mesoporous Silica Membranes for Ethyl Lactate Separation. *International Journal of Engineering Research and Technology*: ESRSA Publications; 2015.

[144] Tomita T, Nakayama K, Sakai H. Gas separation characteristics of DDR type zeolite membrane. *Microporous and Mesoporous Materials.* 2004; 68(1):71-75.

[145] Lee H, Suda H, Haraya K. Gas permeation properties in a composite mesoporous alumina ceramic membrane. Korean Journal of Chemical Engineering. 2005; 22(5):721-728.

[146] Julian A, Juste E, Chartier T, Del Gallo P and Richet N. Catalytic Membrane Reactor: Multilayer membranes elaboration. Catalytic Membrane Reactor: Multilayer membranes elaboration. *Proceedings of the 10th International Conference of the European Ceramic Society*; 2007. p. 718-722.

[147] Sharma M, Wanchoo R, Toor AP. Amberlyst 15 Catalyzed Esterification of Nonanoic Acid with 1-Propanol: Kinetics, Modeling, and Comparison of Its Reaction Kinetics with Lower Alcohols. Industrial & Engineering Chemistry Research. 2014; 53(6):2167-2174.

[148] Siebert TE, Smyth HE, Capone DL, Neuwöhner C, Pardon KH, Skouroumounis GK, et al. Stable isotope dilution analysis of wine fermentation products by HS-SPME-GC-MS. *Analytical and bioanalytical chemistry.* 2005; 381(4):937-947.

[149] Akbay EÖ, Altıokka MR. Kinetics of esterification of acetic acid with n-amyl alcohol in the presence of Amberlyst-36. *Applied Catalysis A: General.* 2011; 396(1):14-19.

[150] Kumar H, Alén R. Recovery of aliphatic low-molecular-mass carboxylic acids from hardwood kraft black liquor. *Separation and Purification Technology.* 2015; 142:293-298.

[151] Rohde MP. *In-situ H_1tn2O Removal Via Hydrophilic Membranes During Fischer-Tropsch and Other Fuel Related Synthesis Reactions.* : KIT Scientific Publishing; 2011.

[152] Pighin E, Díez V, Di Cosimo J. Synthesis of ethyl lactate from triose sugars on Sn/Al 2 O 3 catalysts. *Applied Catalysis A: General.* 2016; 517:151-160.

[153] Khudsange CR, Wasewar KL. Process intensification of esterification reaction for the production of propyl butyrate by pervaporation. *Resource-Efficient Technologies.* 2017; 3(1):88-93.

[154] Rathod AP, Wasewar KL, Sonawane SS. Intensification of Esterification Reaction of Lactic Acid with Iso-propanol using Pervaporation Reactor. *Procedia Engineering.* 2013; 51:456-460.

[155] Chandane VS, Rathod AP, Wasewar KL. Enhancement of esterification conversion using pervaporation membrane reactor. *Resource-Efficient Technologies.* 2016; 2:S47-S52.

[156] Mitsutani A. Future possibilities of recently commercialized acid/base-catalyzed chemical processes. Catalysis today. 2002; 73(1):57-63.

[157] Mandake M, Aneka S, Walke S. Kinetic Study of Catalyzed and Uncatalyzed Esterification Reaction of Acetic acid with Methanol. *American International Journal of Research in Science, Technology, Engineering & Mathematics.* 2013; 2013:13-225.

[158] Nie H, Xu R, Zhang F, Zhou Z, Zhang Z, Yang G. Thermodynamic and kinetic studies on alkoxylation of camphene over cation exchange resin catalysts. *AIChE Journal.* 2015; 61(6):1925-1932.

[159] Lilja J, Wärnå J, Salmi T, Pettersson LJ, Ahlkvist J, Grénman H, et al. Esterification of propanoic acid with ethanol, 1-propanol and butanol over a heterogeneous fiber catalyst. *Chemical Engineering Journal.* 2005; 115(1–2):1-12.

[160] Mekala M, Thamida SK, Goli VR. Pore diffusion model to predict the kinetics of heterogeneous catalytic esterification of acetic acid and methanol. Chemical Engineering Science. 2013; 104:565-573.

[161] Sharma M, Toor AP, Wanchoo RK. Esterification of Pentanoic Acid with 1-Propanol by Sulfonated Cation Exchange Resin: Experimental and Kinetic Studies. Chemical Engineering Communications. 2016; 203(6):801-808.

[162] Okon E, Shehu H and Gobina E. An Experimental Analysis of Lactic Acid Esterification Process Using Langmuir-Hinshelwood Model. Key Engineering Materials: Trans Tech Publ; 2017. p. 36-41.

[163] Okon Edidiong, Habiba S and Edward G. Validation of a Novel Method for Ethyl Lactate Separation Using Langmuir Hinshelwood Model. The World Congress on Engineering and Computer Science: Springer; 2015. p. 499-512.

[164] Zuriarrain A, Zuriarrain J, Puertas AI, Dueñas MT, Berregi I. Quantitative determination of lactic and acetic acids in cider by 1 H NMR spectrometry. *Food Control.* 2015; 52:49-53.

[165] Rastegari H, Ghaziaskar HS. From glycerol as the by-product of biodiesel production to value-added monoacetin by continuous and selective esterification in acetic acid. *Journal of Industrial and Engineering Chemistry.* 2015; 21:856-861.

[166] Miao S, Shanks BH. Esterification of biomass pyrolysis model acids over sulfonic acid-functionalized mesoporous silicas. *Applied Catalysis A: General.* 2009; 359(1):113-120.

APPENDICES

APPENDIX A: RELEVANT PUBLICATIONS RESULTING FROM THIS WORK

[1] Edidiong Okon, Habiba Shehu, Mohammed Kajama and Edward Gobina. Investigation of Carrier Gas Transport through Silica Membrane for Ethyl Lactate Separation and VOC Emission Applications. *International Journal of Current Research. 2015;* Vol. 7, Issue, 04, pp.14975-14979. http://www.journalcra.com.

[2] Edidiong Okon, Habiba Shehu, Mohammed Kajama, Ngozi Nwogu, Ifeyinwa Orakwe and Edward Gobina. Cation-exchange resin Characterisation and Carrier gas Performance with Mesoporous Silica Membranes for Ethyl lactate Separation. *International Journal of Engineering Research & Technology. 2015;* Vol. 4 - Issue 04, pp. 465-469. 10.17577/IJERTV4IS040606.

[3] Okon Edidiong, Shehu Habiba, Edward Gobina. Gas Transport through Inorganic Ceramic Membrane and Cation-exchange resins Characterization for Ethyl lactate Separation. *Transaction on Engineering Technologies. Book Chapter 29: Springer-link Science + Business Media Dordrecht. 2015; Pp 1-12. http://dx.doi.org/10.10007/978-94-017-7236-5-29.*

[4] Edidiong Okon, Habiba Shehu, Edward Gobina. Characterisation of Inorganic Composite Ceramic Membrane for Lactic Acid Esterification Processes. *Advanced Materials Research. 2015; Vol 1102, Pp. 99-102. 10.4028/www.scientific.net/AMR.1102.9.*

[5] Edidiong Okon, Habiba Shehu, Ngozi Nwogu, Mohammed Kajama, Ifeyinwa Orakwe and Edward Gobina. Resin Characterization and Tubular Membrane Transport with Single Gases for Ethyl Lactate Separations for Industrial Purposes. 2015. *Journal of Material Science and Chemical Engineering 2015;* 3(9); pp 1-7. http://dx.doi.org/10.4236/msce.

[6] Edidiong Okon, Habiba Shehu, Edward Gobina. Initial Study of Batch Process Esterification of Lactic acid and Ethanol Catalysed by Cation-exchange resins and Carrier Gas Permeation. *American International Journal of Research in Science, Technology, Engineering & Mathematics. 2015; Vol. 2(11), pp. 175-180. http://iasir.net/AIJRSTEMpapers/AIJRSTEM15-507.pdf.*

[7] Okon Edidiong, Shehu Habiba, Edward Gobina. Novel Application of Gas Transport Properties with Ceramic Membrane for VOC Emission and Lactic Acid Esterification. *European Journal of Engineering and Technology. 2014; 2(2); Pp 37-44. http://www.ejet.com/.*

[8] Okon Edidiong, Shehu Habiba, Edward Gobina. Synthesis of Gas Transport through Nano Composite Ceramic Membrane for Esterification and Volatile Organic Compound Separations. *Journal of Mechanics Energy and Automation. 2014;(4); Pp 905-913. http://www.jmea.com/.*

[9] Edidiong Okon, Mohammed Nasir Kajama and Edward Gobina. Gas Permeation on Silica Membrane for Lactic Acid Esterification Applications. *Journal of Energy Power Sources, 2014;* Vol. 1, Issue 5, pp. 265-269. http://www.ethanpublishing.com/.

[10] Edidiong Okon, Mohammed Nasir Kajama, Habiba Shehu, Ngozi Nwogu and Edward Gobina. Surface Area Analysis and Gas Transport Properties with Inorganic Ceramic Membranes. *International Journal of Current Research, 2014;* Vol. 6, Issue 11, pp. 9569-9575. http://www.journalcra.com.

[11] Edidiong Okon, Habiba Shehu, Ngozi Nwogu, Mohammed Kajama, Ifeyinwa Orakwe and Edward Gobina. Experimental Characterisation of Cation-exchange Resin for Biomass Green Solvent Production. *International Journal of Scientific Engineering and Technology. 2016; 5(4); Pp 173 – 179.* 10.17950/ijset/v5s4/403.

[12] Okon E, Shehu H and Gobina E. Evaluation and Characterisation of composite Mesoporous Membrane for Lactic acid and Ethanol Esterification. Journal of Advance Chemical Engineering. 2016; 6(2), pp 1-5. http://dx.doi.org/10.4172/2090-4568.1000147.

[13] Okon Edidiong, Shehu Habiba, Mohammed Kajama and Edward Gobina. An Experimental study of catalysts and carrier gas transport through membranes for improved yield of ester product. *Transaction on Engineering Technologies. Book Chapter 11: Springer-link Science + Business Media Dordrecht. 2016; Pp 139 - 150. http://dx.doi.org/10.1007/978-981-10-1088-0-11.*

[14] Okon Edidiong, Shehu Habiba and Gobina Edward. Novel Study of catalysts and membranes in esterification reactions. *Transaction on Engineering Technologies. Book Chapter 25: Springer-link Science + Business Media Dordrecht. 2016; Pp 329 -340. http://dx.doi.org/10.1007/978-981-10-1088-0-25.*

[15] Okon Edidiong, Shehu Habiba and Edward Gobina. Validation of a Novel Method for Ethyl Lactate Separation Using Langmuir Hinshelwood Model. *Transaction on Engineering Technologies. Chapter 35: Springer-link Science + Business Media Dordrecht. 2017; Pp 499-512. http://dx.doi.org/10.1007/978-981-10-2717-8-35*. .

[16] Okon, E., Shehu, H., Orakwe, I. and Gobina E. Advanced Catalytic Membrane Characterisation and Gas Permeation Properties for Enhanced Ethyl Lactate Conversion. Journal of Materials Science and Chemical Engineering, 2017; 5 (3), Pp 1-16. *http://doi.org/10.4236/msce.2017.53001*.

[17] Edidiong Okon, Habiba Shehu and Edward Gobina. Evaluation of the performance of α-alumina nano-porous ceramic composite membrane for esterification applications in petroleum refinery. Catalysis Today, (2017). http://dx.doi.org/10.1016/j.cattod.2017.05.089.

[18] Edidiong Okon, Habiba Shehu, Edward Gobina. Novel esterification reaction from biomass product by coupled acetate membrane and catalysts for ethyl lactate separation. International Journal of Hydrogen Energy, (2017). http://dx.doi.org/10.1016/j.ijhydene.2017.07.230. Page 1-10.

[19] Shuaibu Baba, **Edidiong Okon**, Ngozi Nwogu, Habiba Shehu and Edward Gobina. Characterization of Silica Membranes Exhibiting an Ordered Porosity for Gas Separation Processes. International Journal of Mechanical Engineering and Automation. Volume 2, Number 10, 2015, pp. 476-481. *www.ethanpublishing.com/index.php?m=content&c=index.*

[20] Ifeyinwa Orakwe, **Edidiong Okon** and Edward Gobina. Development of Catalytic Membrane Reactors for Esterification of Lactic Acid and Hydrogenation of Water for Oxygen Removal. International Journal of Scientific Engineering and Technology. 2016; 5(6), pp 335 – 338. 10.17950/ijset/v5s6/603.

[21] Mohammed Nasir Kajama, Habiba Shehu, **Edidiong Okon** and Ifeyinwa Orakwe. Single gas Permeation on γ-Alumina ceramic support. Journal of Advance Chemical Engineering. 2016; 6(2), pp 1-5. http://dx.doi.org/10.4172/2090-4568.1000154.

[22] Habiba Shehu, **Edidiong Okon** and Edward Gobina. Initial Study of Gas Separations and Esterification using composite Y- Type Zeolite Membrane. *International Journal of scientific Research. 2015; Vol 4(5), pp 5-8. www.citefactor.org/.../**initial-study-of-gas-separations-and-esterification***.

[23] Habiba Shehu, **Edidiong Okon**, Mohammed Kajama, Ngozi Nwogu, Ify Orakwe and Edward Gobina. An Initial Study of the Selectivity of Methane over Carbon Dioxide and Inert Gases Using A Y- Type Zeolite Membrane. *International Journal of Current Research.* 2015; Vol. 7, Issue, 04, pp.14986-14990. http://www.journalcra.com.

[24] Mohammed Nasir Kajama, Habiba Shehu, **Edidiong Okon**, Edward Gobina. Preparation and Characterization of Inorganic Membranes for Hydrocarbon Separation from N_2 for Environmental Applications. *Energy and Environment Research. 2015;* 5(1) 110-120. 10.5539/eer.v5n1p110 .

[25] Ngozi N, **Edidiong O**, Edward G. Integration of Gas Transport through a Composite Catalytic Inorganic Ceramic Membrane for Environmental Gas Separation Processes. *Journal of Scientific Engineering and Technology. 2014; 9(3); Pp 1184 – 1188. http://www.jset.com/.*

[26] N. C. Nwogu, M.N. Kajama**, E. P. Okon**, H. Shehu & E. Gobina. Testing of Gas Permeance Techniques of a Fabricated CO_2 Permeable Ceramic Membrane for Gas Separation Purposes. *International Journal of Advance Research in Computer Science and Management Studies*. 2014; Volume 2, Issue 9, pp. 429-436. http://www.ijarcsms.com/.

[27] Mohammed Nasir Kajama, Habiba Shehu, **Edidiong Okon**, Ify Orakwe and Edward Gobina. VOC oxidation in excess of oxygen using flow-through catalytic membrane reactor. International journal of hydrogen energy (Elsevier). 2016; 4, 164, pp1-6. 10.1016/j.ijhydene.2016.04.164.

[28] Habiba Shehu, **Edidiong Okon**, Ifeyinwa Orakwe and Edward Gobina. Study of the selectivity of methane over carbon dioxide using composite inorganic membranes for Natural Gas Processing. Journal of Advance Chemical Engineering. 2016; 6(2), pp 1-5. http://dx.doi.org/10.4172/2090-4568.1000150.

[29] N. C. Nwogu, M.N. Kajama, **E. P. Okon**, H. Shehu & E. Gobina. A Novel Performance of Ordered Porous Ceramic Materials in Hydrogen Recovery Processes for Sustainable Energy Potential. *International Journal of Advance Research in Computer Science and Management Studies*. 2014; Volume 2, Issue 9, pp. 44-50. http://www.ijarcsms.com/.

APPENDIX B: PUBLISHED CONFERENCE PROCEEDINGS

[1] Edidiong, O. and E, G. 2015. Initial Study of Heterogeneous Catalysts Behaviour and Carrier Gas Permeation with Catalytic Inorganic Ceramic Membrane for Lactic Acid Esterification Applications. *Proceedings of the World Congress on Engineering 2015; Vol II WCE 2015, July 1 - 3, 2015, London, UK. www.iaeng.org/publication/WCE2015/WCE2015_pp1287-1291.pdf.*

[2] Edidiong, O., Habiba, S., Mohammed, K., Adesola, O., Ngozi, N., Ifeyinwa, O. and Edward Gobina, 2015. Hydrodynamic Performance in Mesoporous Silica Membrane for Lactic Acid and Esterification. *Proceedings of the World Congress on Engineering. 2015; Vol II WCE 2015, July 1 - 3, 2015, London, UK.* www.iaeng.org/publication/WCE2015/WCE2015_pp781-784.pdf.

[3] Okon E, Shehu H and Gobina E. Gas Transport and Characterization of Inorganic Ceramic Membrane for Lactic Acid Esterification. Lecture notes in Engineering and Computer Science: *Proceedings of the World Congress on Engineering and Computer Science 2014, Vol II, WCECS 2014, 22-24 October 2104, San Francisco, USA. www.iaeng.org/publication/WCECS2014/WCECS2014_pp590-594.pdf.*

[4] Okon E, Shehu H and Gobina E. Batch Process Esterification of Lactic acid Catalysed by Cation-exchange resins for the Production of Environmental-friendly Solvent. *Proceedings of the World Congress on Engineering and Computer Science 2014, Vol II, WCECS 2015, 21--23 October, 2015, San Francisco, USA. www.iaeng.org/publi**cation**/WCECS2015/WCECS2015_pp623-628.pdf.*

[5] Okon E, Shehu H and Gobina E. Experimental Study of Gas Transport through a Ceramic Membrane. Annual Environmental and Clean Technology Conference. Glasgow, United Kingdom, 26 June, 2014. *www.setn.org.uk/wordpress/wp-content/uploads/.../Poster-abstracts.pdf.*

[6] Okon E and Gobina E. Solid cation-exchange resin catalysts esterification of lactic acid with ethanol: A novel kinetic study. *Nanotech France 2016, NanoMetrology France 2016, NanoMatEn 2016 and European Graphene Forum – EGF 2016, Joint Conferences Proceedings. 1-3rd June, 2016, Paris, France.*http://www.setcor.org/files/papers/1478387399_Nanotech%20France%202016%20Procceding%20papers%20document.pdf.

[7] Edidiong Okon, Habiba Shehu and Edward Gobina. An Experimental Analysis of lactic acid esterification process using Langmuir-Hinshelwood Model. Proceedings of the 2016 International conference on Nanotechnology and Nanomaterials in Energy (ICNNE 2016), 2-4th June, 2016, Paris, France. http://www.ttp.net/978-3-0357-1016-8.html .

[8] O Edidiong, S Habiba, and E Gobina. Esterification of Lactic Acid and Ethanol using Heterogeneous Catalysts for the Production of a Bio-based Chemical. Lecture Notes in Engineering and Computer Science: Proceedings of The International MultiConference of Engineers and Computer Scientists 2017, 15-17 March, 2017, Hong Kong, pp811-817.
http://www.iaeng.org/publication/IMECS2017/IMECS2017_pp806-810.pdf.

[9] Edidiong Okon, Habiba Shehu and Edward Gobina. Effect of Resins and Membrane Permeation for improved selectivity. *Proceedings of the World Congress on Engineering 2017; Vol II WCE 2017, July 5 - 7, 2017, London, UK. pp1059-1065.*
http://www.iaeng.org/publication/WCE2017/WCE2017_pp .1-7 pdf.

[10] Okon E, Shehu H and Edward Gobina. Synthesis and Permeability of a silica/γ-alumina composite membrane with carrier gases for the analysis of Esterification Product. *International Conference & Exhibition on Advanced & Nano Materials 2017 Proceeding August 7-9, 2017, Toronto, Canada. Pp 45-52.* http://iaemm.com.

APPENDIX C: CONFERENCES ATTENDED

[1] Okon E, Shehu H and Edward Gobina. Gas Transport and Characterization of Inorganic Ceramic Membrane for Lactic Acid Esterification. Oral presentation at the World Congress on Engineering and Computer Science (WCECS 2014), Berkeley, San Francisco, California, USA, 22-24 October, 2014. Won best student paper award at the Conference.

[2] Okon E, Shehu H and Edward Gobina. Experimental Study of Gas Transport through a Ceramic Membrane. Poster presentation at the 8th Annual Environmental and Clean Technology Conference. Glasgow, United Kingdom, 26 June, 2014 (Poster presentation).

[3] Okon E, Shehu H and Edward Gobina. Characterisation of Inorganic Composite Ceramic Membrane for Lactic Acid Esterification Processes. Oral presentation at the 2nd International Conference on Sensors and Materials Manufacturing Science, January 17-18, 2015, Paris, France (Oral presentation).

[4] Edidiong, O. and Edward Gobina, 2015. Initial Study of Heterogeneous Catalysts Behaviour and Carrier Gas Permeation with Catalytic Inorganic Ceramic Membrane for Lactic Acid Esterification Applications. *World Congress on Engineering.* 1-3rd July, 2015, London, United Kingdom. Won best student paper award at the Conference.

[5] Edidiong, O., Habiba, S., Mohammed, K., Adesola, O., Ngozi, N., Ifeyinwa, O. and Edward Gobina, 2015. Hydrodynamic Performance in Mesoporous Silica Membrane for Lactic Acid and Esterification. World Congress on Engineering. 2015; Vol II WCE 2015, July 1 - 3, 2015, London, UK. Won best student paper award at the Conference.

[6] Edidiong O, Habiba Shehu and Edward Gobina (2015). Composite inorganic membrane characterization and gas permeation for lactic acid esterification. Advanced Membrane Technology VI: Water, Energy, and New Frontiers. An ECI Conference Series. February 8-13, 2015, Sicily, Italy (Poster Presentation).

[7] Okon E, Shehu H and Edward Gobina. Batch Process Esterification of Lactic acid Catalysed by Cation-exchange resins for the Production of Environmental-friendly Solvent. Oral presentation at the *International Conference on Chemical Engineering; World Congress on Engineering and Computer Science (WCECS 2015), Berkeley, San Francisco, California, USA, 21-23 October, 2015.* Won best student paper award at the Conference.

[8] Okon E, Shehu H and Edward Gobina. Evaluation and characterization of composite mesoporous membrane for lactic acid and ethanol esterification. Oral presentation at the 3rd *International conference on Mechanical and Aerospace Engineering (Mechaero 2015). San Francisco, California, USA, 5-7 October, 2015.*

[9] Okon E, Shehu H and Edward Gobina. An Experimental analysis of lactic acid esterification process using Langmuir-Hinshelwood model. Oral presentation at the 2016 International Conference on Nanotechnology and Nanomaterials in Energy (ICNNE2016). Paris, France, 2 - 4th June, 2016.

[10] Okon E and Edward Gobina. Solid cation-exchange resin catalysts esterification of lactic acid with ethanol: A novel kinetic study. Oral presentation at the Nanotech France 2016 Conference and Exhibition (Nanotech France, 2016). Paris, France, 1-3rd June, 2016.

[11] Okon E and Edward Gobina. Experimental study of carrier gases permeability with ceramic membrane for ethyl lactate esterification product analysis. Poster presentation at the Emerging and Hybrid Membrane Technology. Swansea, United Kingdom, 10th June, 2016.

[12] Okon E and Edward Gobina. Evaluation Performance of α-alumina nano-porous ceramic composite membrane for Esterification applications in Petroleum Refinery. Poster presentation at the International Conference on Catalysis and Chemical Engineering (CCE-2017), Baltimore, USA, February 22-24, 2017.

[13] Okon E and Edward Gobina. Application of cellulose acetate membrane and resin catalysts in ethyl lactate intensification process for improved yield. Poster presentation at the International Conference on Catalysis and Chemical Engineering (CCE-2017), Baltimore, USA, February 22-24, 2017.

[14] Edidiong, O, Habiba S and Edward G. Esterification of Lactic Acid and Ethanol using Heterogeneous Catalysts for the Production of a Bio-based Chemical. The International MultiConference of Engineers and Computer Scientists 2017, March, 15-17 2017, Hong Kong.

[15] Edidiong, O, Habiba S and Edward Gobina, 2017. Effect of Resins and Membrane Permeation for improved selectivity. World Congress on Engineering. 5-7th July, 2017, Imperial College, London, United Kingdom. Won best student paper award at the Conference.

[16] Okon E, Shehu H and Edward Gobina. Novel esterification reaction from biomass product by coupled acetate membrane and catalysts for ethyl lactate separation. International Conference on Catalysis in Membrane Reactors July 10th to 13th, 2017, Houston, Texas, USA.

[17] Okon E, Shehu H and Edward Gobina. Synthesis and Permeability of a silica/γ-alumina composite membrane with carrier gases for the analysis of Esterification Product. International Conference & Exhibition on Advanced & Nano Materials. August 7-9th, 2017, Four Point by Sheraton, Toronto, Canada.

[18] Okon E, Shehu H and Edward Gobina. Thermal Stability study of catalysts in Esterification reaction Processes. Global Conference on Catalysis and Reaction Engineering. October 19-21, 2017 at Hampton Inn Tropicana and Event Centre, Las Vegas, Nevada, USA.

APPENDIX D: BOOK CHAPTER PUBLICATIONS

[1] Okon E, Shehu H, Edward Gobina. Gas Transport through Inorganic Ceramic Membrane and Cation-exchange resins Characterization for Ethyl lactate Separation. *Transaction on Engineering Technologies*. **Chapter 29**. Springer-link Science + Business Media Dordrecht. 2015. Pp 1-12. http://dx.doi.org/10.10007/978-94-017-7236-5-29.

[2] Okon Edidiong, Shehu Habiba, Mohammed Kajama and Edward Gobina. An Experimental study of catalysts and carrier gas transport through membranes for improved yield of ester product. *Transaction on Engineering Technologies.* **Chapter 11***: Springer-link Science + Business Media Dordrecht. 2016; Pp 139 - 150.* *http://dx.doi.org/10.1007/978-981-10-1088-0-11.*

[3] Okon Edidiong, Shehu Habiba and Edward Gobina. Novel Study of catalysts and membranes in esterification reactions. *Transaction on Engineering Technologies.* **Chapter 25***: Springer-link Science + Business Media Dordrecht. 2016; Pp 329 -340.* *http://dx.doi.org/10.1007/978-981-10-1088-0-25.*

[4] Shehu Habiba, **Okon Edidiong** and Edward Gobina. Novel Composite inorganic ceramic membranes for gas separations and environmental applications. *Transaction on Engineering Technologies.* **Chapter 5***: Springer-link Science + Business Media Dordrecht. 2016; Pp 59-72.* *http://dx.doi.org/10.1007/978-981-10-1088-0-5.*

[5] Edidiong Okon, Habiba Shehu, Edward Gobina. Characterisation of Inorganic Composite Ceramic Membrane for Lactic Acid Esterification Processes. **Chapter 3.** Composites, Advanced Materials and Nano Materials. 2015; Vol 1102, Pp. 99-102. 10.4028/www.scientific.net/AMR.1102.99.

[6] Edidiong Okon, Habiba Shehu, Edward Gobina. An Experimental Analysis of Lactic Acid Esterification Process Using Langmuir-Hinshelwood Model. **Chapter 36.** Key Engineering Materials. 2017; Vol 733, Pp. 36-41. 10.4028/www.scientific.net/KEM.733.36.

[7] Shehu Habiba, **Okon Edidiong** and Edward Gobina. Separation of Methane from Shuttle Tanker Vents Gases by Adsorption on a Polyurethane/Zeolite Membrane. **Chapter 42.** Key Engineering Materials. 2017; Vol 733, Pp 42-46. 10.4028/www.scientific.net/KEM.733.42.

[8] Okon Edidiong, Shehu Habiba and Edward Gobina. Validation of a Novel Method for Ethyl Lactate Separation Using Langmuir Hinshelwood Model. *Transaction on Engineering Technologies.* **Chapter 35***: Springer-link Science + Business Media Dordrecht. 2017; Pp 499-512.* *http://dx.doi.org/10.1007/978-981-10-2717-8-35.*

[9] Shehu Habiba, Adebayo Ajayi, **Okon Edidiong** and Edward Gobina. Recovery of VOC from Offshore and Onshore Shuttle Tankers Using Structured Y-Type Zeolite Membranes. *Transaction on Engineering Technologies.* **Chapter 38***: Springer-link Science + Business Media Dordrecht. 2017; Pp 541-553.* *http://dx.doi.org/10.1007/978-981-10-2717-8-38.* .

APPENDIX E: MEMBRANE CHARACTERISATION RESULTS: SEM OF SUPPORT AND SILICA COATED MEMBRANE

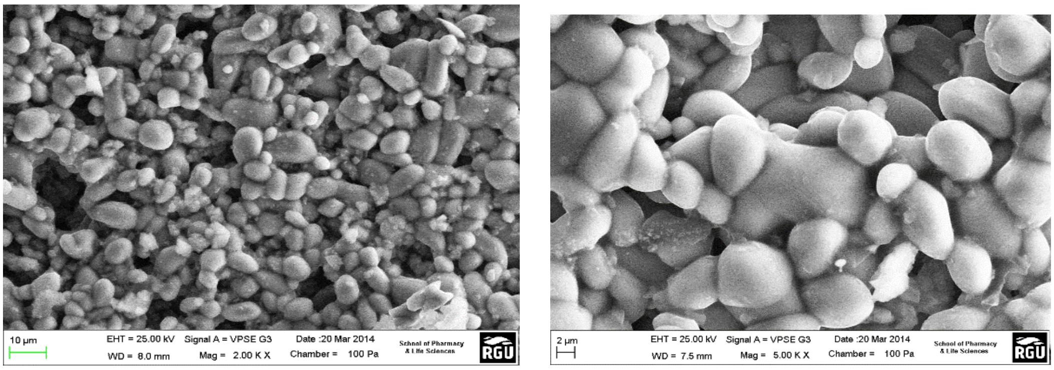

(a) Support inner surface (b) Support outer surface

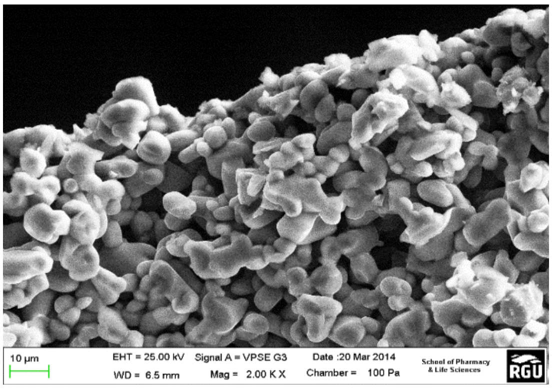

(c) Support membrane cross section

Figure B1: SEM surface micrograph of the inner (a) and outer (b) and cross section of silica coated membrane at different magnification.

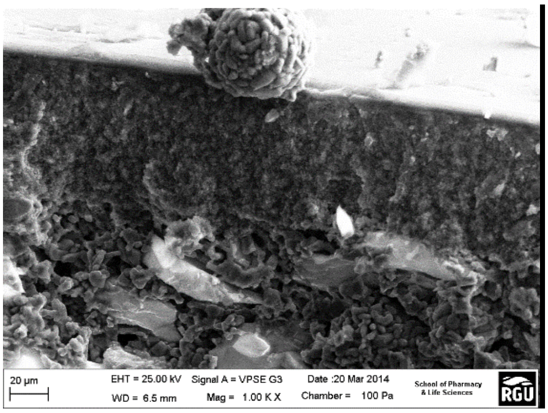

(a) cross section

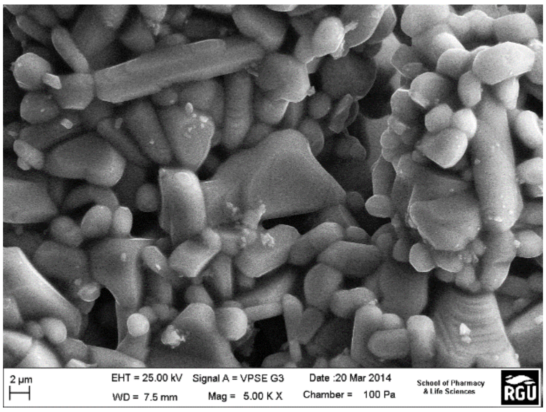

(b) inner surface

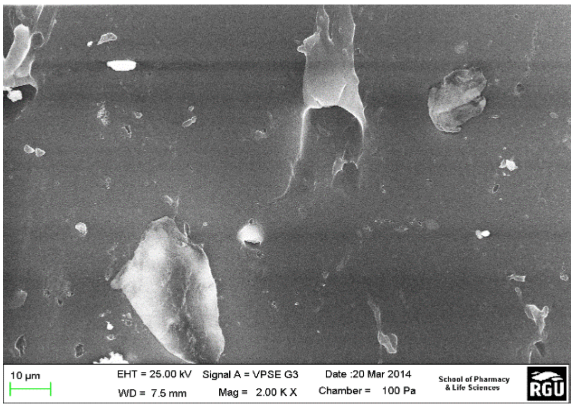

(c) Outer surface

Figure B2: SEM surface micrograph of the cross section (a) inner, (b) and outer (c) silica coated membrane at different magnification.

APPENDIX F: CALCULATION OF GAS FLUX

The flux of the helium carrier gas through the support and silica membrane was calculated at each temperature and transmembrane pressure. The following depicts a sample calculation for flux through the membranes from the measured values and stated conditions. The gas flux was calculated using the following equation:

$$J = \frac{Q}{A}$$

Where J = Gas flux (mol m^{-2} s^{-1}), Q = flow rate of the gases (mol s^{-1}), A= membrane surface area (m^2).

To determine the area of the membrane the following formula below was used:

$$\mathbf{A} = \frac{\mathbf{2\pi L(r_1 - r_2)}}{\mathbf{In(r_1 / r_2)}}$$

Where A = membrane surface area (m^2), L = length of the membrane (0.366m), r_1 = outer pore radius (0.10m), r_2 = inner pore radius (0.007 m), π = constant (3.142).

The membrane area was calculated as detailed below:

$$\boldsymbol{A} = \frac{\mathbf{2*3.142*0.366}\boldsymbol{m}\mathbf{*(0.01-0.007)}}{\boldsymbol{In}(\frac{\mathbf{0.01}}{\mathbf{0.007}})}$$

$$\boldsymbol{A} = \frac{\mathbf{6.899}\boldsymbol{x}\mathbf{10-3}}{\mathbf{0.3566}} = 0.0193 \text{ m}^2$$

APPENDIX G: CALCULATION OF GAS FLOW RATE

The gas flow of helium was recorded as 1.233L/min at the gauge pressure of 0.30bar and at 298K. Thus, the volume of gas permeating through the membrane obtained using a suitable conversion factor (22.4 L/min = 1 mols^{-1}) was calculated as detailed below:

$$\boldsymbol{Q = \frac{1.233}{60*22.4} = 0.000917 mols^{-1}}$$

The values of the calculated membrane area and flow rate for helium was then used to determine the flux of helium at 0.30bar and 298K as detailed below:

$$J = \frac{Q}{A}$$

$$\boldsymbol{J} = \frac{\mathbf{0.000917}}{\mathbf{0.0193}} = 0.0475\ \mathrm{molm^{-2}s^{-1}}$$

APPENDIX H: CALCULATION OF GAS PERMEANCE

The following is an example calculation of gas permeance at a specified pressure, using the equation as described below. For example, the permeation of helium gas through the ceramic membrane at a temperature of 298 K and at 0.30 bar pressure is calculates below. The permeance is then obtained from the flux using the equation:

$$Q_i = \frac{J}{\Delta P}$$

Where ΔP is the transmembrane pressure drop (bar), J = flux (mol m^{-2}s^{-1}) and Qi is the permeance (mol m^{-2} s^{-1} Pa^{-1}). Thus, the inlet gauge pressure for helium gas at 298K was obtained using a suitable conversion factor (1bar = 100000Pascal), Therefore the gauge pressure at 0.30bar was obtained to 3000Pascal and this was used for the permeance calculation of helium gas at 298K. From the equation the calculated flux value is then used to calculate the gas permeance of helium at 0.30 bar and at 298 K, as detailed below:

$$Q_i = \frac{\mathbf{0.0475}\ \boldsymbol{molm^{-2}s^{-1}}}{30000} = 1.583 \text{ X } 10^{-6}\ \mathrm{molm^{-2}s^{-1}Pa^{-2}}$$

The above process was then repeated to calculate the permeance of each test gas at the varying experimental conditions and throughout each membrane.

APPENDIX I: CALCULATION OF MEMBRANE SELECTIVITY

The Knudsen experimental selectivity was calculated using the permeance ratio of CO_2 with respect to each single gas at each gauge pressure (bar) with the ceramic membrane. The helium selectivity is calculated from the ratio of the helium permeance to CO_2 permeance as shown in the equation below:

$$\propto_{kHe/CO_2} = \sqrt{\frac{M_{weight\ CO2}}{M_{weightHe}}}$$

Where α_k = Permeance ratio of CO_2/He, $M_{weightHe}$ = Molecular weight of He (g/mol) and $M_{weightCO2}$= Molecular weight of CO_2 (g/mol). An example at helium permselectivity at 0.30bar at 298K is shown below:

Table E1: Permeance ratio of CO_2/Ar, CO_2/He and CO_2/N_2 gases with ceramic membrane at 298K.

Gauge pressure (bar)	Permeance ratio of CO_2/Ar	Permeance ratio of CO_2/He	Permeance ratio of CO2/N2
0.01	0.804	0.643	0.865
0.02	0.898	0.657	0.844
0.03	0.811	0.602	0.854
0.04	0.696	0.588	0.759
0.05	0.675	0.572	0.855
0.06	0.724	0.533	0.819
0.07	0.675	0.496	0.769
0.08	0.699	0.510	0.773
0.09	0.728	0.525	0.789

The Knudsen theoretical selectivity was calculated using the square root of the molecular weight of the individual gases (He, Ar and N_2) with respect to the CO_2. The Knudsen theoretical selectivity calculation for helium gas is shown below:

$$\propto_k = \sqrt{\frac{M_{weight\ He}}{M_{weightCO2}}}$$

Where $\propto_k$ = Knudsen theoretical selectivity, $M_{weightHe}$ = Molecular weight of helium (g/mol) and $M_{weightCO2}$ = Molecular weight of CO_2 (g/mol).

Table E2 : Calculated Knudsen selectivity values of gases with respect to CO_2.

Gases	**Knudsen selectivity ($\propto_k$)**
α_kHe/CO_2	0.30
α_kAr/CO_2	0.95
$\alpha_k N_2/CO_2$	0.79

APPENDIX J: CALCULATION OF THICKNESS FOR SILICA MEMBRANE

The thickness of the gas through the membrane can be obtained from the equation:

$$L = \frac{W_2 - W_1}{A\rho(1-\varepsilon)}$$

Where L = membrane thickness (m), A = membrane are (m^2), ρ = the theoretical density of alumina ($2.1gcm^{-3}$), W_1= initial weight of the alumina support (g), ε = membrane porosity (45 %), W_2 = total weight of the support and membrane (g). The thickness of the 1st dip-coated membrane was calculated as shown below:

$$L = \frac{48.3g - 48.0g}{0.0193m2\ x\ 2.1g\ (1-0.45)^{-}} = \frac{0.3g}{22.2915} = 0.013\text{m}$$

APPENDIX K: CALCULATION OF GAS PERMEABILITY

The permeability of the gas through the membrane can be obtained from the equation:

$$\text{F} = \frac{\text{J} * \delta}{\Delta\text{P}}$$

Where δ is the membrane thickness (m), F = permeability (mol m $s^{-1}m^{-2}$ Pa^{-1}), J = flux (mol m^{-2} s^{-1}) and ΔP is the transmembrane pressure drop (bar). The thickness of the membrane was determine using appendix J. An example of permeability calculation for helium gas at 0.30bar through the unmodified support at 298K, as detailed below:

$$F = \frac{\mathbf{0.0475}\ \boldsymbol{molm^{-2}s^{-1}} \quad \boldsymbol{X}\ \mathbf{0.013}\boldsymbol{m}}{30000} = 2.058 \text{ x } 10^{-8}$$

APPENDIX L: CALCULATION OF AMOUNT OF SOLVENT FOR GC-MS ANALYSIS

The concertation of the lactic acid feed before the injection of the solvent unto the GC-MS was determine as shown in the equation below. The dilution factor was first of all calculated and the amount was converted from percentage to ppm.

1% = 10,000ppm

1mL → 100mL

0.1mL → 10

0.01mL → 1 = 10μL

In other to analyse the solvent on the GC-MS, 10 µL of the ester product was measured in all cases using a µL pipette and was further diluted using a diluting solvent.

N/B: This method was also used for the inject of the lactic acid feed that was obtained from the membrane process.

APPENDIX M: LACTIC ACID FEED CONVERSION

The conversion of the lactic acid using each cation-exchange resin was calculated using the following equation:

$$\textbf{Conversion (\%)} = \frac{C_{O} - C_{i}}{C_{o}} \; x \; \mathbf{100} \; \%$$

Where C_o represent the initial concentration of the lactic acid that was used as reactant at determined reaction time and C_i represent the concentration of the lactic acid that was obtained at the end of the reaction time from the GC-MS analysis respectively. A typical example of the ester product conversion catalysed with amberlyst 36 catalysts at 60 °C is shown below:

$$\text{Lactic acid feed conversion (\%)} = \frac{90-0.8304}{90} * 100 = \frac{89.1696}{90} * 100$$

Lactic acid feed conversion (%) = 0.99077 * 100

Lactic acid feed conversion (%) = 99.077%

N/B: This equation was used for the calculation of the ester product conversion for both the batch process esterification and the process intensification of catalysts coupled with the cellulose acetate membrane at different reaction temperature.

APPENDIX N: SCANNED COPY OF GC-MS METHOD

Appendix N describe the GC-MS method that was build and used for the analysis of the lactic acid feed result.

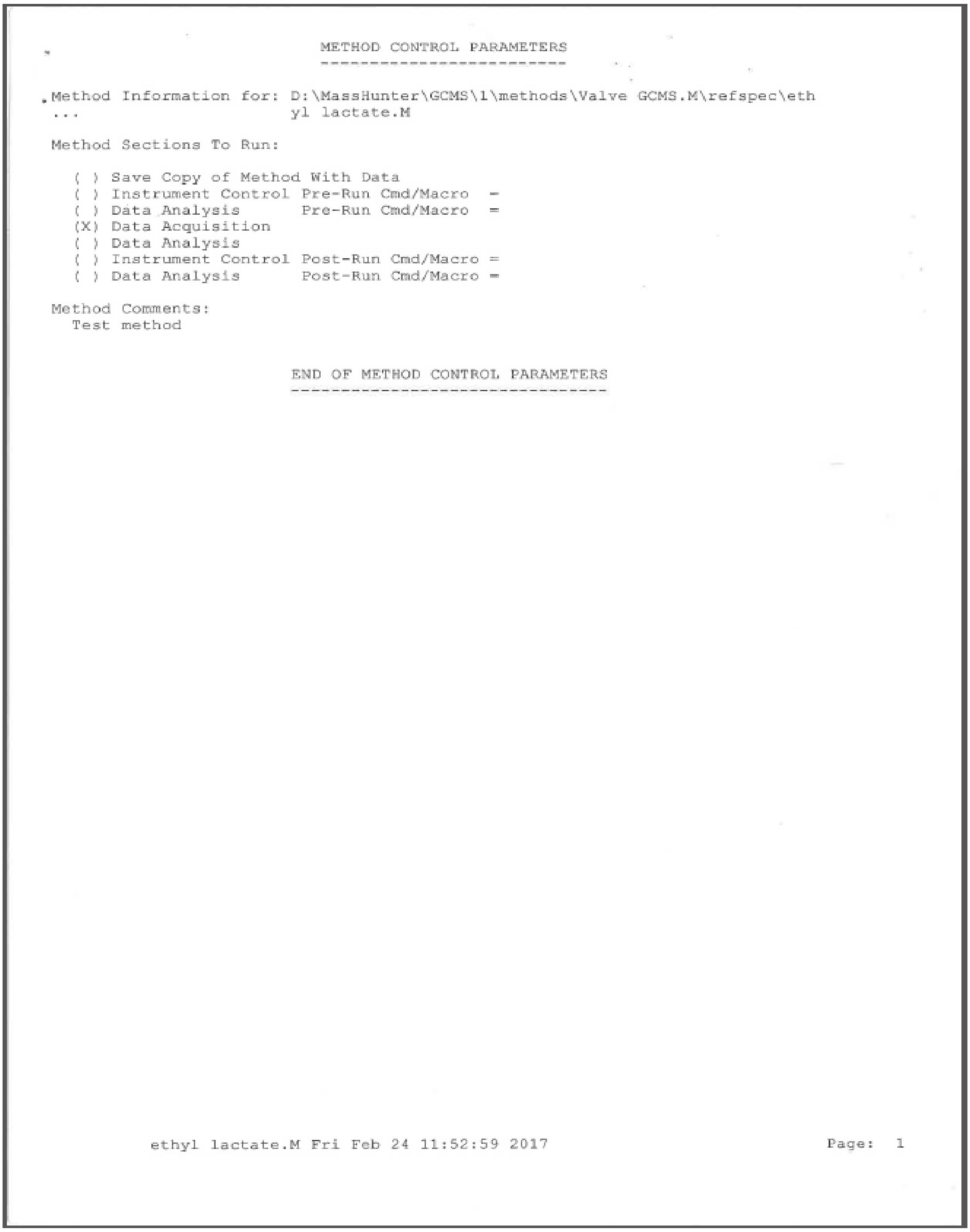

```
                         METHOD CONTROL PARAMETERS
                         -------------------------

Method Information for: D:\MassHunter\GCMS\1\methods\Valve GCMS.M\refspec\eth
...                     yl lactate.M

Method Sections To Run:

  ( ) Save Copy of Method With Data
  ( ) Instrument Control Pre-Run Cmd/Macro  =
  ( ) Data Analysis      Pre-Run Cmd/Macro  =
  (X) Data Acquisition
  ( ) Data Analysis
  ( ) Instrument Control Post-Run Cmd/Macro =
  ( ) Data Analysis      Post-Run Cmd/Macro =

Method Comments:
  Test method

                      END OF METHOD CONTROL PARAMETERS
                      --------------------------------
```

```
ethyl lactate.M Fri Feb 24 11:52:59 2017                          Page:  1
```

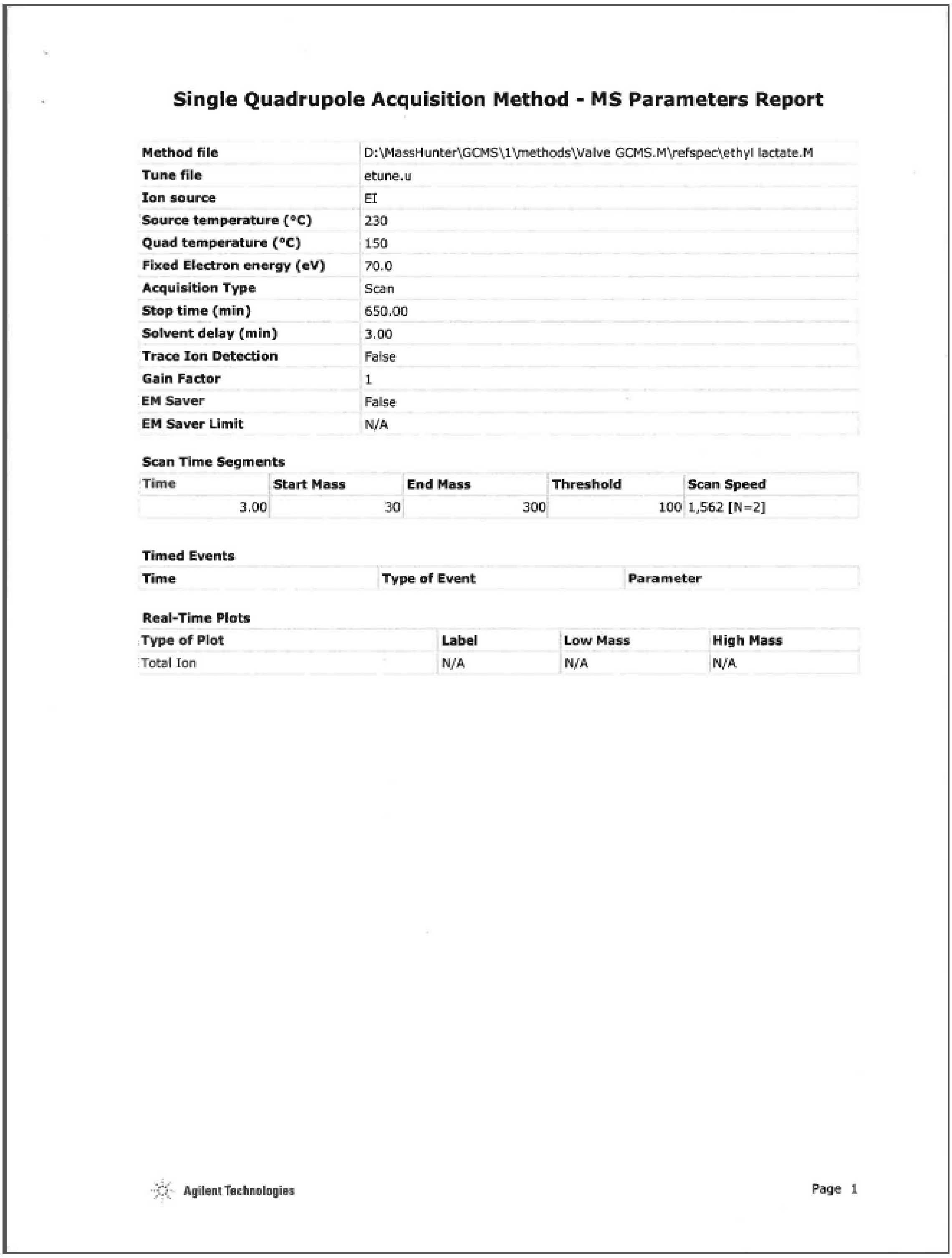

Single Quadrupole Acquisition Method - MS Parameters Report

Method file	D:\MassHunter\GCMS\1\methods\Valve GCMS.M\refspec\ethyl lactate.M
Tune file	etune.u
Ion source	EI
Source temperature (°C)	230
Quad temperature (°C)	150
Fixed Electron energy (eV)	70.0
Acquisition Type	Scan
Stop time (min)	650.00
Solvent delay (min)	3.00
Trace Ion Detection	False
Gain Factor	1
EM Saver	False
EM Saver Limit	N/A

Scan Time Segments

Time	**Start Mass**	**End Mass**	**Threshold**	**Scan Speed**
3.00	30	300	100	1,562 [N=2]

Timed Events

Time	**Type of Event**	**Parameter**

Real-Time Plots

Type of Plot	**Label**	**Low Mass**	**High Mass**
Total Ion	N/A	N/A	N/A

Agilent Technologies

Page 1

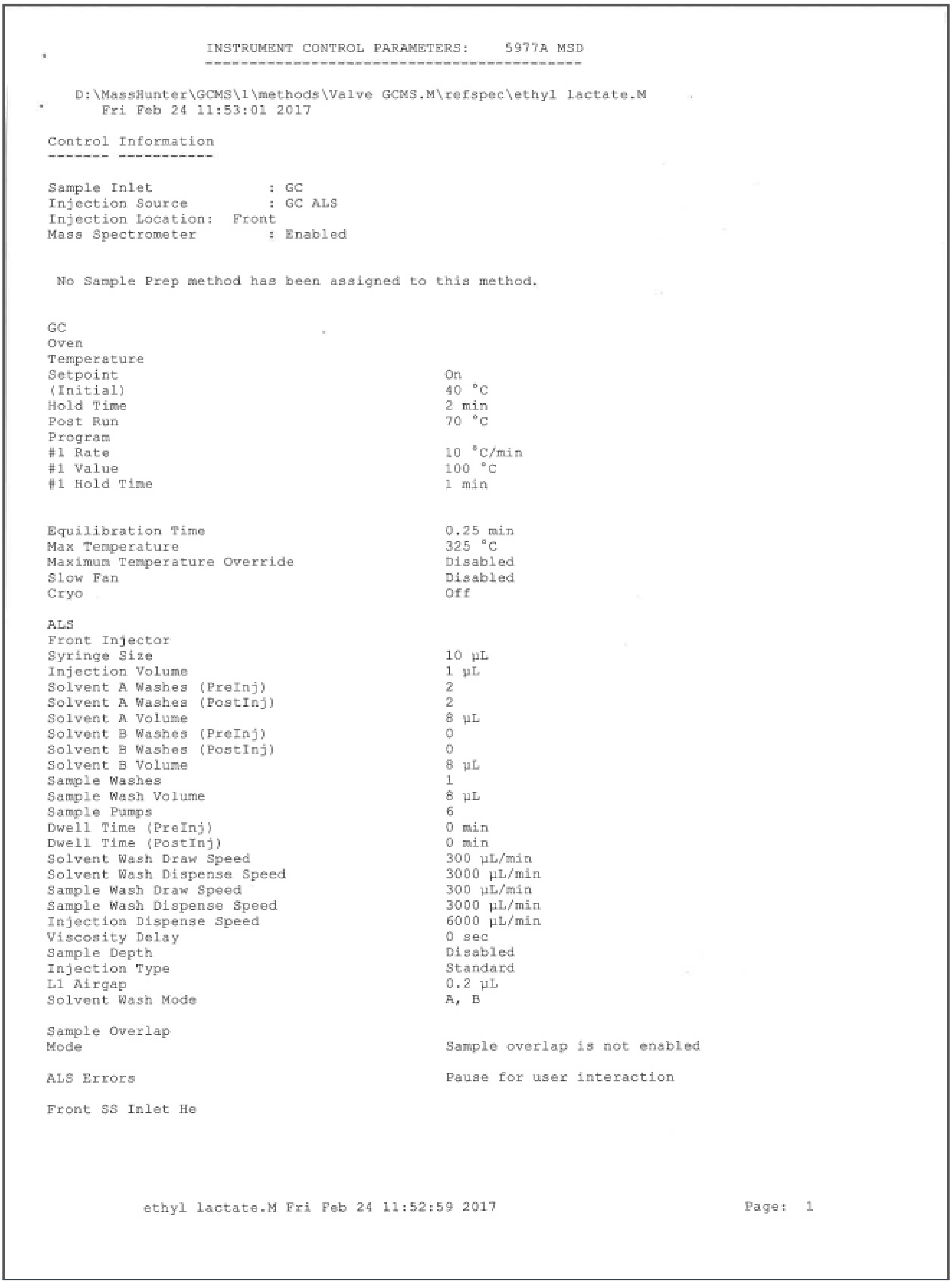

```
                  INSTRUMENT CONTROL PARAMETERS:    5977A MSD
                  -------------------------------------------

   D:\MassHunter\GCMS\1\methods\Valve GCMS.M\refspec\ethyl lactate.M
      Fri Feb 24 11:53:01 2017

Control Information
------- -----------

Sample Inlet            : GC
Injection Source        : GC ALS
Injection Location:  Front
Mass Spectrometer       : Enabled


 No Sample Prep method has been assigned to this method.


GC
Oven
Temperature
Setpoint                                      On
(Initial)                                     40 °C
Hold Time                                     2 min
Post Run                                      70 °C
Program
#1 Rate                                       10 °C/min
#1 Value                                      100 °C
#1 Hold Time                                  1 min


Equilibration Time                            0.25 min
Max Temperature                               325 °C
Maximum Temperature Override                  Disabled
Slow Fan                                      Disabled
Cryo                                          Off

ALS
Front Injector
Syringe Size                                  10 µL
Injection Volume                              1 µL
Solvent A Washes (PreInj)                     2
Solvent A Washes (PostInj)                    2
Solvent A Volume                              8 µL
Solvent B Washes (PreInj)                     0
Solvent B Washes (PostInj)                    0
Solvent B Volume                              8 µL
Sample Washes                                 1
Sample Wash Volume                            8 µL
Sample Pumps                                  6
Dwell Time (PreInj)                           0 min
Dwell Time (PostInj)                          0 min
Solvent Wash Draw Speed                       300 µL/min
Solvent Wash Dispense Speed                   3000 µL/min
Sample Wash Draw Speed                        300 µL/min
Sample Wash Dispense Speed                    3000 µL/min
Injection Dispense Speed                      6000 µL/min
Viscosity Delay                               0 sec
Sample Depth                                  Disabled
Injection Type                                Standard
L1 Airgap                                     0.2 µL
Solvent Wash Mode                             A, B

Sample Overlap
Mode                                          Sample overlap is not enabled

ALS Errors                                    Pause for user interaction

Front SS Inlet He




           ethyl lactate.M Fri Feb 24 11:52:59 2017                                  Page:  1
```

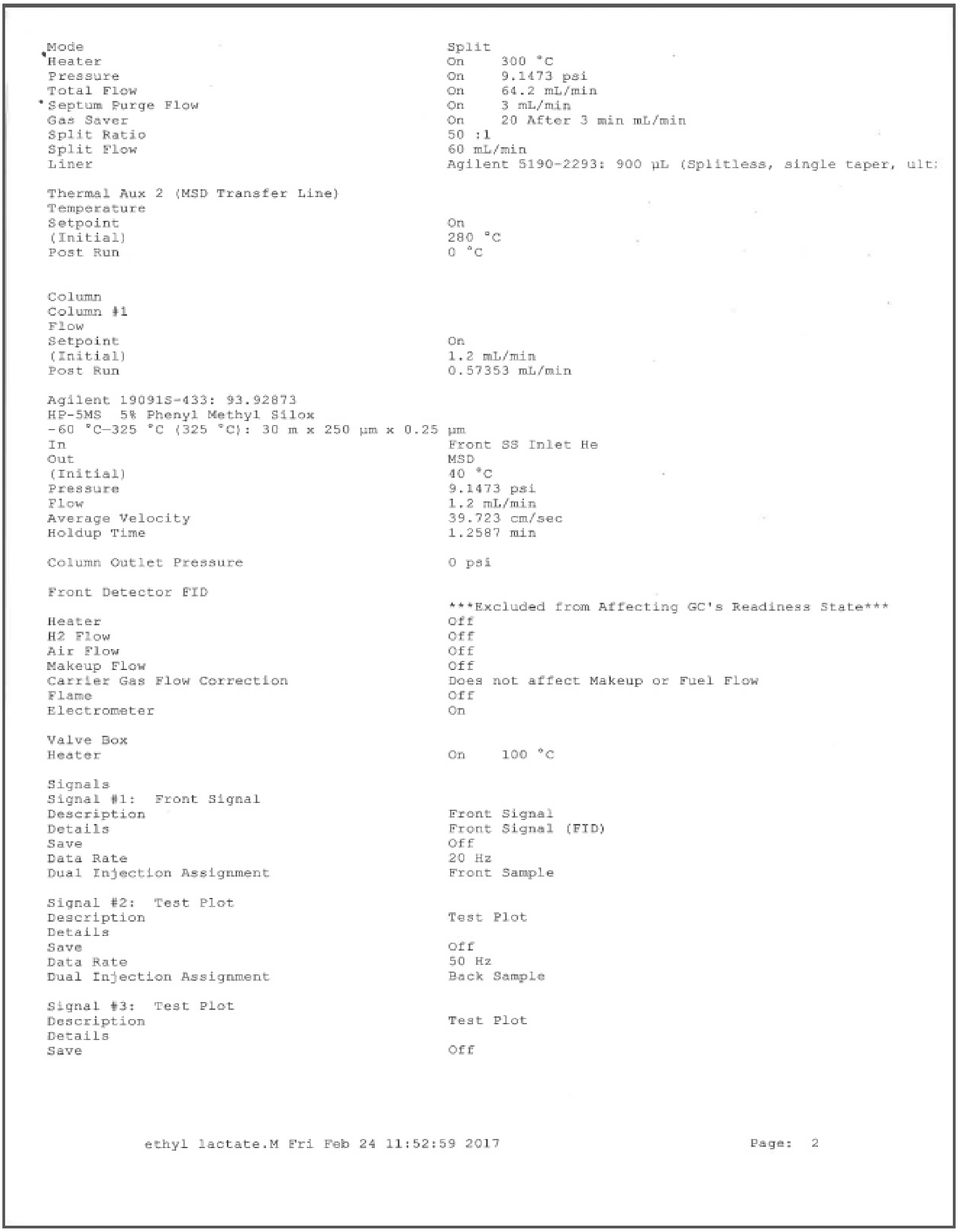

```
Mode                                         Split
Heater                                       On     300 °C
Pressure                                     On     9.1473 psi
Total Flow                                   On     64.2 mL/min
Septum Purge Flow                            On     3 mL/min
Gas Saver                                    On     20 After 3 min mL/min
Split Ratio                                  50 :1
Split Flow                                   60 mL/min
Liner                                        Agilent 5190-2293: 900 µL (Splitless, single taper, ult:

Thermal Aux 2 (MSD Transfer Line)
Temperature
Setpoint                                     On
(Initial)                                    280 °C
Post Run                                     0 °C


Column
Column #1
Flow
Setpoint                                     On
(Initial)                                    1.2 mL/min
Post Run                                     0.57353 mL/min

Agilent 19091S-433: 93.92873
HP-5MS  5% Phenyl Methyl Silox
-60 °C-325 °C (325 °C): 30 m x 250 µm x 0.25 µm
In                                           Front SS Inlet He
Out                                          MSD
(Initial)                                    40 °C
Pressure                                     9.1473 psi
Flow                                         1.2 mL/min
Average Velocity                             39.723 cm/sec
Holdup Time                                  1.2587 min

Column Outlet Pressure                       0 psi

Front Detector FID
                                             ***Excluded from Affecting GC's Readiness State***
Heater                                       Off
H2 Flow                                      Off
Air Flow                                     Off
Makeup Flow                                  Off
Carrier Gas Flow Correction                  Does not affect Makeup or Fuel Flow
Flame                                        Off
Electrometer                                 On

Valve Box
Heater                                       On     100 °C

Signals
Signal #1:  Front Signal
Description                                  Front Signal
Details                                      Front Signal (FID)
Save                                         Off
Data Rate                                    20 Hz
Dual Injection Assignment                    Front Sample

Signal #2:  Test Plot
Description                                  Test Plot
Details
Save                                         Off
Data Rate                                    50 Hz
Dual Injection Assignment                    Back Sample

Signal #3:  Test Plot
Description                                  Test Plot
Details
Save                                         Off



          ethyl lactate.M Fri Feb 24 11:52:59 2017                      Page:  2
```

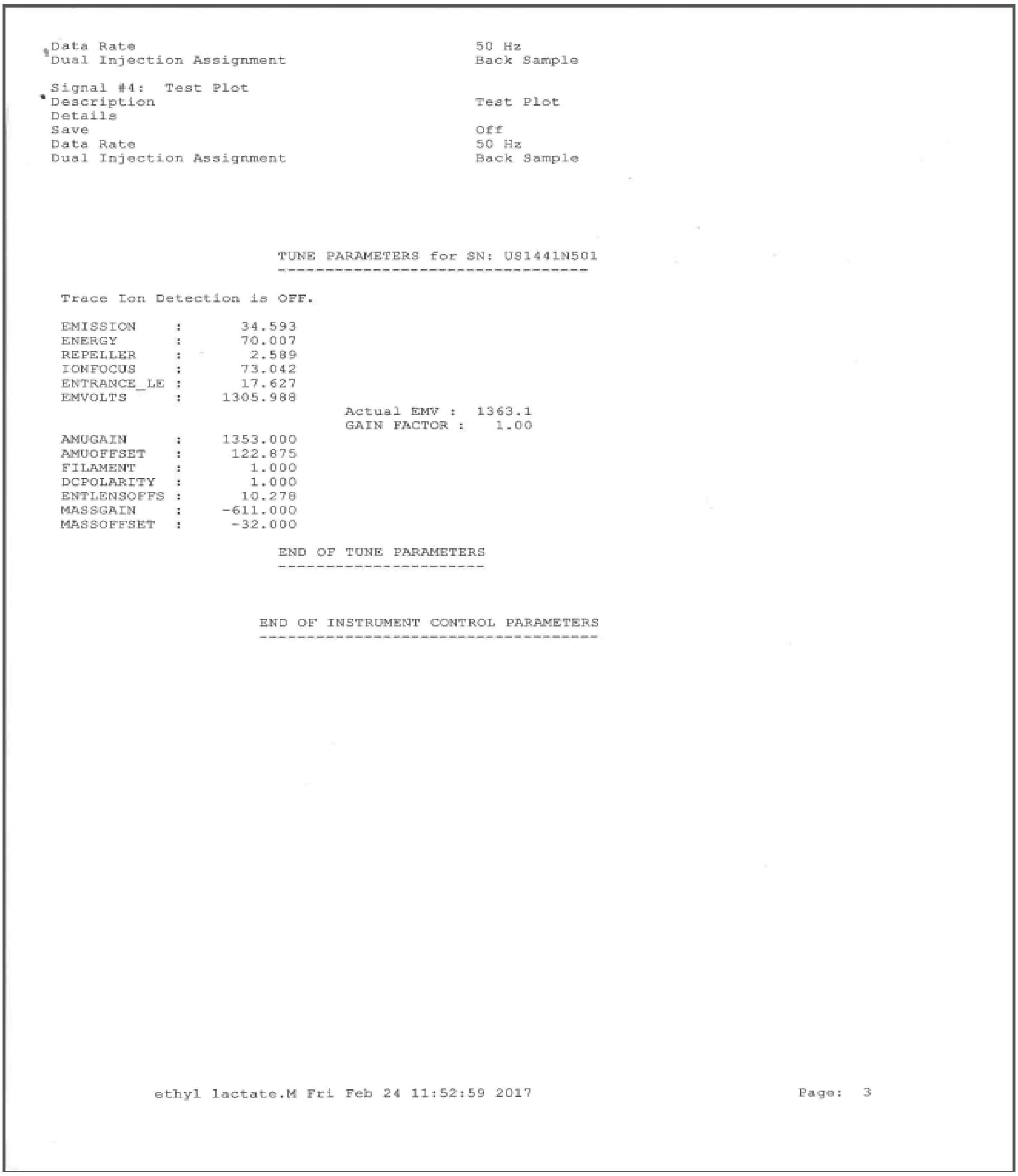

```
Data Rate                                     50 Hz
Dual Injection Assignment                     Back Sample

Signal #4:  Test Plot
Description                                   Test Plot
Details
Save                                          Off
Data Rate                                     50 Hz
Dual Injection Assignment                     Back Sample



                        TUNE PARAMETERS for SN: US1441N501
                        ---------------------------------

 Trace Ion Detection is OFF.

 EMISSION     :       34.593
 ENERGY       :       70.007
 REPELLER     :        2.589
 IONFOCUS     :       73.042
 ENTRANCE_LE  :       17.627
 EMVOLTS      :     1305.988
                                Actual EMV :  1363.1
                                GAIN FACTOR :    1.00
 AMUGAIN      :     1353.000
 AMUOFFSET    :      122.875
 FILAMENT     :        1.000
 DCPOLARITY   :        1.000
 ENTLENSOFFS  :       10.278
 MASSGAIN     :     -611.000
 MASSOFFSET   :      -32.000

                        END OF TUNE PARAMETERS
                        ----------------------


                      END OF INSTRUMENT CONTROL PARAMETERS
                      ------------------------------------




           ethyl lactate.M Fri Feb 24 11:52:59 2017                    Page:  3
```

Figure N1: Scanned copy of method used in the autosampler Agilent Gas Chromatograph-mass spectrometry for the lactic acid feed analysis.

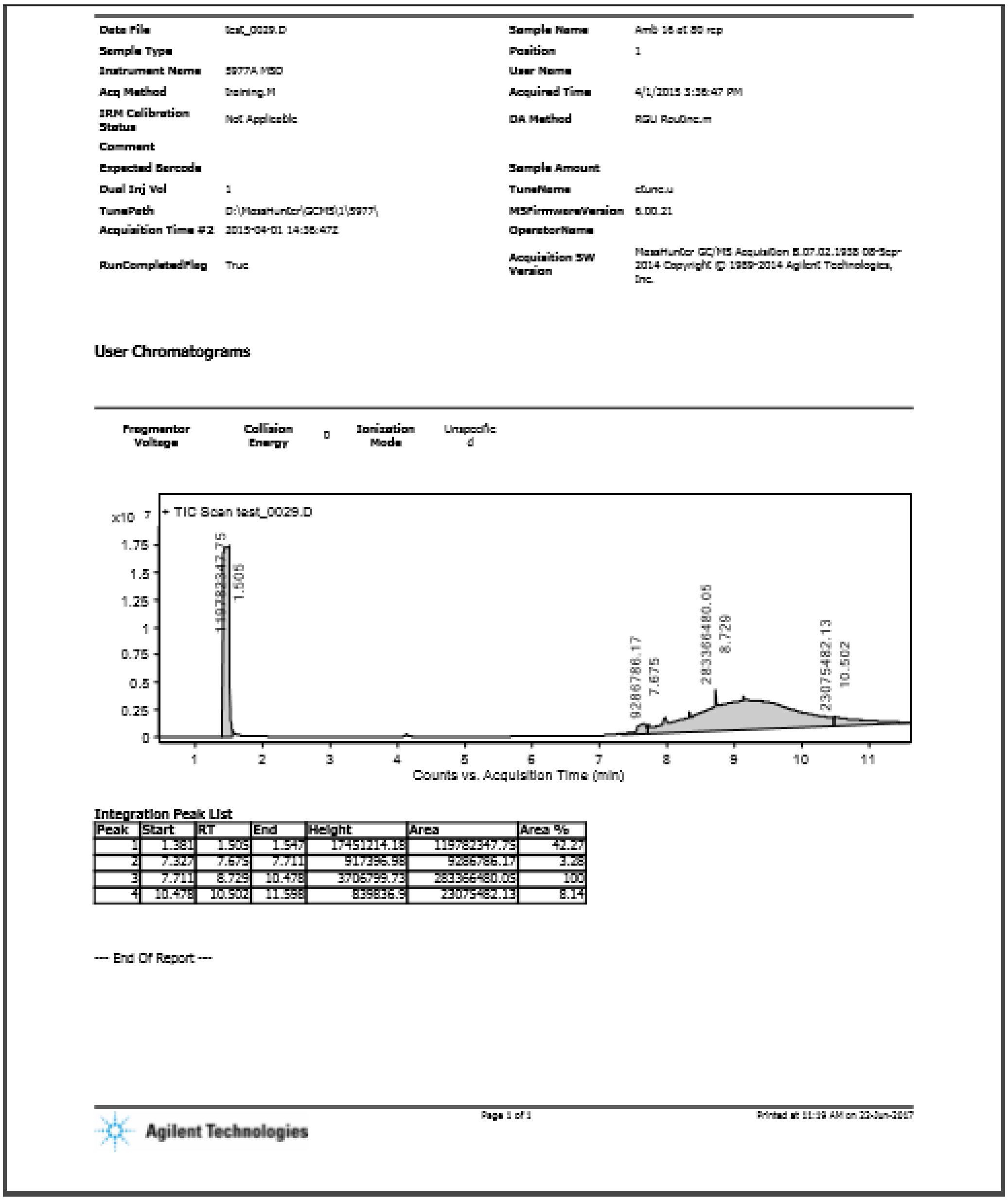

Data File	test_0029.D	**Sample Name**	Amb 16 at 80 rep
Sample Type		**Position**	1
Instrument Name	5977A MSD	**User Name**	
Acq Method	training.M	**Acquired Time**	4/1/2015 3:38:47 PM
IRM Calibration Status	Not Applicable	**DA Method**	RGU RouOnc.m
Comment			
Expected Barcode		**Sample Amount**	
Dual Inj Vol	1	**TuneName**	atune.u
TunePath	D:\MassHunter\GCMS\1\5977\	**MSFirmwareVersion**	6.00.21
Acquisition Time #2	2015-04-01 14:38:47Z	**OperatorName**	
RunCompletedFlag	True	**Acquisition SW Version**	MassHunter GC/MS Acquisition B.07.02.1938 08-Sep-2014 Copyright © 1989-2014 Agilent Technologies, Inc.

User Chromatograms

Fragmentor Voltage		**Collision Energy**	0	**Ionization Mode**	Unspecified	

Integration Peak List

Peak	Start	RT	End	Height	Area	Area %
1	1.381	1.505	1.547	17451214.18	119782347.75	42.27
2	7.327	7.675	7.711	917396.98	9286786.17	3.28
3	7.711	8.729	10.478	3706799.73	283366480.05	100
4	10.478	10.502	11.598	839836.9	23075482.13	8.14

--- End Of Report ---

Agilent Technologies

Page 1 of 1

Printed at 11:19 AM on 22-Jun-2017

Figure N2: GC-MS chromatogram of lactic acid feed catalysed with amberlyst 16 at 80 ºC.

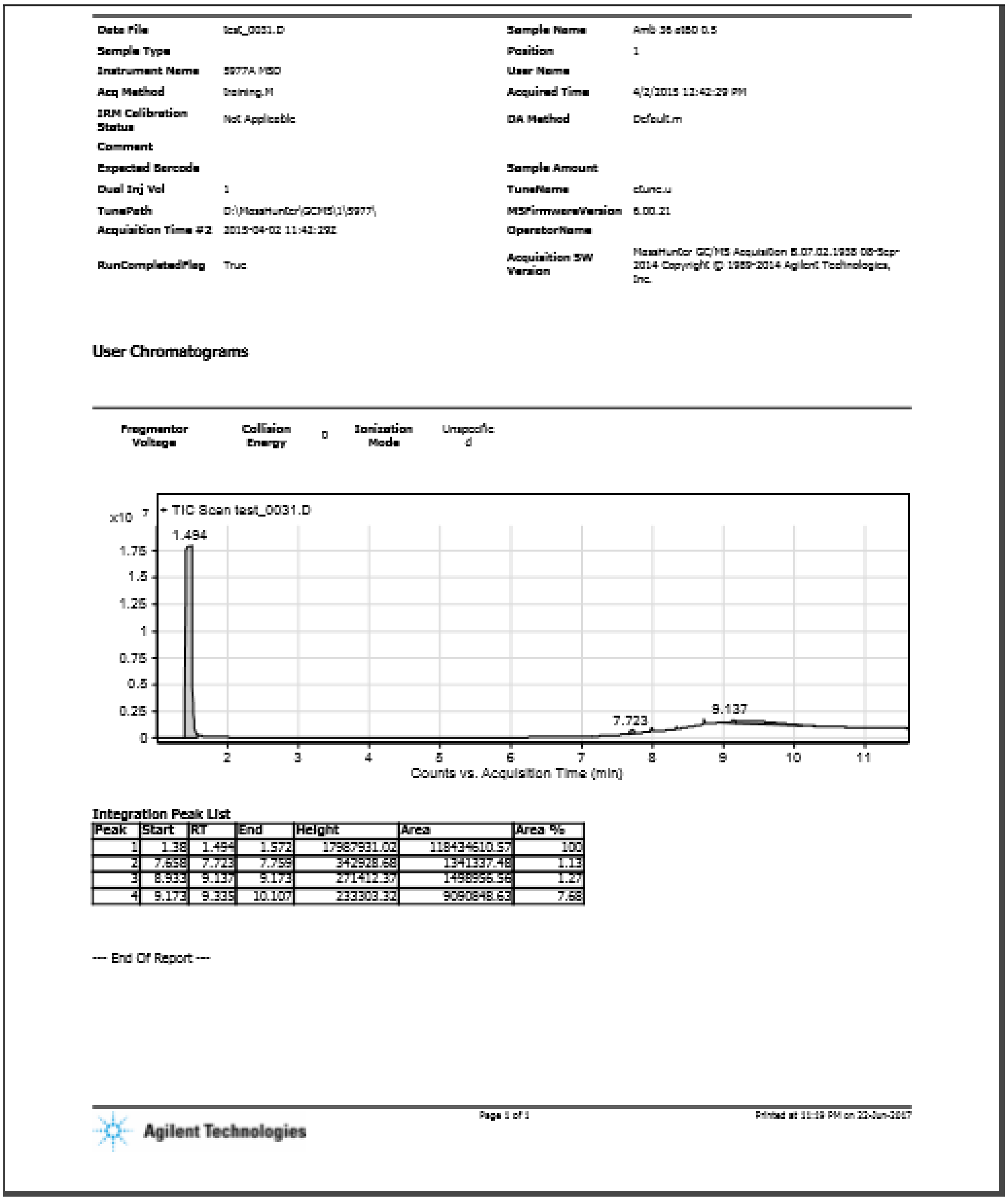

Data File	test_0031.D	**Sample Name**	Amb 36 al80 0.5
Sample Type		**Position**	1
Instrument Name	5977A MSD	**User Name**	
Acq Method	training.M	**Acquired Time**	4/2/2015 12:42:29 PM
IRM Calibration Status	Not Applicable	**DA Method**	Default.m
Comment			
Expected Barcode		**Sample Amount**	
Dual Inj Vol	1	**TuneName**	atune.u
TunePath	D:\MassHunter\GCMS\1\5977\	**MSFirmwareVersion**	6.00.21
Acquisition Time #2	2015-04-02 11:42:29Z	**OperatorName**	
RunCompletedFlag	True	**Acquisition SW Version**	MassHunter GC/MS Acquisition B.07.02.1938 08-Sep-2014 Copyright © 1989-2014 Agilent Technologies, Inc.

User Chromatograms

Fragmentor Voltage		**Collision Energy**	0	**Ionization Mode**	Unspecified

Integration Peak List

Peak	Start	RT	End	Height	Area	Area %
1	1.38	1.494	1.572	17987931.02	118434610.57	100
2	7.638	7.723	7.759	342928.68	1341337.48	1.13
3	8.933	9.137	9.173	271412.37	1498996.56	1.27
4	9.173	9.335	10.107	233303.32	9090848.63	7.68

--- End Of Report ---

Page 1 of 1

Printed at 11:19 PM on 22-Jun-2017

Figure N3: GC-MS chromatogram of lactic acid feed catalysed with amberlyst 16 at 100 ºC.

APPENDIX O: MATHEMATICAL MODEL DESCRIPTION

Appendix O describe the permeance and flow rate vs gauge pressure plot using Minitab 2016 model.

Description for the mathematical model

Login to the University computer network and click on the Minitab 16 icon

Data Entry

In columns C1 to C4 enter the experimental results for the gases. Use headings He, Ar, N_2 and CO_2 in the space provided above the first row. We need four rows as we have 4 pieces of data for each sample. Create two further column of labels, Gauge pressure (C5) and Gases (C6) and type in these columns the abbreviations for the variables measured (the gases He-CO_2) and the sample collected (gauge pressure, No1..No10). These labels will be used when plotting. Add the following labels above the columns indicated: PC1 (C7), PC2 (C8), …PC4 (C10), and Scores1 (C11), Scores2 (C12), … Scores4 (C14). We need 4 columns for the PC information, as the four gases will give us 4 new variables (PCs). We will also need 4 columns for Scores information.

Data Analysis

Select **Stat**⎸ **Multivariate**⎸ **Principal Components**

In the Principal Components Analysis dialog box for *Variables*, highlight He – CO_2 and click **Select**.
Set the *Number of components to be computed* to **4**.
Set the *Type of Matrix* to **Correlation**.
For *Storage*, select the **Coefficients** box and enter PC1 – PC4 (C7-C10)
For *Storage*, select the **Scores** box and enter Scores1 – Scores5 (C11-C14) click **OK.**
You can leave **Eigenvalues** Blank
For Graphs, select *Scree*, *Score* and *Loading Plot.*

The output in the Session Window will appear as in the table N1 below. In addition, 3 graphs will be produced.